Investigating Defects and Magnetism in Nanocrystals by Magnetic Spectroscopies

Michael C. De Siena

A dissertation
submitted in partial fulfillment of the
requirements for the degree of

Doctor of Philosophy

University of Washington

2020

Reading committee:

Daniel R. Gamelin, Chair

Brandi M. Cossairt

Peter J. Pauzauskie

Program authorized to offer degree:

Chemistry

University of Washington

Abstract

Investigating Defects and Magnetism in Nanocrystals by
Magnetic Spectroscopies

Michael C. De Siena

Chair of the Supervisory Committee:
Professor Daniel R. Gamelin
Department of Chemistry

Magnetically-active nanocrystals have long attracted significant attention for their prospective applications in spintronics and other emergent technologies. Additionally, nanocrystals doped with magnetic impurities are also of interest for various phosphor, and other opto-electronic technologies. In order to improve and facilitate the use of these materials for devices, a thorough understanding of their electronic and magnetic properties is needed. Here, we explore the incorporation and speciation of transition metal-dopants in luminescent nanocrystals by taking advantage of their magnetic properties, as well as the effects of size confinement on the magnetic properties of nanocrystals. Chapter 1 introduces nanocrystals with magnetically-active dopants, explores the spectroscopic techniques used to investigate said nanocrystals, and expands upon the evolution of magnetism upon size confinement. Chapter 2 investigates through a combination of electron paramagnetic resonance (EPR) and photoluminescence spectroscopies the speciation of Mn^{2+} dopants in halide perovskite

nanocrystals during typical post-synthetic anion exchange manipulations. This study reveals that during the anion exchange process, Mn^{2+} dopants cluster into regions of high lighter-halide (*i.e.*, Cl^- ions) concentrations forming antiferromagnetic domains. Chapter 3 discusses using variable-temperature magnetic circular dichroism (MCD) spectroscopy to study the magnetic band gap splittings in colloidal EuS and EuSe nanocrystals as well as EPR spectroscopy to investigate the magnetization of EuS nanocrystals and the role trivalent impurity ions have on this magnetism. These studies document the giant band-gap splittings in europium(II) monochalcogenide nanocrystals as well as reveal how common approaches for mediating the magnetic ordering temperature (Curie temperature) of bulk EuS may not be suited for accomplishing the same in nanocrystals. This latter study also addresses what role of trivalent impurity ions play in the magnetization of EuS nanocrystals. In Chapter 4, we introduce the first preparation of nanocrystals of the chromium trihalides (Br^-, I^-). These materials have been shown to have layer-dependent magnetism as exfoliated bulk materials. We show that these effects also apply to nanocrystals of the materials though magnetic circular dichroism spectroscopy measurements. We additionally investigate the effects of lateral size miniaturization. In short, this work focuses on using unique magnetic spectroscopic tools to investigate the properties opto-electronic and magnetic properties of materials at the nanoscale.

In memory of

Carmine Lionelli

Acknowledgments

First off, I want to thank Prof. Daniel Gamelin for welcoming me into his lab at the University of Washington and for providing every resource possible for me to develop as a scientist. Your ability to weave a scientific story has truly been inspiring and given me something to continue to strive for as I continue on my journey in chemistry. Thank you for all the times we've just chatted about cool science ideas, for involving me in several interdisciplinary research projects, and most importantly, for giving me the freedom to pursue my own research path.

Next, I want to thank my committee members. Prof. Brandi Cossairt, I have always truly valued your feedback and help, especially during planning for the MEM-C lecture. Prof. Peter Pauzauskie, thank you for all your help over the years as we've discussed our collaborative work together. I have always enjoyed the opportunity to learn from you. Profs. Cody Schlenker and Vince Holmberg, thank you for taking the time to listen to my science over the past few years and for always being able to provide guidance in my science.

The Gamelin Group has been an incredible and supportive home these past several years and I want to thank all members for making this an incredible experience and for sharing in this journey with me. I want to thank Prof. Alina Schimpf who first made me feel welcome and at home in the lab. I always appreciated our nearly daily coffee trips to the library and am indebted to you for introducing me to sour beers and Brouwers. Dr. Kim Hartstein, thank you for all the emotional support over the years. Your friendship has meant so much to me. I miss our adventures in trying new restaurants with Alina and hope that you have success in all your future plant growing adventures. I want to thank Dr. Heidi Nelson for your vital contributions to the CHB 212 office camaraderie. Dr. Charlie Barrows, thank you for your friendship over the years and for always livening up the lab environment. Dr. Patrick Whitham, you have taught me so much about keeping things from falling apart in the lab. I will miss having your tiramisù during my lasagna dinner parties. Thank you, Prof. Katie Knowles, for all your guidance when I was starting out in the lab and for always being willing to help teach me things when I didn't understand them. Dr. Arianna Marchioro, I always enjoyed our group wine and cheese outings and am also so grateful for your mentorship in spectroscopy. Dr. Rachel Fainblat, thank you for helping us all to stay sane during late night magnet runs. I next want to thank Dr. Kira Hughes. Your friendship has been so important to me especially during the dark days of Kim's absence in the lab. Thank you for always encouraging me to take unnecessary coffee breaks. Christian Erickson, thank you for both pushing me to make the best arguments I could and for always being willing to help me when needed in lab. I next want to thank Alec Rachkov. I enjoyed mentoring you and learned so much from you too. I look forward to watching how you continue your scientific journey. Jose Araujo, you have been an amazing friend these past few years. Thank you for always being up for a trip to the local fish store and for helping me realize my crazy building projects. Next, I want to thank two people without whom I would never have learned as much as I did during this experience. Prof. Emily Tsui, you taught me so much about science and how to run reactions. You have always been able and willing

to help me learn as much as I can. I am so grateful that we have become friends and look forward to watching your career grow. Prof. Sid Creutz, I am so grateful for your friendship and for you putting up with me as we worked together over these past few years. I have been so lucky to have your guidance as I've worked to finish up my various research projects and have learned so much from you.

I have always enjoyed fish keeping but hadn't kept an aquarium since high school. Then, through getting to know Jose in the lab several years ago, I learned that we shared an interest in aquarium keeping and was then encouraged by him to setup my own aquarium again. We subsequently went to a fish store and I left with a new tank and a bunch of related equipment going way past what I had originally planned to buy but that is par for the course in this hobby. Through this, Jose and I became "fish friends" and one aquarium turned into way too many. This hobby has given me many friends and a wonderful community here in Seattle. I have learned so much through this hobby from all of my friends in the local Seattle aquarium scene especially from Steve Waldron at Aquarium Zen who has helped me to develop my eye for aquascaping and for being a great resource in fish keeping. Through this hobby, I joined the Greater Seattle Aquarium Society and have been so grateful for this welcoming community. This hobby and community have been my oasis during my time in grad school and for it I am so thankful.

Lastly, my family means everything to me and without their support I would never have been able to do this. To my siblings: Marissa, Alyssa, Alaina, and James, thank you for your love and support these past few years. I would not have come as far without all your support and now I can finally answer your question of what I even do with this work. To my parents whose constant support has allowed me to go this far with my education. To my father who has inspired my love of science and always encouraged me to pursue my own path. And finally, to my mother who's love and support has meant so much to me, thank you for all that you have sacrificed for me. To all of my family, thank you.

Table of Contents

List of Figures and Schemes

List of Tables

Chapter 1: Introduction

1.1 Overview

Semiconductor nanocrystals (NCs) have attracted considerable research attention for their potential in several applications such as in solid-state lighting, solar energy conversion, and bioimaging.[1-6] The desired properties of NCs for these various applications can further be tuned through the introduction of impurity defects, or dopants.[7-11] For example, dopant ions can impart new luminescence pathways in NCs that then affect how these materials are used in lighting and phosphor technologies. In order to fully utilize these materials, a thorough understanding of their electronic and magnetic properties, including how these can be further tuned through strategies such as doping, is required. First, we begin with an introduction to the general effects of doping NCs with transition metals and lanthanide ions, paying particular attention to the effects of doping paramagnetic ions. Second, the effects of size confinement on fundamental magnetic properties will be introduced. This will involve a discussion of how one of the most distinct "defects" in NCs, the surface, affects magnetic properties. Third, we will discuss how magnetic spectroscopies can be used to study these systems. This section will introduce the fundamentals of electron paramagnetic resonance (EPR) spectroscopy and how, in conjunction with magnetic circular dichroism (MCD) spectroscopy, it can be used to elucidate the long-range magnetic ordering properties of NCs. We demonstrate that these tools can provide magnetic information as well as information about the speciation of dopants in NCs. This work is intended as an overview of the types of effects that incorporating magnetic dopants and modifying other types of defects have on the electronic and magnetic properties of NCs with particular focus on the spectroscopies used.

1.2 A brief introduction to doping nanomaterials with magnetically-active impurities

1.2.1 Doping nanocrystals for luminescence applications

Photoexcitation of semiconductor NCs moves an electron from the valence band (VB) to the conduction band (CB) forming an excitonic excited state. In undoped NCs, this excited state commonly relaxes to the ground state either through emission of a photon, or through various nonradiative processes such as ones involving additional trap states that may be present in the system (Scheme 1.1).[6] When luminescently-active dopant ions, often referred to as activators, are incorporated into these NC systems, they introduce new pathways for the relaxation from the excited state to the ground state. Two well-studied examples of transition metal dopants for this process are Mn^{2+} and Cu^{+}.[11-14]

Cu^{+} incorporation in NCs introduces a well-defined "engineered" hole trap to the electronic structure. With this Cu^{+} hole trap state present, the excitonic state formed upon photoexcitation of

Cu^{+}-doped NCs first relaxes nonradiatively to the Cu^{+} hole trap state and then subsequently radiatively to the ground state.[11] This process results in luminescence that is both considerably red-shifted from that of the exciton and very broad, a result of the large reorganization energy associated with this transition.[15] This process is depicted below in Scheme 1.1. In contrast, Mn^{2+} activator NC systems do not introduce a specific Mn-based trap to the electronic structure. Rather, Mn^{2+} dopants introduce Mn^{2+}-based *d–d* states that can be activated through an energy transfer processes as depicted below in Scheme 1.1.[12]

Scheme 1.1 Common photoluminescence mechanisms in doped-nanocrystals.

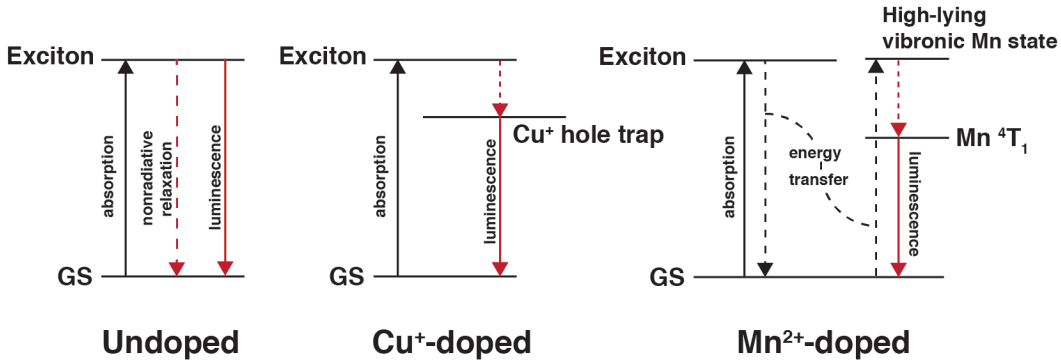

To further expand upon this process, we can use the example of Mn^{2+}:$CsPbCl_3$ NCs, a doped-perovskite NC material that is attracting interest for its possible use in LEDs and other phosphor-based technologies.[14,16-18] This system is similar to the generic case described above; however, there is an additional intermediate charge-separated state that is needed for the energy transfer process.[19] From the exciton state there are three competing pathways for relaxation. First, the exciton can just relax (either radiatively or nonradiatively) to the ground state. Second, it can directly transfer energy to an excited Mn^{2+}-based state. Last, it can undergo a thermally-activate exciton fission process to populate a charge-separated state. This charge-separated state can then undergo energy transfer to the excited Mn^{2+}-based state. Once the Mn^{2+}-based state is populated, emission from that state to the ground state can occur and this results in the characteristic Mn^{2+}-centered luminescence in these materials. This process is depicted below in Figure 1.1a. The competition between the two radiative recombination pathways in this material can then be modulated by varying the concentration of Mn^{2+} dopants. This effect is visually depicted in Figure 1.1b.

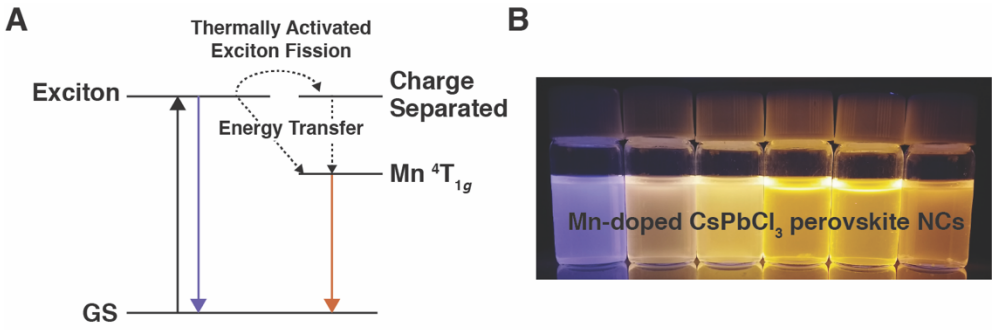

Figure 1.1. Luminescence in Mn^{2+}:$CsPbCl_3$ NCs. (A) Luminescence sensitization scheme for Mn^{2+}:$CsPbCl_3$ NCs depicting the role of the charge-separated state to sensitizing Mn^{2+} emission. **(B)** Photograph of Mn^{2+}:$CsPbCl_3$ NCs under UV excitation as the concentration of Mn^{2+} doped is varied. Adapted with permission from ref. 19. Copyright 2017 American Chemical Society.

1.2.2 Doping nonmagnetic nanocrystals with magnetic impurities

In addition to introducing new luminescence pathways in NCs, Mn^{2+} dopants can also impart new magnetic properties.[20-25] Mn^{2+} ions in semiconductor NCs typically have a high-spin, paramagnetic, d^5 electron configuration. II-VI semiconductor NCs (*i.e.* II = Zn, Cd, Hg, VI = S, Se, Te) doped with Mn^{2+} are characteristic dilute magnetic semiconductors (DMSs).[20] These DMS materials display unique magnetic properties resulting from the incorporation of the magnetically-active Mn^{2+} dopants. These systems have demonstrated spin-glass transitions at low temperature.[20,26] Moreover, the magnetic Mn^{2+} dopants lead to an exchange interaction between the host NC and the dopant. In the case of Mn^{2+}:II-VI NCs, this exchange is between the *sp* band electrons of the parent host and the *d* electrons of the dopant Mn^{2+} ions and is referred to as *sp-d* exchange.[20] This exchange mechanism leads to properties such as large Zeeman band splittings, giant Faraday rotation, and magnetic polaron formation in addition to other effects.[25,27-29] The strength of this exchange interaction depends on the covalency of the material.[20] This exchange interaction tends to be stronger in more covalent materials like II-VI semiconductors.

In contrast, perovskite NCs of the form $CsPbX_3$ (X = Cl, Br, I) are highly ionic materials.[19] Due to this high ionicity, any exchange interaction between a Mn^{2+} dopant and the host lattice (which in this case would take the form of *pp-d* exchange rather than *sp-d* exchange owing to the nature of the bands in the perovskite material) is expected to be very weak, and these DMS properties will not be realized. However, the exchange interaction between Mn^{2+} dopants (Mn^{2+}–Mn^{2+} exchange) will still be present and will depend on the concentration of Mn^{2+} in the lattice due to changes to the distribution and spacing of Mn^{2+} dopant ions.

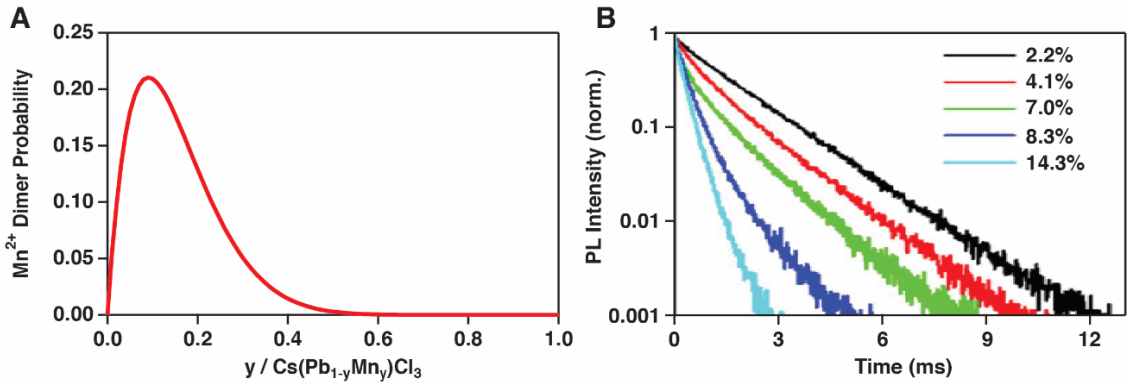

Figure 1.2. Dimers in Mn^{2+}:$CsPbCl_3$ NCs. (A) Mn^{2+} Dimer probability in $CsPbCl_3$ as a function of Mn^{2+} concentration. **(B)** Photoluminescence decay curves measured for Mn^{2+}:$CsPbCl_3$ with varied Mn^{2+} concentration. Mn^{2+} concentrations are given in the panel as a percentage of lead-site occupancy. Panel B adapted with permission from ref. 19. Copyright 2017 American Chemical Society.

Figure 1.2a above illustrates the increase in the concentration of Mn^{2+}–Mn^{2+} dimers with increased concentration of Mn^{2+}. These dimers have two main effects on the properties of Mn^{2+}:$CsPbX_3$ NCs. The first affects the Mn^{2+}-centered luminescence. The luminescent transition in Mn^{2+}:$CsPbX_3$ NCs of isolated $[MnCl_6]^{4-}$ octahedra can be expressed as $\langle {}^4T_{1g}|\mu|{}^6A_{1g}\rangle$. This Mn^{2+} *d–d* transition is formally forbidden. As a result, the lifetime of this transition is quite long, typically on the order of milliseconds.[19,30] In contrast, the luminescent transition of Mn^{2+} dimers can be expressed as $\langle {}^4T_{1g}\,,\ {}^6A_{1g}|\mu|{}^6A_{1g}\,,\ {}^6A_{1g}\rangle$. This transition picks up some spin allowedness through an exchange interaction; this process is known as the Tanabe mechanism of intensity gaining, and manifests as a shortening of the Mn^{2+} luminescence lifetime.[31-32] Figure 1.2b shows the shortening of the Mn^{2+} luminescence decay curve as the concentration of Mn^{2+} in the $CsPbCl_3$ NC lattice increases. Dimer formation contributes to this, but is most likely not the dominant reason for the lifetime shortening. The dominant effect is most likely luminescence concentration quenching as increased Mn^{2+} concentration increases the probability that the energy of the Mn^{2+}-based excited state can transfer amongst Mn^{2+} dopants in the NC and is ultimately quenched by some nonradiative process or trap.[33]

The second main effect of Mn^{2+} dimers in perovskite NCs involves the overall magnetic ordering of the material. Isolated Mn^{2+} dopants are paramagnetic impurities, while the magnetic ordering of Mn^{2+} dimers depends on the overall sign and magnitude of the exchange interaction. In perovskite NCs, this exchange interaction leads to an overall antiferromagnetic ordering between nearest-neighbor Mn^{2+} ion pairs. This difference in magnetic ordering can be easily observed experimentally through EPR measurements. The paramagnetic Mn^{2+} dopants will have a large signal that is observable at room temperature, while the antiferromagnetic Mn^{2+} pairs will be EPR silent. As the concentration of Mn^{2+} in $CsPbCl_3$ increases, the prevalence of manganese clusters containing Mn^{2+}– Mn^{2+} nearest-neighbor antiferromagnetic interactions increases, and the observed EPR signal will decrease. We have recently observed that the concentration of these EPR-silent Mn^{2+} clusters can also be tuned by varying the anion composition and have used EPR measurements to study the

thermodynamic processes driving this process, which have ramifications for doped-perovskite NCs in general. This work will be presented in Chapter 2.

1.2.3 Tuning properties of magnetic nanocrystals via doping

We have so far introduced how dopant ions in NCs can impart new luminescence properties and how magnetic dopants can impart new magnetic properties and provide an additional handle to study fundamental properties of the host material. Now, we turn to how dopants can be used to modulate already magnetic nanomaterials.

The divalent europium chalcogenides are a classic example of magnetic semiconductors. In comparison to DMSs, where magnetic properties are introduced into the material via a magnetically-active impurity, these materials are intrinsically magnetic. The europium(II) chalcogenides have a rich diversity of magnetic ordering behavior ranging from antiferromagnetic to metamagnetic and ferromagnetic with ordering temperatures ranging from 5 K (EuSe, T_N) to 69 K (EuO, T_C).[34] These materials display a high degree of spin polarization[35] resulting from a ferromagnetic band gap splitting, and have attracted attention for "spin-filtering" applications.[36] This band gap splitting will be further discussed in Chapter 4. There has been considerable work done to raise the ordering temperatures of the europium(II) chalcogenides, with particular focus on EuS and EuO.[34,37] In bulk systems of EuS and EuO, this has been realized through the incorporation of excess itinerant electrons.[34,37-40] Excess carriers enhance the indirect exchange in the materials, resulting in an increased Curie temperature (T_C).[34,38-39] These carriers can be introduced through doping with either trivalent lanthanide ions or halide ions.[34] Of these two approaches, doping with trivalent lanthanides, typically Gd^{3+}, is more common. As Gd^{3+} is doped into bulk EuS, there is an increase in T_C until a critical dopant concentration; past this concentration, T_C decreases until the material becomes overall antiferromagnetic and more similar in magnetic behavior to GdS. This is depicted below in Figure 1.3.

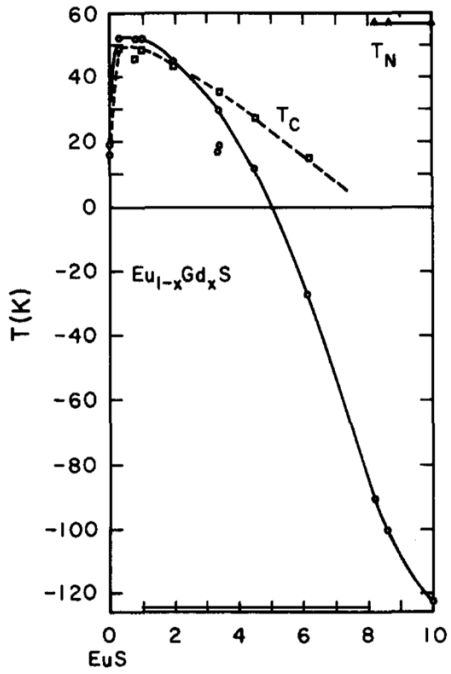

Figure 1.3. Ordering temperatures for $Eu_{1-x}Gd_xS$. Curie-Weiss constant (open circle), Curie (open square) and Néel (open triangle) temperature for $Eu_{1-x}Gd_xS$ as a function of Gd^{3+} content. Figure reprinted from Ref. 34, with permission from Elsevier.

This Gd^{3+} doping approach has not only been used to tune T_C of bulk EuO and EuS, but also to tune T_C of EuS NCs.[41-42] Although a modest increase in T_C upon Gd^{3+} incorporation in EuS NCs has been reported, it remains unclear if the mechanism for this effect (*i.e.*, introduction of free carriers) is the same in the NC systems compared to the bulk. We will expand upon approaches to introduce free carriers into EuS NCs in Chapter 3.

As the concentration of a dopant in a material continues to increase, it becomes no longer advantageous to think of the system as that of a doped material but rather as that of an alloy or solid solution between the undoped host material and the analogous dopant-based material. The formation of these solid solutions is commonly used to tune the band gap between two semiconductors (*e.g.*, solid solutions between $CsPbBr_3$ and $CsPbI_3$) in a process known as band gap engineering. An analogous approach can be used to tune the magnetic ordering properties of two different materials. This approach has been utilized in tuning the magnetic properties of the chromium trihalides, specifically between that of $CrCl_3$ and $CrBr_3$.[43] We will show that the magnetic properties of CrI_3 nanoplatelets can also be tuned through forming solid solutions with $CrBr_3$ in Chapter 4.

1.3 Size effects on magnetic properties

1.3.1 Overview of superparamagnetism

A ferromagnetic particle consists of several magnetic domains separated by domain walls. Within each domain, all spins are aligned in the same direction. However, the spin direction between domains is not aligned. An external magnetic field is required to align the spins of the individual magnetic domains within the particle and in turn generate a net magnetization. As the size of the magnetic particle decreases, it is more energetically favorable for the particle to support fewer magnetic domains. Eventually, the particle can only support a single magnetic domain. In this state, there is no barrier to magnetization reversal and the particle is considered superparamagnetic. This is depicted schematically in Scheme 1.2 below. Superparamagnetic particles have found use in several vital medical applications such as MRI contrast agents[44-45] as well as in more experimental medical applications in treating cancer (*i.e.*, magnetic hyperthermia).[46-47]

Scheme 1.2. Evolution of superparamagnetism

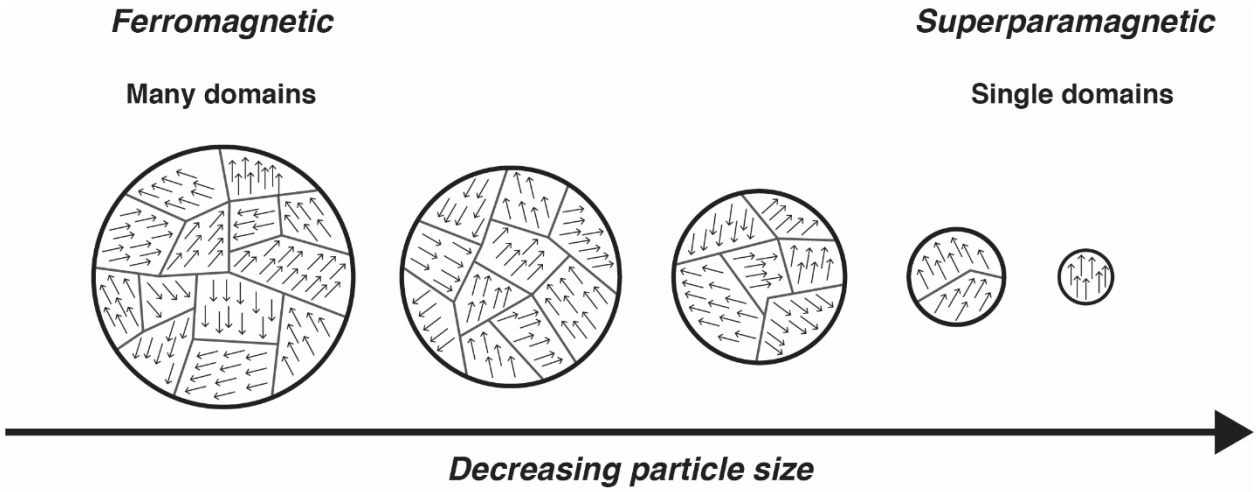

Domains form in magnetic particles in order to minimize the overall energy of the system. Specifically, the overall energy of magnetic domain formation is affected by exchange energy, magnetostatic energy, magnetic anisotropy energy (magnetocrystalline and magnetoelastic anisotropy), and Zeeman energy. When spins in a particle align (an effect of exchange and magnetic anisotropy interactions) they generate an internal magnetic field. This field contains some amount of magnetostatic energy which destabilizes the system. To balance this destabilizing magnetostatic energy, a magnetic particle subdivides into several domains with different spin directions that are separated by domain walls. This lowers the overall induced magnetic field and therefore the magnetostatic energy. However, the formation of the domain walls incurs an energy cost. In a domain wall the individual spins gradually transition from the direction of one domain to that of the next domain and this gradual change in spin alignment costs some exchange and magnetocrystalline anisotropy energy. At a critical

size, the energetic cost of domain wall formation outcompetes the benefit of domain formation resulting in a single-magnetic domain particle. It is at this size that a particle can be superparamagnetic.

In a superparamagnetic particle, the magnetization direction can flip (typically either parallel or antiparallel to the easy axis) rapidly due to thermal fluctuations. Because of this, the particle appears to have no net magnetization. For this to happen, the thermal energy of the system must be sufficient to overcome the energy barrier to magnetization reversal (*i.e.*, the energy associated with changing the magnetization direction 180°) otherwise the particle is considered "blocked." Equation 1.1 defines this energy barrier to magnetization reversal. Here, K represents the magnetocrystalline anisotropy

$$E_{Mag.\ reversal} = K \cdot V \tag{1.1}$$

constant of the material and V represents the particle volume. We therefore see that as the particle volume decreases, the energy barrier decreases. At some point the energy barrier will be on the order of k_BT and the particle will not be blocked. This relation between volume and blocking temperature will be further discussed in Chapter 4 with respect to CrI_3 nanoplatelets.

1.3.2 Surface effects on magnetization

As the size of a particle enters the nanoscale, the surface-to-volume ratio drastically increases. This can have a profound impact on a material's physical and chemical properties. This increase can be an advantage for certain applications, particularly for catalysis with noble metal nanoparticles where the relative increase of a catalytically-active surface allows for a decrease in the total mass of catalyst needed.[48-49] NC surfaces are often more mobile and disordered and this can facilitate new reactivity.[50] These surfaces contain a large amount of dangling bonds, that is, undercoordinated and unpasivated surface sites. These sites can have several deleterious effects on a NC's optical properties such as introducing traps and lowering quantum yield.[51-54] Moreover, it is these undercoordinated and unpasivated surface atoms that can have strong effects on a material's magnetic properties. The exchange interaction of surface atoms will be different from that of core atoms because of this difference in local bonding structure. This local difference in exchange interactions means that the overall exchange energy of a particle and resulting magnetic properties will be affected by the composition of surface sites.

Figure 1.4 below shows the percentage of edge sites in a hexagonal nanoplatelet of CrI_3 as a function of nanoplatelet diagonal. This system is experimentally investigated in Chapter 4. The Cr edge sites in this crystal are undercoordinated and this effects their contribution to the overall magnetization. As the size of the nanoplatelet decreases, particularly below 10 nm, edge site Cr contributions should begin to dominate the magnetic properties of the material and this will affect such things as Curie and blocking temperature as well as overall net magnetic moment. In the case of CrI_3 nanoplatelets, we also hypothesize that these edge sites can affect the overall magnetic ordering between layers. Because of the undercoordination of edge Cr sites, the spin direction of these edge

sites is not pinned in the same way as internal Cr sites. This suggests that it may be possible for the spin direction of an individual CrI_3 layer to more easily flip direction as edge sites begin to dominate.

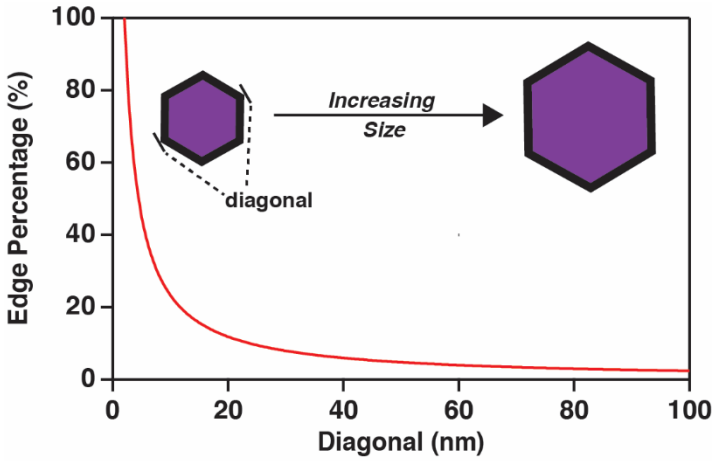

Figure 1.4. Percent of edge sites in a hexagonal nanoplatelet. The effect of nanoplatelet diagonal on the percentage of edge sites in an idealized CrI_3 nanoplatelet.

The surface of a NC is also more susceptible to oxidation than the core. This is especially problematic for NCs composed of redox-active metals such as $Fe^{2+/3+}$, $Sm^{2+/3+}$, and $Eu^{2+/3+}$. This case is investigated in Chapter 3 as applied to $Eu^{2+}S$ NCs. In such NCs, the surface can be heavily oxidized to Eu^{3+}. This trivalent europium does not participate in the same way as the divalent europium to the overall magnetization and instead acts to dilute it. Eu^{3+} also has considerable spin-orbit coupling compared to Eu^{2+}, which can affect the spin-lattice relaxation of the NC system. This is observed experimentally in the ferromagnetic resonance experiment discussed in Chapter 3.

1.4 Applying spectroscopic tools to study magnetization

1.4.1 Electron paramagnetic resonance spectroscopy of magnetic and doped inorganic nanocrystals

Electron paramagnetic resonance (EPR) spectroscopy is a powerful tool for investigation of NCs with paramagnetic dopants such as Mn^{2+} or magnetically ordered NCs. The EPR experiment, at its most basic, measures the amount of microwave radiation absorbed by a system as a function of applied magnetic field. In principle, all paramagnetic ($J \neq 0$) metal ions can give an EPR signal; however, in systems with large spin-orbit coupling or large zero field splittings, signals are only observed at liquid helium temperatures and/or with high resonance energies, sometimes outside of the microwave region. Significant spin-orbit coupling results in fast spin-lattice relaxation (T_1) times, which are inversely proportional to EPR linewidth and lengthen as temperature is lowered. As a result, in systems with significant spin-orbit coupling (*e.g.* Co^{2+}) the EPR signal is "broadened out" at room temperature (*i.e.* unobservable) but can be detected at liquid helium temperatures where T_1 increases.[55]

EPR of doped nanocrystals is particularly powerful as it can provide information about the local coordination environment of the magnetically-active dopant. A significant amount of this information is contained in the hyperfine splitting. Figure 1.5 illustrates this splitting for a simple octahedral Mn^{2+} S = 5/2 system. In Figure 1.5a, the Zeeman splitting for the octahedral S = 5/2 system with an X-band resonance condition is plotted with no additional spin parameters. In this case a single resonance would be observed corresponding to the $\Delta M_S = \pm 1$ transitions. The electron spin of the ion, S, can then interact with the nuclear spin of the ion, I. The hyperfine interaction Hamiltonian can be expressed as in eq. 1.2 below where I and S are the nuclear and electron spin operators respectively and A is the hyperfine coupling constant. For $^{55}Mn^{2+}$ as in Figure 1.5, the nuclear spin, I, is 5/2.

$$\hat{H} = A \cdot \hat{I}\hat{S} \tag{1.2}$$

This nuclear spin will couple to the electron spin and split each individual M_S line into six lines corresponding to $-M_I - +M_I$. This is depicted below in Figure 1.5b,c. This splitting then results in experimentally observing six lines that satisfy the resonance condition. This is depicted by the six vertical red lines in Figure 1.5b,c below. The energetic separation between each line then corresponds to the hyperfine coupling constant.

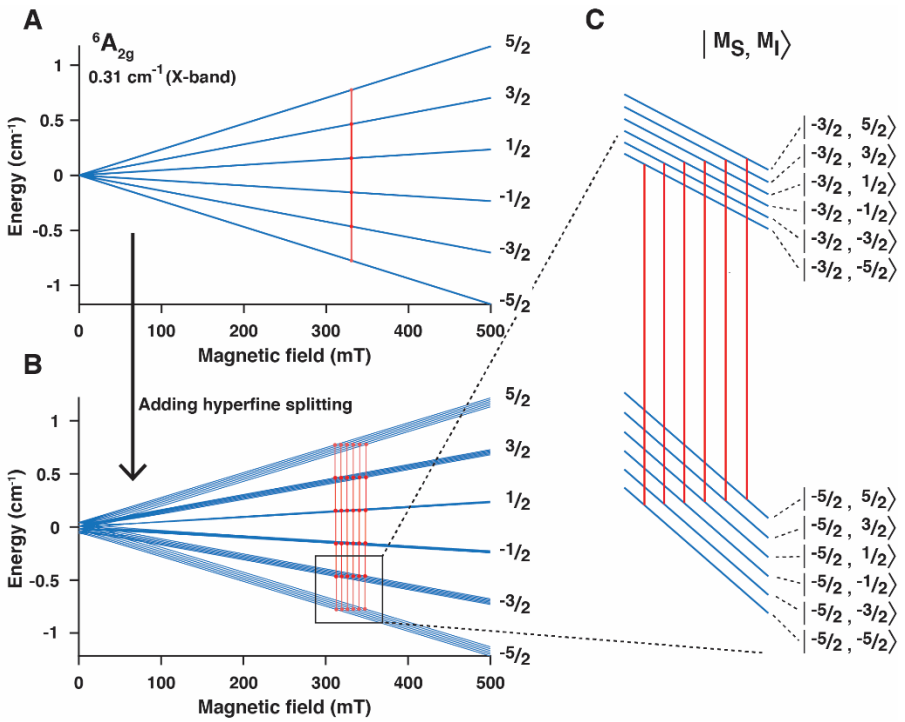

Figure 1.5 Energy level splitting for a simulated octahedral Mn^{2+}, S = 5/2 system. (A) Zeeman splitting for a simulated octahedral Mn^{2+}, S = 5/2 system with no additional spin Hamiltonian parameters (*e.g.* zero-field splitting). A single resonance is observed. **(B)** Simulated energy level splitting for a simulated octahedral Mn^{2+}, S = 5/2 system with the addition of a 200 MHz hyperfine splitting. Six resonances are observed. **(C)** Magnification on the M_S = -5/2 to M_S = -3/2 transition with the addition of the hyperfine splitting. Each individual total spin state is labeled for both electron spin, M_S, and nuclear spin, M_I. The red lines show the transitions that satisfy the selection rule $\Delta M_S = \pm 1$, $\Delta M_I = 0$. The energy level splitting is calculated using EasySpin.[56]

The hyperfine coupling constant provides information about the covalency of the system. Generally, the hyperfine coupling constant decreases as covalency increases.[57] The hyperfine splitting for Mn^{2+} in various lattices is summarized below in Figure 1.6 where this negative dependence on covalency is demonstrated. Here, the x-axis represents the covalency of the lattice calculated from electronegativities[58] and the y-axis gives the hyperfine coupling constant for Mn^{2+} in units of 10^{-4} cm^{-1}. In Chapter 2, an analysis of the evolution of the hyperfine coupling constant in Mn^{2+}:$CsPb(Cl_{1-x}Br_x)_3$ NCs is used to understand the identity of the coordinating anion during the anion exchange process. The hyperfine coupling constant can also provide information about NC dopant incorporation. The surfaces of NCs are often passivated by several different types of ligands with carboxylate groups representing a common type of ligand. Mn^{2+} on the surface of a NC will be affected by the presence of these hard carboxylate ligands that result in a less covalent environment for the Mn^{2+} ions than the core of the NC. Therefore Mn^{2+} on the surface of NCs often displays a different hyperfine splitting than core Mn^{2+} and by using this information one can understand if Mn^{2+} is successfully incorporated into the NC lattice.[59]

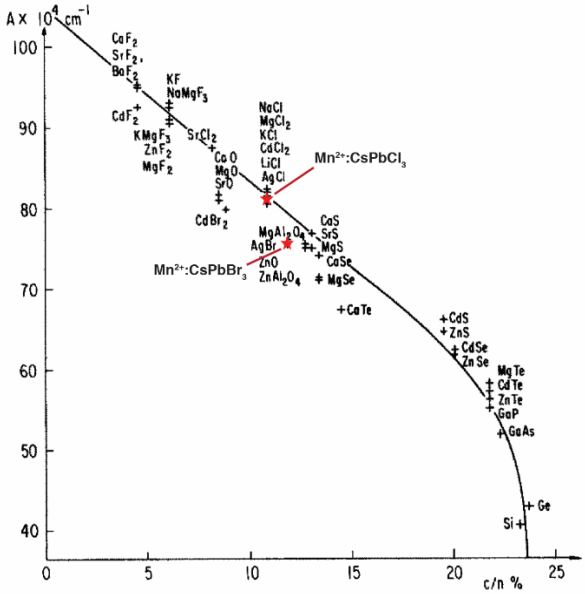

Figure 1.6 Mn^{2+} hyperfine coupling constant dependence on covalency. The hyperfine coupling constant, $|A|$ of Mn^{2+} as a function of the covalency parameter, c, determined from electronegativities divided by the number of ligands. Hyperfine coupling constant of Mn^{2+} in halide perovskite lattice as experimentally measured and discussed in Chapter 3 are marked with red stars. Figure reprinted with modification from Ref. 58, with permission from Elsevier.

In addition to the hyperfine coupling constant, zero-field splitting (ZFS) also provides information about the local coordination environment of the EPR-active dopant. ZFS is a splitting of the electronic state in the absence of any applied magnetic field. This often occurs because of spin-orbit coupling or spin-spin coupling and is often accompanied by a geometric distortion. Figure 1.7a,b illustrates the effects of a rhombic ZFS on the ground state energy levels of a S = 5/2 system (*i.e.* Mn^{2+}) and Figure 1.7c,d show the effects of a rhombic ZFS on a simulated Mn^{2+} EPR spectrum. Here, we see that the ZFS result in additional splittings in the EPR spectrum and it is in fitting these splittings that ZFS is experimentally measured. Through determination of the ZFS, changes to local geometry can be calculated. This has been performed in the case of several perovskite lattices doped with magnetically-active impurities (Mn^{2+}, and Gd^{3+}) and investigation of the temperature-dependent ZFS in these systems was used to determine the phase transitions of the host lattice[60-63] with greater sensitivity than traditional thermal analysis approaches.[61] As applied to NCs, EPR spectroscopy provides significant information about the local environments of dopants via parameters such as hyperfine coupling and ZFS and as such is an indispensable tool in the investigation of how dopants are incorporated into NCs and how changes to the NC can affect things such as dopant speciation.

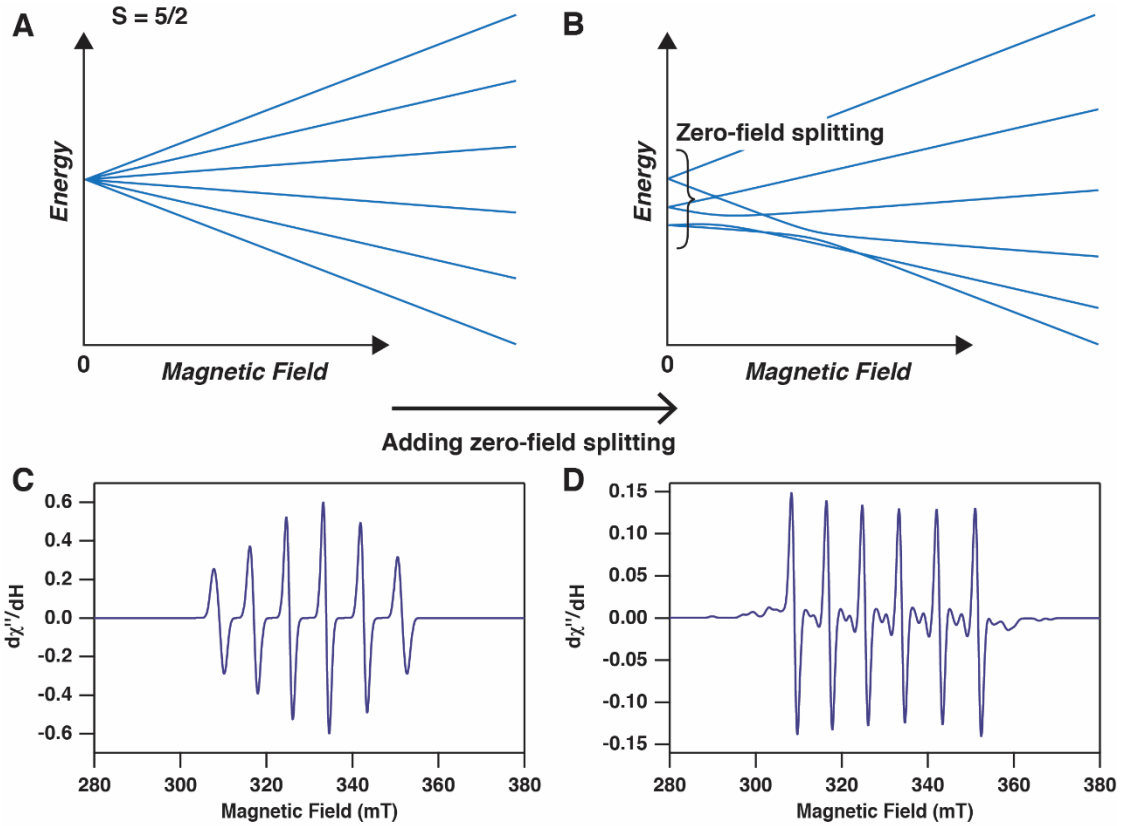

Figure 1.7 Simulated effect of ZFS on the Mn^{2+} spin system. **(A)** Simulated energy level splitting for a Mn^{2+}, S = 5/2 system with no additional spin Hamiltonian parameters. **(B)** Simulated energy level splitting for a Mn^{2+}, S = 5/2 system with the addition of a rhombic ZFS. For simplicity, the hyperfine interaction is omitted in **(A)** and **(B)**. **(C)** Simulated Mn^{2+} EPR spectrum without any added ZFS. A hyperfine splitting of 240 MHz is included. **(D)** Simulated Mn^{2+} EPR spectrum with a rhombic ZFS. A hyperfine splitting of 240 MHz is included and values for *D* (126 MHz) and *E* (20 MHz) are taken from the literature for Mn^{2+}:$CsPbCl_3$.[60] Energy level splittings and spectra are simulated using EasySpin.[56]

As EPR spectroscopy is an absorptive technique, the Beer-Lambert law can be applied. However, rather than provide information about a molecule or material's concentration in solution as typically accomplished when applied to UV/Vis spectroscopy, applying the Beer-Lambert law to EPR spectroscopy provides information about the amount of spins present, or magnetization, and is usually referred to as spin quantification. EPR spectra are typically plotted in the derivative mode as demonstrated below in Figure 1.8a for a Mn^{2+} system. To perform spin quantification, the spectrum needs to be integrated twice. The first integration yields the EPR spectrum in absorptive mode. This is shown below in Figure 1.8b. This is a plot of the microwave power absorbed as a function of magnetic field and is referred to as the EPR susceptibility. Integrating the area of this EPR susceptibility then yields a proportional magnetization and is depicted by the gray-dashed area in Figure 1.8b below. This double-integration yields a proportional magnetization as the absolute values for the strength of an

EPR signal are often arbitrary and can depend on several external factors such as microwave cavity design.[64] The ability to use EPR spectroscopy to measure total system spin or magnetization allows for tracking the evolution of spin concentration across a series of reactions. This is discussed further in Chapter 2, where EPR spin quantification is used to track the relative concentration of Mn^{2+} spins in Mn^{2+}:$CsPb(Cl_{1-x}Br_x)_3$ NCs during the course of anion exchange reactions. By maintaining a fixed Mn^{2+} concentration in the EPR experiment yet observing a loss of Mn^{2+} spin quantitatively, it is possible to assign this loss to antiferromagnetic coupling. Additionally, through temperature-dependent spin quantification, magnetic ordering behavior can be investigated allowing for things such as Curie temperature to be determined. This is performed analogously to more conventional measurements of magnetic ordering such as SQUID magnetometry. This approach will be used in Chapter 3 to explore the magnetic ordering of EuS NCs.

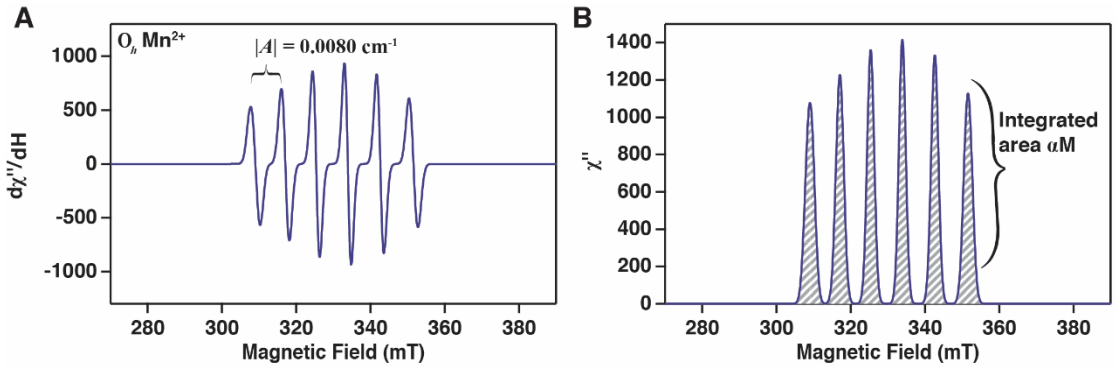

Figure 1.8 Simulated X-band EPR spectra for Mn^{2+}. EPR spectra for a simulated Mn^{2+} species plotted in the derivative **(A)** and absorptive **(B)** modes. The shaded area in **(B)** represents the proportional magnetization. Spectra are simulated using EasySpin[56] for a Mn^{2+} spin system with an 80×10^{-4} cm^{-1} hyperfine coupling constant and ZFS is omitted for simplicity.

1.4.2 Magneto-circular dichroism spectroscopy for measuring magnetization in ordered inorganic nanocrystals

Similar to EPR spectroscopy as mentioned above, MCD spectroscopy can likewise be use to measure magnetization in lieu of conventional approaches like SQUID magnetometry or vibrating-sample magnetometry (VSM). MCD spectroscopy measures the differential absorption of left and right circularly-polarized light in a molecule/material in an applied external magnetic field. This is illustrated below in Figure 1.9 for A-term MCD. In this picture, there is a triplet (J = 1) excited state that experiences a Zeeman splitting into three individual M_J states with an applied magnetic field. MCD spectroscopy then probes this Zeeman splitting by taking advantage of the difference in selection rules for different polarizations of circularly polarized light ($\sigma^+ = -M_J$; $\sigma^- = +M_J$). A-term MCD refers to probing this effect when the excited state experiences a Zeeman splitting whereas C-term MCD refers

to the ground state experiencing a Zeeman splitting. MCD spectra are often plotted as a differential absorbance, ΔA, because the probed splitting is often small. This is depicted below in Figure 1.9b.

MCD spectroscopy can provide a wealth of information regarding the electronic and spin structure of a molecule/material. The focus in this work is on applying MCD spectroscopy to study magnetic ordering and the reader is referred elsewhere[65] for a thorough discussion of MCD spectroscopy. In magnetic materials, the magnitude of the integrated MCD signal is proportional to total magnetization. This is analogous to EPR spectroscopy as discussed above. Temperature-dependent MCD measurements allow for the observation of magnetic ordering behavior. This approach will be expanded upon in Chapter 3 and 4 for measurements of magnetic ordering in EuS, EuSe, CrI_3, $CrBr_3$, and mixed $Cr(Br_{1-x}I_x)_3$ alloys. MCD spectroscopy can also be used to measure magnetic hysteresis by monitoring a single MCD transition's dependence on magnetic field. This provides similar data to *H-M* sweeps in magnetometry (SQUID, VSM). There are several distinctions with using MCD or EPR spectroscopy to measure these effects as compared to magnetometry. Foremost, MCD and EPR are spectroscopic techniques whereas magnetometry is a bulk technique. Because of this, MCD and EPR spectroscopy can differentiate the magnetic effects of individual components of mixtures. In contrast, magnetometry enables measurements of all samples including diamagnets whereas MCD and EPR spectroscopy can only measure samples that are MCD- or EPR-active. MCD spectroscopy can also be more sensitive to orientation effects than magnetometry especially in magnetic hysteresis measurements. This is observed in MCD hysteresis measurements of CrI_3 compared to VSM data. In these data, inflections in the hysteresis which are assigned to spin-flips of individual CrI_3 layers are amplified in the MCD measurement. This will be further discussed in Chapter 4.

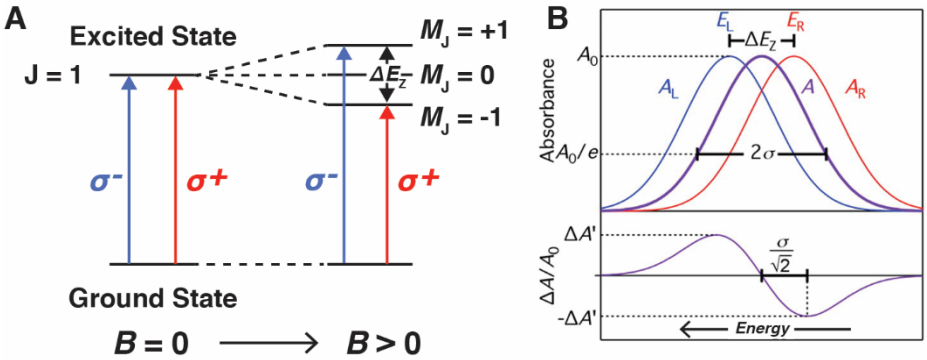

Figure 1.9 A-term MCD splitting. (A) MCD effect illustrated for a simple triplet (J = 1) system showing the different selection rules for left and right circularly-polarized light. **(B)** Zeeman splitting probed by absorption (top) and MCD (bottom) illustrating the differential nature of the MCD experiment. Panel B adapted with permission from ref. 25. Copyright 2015 American Chemical Society.

1.5 Summary & conclusions

In summary, dopants in NCs can impart new photophysical and magnetic properties to their host materials. Paramagnetic dopants can affect both NC luminescence through the introduction of new recombination pathways as well as introduce new magnetic properties typical of dilute magnetic semiconductors. Dopants can also be used to tune the magnetic properties of magnetic nanocrystals by mediating exchange interactions as exemplified in doped-EuS materials. The magnetic properties of a material are also affected by particle size. As ferromagnetic particles decrease in size, they can support fewer magnetic domains leading to the eventual turn-on of superparamagnetism. NC surfaces or edges can have a different contribution to the magnetic properties of a material because of differences in bonding and exchange interactions. As such, a particle's size, and therefore its surface-to-volume ratio, can tune the effects of the surface on magnetic properties. Both EPR and MCD spectroscopy allow for these effects to be probed. EPR spectroscopy enables the study of paramagnetic dopants in NCs and can provide information about the dopant's local environment and in turn about chemical processes and speciation with the host lattice. EPR and MCD spectroscopy can also be used to observe magnetic ordering because of the relation between the EPR and MCD signals to magnetization. Through applying these spectroscopic tools, much about a NC's magnetic properties and overall structure can be determined providing vital information for the advancement of fundamental nanomaterials research.

1.6 References

1. Talapin, D. V.; Lee, J.-S.; Kovalenko, M. V.; Shevchenko, E. V. Prospects of Colloidal Nanocrystals for Electronic and Optoelectronic Applications. *Chem. Rev.* **2010,** *110*, 389-458.
2. Comin, A.; Manna, L. New materials for tunable plasmonic colloidal nanocrystals. *Chem. Soc. Rev.* **2014,** *43*, 3957-3975.
3. Hillhouse, H. W.; Beard, M. C. Solar cells from colloidal nanocrystals: Fundamentals, materials, devices, and economics. *Curr. Opin. Colloid Interface Sci.* **2009,** *14*, 245-259.
4. Parak, W. J.; Gerion, D.; Pellegrino, T.; Zanchet, D.; Micheel, C.; Williams, S. C.; Boudreau, R.; Gros, M. A. L.; Larabell, C. A.; Alivisatos, A. P. Biological applications of colloidal nanocrystals. *Nanotechnology* **2003,** *14*, R15-R27.
5. Pu, C.; Ma, J.; Qin, H.; Yan, M.; Fu, T.; Niu, Y.; Yang, X.; Huang, Y.; Zhao, F.; Peng, X. Doped Semiconductor-Nanocrystal Emitters with Optimal Photoluminescence Decay Dynamics in Microsecond to Millisecond Range: Synthesis and Applications. *ACS Cent. Sci.* **2016,** *2*, 32-9.
6. Smith, A. M.; Nie, S. Semiconductor Nanocrystals: Structure, Properties, and Band Gap Engineering. *Acc. Chem. Res.* **2010,** *43*, 190-200.
7. Norris, D. J.; Efros, A. L.; Erwin, S. C. Doped Nanocrystals. *Science* **2008,** *319*, 1776.
8. Agrawal, A.; Johns, R. W.; Milliron, D. J. Control of Localized Surface Plasmon Resonances in Metal Oxide Nanocrystals. *Annu. Rev. Mater. Res.* **2017,** *47*, 1-31.
9. Schimpf, A. M.; Knowles, K. E.; Carroll, G. M.; Gamelin, D. R. Electronic Doping and Redox-Potential Tuning in Colloidal Semiconductor Nanocrystals. *Acc. Chem. Res.* **2015,** *48*, 1929-1937.

10. Pradhan, N.; Das Adhikari, S.; Nag, A.; Sarma, D. D. Luminescence, Plasmonic, and Magnetic Properties of Doped Semiconductor Nanocrystals. *Angew. Chem. Int. Ed.* **2017,** *56*, 7038-7054.
11. Knowles, K. E.; Hartstein, K. H.; Kilburn, T. B.; Marchioro, A.; Nelson, H. D.; Whitham, P. J.; Gamelin, D. R. Luminescent Colloidal Semiconductor Nanocrystals Containing Copper: Synthesis, Photophysics, and Applications. *Chem. Rev.* **2016,** *116*, 10820-10851.
12. Beaulac, R.; Archer, P. I.; Gamelin, D. R. Luminescence in colloidal Mn^{2+}-doped semiconductor nanocrystals. *J. Solid State Chem.* **2008,** *181*, 1582-1589.
13. Nag, A.; Chakraborty, S.; Sarma, D. D. To Dope Mn^{2+} in a Semiconducting Nanocrystal. *J. Am. Chem. Soc.* **2008,** *130*, 10605-10611.
14. Guria, A. K.; Dutta, S. K.; Adhikari, S. D.; Pradhan, N. Doping Mn^{2+} in Lead Halide Perovskite Nanocrystals: Successes and Challenges. *ACS Energy Lett.* **2017,** *2*, 1014-1021.
15. Nelson, H. D.; Li, X.; Gamelin, D. R. Computational Studies of the Electronic Structures of Copper-Doped CdSe Nanocrystals: Oxidation States, Jahn–Teller Distortions, Vibronic Bandshapes, and Singlet–Triplet Splittings. *J. Phys. Chem. C* **2016,** *120*, 5714-5723.
16. Zou, S.; Liu, Y.; Li, J.; Liu, C.; Feng, R.; Jiang, F.; Li, Y.; Song, J.; Zeng, H.; Hong, M.; Chen, X. Stabilizing Cesium Lead Halide Perovskite Lattice through Mn (II)-Substitution for Air-Stable Light-Emitting Diodes. *J. Am. Chem. Soc.* **2017,** *139*, 11443–11450.
17. Li, F.; Xia, Z.; Gong, Y.; Gu, L.; Liu, Q. Optical properties of Mn^{2+} doped cesium lead halide perovskite nanocrystals via a cation–anion co-substitution exchange reaction. *J. Mater. Chem. C* **2017,** *5*, 9281-9287.
18. Xu, W.; Li, F.; Lin, F.; Chen, Y.; Cai, Z.; Wang, Y.; Chen, X. Synthesis of $CsPbCl_3$-Mn Nanocrystals via Cation Exchange. *Adv. Opt. Mater.* **2017,** *5*, 1700520.
19. Yuan, X.; Ji, S.; De Siena, M. C.; Fei, L.; Zhao, Z.; Wang, Y.; Li, H.; Zhao, J.; Gamelin, D. R. Photoluminescence Temperature Dependence, Dynamics, and Quantum Efficiencies in Mn^{2+}-Doped $CsPbCl_3$ Perovskite Nanocrystals with Varied Dopant Concentration. *Chem. Mater.* **2017,** *29*, 8003-8011.
20. Furdyna, J. K. Diluted magnetic semiconductors. *J. Appl. Phys.* **1988,** *64*, R29-R64.
21. Dietl, T. A ten-year perspective on dilute magnetic semiconductors and oxides. *Nat. Mater.* **2010,** *9*, 965-974.
22. Viswanatha, R.; Pietryga, J. M.; Klimov, V. I.; Crooker, S. A. Spin-Polarized Mn^{2+} Emission from Mn-Doped Colloidal Nanocrystals. *Phys. Rev. Lett.* **2011,** *107*, 067402.
23. Kittilstved, K. R.; Gamelin, D. R. Activation of High-TC Ferromagnetism in Mn^{2+}-Doped ZnO using Amines. *J. Am. Chem. Soc.* **2005,** *127*, 5292-5293.
24. Ochsenbein, S. T.; Feng, Y.; Whitaker, K. M.; Badaeva, E.; Liu, W. K.; Li, X.; Gamelin, D. R. Charge-controlled magnetism in colloidal doped semiconductor nanocrystals. *Nat. Nanotechnol.* **2009,** *4*, 681-687.
25. Barrows, C. J.; Vlaskin, V. A.; Gamelin, D. R. Absorption and Magnetic Circular Dichroism Analyses of Giant Zeeman Splittings in Diffusion-Doped Colloidal $Cd_{1-x}Mn_xSe$ Quantum Dots. *J. Phys. Chem. Lett.* **2015,** *6*, 3076-3081.
26. McAlister, S. P.; Furdyna, J. K.; Giriat, W. Magnetic susceptibility and spin-glass transition in $Zn_{1-x}Mn_xTe$. *Phys. Rev. B* **1984,** *29*, 1310-1314.
27. Beaulac, R.; Schneider, L.; Archer, P. I.; Bacher, G.; Gamelin, D. R. Light-Induced Spontaneous Magnetization in Doped Colloidal Quantum Dots. *Science* **2009,** *325*, 973.

28. Beaulac, R.; Feng, Y.; May, J. W.; Badaeva, E.; Gamelin, D. R.; Li, X. Orbital pathways for Mn^{2+}-carrier sp-d exchange in diluted magnetic semiconductor quantum dots. *Phys. Rev. B* **2011,** *84*, 195324.
29. Nelson, H. D.; Bradshaw, L. R.; Barrows, C. J.; Vlaskin, V. A.; Gamelin, D. R. Picosecond Dynamics of Excitonic Magnetic Polarons in Colloidal Diffusion-Doped $Cd_{1-x}Mn_xSe$ Quantum Dots. *ACS Nano* **2015,** *9*, 11177-11191.
30. Xu, K.; Meijerink, A. Tuning Exciton–Mn^{2+} Energy Transfer in Mixed Halide Perovskite Nanocrystals. *Chem. Mater.* **2018,** *30*, 5346-5352.
31. Ferguson, J.; Guggenheim, H. J.; Tanabe, Y. Exchange Effects in the Electronic Absorption Spectrum of Mn(II) in Perovskite Fluorides. *J. Appl. Phys.* **1965,** *36*, 1046-1047.
32. Bradshaw, L. R.; May, J. W.; Dempsey, J. L.; Li, X.; Gamelin, D. R. Ferromagnetic excited-state Mn^{2+} dimers in $Zn_{1-x}Mn_xSe$ quantum dots observed by time-resolved magnetophotoluminescence. *Phys. Rev. B* **2014,** *89*, 115312.
33. *Phosphor Handbook*, 2nd ed.; Yen, W., Shionoya, S., Yamamoto, H., Eds.; CRC Press: Boca Raton, 2007.
34. Mauger, A.; Godart, C. The magnetic, optical, and transport properties of representatives of a class of magnetic semiconductors: The europium chalcogenides. *Phys. Rep.* **1986,** *141*, 51-176.
35. Moodera, J. S.; Hao, X.; Gibson, G. A.; Meservey, R. Electron-Spin Polarization in Tunnel Junctions in Zero Applied Field with Ferromagnetic EuS Barriers. *Phys. Rev. Lett.* **1988,** *61*, 637-640.
36. Moodera, J. S.; Santos, T. S.; Nagahama, T. The phenomena of spin-filter tunnelling. *J. Phys.: Condens. Matter* **2007,** *19*, 165202.
37. Wachter, P. Europium chalcogenides: EuO, EuS, EuSe and EuTe. In *Handbook on the Physics and Chemistry of Rare Earths*; Elsevier: North-Holland, 1979; Vol. 2, pp 507-574.
38. Mairoser, T.; Loder, F.; Melville, A.; Schlom, D. G.; Schmehl, A. Influence of chemical doping on the magnetic properties of EuO. *Phys. Rev. B* **2013,** *87*, 014416.
39. Mairoser, T.; Schmehl, A.; Melville, A.; Heeg, T.; Canella, L.; Böni, P.; Zander, W.; Schubert, J.; Shai, D. E.; Monkman, E. J.; Shen, K. M.; Schlom, D. G.; Mannhart, J. Is There an Intrinsic Limit to the Charge-Carrier-Induced Increase of the Curie Temperature of EuO? *Phys. Rev. Lett.* **2010,** *105*, 257206.
40. Gambino, R. J.; Fumagalli, P.; Ruf, R. R.; McGuire, T. R.; Bojarczuk, N. Magneto-optic spectra of EuS-Gd and EuS-Tb films. *IEEE Trans. Magn.* **1992,** *28*, 2973-2975.
41. Kar, S.; Boncher, W. L.; Olszewski, D.; Dollahon, N.; Ash, R.; Stoll, S. L. Gadolinium Doped Europium Sulfide. *J. Am. Chem. Soc.* **2010,** *132*, 13960-13962.
42. Selinsky, R. S.; Han, J. H.; Morales Pérez, E. A.; Guzei, I. A.; Jin, S. Synthesis and Magnetic Properties of Gd Doped EuS Nanocrystals with Enhanced Curie Temperatures. *J. Am. Chem. Soc.* **2010,** *132*, 15997-16005.
43. Abramchuk, M.; Jaszewski, S.; Metz, K. R.; Osterhoudt, G. B.; Wang, Y.; Burch, K. S.; Tafti, F. Controlling Magnetic and Optical Properties of the van der Waals Crystal $CrCl_{3-x}Br_x$ via Mixed Halide Chemistry. *Adv. Mater.* **2018,** *30*, 1801325.
44. Neuwelt, E. A.; Hamilton, B. E.; Varallyay, C. G.; Rooney, W. R.; Edelman, R. D.; Jacobs, P. M.; Watnick, S. G. Ultrasmall superparamagnetic iron oxides (USPIOs): a future alternative magnetic resonance (MR) contrast agent for patients at risk for nephrogenic systemic fibrosis (NSF)? *Kidney Int.* **2009,** *75*, 465-474.

45. Weinstein, J. S.; Varallyay, C. G.; Dosa, E.; Gahramanov, S.; Hamilton, B.; Rooney, W. D.; Muldoon, L. L.; Neuwelt, E. A. Superparamagnetic Iron Oxide Nanoparticles: Diagnostic Magnetic Resonance Imaging and Potential Therapeutic Applications in Neurooncology and Central Nervous System Inflammatory Pathologies, a Review. *J. Cereb. Blood Flow Metab.* **2009,** *30*, 15-35.
46. Jordan, A.; Scholz, R.; Wust, P.; Fähling, H.; Roland, F. Magnetic fluid hyperthermia (MFH): Cancer treatment with AC magnetic field induced excitation of biocompatible superparamagnetic nanoparticles. *J. Magn. Magn. Mater.* **1999,** *201*, 413-419.
47. Yu, M. K.; Jeong, Y. Y.; Park, J.; Park, S.; Kim, J. W.; Min, J. J.; Kim, K.; Jon, S. Drug-Loaded Superparamagnetic Iron Oxide Nanoparticles for Combined Cancer Imaging and Therapy In Vivo. *Angew. Chem. Int. Ed.* **2008,** *47*, 5362-5365.
48. Zhou, K.; Li, Y. Catalysis Based on Nanocrystals with Well-Defined Facets. *Angew. Chem. Int. Ed.* **2012,** *51*, 602-613.
49. Zhang, H.; Jin, M.; Xia, Y. Noble-Metal Nanocrystals with Concave Surfaces: Synthesis and Applications. *Angew. Chem. Int. Ed.* **2012,** *51*, 7656-7673.
50. Tsui, E. Y.; Hartstein, K. H.; Gamelin, D. R. Selenium Redox Reactivity on Colloidal CdSe Quantum Dot Surfaces. *J. Am. Chem. Soc.* **2016,** *138*, 11105-11108.
51. Boles, M. A.; Ling, D.; Hyeon, T.; Talapin, D. V. The surface science of nanocrystals. *Nat. Mater.* **2016,** *15*, 141-153.
52. Jones, M.; Lo, S. S.; Scholes, G. D. Quantitative modeling of the role of surface traps in CdSe/CdS/ZnS nanocrystal photoluminescence decay dynamics. *Proc. Natl. Acad. Sci.* **2009,** *106*, 3011.
53. Krause, M. M.; Kambhampati, P. Linking surface chemistry to optical properties of semiconductor nanocrystals. *Phys. Chem. Chem. Phys.* **2015,** *17*, 18882-18894.
54. Houtepen, A. J.; Hens, Z.; Owen, J. S.; Infante, I. On the Origin of Surface Traps in Colloidal II–VI Semiconductor Nanocrystals. *Chem. Mater.* **2017,** *29*, 752-761.
55. Zverev, G. M.; Prokhorov, A. M. Electron Paramagnetic Resonance and Spin-Lattice Relaxation of Co^{2+} in Corundum. *Sov. Phys. JETP* **1961,** *12*, 41-45.
56. Stoll, S.; Schweiger, A. EasySpin, a comprehensive software package for spectral simulation and analysis in EPR. *J. Magn. Reson.* **2006,** *178*, 42-55.
57. Matumura, O. Electron Spin Resonance of Mn-activated Phosphors. *J. Phys. Soc. Jpn.* **1959,** *14*, 108.
58. Šimánek, E.; Müller, K. A. Covalency and hyperfine structure constant A of iron group impurities in crystals. *J. Phys. Chem. Solids* **1970,** *31*, 1027-1040.
59. Stefan, M.; Nistor, S. V.; Ghica, D.; Mateescu, C. D.; Nikl, M.; Kucerkova, R. Substitutional and surface Mn^{2+} centers in cubic ZnS:Mn nanocrystals. A correlated EPR and photoluminescence study. *Phys. Rev. B* **2011,** *83*, 045301.
60. Cape, J. A.; White, R. L.; Feigelson, R. S. EPR Study of the Structure of $CsPbCl_3$. *J. Appl. Phys.* **1969,** *40*, 5001-5005.
61. Cohen, M. I.; Young, K. F.; Chang, T. T.; Brower, W. S. Phase Transitions in $CsPbCl_3$. *J. Appl. Phys.* **1971,** *42*, 5267-5272.
62. Vaills, Y.; Buzaré, J. Y. EPR studies of Gd^{3+} centres in the cubic phase of $CsCaCl_3$ and $CsPbCl_3$. *J. Phys. Chem. Solids* **1987,** *48*, 363-370.

63. Zheng, W.-C. Investigation of the EPR spectra of $CsPbCl_3:Mn^{2+}$ and $CsSrCl_3:Mn^{2+}$ in the cubic-tetragonal phase transition. *Ferroelectrics* **1995,** *166*, 91-94.
64. Eaton, G. R.; Eaton, S. S.; Barr, D. P.; Weber, R. T., Quantitative EPR. Springer: Vienna, 2010.
65. Piepho, S. B.; Schatz, P. N. *Group theory in spectroscopy: with applications to magnetic circular dichroism*, Eds.; Wiley: New York, 1983.

Chapter 2: Spinodal Decomposition During Anion Exchange in Colloidal Mn^{2+}-Doped $CsPbX_3$ (X = Cl, Br) Perovskite Nanocrystals

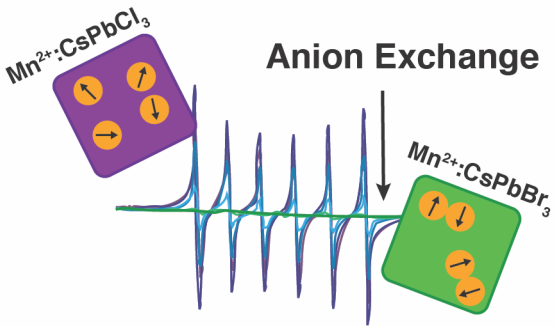

Reproduced with permission from:
De Siena, M. C.; Sommer, D. E.; Creutz, S. E.; Dunham, S. T.; Gamelin, D. R. Chem. Mater. 2019, *31*, 7711-7722.

2.1 Overview

Manganese(II)-doped cesium-lead-chloride (Mn^{2+}:$CsPbCl_3$) perovskite nanocrystals have recently been developed as promising luminescent materials and attractive candidates for white-light generation. One approach to tuning the luminescence of these materials has involved anion exchange to incorporate Br^-, but the effects of anion exchange on Mn^{2+} speciation in doped metal-halide perovskites is not well understood at a microscopic level. Here, we use a combination of X-band electron paramagnetic resonance (EPR) and photoluminescence spectroscopies to monitor the Mn^{2+} dopants in Mn^{2+}:$CsPbCl_3$ nanocrystals during $Cl^- \rightarrow Br^-$ anion exchange. Analytical measurements show that the nanocrystals retain their Mn^{2+} over the course of $Cl^- \rightarrow Br^-$ anion exchange and they continue to show strong Mn^{2+} *d–d* luminescence but, surprisingly, the Mn^{2+} EPR intensities all but vanish. Further results suggest that Mn^{2+} ions migrate during anion exchange to form clusters that are still luminescent but show no EPR signal due to antiferromagnetic superexchange coupling. Monte Carlo simulation and analysis of the Mn^{2+}:$CsPb(Cl_{1-x}Br_x)_3$ lattice at various halide compositions (x) bolsters this interpretation by indicating a propensity for Mn^{2+}-Cl^- units to cluster as the Br^- content increases, increasing the probability of nearest-neighbor Mn^{2+}-Mn^{2+} interactions. The driving force for this clustering is retention of the stronger Mn-Cl bonds compared to Mn-Br bonds. In addition, modeling predicts spinodal decomposition to form Mn^{2+}-enriched domains even at the endpoint compositions of x = 0 and 1, with Mn^{2+} ordering in next-nearest-neighbor positions driven by Coulomb interactions and lattice-strain minimization. These results have important implications for both fundamental studies and applications of doped and alloyed metal-halide perovskites.

2.2 Introduction

The facile synthesis, efficient and widely tunable luminescence,[1-2] and high defect tolerance[3] of cesium-lead-halide perovskite ($CsPbX_3$, X = Cl, Br, I) nanocrystals (NCs) have made these materials attractive for application in light-emitting diodes,[4-6] photovoltaics,[7-8] photodetectors,[9-10] and other optoelectronic technologies. The luminescence of $CsPbX_3$ NCs is easily tuned *via* post-synthetic anion exchange,[11-12] and has also been modified by deliberate introduction of impurities, for example divalent manganese[6,13-16] or trivalent lanthanides.[16-18] Among these materials, Mn^{2+}-doped perovskite NCs have

attracted particular attention for both their fundamental properties and for potential lighting and energy-conversion applications.[6,13-16,19-22] Mn^{2+}:$CsPb(Cl_{1-x}Br_x)_3$ NCs usually show the coexistence of sharp, composition-tunable excitonic emission with broad, orange Mn^{2+} $^4T_{1g} \rightarrow {}^6A_{1g}$ *d-d* emission, providing the ability to generate white light.

Although Mn^{2+} is readily doped into $CsPbCl_3$ NCs, it has proven surprisingly challenging to dope Mn^{2+} into $CsPbBr_3$ NCs directly.[6,23] Similarly, Mn^{2+} is readily inserted into $CsPbCl_3$ NCs by post-synthetic partial cation exchange,[16,24-25] but the same approach has not been fruitful for doping Mn^{2+} into $CsPbBr_3$ NCs. Mn^{2+}-doped $CsPb(Cl_{1-x}Br_x)_3$ NCs ($0 < x \leq 1$) can be accessed by post-synthetic $Cl^- \rightarrow Br^-$ anion exchange starting from pre-formed Mn^{2+}:$CsPbCl_3$ NCs, and this approach additionally allows the PL of a given ensemble of NCs to be tracked as a function of x. Such studies have revealed an unusual trend of increasing excitonic PL intensities and decreasing Mn^{2+} *d-d* PL intensities with increasing Br^- content.[6,26-28] Compositional analysis before and after anion exchange argues against Mn^{2+} loss as the main cause of the decreasing Mn^{2+} luminescence following anion exchange,[20] and instead, more complex photophysical phenomena such as thermally assisted $Mn^{2+} \rightarrow$ exciton back energy transfer at high Br^- content (narrow exciton-Mn^{2+}($^4T_{1g}$) energy gap) have been implicated.[6,26]

A common postulation in discussions of anion exchange in metal-halide perovskites is that the cation sublattice is effectively rigid and remains intact.[6,11,29] Given the ease of Mn^{2+} (or other cation) insertion into $CsPbCl_3$ NCs by cation exchange or diffusion doping,[15-16,30-31] however, it appears likely that *both* cations and anions may migrate within the NCs during anion exchange. Pb^{2+} migration may be undetectable in undoped perovskites, but in Mn^{2+}-doped $CsPbX_3$ perovskites cation migration during anion exchange could potentially generate detectable non-random Pb^{2+} and Mn^{2+} spatial distributions. Spinodal decomposition has already been reported in $CsPbCl_3$ nanoplatelets at high Mn^{2+} content (>6%) under solvothermal diffusion-doping conditions (80 mol % Mn to Pb, autoclave, 200 °C for 2–5 h),[32] forming what appear to be $CsMnCl_3$ inclusions within the $CsPbCl_3$ lattice. On the other hand, solid-state ^{133}Cs nuclear magnetic resonance (NMR) spectroscopy has been used to rule out formation of even small (radius ≥ ~2.2 nm (~3 unit cells)) $CsMnCl_3$ inclusions in bulk 3% Mn^{2+}:$CsPbX_3$ (X = Cl or Br) powders, but the possibility of smaller clusters could not be addressed.[33] Neither of these studies examined mixed-halide compositions. The effect of anion exchange on Mn^{2+} dopants *within* metal-halide perovskite NCs has not yet been examined.

Here, we use X-band electron paramagnetic resonance (EPR) and PL spectroscopies to track Mn^{2+} ions during the post-synthetic transformation of Mn^{2+}-doped $CsPbCl_3$ NCs into Mn^{2+}-doped $CsPb(Cl_{1-x}Br_x)_3$ ($0 < x \leq 1$) NCs by room-temperature anion exchange. These experiments reveal that Mn^{2+} ions do indeed migrate within the NCs, clustering together in nearest-neighbor positions as Cl^- is replaced by Br^- in the lattice. Density functional theory (DFT)-based Monte Carlo modeling predicts such Mn^{2+} clustering, driven by differential Mn-X bond strengths. Even in the Mn^{2+}:$CsPbCl_3$ and Mn^{2+}:$CsPbBr_3$ composition limits, the modeling predicts spinodal decomposition to form domains of a new ordered phase with second-nearest-neighbor Mn^{2+}-Mn^{2+} correlations, rather than the randomly doped Mn^{2+}:$CsPbX_3$ typically assumed. This spinodal decomposition is driven by

Coulomb effects and lattice-strain minimization. Overall, these combined experimental and modeling results highlight the structural richness and complexity of alloyed metal-halide perovskites. In particular, the observation of anion-dependent B-site cation distributions has important ramifications for the interpretation of the physical properties displayed by doped or alloyed perovskite NCs and for harnessing those properties in next-generation photonics applications.

2.3 Methods

2.3.1 Chemicals. Unless otherwise stated, all chemicals were used as purchased without further purification. Lead(II) acetate trihydrate (99.9%) was purchased from Baker. Cesium acetate (99.9%), cesium bromide (99.9%), manganese(II) bromide hydrate (98%), and lead bromide (99.98+%) were purchased from Alfa Aesar. Manganese(II) acetate tetrahydrate (99.999%) was purchased from Strem. Oleylamine (70%, technical grade), oleic acid (90%, technical grade), trimethylsilyl bromide (97%), trimethylsilyl chloride (99%), boron nitride, and 3-methylpentane (99%, further dried over sodium benzophenone and distilled before use) were purchased from Sigma-Aldrich. Anhydrous toluene was purified through an alumina column pressurized with Ar. $Mn(oleate)_2$ was synthesized according to a literature procedure.[34] Hydrochloric acid (ACS plus), ethyl acetate (ACS), and acetone (ACS) were purchased from Fisher Chemical.

2.3.2 Synthesis of Mn^{2+}:$CsPbCl_3$ NCs and undoped $CsPbCl_3$ NCs. The synthesis of Mn^{2+}:$CsPbCl_3$ was adapted with modification from the literature.[15] Briefly, in a glovebox under dinitrogen atmosphere, 0.1 mmol of CsOAc was added to a scintillation vial followed by 5 mL of toluene. This step was performed under inert conditions because CsOAc is highly deliquescent. The vial was then removed from the glovebox and 0.1 mmol of $PbOAc_2{\cdot}3H_2O$, 0.005 mmol of $MnOAc_2{\cdot}4H_2O$, 100 µL of oleylamine, and 450 µL of oleic acid are added. The mixture was allowed to stir capped at RT for 30 min to completely solubilize the acetate salts. Concentrated HCl acid (100 µL) was then injected while stirring and the reaction was allowed to proceed for 1 min. After this step, the NC solution was transferred to centrifuge tubes and flocculated with the addition of anhydrous ethyl acetate, followed by centrifugation and resuspension with hexanes. This precipitation-centrifugation-suspension step was carried out an additional time to remove unreacted species. After these two washing steps there was no further change in Mn^{2+} concentration as measured by inductively coupled plasma–atomic emission spectroscopy. The final product was dried *in vacuo*, transferred to the glovebox, and resuspended in hexanes for further manipulation. The Mn^{2+}:$CsPbCl_3$ NC samples prepared for these studies typically showed photoluminescence quantum yields (PLQYs) of ~40% for the Mn^{2+} *d-d* transition. Undoped $CsPbCl_3$ NCs were made similarly, with the omission of the $MnOAc_2{\cdot}4H_2O$. The doped and undoped NCs were stored under inert atmosphere and did not show any noticeable degradation over the course of the study.

2.3.3 Synthesis of 0.1% Mn^{2+}:$CsPbBr_3$ bulk powder. Bulk powders were synthesized by grinding the reactants in a planetary ball mill using a zirconia grinding jar and balls (Ø30 mm) for 1 hr at 600 rpm. The resulting powder is further annealed at 250°C for 30 min. For the synthesis, 3 mmol CsBr, 0.003 mmol $MnBr_2{\cdot}xH_2O$, and 2.997 mmol $PbBr_2$ were used.

2.3.4 General Anion Exchange. A 0.1 M solution of TMS-Br in hexanes was prepared for use in anion-exchange reactions. In a general anion-exchange reaction, a specific amount of TMS-Br solution was titrated into a solution of $CsPbCl_3$ NCs. The mixture was allowed to react until there was no further change in the energy of the excitonic emission. Following complete reaction, the solution was removed *in vacuo* to remove the TMS-Cl byproduct, and the NCs were then resuspended for further measurements. The time delay between TMS-Br addition and EPR measurement was less than ~10 min.

2.3.5 Reverse Anion Exchange. In a general reverse-anion-exchange reaction, a solution of $CsPbBr_3$ NCs was dried to a powder and a specific amount of neat TMS-Cl was added. The NCs suspend in the TMS-Cl. The mixture was allowed to react until the desired exciton emission energy was reached. Following reaction, the solution was removed *in vacuo* to remove unreacted TMS-Cl and the TMS-Br byproduct, and the NCs were then resuspended in 3-methylpentane for further measurements.

2.3.6 General Characterization. UV-Vis measurements were performed on an Agilent Cary 60 spectrophotometer. Samples were prepared for powder X-ray diffraction (XRD) by depositing NCs from solution onto a silicon substrate and analyzed on a Bruker D8 Discover diffractometer. TEM samples were prepared by drop casting suspensions of NCs onto 400 mesh carbon-coated copper grids from TED Pella, Inc. and dried under an inert atmosphere. TEM images were obtained on an FEI TECNAI G2 F20 microscope operated at 200 kV. Size distributions were determined by analysis of >200 individual NCs. Elemental composition was determined on nitric-acid-digested samples using inductively coupled plasma–atomic emission spectroscopy (ICP-AES) with a PerkinElmer 8300 spectrometer. For EDS analysis, samples were drop cast onto silicon substrates and coated with a ~200 nm thick layer of carbon; spectra were acquired in an FEI Sirion Scanning Electron Microscope operating at 30 kV using an Oxford EDS spectrometer. Standardless quantification was used. PLQY measurements were performed according to procedures described previously.[18]

2.3.7 EPR Measurements. Continuous-wave electron paramagnetic resonance (EPR) measurements were performed on a Bruker EMX spectrometer operated at X-band frequencies equipped with an LN_2 variable-temperature sample-cooling unit.

2.3.8 ^{133}Cs Solid-State NMR Measurements. Solid-state MAS NMR spectra of ^{133}Cs (91.8 MHz at 16.5 T) were recorded on a Bruker Avance III 16.5 T spectrometer equipped with a 3.2 mm Phoenix HXY probe. NC samples were dried and mixed with boron nitride forming a powder suitable for packing. The powders were then packed into 3.2 mm zirconia rotors and closed using Vespel caps. The samples were spun at 3 kHz MAS using dry air and the temperature was maintained at 298 K. ^{133}Cs shifts were referenced to solid CsCl (δ = 223.2 ppm).[35] Relaxation delays ranged from 6 – 10 minutes depending on the samples. The saturation-recovery experiments were performed by applying a train of 30 $\pi/2$ pulses spaced by 3 ms in keeping with a previous report.[33] For analysis and discussion of these results see Appendix A (Figure A16, Table A1).

2.3.9 Photoluminescence Measurements. Room-temperature photoluminescence measurements were performed on solutions of NCs excited with a 365 nm LED or a 375 or 405 nm

laser diode and collected with an OceanOptics USB 2000+ spectrometer or an LN_2-cooled charge-coupled device (CCD) mounted to a monochromator. Spectra are corrected for the instrument response. Liquid helium photoluminescence experiments were performed on films of NCs sandwiched between quartz plates. Samples were mounted in a flow cryostat with a variable-temperature sample compartment.

For lifetime measurements, photoexcitation was provided by a 375 or 405 nm laser diode modulated using the square pulse waveform output of a function generator at a 10 Hz repetition rate. The PL was coupled into a fiber and passed to a monochromator equipped with LN_2-cooled CCD and photomultiplier tube (PMT) detectors. Photoluminescence decay kinetics were measured using a multichannel scaler, averaging over several thousand laser pulses.

2.3.10 Modeling. Characterization of the space of low-energy alloy configurations on the Pb- and halide-sublattices at the level of first-principles theory is limited by the computational demands introduced by the alloy degrees of freedom. For instance, a fixed lattice of n Pb sites and $3n$ halide sites admits 2^{4n} possible configurations of Pb/Mn and halide, and determining the *ab initio* ground-state energy of each configuration requires optimization of both electronic and ionic degrees of freedom. While the number of configurations could be reduced by equivalence under symmetry operations from the space group of the underlying lattice, the number of structural calculations required to sufficiently sample the configuration space is still at best computationally inefficient, and at worst infeasible.[36]

To reduce the computational complexity of the problem, we built a model for the bulk energetics of halide mixing in the presence of substitutional Mn^{2+} using the cluster expansion (CE) formalism.[37] To elaborate, the configuration of various chemical components on a lattice of N sites can be represented by a vector $\boldsymbol{\sigma} = (\sigma_1, \sigma_2, \dots, \sigma_{\mathrm{N}})$, where if M_i chemical components can occupy lattice site i, then admissible values of the site occupation variable σ_i are $\sigma_i \in \{0,1, \dots, M_i - 1\}$. Similarly, a cluster of sites can be represented by a vector $\alpha = (\alpha_1, \alpha_2, \dots, \alpha_N)$ that spans all sites in the lattice, where $\alpha_i = 0$ if site i is not in the cluster, and $\alpha_i \in \{1, \dots, M_i - 1\}$ elsewise. Then, orthogonal, single-site functions that faithfully represent the occupation of lattice sites in a cluster can be defined in the basis of Chebyshev polynomials:

$$\phi_{\alpha_i, M_i}(\sigma_i) = \begin{cases} 1 & \text{if } \alpha_i = 0 \\ -\cos\left(2\pi \left\lceil \frac{\alpha_i}{2} \right\rceil \frac{\sigma_i}{M_i}\right) & \text{if } \alpha_i > 0 \text{ and odd} \\ -\sin\left(2\pi \left\lceil \frac{\alpha_i}{2} \right\rceil \frac{\sigma_i}{M_i}\right) & \text{if } \alpha_i > 0 \text{ and even} \end{cases} \tag{2.1}$$

Here, $\lceil \dots \rceil$ in eq 1 denotes the ceiling function.[38] The ground-state energy, $E(\boldsymbol{\sigma})$, of a given configuration of alloyed species can be expanded in a complete, orthonormal, basis of cluster functions as $E(\boldsymbol{\sigma}) = E_0 + \sum_\alpha J_\alpha \, g_\alpha \bar{\Gamma}_\alpha(\boldsymbol{\sigma})$, where the cluster function $\Gamma_\alpha(\boldsymbol{\sigma}) = \prod_i \phi_{\alpha_i, M_i}(\sigma_i)$ is a product of single-site functions in cluster α, and the overline $\bar{\Gamma}_\alpha$ denotes an average over clusters equivalent under symmetry operations of the underlying lattice. Hence, the sum in the expansion is carried out over symmetrically distinct clusters, and each cluster carries a multiplicity factor g_α. The coefficients of the expansion J_α are commonly called effective cluster interactions (ECIs) and constitute a coarse-grained

description of the underlying electronic and ionic degrees of freedom that contribute to the ground-state energy of a configuration. Once the ECIs have been determined, the energy of any configuration on the lattice can be rapidly calculated.

The ECIs were determined from density functional theory (DFT) calculations of the energies of 200 distinct structures. To enhance model sparsity and optimize bias-variance tradeoff, cluster selection and ECI fitting were carried out using a Least Absolute Shrinkage and Selection Operator (LASSO) regression combined with 10-fold cross-validation to determine the regularization parameter.[39] The CE model was found to have a root-mean squared error (RMSE) of ~2 meV/atom. Monte Carlo (MC) simulations using the CE energy model and the Metropolis-Hastings algorithm with Kawasaki exchange were used to sample room-temperature, equilibrium alloy configurations in the canonical ensemble for various fixed Pb/Mn and Cl/Br compositions. Each MC run was initialized with a random configuration of alloy components, and a minimum of 1000 MC passes were performed to statistically sample the energy and short-range order observables, as discussed in the Results and Analysis section. Each MC pass is defined as the number of MC trial moves equal to the number of alloyed sites in the simulation cell, where each simulation cell consisted of 32000 alloyed sites. The *CASM* software and *Scikit-learn* libraries were used in automating the first-principles calculations, developing the cluster expansion, and performing MC.[40-45]

DFT calculations based on the all-electron projector-augmented wave (PAW) method were performed using the Vienna *Ab Initio* Simulation Package (VASP).[46-50] The conjugate gradient algorithm was used for structural optimization, and the volume, shape, and atomic positions were relaxed until interatomic Hellmann-Feynman forces were less than 0.01 eV/Å. To reduce total computation time, the structure was optimized using the Perdew-Burke-Ernzerhof (PBE) exchange-correlation functional in the generalized gradient approximation (GGA).[51] In the pseudopotentials, 9 electrons of Cs ($5s^2 5p^6 6s^1$), 4 electrons of Pb ($6s^2 6p^2$), 7 electrons of Cl ($3s^2 3p^5$), 7 electrons of Br ($4s^2 4p^5$), and 7 electrons of Mn ($3d^5 4s^2$) were treated as valence electrons. The plane-wave basis cut-off was set to 520 eV, and a Gamma-centered Monkhorst Pack *k*-point mesh was used for Brillouin-zone integration.[52] A *k*-point density of 5000 *k*-points per reciprocal number of atoms, which amounts to a 10×10×10 *k*-point mesh for a 5-atom, cubic unit cell, was found to be well-converged for various simulation cell sizes.

2.4 Results and Analysis

2.4.1 Synthesis and General Characterization. Figure 2.1 plots general characterization data for a representative sample of as-synthesized Mn^{2+}:$CsPbCl_3$ NCs. The average concentration of Mn^{2+} in this sample is 1.1%, as determined by ICP-AES. Figure 2.1A plots powder-X-ray diffraction data for this sample. The NC data index well to the pattern for orthorhombic $CsPbCl_3$, and no additional phases are observed. Figure 2.1B shows a representative TEM image of these NCs. The NCs are approximately cubic in shape with good size homogeneity and an average particle edge length of 6.9 ± 0.4 nm. Figure 2.1C plots room-temperature absorption and PL spectra of these NCs. The absorption spectrum shows a sharp first-exciton band centered at 395 nm, and the PL spectrum shows

narrow excitonic PL at 400 nm as well as an intense, broad band centered at 610 nm assigned as the $^4T_{1g} \rightarrow {}^6A_{1g}$ ligand-field transition of octahedral Mn^{2+}. Figure 2.1D plots the room-temperature X-band EPR spectrum of these Mn^{2+}:$CsPbCl_3$ NCs. This spectrum shows a resonance at $g = 2.01$, split into six lines by hyperfine coupling with the Mn^{2+} nuclear spin. From this splitting, a hyperfine coupling constant of 80.9 $x10^{-4}$ cm^{-1} is obtained, consistent with previous reports.[13,53] As noted previously, this hyperfine splitting is very large compared to those of Mn^{2+}-doped chalcogenide II-VI semiconductor NCs, reflecting the high ionicity of Mn^{2+} bonding in the $CsPbCl_3$ lattice.[54]

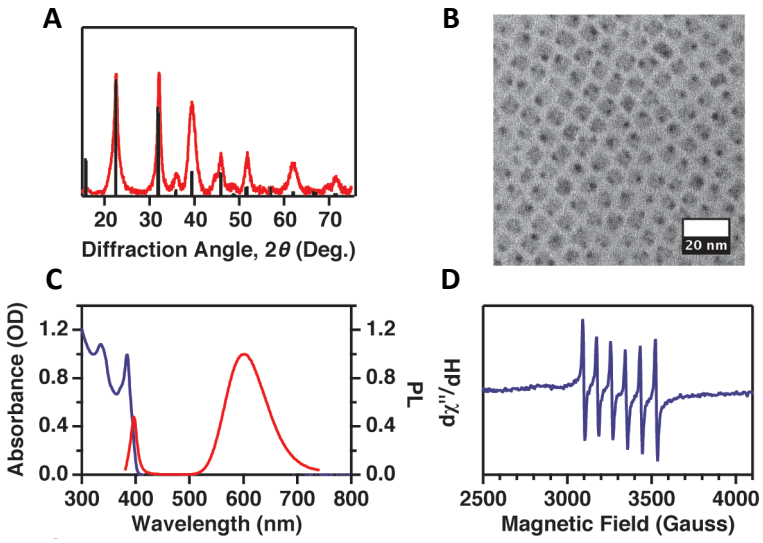

Figure 2.1. Characterization of representative colloidal 1.1% Mn^{2+}:$CsPbCl_3$ NCs. **(A)** Powder X-ray diffraction data collected for Mn^{2+}:$CsPbCl_3$ NCs drop-cast on a silicon substrate (red) and literature pattern (black) for orthorhombic $CsPbCl_3$ NCs. The NC data are consistent with the literature pattern. **(B)** TEM image of Mn^{2+}:$CsPbCl_3$ NCs, with scale bar representing 20 nm. The average edge length is 6.9 ± 0.4 nm. **(C)** Absorption (blue) and photoluminescence (red) spectra of the Mn^{2+}:$CsPbCl_3$ NCs. A 365 nm diode was used for photoexcitation. **(D)** X-band electron paramagnetic resonance (EPR) spectrum of the Mn^{2+}:$CsPbCl_3$ NCs. All data were collected at room temperature.

2.4.2 General Anion-Exchange Reactions. Trimethylsilyl halides (TMS-X, X = Cl, Br, I) have been demonstrated as useful anion-exchange reagents in elpasolite (double-perovskite) NCs[55] and $CsPbX_3$ NCs and thin films.[56] Here, we apply TMS-Br to induce anion exchange in Mn^{2+}:$CsPbCl_3$ perovskite NCs. Figure 2.2 summarizes the evolution of Mn^{2+}:$CsPbX_3$ NC physical characteristics during this anion exchange. Figure 2.2A shows that the first absorption maximum shifts to lower energy with added TMS-Br, consistent with $Cl^- \rightarrow Br^-$ anion exchange. At the endpoint of the reaction (excess TMS-Br), SEM/EDX measurements confirm essentially complete halide exchange with no significant change in Mn^{2+} content (see Figure A1).

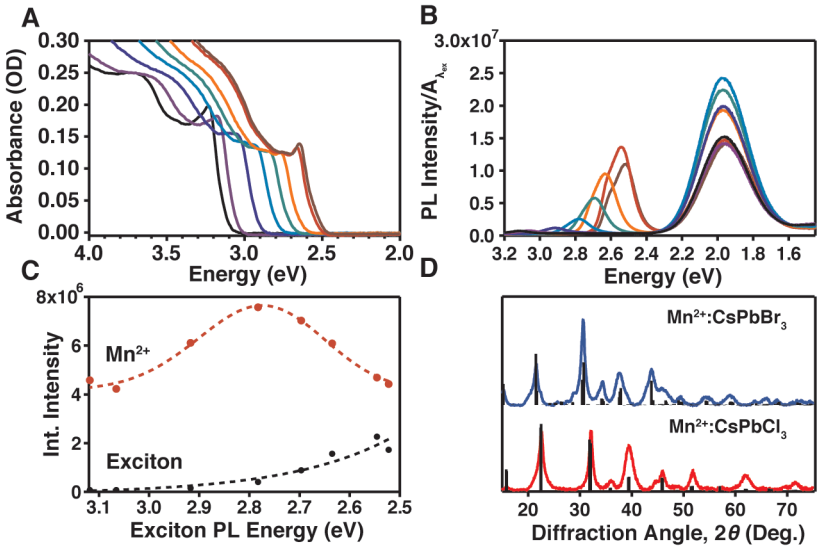

Figure 2.2. (A) UV/Vis absorption spectra of 1.1% Mn^{2+}:$CsPbCl_3$ NCs collected during the course of an anion exchange reaction using trimethylsilyl bromide (TMS-Br). **(B)** Corresponding PL spectra collected during the course of anion exchange. NCs were photoexcited at 375 nm. The PL spectra are plotted relative to the optical density of the sample at the excitation wavelength, allowing relative changes in quantum yield during anion exchange to be assessed. **(C)** Total integrated excitonic (black) and Mn^{2+} *d-d* (orange) PL intensities from the data in panel B, plotted against the energy of the excitonic PL. The dashed lines are guides to the eye. **(D)** Powder X-ray diffraction data collected before and after anion exchange. Both patterns are consistent with the orthorhombic phase.

Figure 2.2B plots PL spectra collected as a function of added TMS-Br. These data also show a red-shift of the excitonic emission with added bromide, but there is no clear change in the energy of the Mn^{2+} *d-d* emission. A blue shoulder in the excitonic region appears with greater bromide incorporation, attributed to sample inhomogeneity. These PL spectra have been corrected for the optical density of the sample at the excitation wavelength, allowing quantitative analysis of their integrated intensities (*i.e.*, relative PL quantum yields) over the course of the anion-exchange reaction, and these intensities are summarized in Figure 2.2C. The same PL spectra normalized to their total integrated intensities (which corrects for changes in PL quantum yield) or normalized to the exciton maxima (for comparison with published data[6,57]) are provided in Appendix A (Figure A2). From Figure 2.2C, the excitonic PL becomes much brighter as Br^- is incorporated, whereas the Mn^{2+} PL intensity first grows but then decreases with increasing Br^- incorporation. These trends are generally consistent with previous data,[6,26] but show substantially more Mn^{2+} PL from the resulting Mn^{2+}:$CsPbBr_3$ NCs than observed in other samples.[6] Overall, these data demonstrate that Mn^{2+} PL is still sensitized by NC photoexcitation even after complete $Cl^- \rightarrow Br^-$ anion exchange. Figure 2.2D plots powder X-ray diffraction data collected before and after NC anion exchange. The orthorhombic crystal structure of the parent Mn^{2+}:$CsPbCl_3$ NCs is preserved upon conversion to Mn^{2+}:$CsPbBr_3$.

According to previous literature, the changes in Mn^{2+} and exciton PL intensities with anion exchange (Figure 2.2C) can be attributed to two effects. First, the increase in both the excitonic and Mn^{2+} PL intensities with initial Br^- incorporation is consistent with observations made for analogous undoped NCs; the exciton PL quantum yield in undoped $CsPbCl_3$ NCs generally increases substantially with $Cl^- \rightarrow Br^-$ anion exchange,[11-12] because narrowing the perovskite energy gap diminishes non-radiative recombination losses by reducing the number of accessible surface traps.[58] Second, the decrease in Mn^{2+} PL intensity at larger Br^- content and the corresponding increase in excitonic PL intensity could reflect thermally assisted "back" energy transfer from Mn^{2+} to repopulate the excitonic excited state when their energy difference narrows sufficiently.[6,26] It is conceivable that such back energy transfer does occur in Mn^{2+}:$CsPb(Cl_{1-x}Br_x)_3$ NCs with large x, but as noted previously, this system is vastly different from the well-studied system of dual-emitting II-VI Mn^{2+}-doped NCs.[59-60] For example, in dual-emitting II-VI Mn^{2+}-doped NCs, forward energy transfer is fast and thermally assisted back energy transfer is strongly suppressed when the temperature is lowered, yielding almost exclusively Mn^{2+} PL at low temperatures, but the PL of Mn^{2+}:$CsPb(Cl_{0.22}Br_{0.78})_3$ NCs prepared here does not show an analogous temperature dependence (see Figures A8-9). Instead, the excitonic PL from these NCs increases and their Mn^{2+} PL decreases with decreasing temperature before both turn over at ~75 K, and substantial excitonic PL is still observed even at 5 K. In fact, this temperature dependence appears very similar to the behavior reported for Mn^{2+}:$CsPbCl_3$ NCs,[54] which have too large an energy gap for back energy transfer. These observations support the conclusion of a more complicated origin of the spectral changes in Mn^{2+}:$CsPb(Cl_{1-x}Br_x)_3$ NCs with anion exchange. As detailed below, the experiments performed here identify a new and unrecognized complication contributing to such PL trends: Mn^{2+} clustering within the NC lattice during anion exchange.

2.4.3 Evidence for Mn^{2+} Clustering upon Anion Exchange. To probe Mn^{2+} speciation, EPR measurements were also performed at various stages of anion exchange. For these measurements, anion exchange was performed in a gas-tight EPR tube, and both PL and EPR data were collected after addition of each TMS-Br aliquot. Importantly, the product of the anion-exchange reaction is gaseous TMS-Cl, which can be removed without removing any NCs, and the solvent volume can be kept constant. Consequently, Mn^{2+} *cannot* be lost from the EPR tube because the sample is never removed from the EPR tube throughout the entire experiment.

Figure 2.3A plots the PL spectra of a sample of Mn^{2+}:$CsPbCl_3$ NCs collected during the course of such an anion-exchange reaction. Each spectrum corresponds to a different stage of TMS-Br titration. As in Figure 2.2C, TMS-Br addition redshifts the excitonic PL as the host lattice is converted from $CsPbCl_3$ to $CsPbBr_3$, but the Mn^{2+} *d-d* PL energy remains largely unchanged. In contrast with the data in Figure 2.2C, the spectra in Figure 2.3A have all been normalized to their total integrated areas because the optical density of the solution in the EPR tube was too high to measure accurately, so only trends in relative PL intensities can be interpreted. Nonetheless, the key observation from the PL data is that, as in Figure 2.2C, Mn^{2+} PL is still sensitized by NC photoexcitation even after complete

anion exchange, and hence some if not all of the Mn^{2+} is still intimately integrated with the NCs and likely still inside the NC lattice.

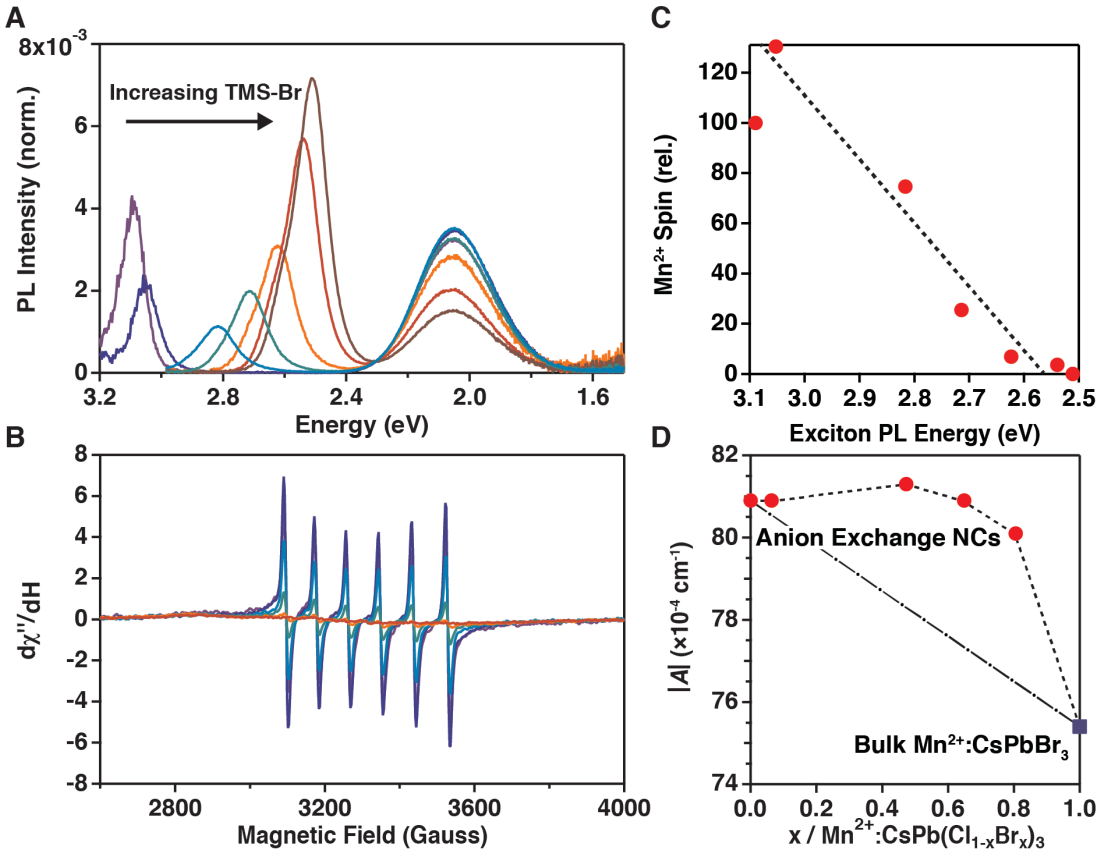

Figure 2.3. (A) PL spectra of 1.1% Mn^{2+}:$CsPbCl_3$ NCs in the EPR tube during the course of an anion exchange reaction, note that Mn^{2+} PL is seen centered at ~610 nm at every stage of the anion exchange reaction. The PL spectra are each normalized to their total integrated PL intensity. A 365 nm diode was used for excitation. Each spectrum was taken at the same NC concentration, and the NCs were never removed from the EPR tube over the entire experiment. **(B)** X-band EPR spectra collected during the course of the same anion exchange reaction as described in panel A. **(C)** Scatter plot of the relative Mn^{2+} spin, determined from double integration of the EPR spectra, *vs* the exciton PL peak energy from (A). The dashed line is a guide to the eye. **(D)** Summary of hyperfine splitting constants, $|A|$, for Mn^{2+}:$CsPb(Cl_{1-x}Br_x)_3$ NCs measured during anion exchange, taken from the spectra collected in (B) and for Mn^{2+}:$CsPbBr_3$ bulk powder taken from the spectra in Figure A6. The dashed line (---) is a guide to the eye, tracing the experimental hyperfine splitting constants. The dot-dashed line (–•–) illustrates the Mn^{2+} hyperfine splittings expected for random solid solutions of halides in $CsPbX_3$. Bromide concentrations are estimated from the known dependence of the excitonic PL energy on x.

Figure 2.3B plots EPR spectra collected during this same anion-exchange reaction. A striking decrease in the Mn^{2+} EPR intensity is observed as TMS-Br is added, and at maximum anion exchange there is no detectable Mn^{2+} EPR signal at all. Again, we stress that this loss of EPR intensity *cannot* be associated with any actual loss of Mn^{2+} from the EPR tube. Figure 2.3C summarizes the change in double-integrated EPR intensity with anion exchange, the latter represented in terms of the excitonic PL energy. This result shows a strong correlation between the incorporation of Br^- into the NCs and the loss of EPR-active Mn^{2+}, despite the retention of Mn^{2+} PL.

ICP-AES measurements confirm that Mn^{2+} is still strongly associated with the perovskite NCs after anion exchange: The starting Mn^{2+} concentration was measured to be 1.1% (of total B-site cations) in these NCs. After complete anion exchange and spectroscopic measurement, the NCs were removed from the EPR tube and washed twice by standard precipitation/centrifugation/resuspension methods to eliminate any Mn^{2+} that may have been expelled from the NCs, and the remaining NC sample was then analyzed by ICP-AES. The resulting Mn^{2+} concentration was still 1%, *i.e.*, within error of the starting concentration. The data thus rule out loss of Mn^{2+} from the NCs. This conclusion is bolstered by the continued absence of any EPR signal even at 120 K; the EPR spectra of plausible solvated Mn^{2+} species (*e.g.*, $Mn(oleate)_2$) are readily detectable at low temperatures (see Figures A3-5). Moreover, this low-temperature result also indicates that the loss of Mn^{2+} EPR intensity does not result from accelerated Mn^{2+} spin relaxation in the $CsPbBr_3$ lattice. For reference, we prepared bulk 0.1% Mn^{2+}:$CsPbBr_3$ and confirmed that its EPR signal is readily detectable at room temperature (see Figure A6).

Insight into this strange loss in Mn^{2+} EPR intensity with anion exchange is obtained by analysis of the Mn^{2+} hyperfine splittings observed in Figure 2.3B. These hyperfine splittings are summarized in Figure 2.3D. In the starting Mn^{2+}:$CsPbCl_3$ NC EPR spectrum (Figure 2.3B), the hyperfine splitting constant is $|A| = 80.9 \times 10^{-4}$ cm^{-1}, consistent with literature results.[13,53] Interestingly, there is little or no detectable change in the hyperfine splitting constant over the entire course of the anion-exchange reaction. For comparison, the EPR spectrum of Mn^{2+}:$CsPbBr_3$ shows a hyperfine splitting of $|A| = 75.4 \times 10^{-4}$ cm^{-1} (see Figure A6), illustrating the trend of decreasing hyperfine splitting with increasing metal-ligand covalency within the local $[MnX_6]^{4-}$ cluster.[61-62] These observations yield the surprising conclusion that essentially *all* EPR-active Mn^{2+} remains exclusively chloride-coordinated, and that Mn^{2+} ions coordinated by bromide are either not present in these NCs or are no longer EPR active. In this vein, it is perhaps telling that the literature does not yet have any clear examples of EPR spectra of Mn^{2+} in $CsPbBr_3$ NCs, and the few examples that have been reported[16,53] show hyperfine splittings *greater* than that of Mn^{2+} in $CsPbBr_3$, suggesting oxygenic Mn^{2+} coordination.

To explain the above observations, we hypothesize that $Cl^- \rightarrow Br^-$ anion exchange causes Mn^{2+} clustering within the perovskite NCs. Because of the 180° M^{2+}-X-M^{2+} bond angle in this lattice, nearest-neighbor Mn^{2+}-Mn^{2+} superexchange coupling in such clusters would be antiferromagnetic[63-64] and hence this Mn^{2+} would be EPR silent, but it could still luminesce. We further hypothesize that this clustering is driven thermodynamically by a preference for Mn-Cl rather than Mn-Br bonding. For example, the bond dissociation energies of Mn-Cl ($MnCl_2$) and Mn-Br ($MnBr_2$) are 392.5 and

332.2 kJ/mol,[65] respectively, reflecting this preference. To test this interpretation, we investigated whether the spectroscopic changes in Figure 2.3 are reversible, *i.e.*, whether $Br^- \rightarrow Cl^-$ anion exchange could reintroduce a Mn^{2+} EPR signal. For this experiment, we first converted 3.7% Mn^{2+}:$CsPbCl_3$ NCs to Mn^{2+}:$CsPbBr_3$ NCs as in Figure 2.3. Following conversion, these NCs were removed from the EPR tube and washed twice by standard precipitation/centrifugation/resuspension methods to eliminate any Mn^{2+} that may have been ejected from the NCs. We then added neat TMS-Cl to the solution to drive the reverse anion exchange, again monitoring the PL and EPR. This reaction was performed under conditions that were otherwise identical to those used for Figure 2.3. In particular, the NCs were again not removed from the EPR tube during the $Br^- \rightarrow Cl^-$ reverse anion exchange, and the NC concentration in the EPR tube was held constant. Figure 2.4A plots the evolution of the PL spectra during this reverse anion exchange. The excitonic PL shifts to higher energy, consistent with chloride incorporation, and concomitantly the relative Mn^{2+} PL intensity increases. The PL spectrum obtained after the full forward and reverse anion-exchange cycle is very similar to the initial spectrum, again consistent with full retention of Mn^{2+} in the NCs. Figure 2.4B plots the corresponding EPR spectra. In this sample, anion exchange to form Mn^{2+}:$CsPbBr_3$ NCs eliminates most but not all of the Mn^{2+} EPR signal; the remaining EPR signal is weak and its hyperfine splittings are unresolved. This breadth is consistent with Mn^{2+} being magnetically concentrated, as hypothesized above. Upon reverse anion exchange, the EPR intensity increases again and hyperfine splittings emerge, consistent with dissociation of Mn^{2+} clusters and randomization of the Mn^{2+} spatial distribution. This recovered hyperfine splitting is described by $|A| = 80.9 \times 10^{-4}$ cm^{-1}, consistent with $[MnCl_6]^{4-}$. From these results we conclude that $Br^- \rightarrow Cl^-$ reverse anion exchange breaks up antiferromagnetic Mn^{2+} clusters formed during the $Cl^- \rightarrow Br^-$ forward anion exchange.

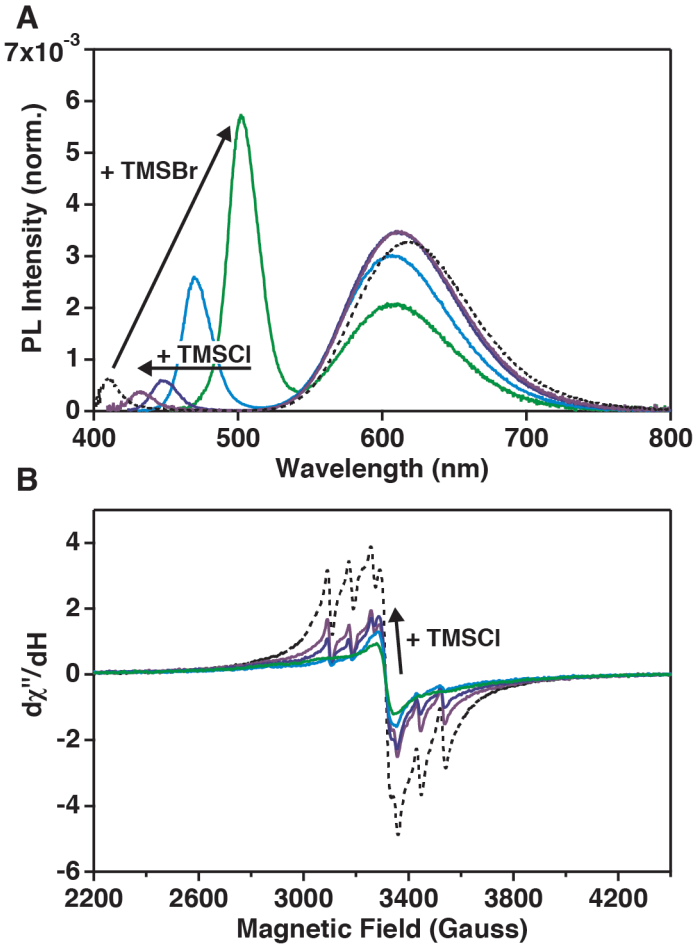

Figure 2.4. (A) Photoluminescence (PL) spectra of 3.7% Mn^{2+}:$CsPbBr_3$ NCs collected during the course of reverse anion exchange. Mn^{2+} PL at ~610 nm is observed at each stage of anion exchange. The PL spectra are normalized to the total integrated PL intensity. **(B)** Corresponding X-band EPR spectra of Mn^{2+}:$CsPbBr_3$ NCs made *via* anion exchange of Mn^{2+}:$CsPbCl_3$ NCs with TMS-Br during the course of a reverse anion exchange reaction using TMS-Cl. Each spectrum is taken at the same NC and Mn^{2+} concentration, as in the experiment of Figure 2.3. The Mn^{2+} hyperfine splitting constant is $|A|$ = 80.9 x10^{-4} cm^{-1}. The broad feature underneath the sharper Mn^{2+} hyperfine lines is assigned to magnetically concentrated Mn^{2+}. EPR and PL spectra of the initial Mn^{2+}:$CsPbCl_3$ NCs are shown as dashed lines.

Effects of Mn^{2+} clustering are also observed by PL. Figure 2.5 summarizes Mn^{2+} PL data collected at 5.2 K for 1.1% Mn^{2+}:$CsPbCl_3$ NCs and for the same Mn^{2+}:$CsPb(Cl_{1-x}Br_x)_3$ NCs after partial bromide exchange (x = 0.78). The main panel plots Mn^{2+} PL decay curves for the two samples, and the corresponding 5.2 K PL spectra are shown in the inset. The Mn^{2+}:$CsPbCl_3$ NCs show monoexponential PL decay with a lifetime of 3.4 ms, consistent with the spin- and parity-forbidden Mn^{2+} $^4T_{1g} \rightarrow {}^6A_{1g}$ ligand-field origin of this emission.[54] In contrast, the Mn^{2+}:$CsPb(Cl_{1-x}Br_x)_3$ NCs

show biexponential PL decay with components of 859 μs and 2.3 ms. We note that the Mn^{2+} PLQY *increases* after this anion exchange, possibly due to reduced exciton trapping prior to energy capture by Mn^{2+}. Shorter Mn^{2+} PL lifetimes are typically observed in bromide compared to chloride lattices (*e.g.*, 54.9 ms in $CsCaCl_3$ *vs* 23 ms in $CsMgBr_3$, respectively, at 10 K[66-67]), attributable to the increased spin-orbit coupling of the heavier halides, but this effect cannot explain the biexponential decay or the short time constant observed in Figure 2.5. Moreover, the hyperfine splittings in the EPR spectra of these NCs (Figure 2.3) indicate that Mn^{2+} remains essentially exclusively coordinated by chloride anions, also ruling out an effect from bromide spin-orbit coupling. Mn^{2+} lifetime shortening due to thermal back energy transfer to the exciton state does not occur at these low temperatures, either. Instead, we propose that this lifetime shortening is attributable to Mn^{2+} clustering. In Mn^{2+}-Mn^{2+} dimers and other clusters, magnetic superexchange coupling generates spin ladders in both the ground and excited states that introduce new spin-allowed components to otherwise spin-forbidden electronic transitions, accelerating radiative decay.[68-69] High Mn^{2+} concentrations also facilitate energy migration to traps, accelerating nonradiative decay. Collectively, the experimental results point to Mn^{2+} migration and clustering induced by $Cl^- \rightarrow Br^-$ anion exchange in Mn^{2+}:$CsPb(Cl_{1-x}Br_x)_3$ NCs.

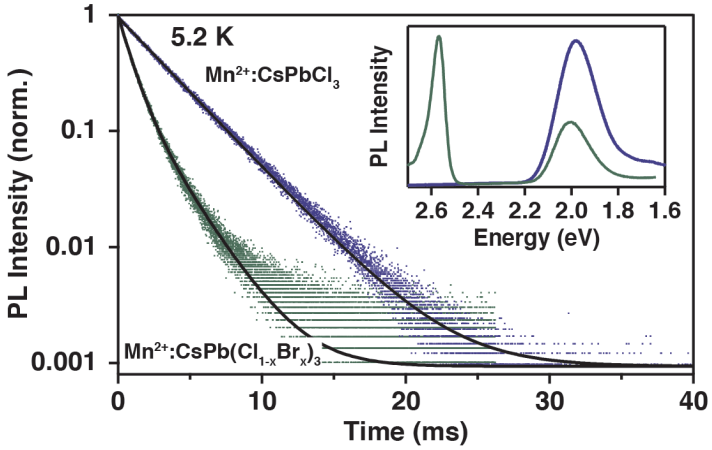

Figure 2.5. Photoluminescence decay curves measured for 1.1% Mn^{2+}:$CsPbCl_3$ NCs (blue) using 375 nm and for 1.1% Mn^{2+}:$CsPb(Cl_{1-x}Br_x)_3$ NCs (x = 0.78) (green) using 405 nm excitation. Both excitation sources were pulsed as square waves at a 10 Hz repetition rate. The data are normalized at time zero. Black lines are fits to the data. The data for the Mn^{2+}:$CsPbCl_3$ NCs are fit to a single-exponential function with a time constant of 3.36 ms. The data for the Mn^{2+}:$CsPb(Cl_{1-x}Br_x)_3$ NCs are fit to a double-exponential function with time constants of 859 μs and 2.3 ms. The inset shows the corresponding PL spectra of the Mn^{2+}:$CsPbCl_3$ (blue) and Mn^{2+}:$CsPb(Cl_{1-x}Br_x)_3$ (green) NCs excited with 405 nm. All data were collected at 5.2 K. EPR spectra of these samples are shown in Figure 2.3. RT absorption spectra of these samples are provided in Figure A7.

2.4.4 Thermodynamics of Mn^{2+} Clustering. To explore the thermodynamics of Mn^{2+} clustering, we modeled atom distributions in Mn^{2+}:$CsPb(Cl_{1-x}Br_x)_3$ using a cluster-expansion energy model and canonical Monte Carlo (MC) methods, as detailed in the Methods section. Figure 2.6 shows energy-minimized distributions of Mn^{2+}, Cl^-, and Br^- ions calculated for x = 0.80 and 1.00. Similar plots for the complete halide composition series are provided in Figure A10. A representative energy-minimization trajectory is also given in Figure A11.

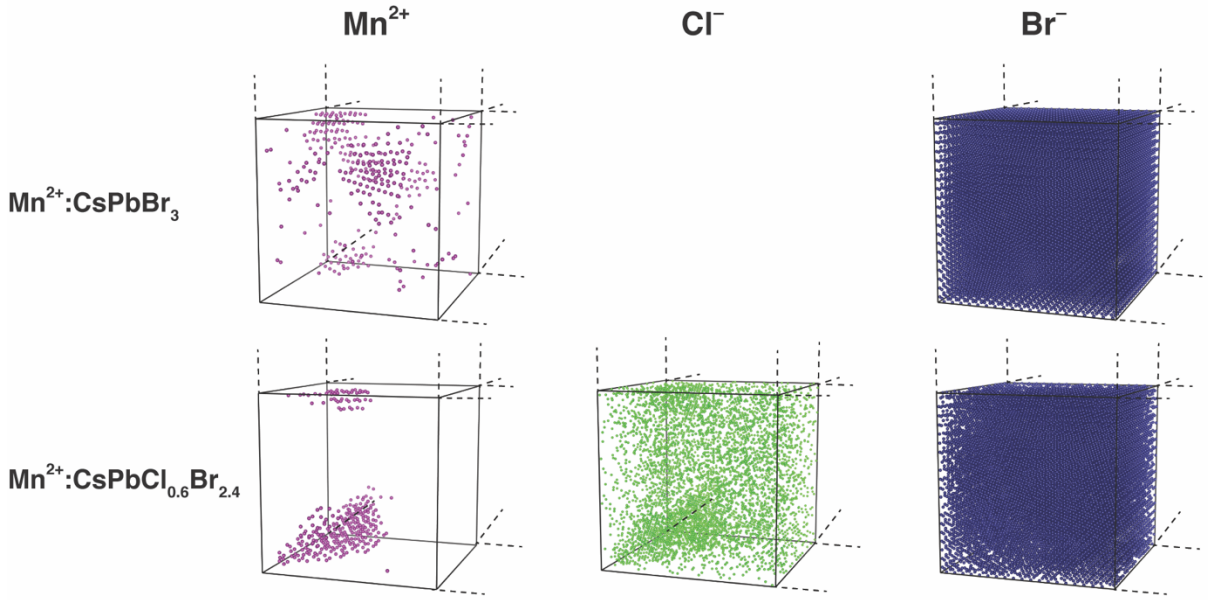

Figure 2.6. Distribution of atoms within a 4% Mn^{2+}:$CsPb(Cl_{1-x}Br_x)_3$ supercell for x = 1.0 (top) and 0.8 (bottom). The distributions of Mn^{2+}, Cl^-, and Br^- ions are shown.

We quantify clustering predicted by the MC simulations in terms of Warren-Cowley type short-range order (SRO) parameters given by eq 2,

$$\eta_i^{(\alpha|\beta)} = \frac{\langle p_i(\alpha|\beta)\rangle - c_\alpha}{1-c_\alpha} \tag{2.2}$$

where $p_i(\alpha|\beta)$ is the conditional probability that any α species has a β species at a lattice distance $i \in$ {1NN, 2NN, 3NN, …}, and iNN is the ith nearest neighbor shell.[70] Because we do not consider anti-site formation in this work, in the case where α = β, iNN denotes the ith nearest neighbor shell on the α sublattice. The fractional composition of the alloy species α is given by c_α, and ⟨…⟩ denotes a thermal average with respect to the canonical ensemble. The SRO parameters measure the degree of pairwise α-β clustering. For nonzero concentrations of species α and β, the SRO parameters vanish identically for a completely disordered state, which in principle occurs only in the limit of infinite temperature. The lower bound for the SRO parameter is given by $-c_\alpha/(1-c_\alpha)$. A value $0 < \eta_i^{(\alpha|\beta)} \leq 1$ indicates a tendency toward ion segregation, and conversely, $-c_\alpha/(1-c_\alpha) \leq \eta_i^{(\alpha|\beta)} < 0$ indicates a tendency toward local mixing with species distinct from β at the ith nearest neighbor.

Figure 2.7 plots Mn^{2+}-Mn^{2+} SRO parameters for 1st, 2nd, and 3rd NN positions as a function of the halide composition parameter, x. Interestingly, the pure and dilute chloride compositions both show segregation of ordered Mn^{2+}-rich domains characterized by Mn^{2+}-Mn^{2+} pairs occupying 2NN sites. The decomposition of an initially random mixture into coexisting Mn^{2+}-enriched and -depleted domains, *i.e.*, spinodal decomposition, suggests a tendency for each Mn^{2+} to maximize its number of Pb^{2+} nearest neighbors in the absence of significant halide mixing. The stability of the Mn^{2+}-enriched phase is consistent with a simple model of Coulomb energy gain.[71] In this picture, there is a transfer of partial charge, δ, between Mn^{2+} and Pb^{2+} nearest neighbors due to their different electronegativities and the high ionicity of the lattice. This transfer leads to nominal oxidation states of $Pb^{(2-\delta)+}$ and $Mn^{(2+\delta)+}$, and it lowers the Coulomb energy by an amount proportional to $-\delta^2/2r$, where $2r$ is the distance between the Pb^{2+} and Mn^{2+} ions. The configuration that maximizes the number of 1NN Mn^{2+}-Pb^{2+} pairs maximizes this Coulomb energy gain. The optimal configuration thus corresponds to Mn^{2+}-Mn^{2+} pairs ordered on 2NN sites. Using DFT and Bader charge analysis,[72] the average charge transferred between 1NN Mn^{2+} and Pb^{2+} is δ = 0.21 and 0.19 in the cases of $Cs_2PbMnCl_6$ and $Cs_2PbMnBr_6$, respectively. This 2NN ordering may also reduce the lattice strain associated with substituting Pb^{2+} with the smaller Mn^{2+}, leading to further stabilization relative to the random alloy. Because superexchange is only a short-range interaction, superexchange coupling between 2NN Mn^{2+} ions is negligible and 2NN ordering therefore cannot explain the experimental clustering concluded from the loss of EPR intensity in Figure 2.3. To explain this observation, 1NN Mn^{2+}-Mn^{2+} clustering is required.

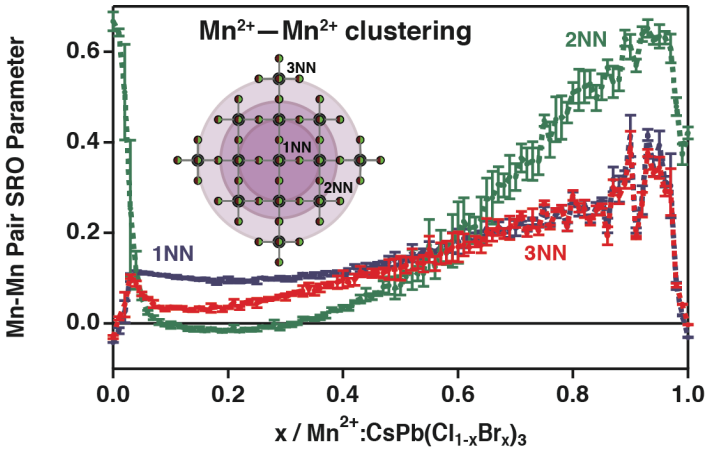

Figure 2.7. Short-range order (SRO) parameters for 1NN, 2NN, and 3NN Mn^{2+}-Mn^{2+} pairs in 4% Mn^{2+}:$CsPb(Cl_{1-x}Br_x)_3$ plotted *vs* the halide composition parameter x, as predicted by cluster-expansion canonical Monte Carlo methods. Spinodal decomposition is observed at both x = 0 and x = 1, and Mn^{2+}-Mn^{2+} 1NN clustering is observed when x > 0. The SRO oscillations near x = 1.0 are due to fluctuations between competing low-energy cluster configurations. The inset shows the 1NN, 2NN, and 3NN sites around a central cation, with chloride/bromide ions depicted in green/brown and lead/manganese ions depicted in gray.

For x = 0, the MC simulations predict no 1NN Mn^{2+}-Mn^{2+} clustering. Figure 2.7 shows a rapid increase in 1NN clustering with Br^- addition in the dilute-bromide limit (small x), followed by non-linear and generally increasing 1NN clustering with increasing Br^- concentration. Indeed, clustering at all Mn^{2+}-Mn^{2+} separations (1NN, 2NN, 3NN) generally increases with increasing x, consistent with Mn^{2+} segregation into enriched crystalline domains as Br^- is added to the lattice. Moreover, the modeling further predicts that Cl^- will also cluster with increasing x, and specifically that the Mn^{2+} and Cl^- ions are themselves correlated. For example, Figure 2.8 plots 1NN and 2NN Mn-Cl and Mn-Br SRO parameters as a function of x. These results show that Mn^{2+}-Cl^- correlations increase and Mn^{2+}-Br^- correlations decrease with increasing x (see Figure A12 for Cl^--Cl^- and Br^--Br^- SRO plots). Although the results generally show anticorrelation for Mn^{2+}-Br^- pairs, there is in fact an initial positive correlation at low bromide concentrations that may result from a slight energy stabilization associated with relieving lattice strain by having a smaller Mn^{2+} dopant next to a larger bromide ion. Overall, these results support the two key conclusions drawn from the experimental results, namely that 1NN Mn^{2+} clustering occurs with increasing x in Mn^{2+}:$CsPb(Cl_{1-x}Br_x)_3$ NCs (Figure 2.3C), and that Mn^{2+} remains coordinated by Cl^- despite the addition of Br^- to the lattice (Figure 2.3D).

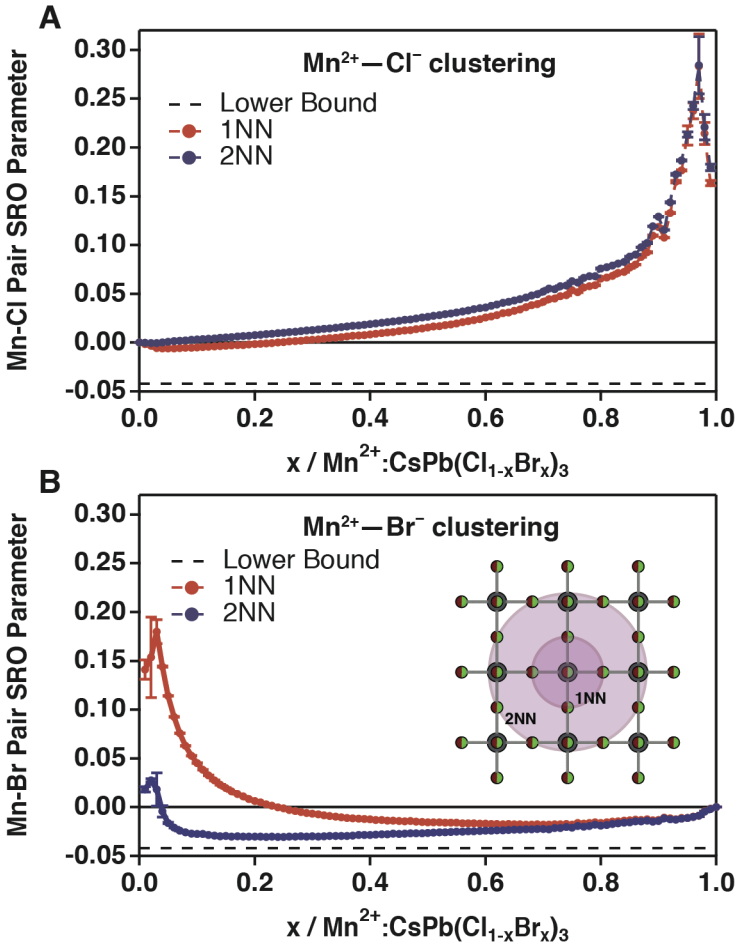

Figure 2.8. Short-range order (SRO) parameters $\eta_i^{(X|Mn)}$ for **(A)** Mn^{2+}-Cl^- and **(B)** Mn^{2+}-Br^- pairs in 4% Mn^{2+}:$CsPb(Cl_{1-x}Br_x)_3$, plotted *vs* the halide composition parameter *x*, as predicted by canonical Monte Carlo simulations. Mn^{2+}-Cl^- clustering becomes more pronounced as more Br^- is incorporated. The inset shows the 1NN and 2NN sites around a central cation, with chloride/bromide ions depicted in green/brown and lead/manganese ions depicted in gray.

2.5 Discussion

The experimental and computational results presented above provide strong evidence of Mn^{2+} clustering in Mn^{2+}:$CsPb(Cl_{1-x}Br_x)_3$ NCs induced by $Cl^- \rightarrow Br^-$ anion exchange. Mn^{2+} is highly mobile in Mn^{2+}:$CsPb(Cl_{1-x}Br_x)_3$ NCs, suggesting that clustering is driven thermodynamically not kinetically. A simple qualitative explanation for this observation can be proposed within the framework of hard-soft acid-base (HSAB) theory. As a hard Lewis acid, Mn^{2+} has a stronger preference for hard Cl^- (Lewis base) ligands relative to softer Br^- ligands. The specific preference of Mn^{2+} for $CsPbCl_3$ compared to $CsPbBr_3$ is evident from the facile incorporation of Mn^{2+} into the former,[16,24-25] and the inability to easily introduce Mn^{2+} into the latter either by direct synthesis or by cation exchange.[6,23] We propose that this preference is a primary driving force behind the Mn^{2+} clustering we have observed

experimentally in Figure 2.3C. Such considerations suggest that as the lattice Cl^- concentration decreases, Mn^{2+} dopants migrate in order to retain their preferred Mn-Cl bonding, eventually requiring two or more Mn^{2+} ions to bind to the same Cl^- anion, in turn increasing the prevalence of 1NN Mn^{2+}-Mn^{2+} pairs and their associated antiferromagnetic superexchange coupling. This process is summarized in Scheme 2.1.

Scheme 2.1. Proposed manganese clustering during $Cl^- \rightarrow Br^-$ anion exchange in Mn^{2+}:$CsPbCl_3$ NCs.

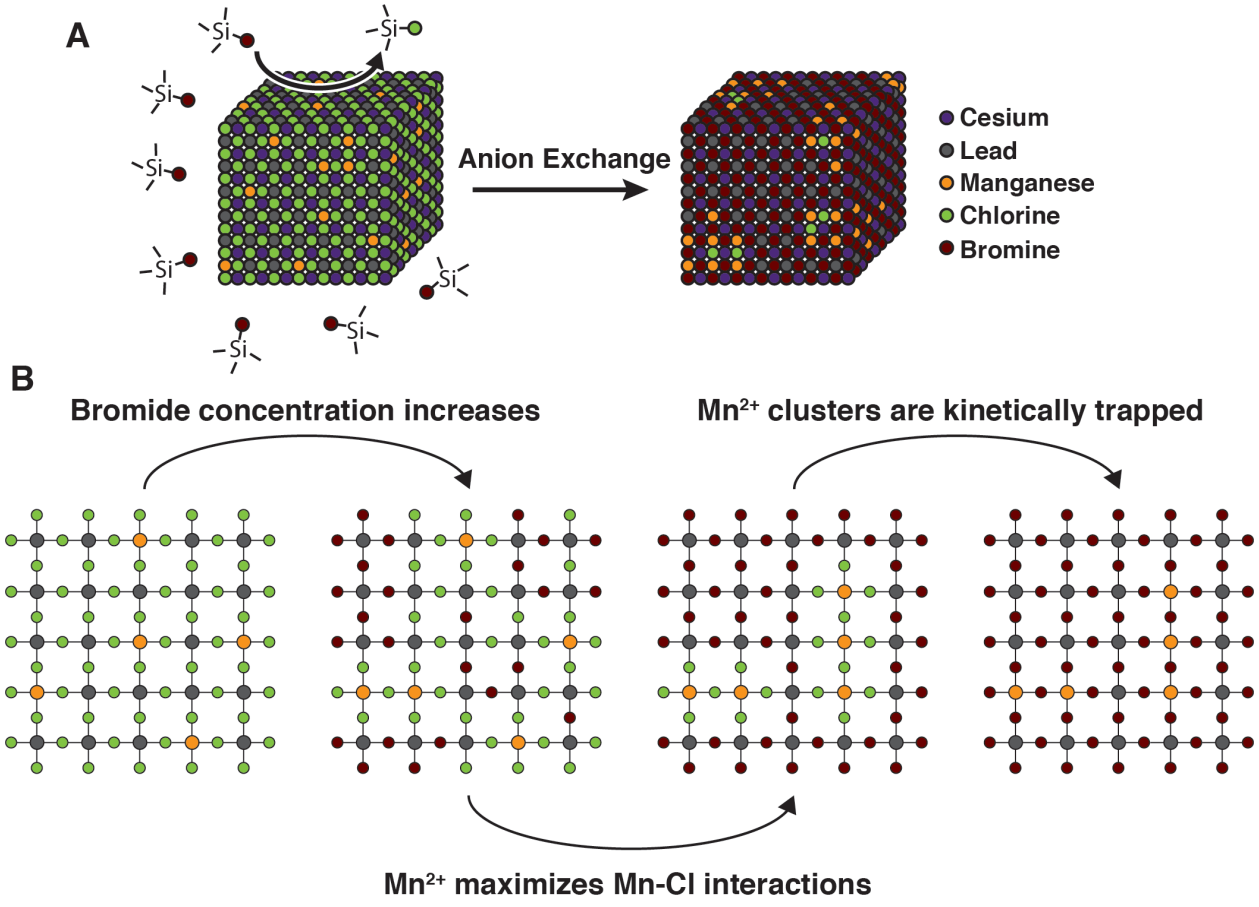

The MC simulations support this interpretation, showing positive and increasing Mn^{2+}-Mn^{2+} 1NN and Mn^{2+}-Cl^- 1NN correlations upon introduction of Br^- into a Mn^{2+}:$CsPbCl_3$ lattice. This situation is an example of spinodal decomposition, in which the free energy of an unstable solid solution is reduced by separating into coexisting phases. This segregation is driven in part by the difference between Mn-Cl and Mn-Br bond enthalpies. Beyond supporting the experimental conclusion of Br^--induced Mn^{2+} clustering in Mn^{2+}:$CsPb(Cl_{1-x}Br_x)_3$ NCs, the MC simulations reveal additional insights not detected experimentally. In particular, the modeling predicts that 2NN

Mn^{2+}-Mn^{2+} ordering is already thermodynamically favored even at the composition endpoints of Mn^{2+}:$CsPbCl_3$ and Mn^{2+}:$CsPbBr_3$. The clustering in these compositions has a strong preference for ordering at the 2NN site, driven by Coulomb interactions and potentially strain minimization. This 2NN ordering cannot explain the Br^--induced loss of EPR intensity, however; antiferromagnetic superexchange coupling requires 1NN Mn^{2+}-Mn^{2+} interactions. Although 1NN Mn^{2+}-Mn^{2+} interactions are not observed or predicted in the $CsPbCl_3$ limit under the conditions examined here, these conditions differ substantially from those that caused formation of spinodal $CsMnCl_3$ phases in $CsPbCl_3$ nanoplatelets, which involved prolonged 200°C solvothermal diffusion doping in the presence of high solvated Mn^{2+} concentrations;[32] the present study provides further evidence of condition-dependent nonrandom Mn^{2+} distributions within doped perovskite NCs.

The conclusions drawn here are based on thermodynamics and should be largely generalizable to bulk and nanocrystalline Mn^{2+}:$CsPb(Cl_{1-x}Br_x)_3$ prepared by different routes, or to Mn^{2+}:$CsPb(Cl_{1-x}Br_x)_3$ NC anion-exchange reactions involving different anion precursors. Still, a kinetic factor is also apparent in the observation that the 1NN Mn^{2+}-Mn^{2+} clustering induced by partial $Cl^- \rightarrow Br^-$ anion exchange is not lost again upon complete conversion to $CsPbBr_3$, where computations suggest the 2NN spinodal ordering would be more stable. The stability of isolated Mn^{2+} in $CsPbBr_3$ is supported by the observation of Mn^{2+} EPR hyperfine splittings in bulk Mn^{2+}:$CsPbBr_3$ prepared by direct synthesis (see Figure A6). This apparent reduction in Mn^{2+} mobility may be associated with the requirement of cation vacancies for cation migration in these lattices, a requirement that is more readily met during anion exchange than under static conditions.

The large structural reorganization and Mn^{2+} clustering in Mn^{2+}:$CsPb(Cl_{1-x}Br_x)_3$ NCs with anion exchange may impact the physical properties of these materials broadly. For example, the loss of Mn^{2+} EPR described here suggests that anion exchange converts paramagnetic Mn^{2+}:$CsPbCl_3$ NCs into antiferromagnetic Mn^{2+}:$CsPb(Cl_{1-x}Br_x)_3$ NCs, which should fundamentally alter the magneto-optical or magneto-transport responses of these materials. Additionally, this Mn^{2+} clustering complicates interpretation of the characteristic *x*-dependence of Mn^{2+} and excitonic PL intensities in Mn^{2+}:$CsPb(Cl_{1-x}Br_x)_3$ NCs noted in several publications,[6,26-28] because Mn^{2+} clustering alters Mn^{2+} radiative decay rates, Mn^{2+} non-radiative decay rates, and very likely also exciton-to-Mn^{2+} energy-transfer rates.

2.6 Conclusion

In summary, we have studied anion exchange in Mn^{2+}-doped $CsPb(Cl_{1-x}Br_x)_3$ NCs by PL and EPR spectroscopies. During the course of $Cl^- \rightarrow Br^-$ anion exchange, we observed disappearance of the Mn^{2+} EPR signal despite retention of strong Mn^{2+}-based PL. These results are interpreted as reflecting clustering of Mn^{2+} dopants during anion exchange to form antiferromagnetically coupled dimers or higher-nuclearity clusters. The thermodynamic driving force for this clustering comes from the stronger Mn-Cl bonding compared to Mn-Br bonding, in keeping with HSAB principles. The EPR hyperfine splittings measured during anion exchange confirm retention of Mn-Cl bonding even when the majority of lattice anions are bromides. DFT-based Monte Carlo modeling supports these

conclusions, predicting strongly correlated Mn^{2+} and Cl^- segregation as bromide is added to the lattice. Monte Carlo modeling further suggests that spinodal decomposition to form ordered Mn^{2+}-enriched domains is thermodynamically favorable even at the $CsPbCl_3$ and $CsPbBr_3$ endpoints of the lattice anion exchange reaction. Mn^{2+} ions are predicted to occupy second-nearest-neighbor positions relative to one another in these spinodal domains.

Overall, these experimental and computational results provide strong evidence that cationic dopants in metal-halide perovskites are generally distributed non-randomly, with dynamic spatial distributions that depend on the lattice's anion composition. Although not explicitly tested here, this conclusion likely extends to other cationic impurities beyond Mn^{2+}, and it likely applies to both bulk and nanostructured perovskites. The high mobility of both cations and anions in perovskite NCs contrasts the behavior established in chalcogenide semiconductor NCs such as CdSe, $Cu_{2-x}S$, or PbS, where cation exchange typically occurs without substantial perturbation of the anion sublattice.[73-74] The findings here of dynamic anion-dependent cation distributions *within* doped perovskite NCs impact the understanding of the stability and electronic or photophysical properties of such doped perovskites, which in turn has ramifications for how these and related metal-halide semiconductor materials may be used in future optoelectronic technologies.

2.7 References

1. Protesescu, L.; Yakunin, S.; Bodnarchuk, M. I.; Krieg, F.; Caputo, R.; Hendon, C. H.; Yang, R. X.; Walsh, A.; Kovalenko, M. V., Nanocrystals of Cesium Lead Halide Perovskites ($CsPbX_3$, X = Cl, Br, and I): Novel Optoelectronic Materials Showing Bright Emission with Wide Color Gamut. *Nano Lett.* **2015,** *15*, 3692-6.
2. Akkerman, Q. A.; Rainò, G.; Kovalenko, M. V.; Manna, L., Genesis, challenges and opportunities for colloidal lead halide perovskite nanocrystals. *Nat. Mater.* **2018,** *17*, 394-405.
3. Kang, J.; Wang, L.-W., High Defect Tolerance in Lead Halide Perovskite $CsPbBr_3$. *J. Phys. Chem. Lett.* **2017,** *8*, 489-493.
4. Li, X.; Wu, Y.; Zhang, S.; Cai, B.; Gu, Y.; Song, J.; Zeng, H., $CsPbX_3$ Quantum Dots for Lighting and Displays: Room-Temperature Synthesis, Photoluminescence Superiorities, Underlying Origins and White Light-Emitting Diodes. *Adv. Funct. Mater.* **2016,** *26*, 2435-2445.
5. Zhang, X.; Lin, H.; Huang, H.; Reckmeier, C.; Zhang, Y.; Choy, W. C. H.; Rogach, A. L., Enhancing the Brightness of Cesium Lead Halide Perovskite Nanocrystal Based Green Light-Emitting Devices through the Interface Engineering with Perfluorinated Ionomer. *Nano Lett.* **2016,** *16*, 1415.
6. Liu, W.; Lin, Q.; Li, H.; Wu, K.; Robel, I.; Pietryga, J. M.; Klimov, V. I., Mn^{2+}-Doped Lead Halide Perovskite Nanocrystals with Dual-Color Emission Controlled by Halide Content. *J. Am. Chem. Soc.* **2016,** *138*, 14954-14961.
7. Swarnkar, A.; Marshall, A. R.; Sanehira, E. M.; Chernomordik, B. D.; Moore, D. T.; Christians, J. A.; Chakrabarti, T.; Luther, J. M., Quantum dot–induced phase stabilization of α-$CsPbI_3$ perovskite for high-efficiency photovoltaics. *Science* **2016,** *354*, 92-95.
8. Akkerman, Q. A.; Gandini, M.; Di Stasio, F.; Rastogi, P.; Palazon, F.; Bertoni, G.; Ball, J. M.; Prato, M.; Petrozza, A.; Manna, L., Strongly emissive perovskite nanocrystal inks for high-voltage solar cells. *Nat. Energy* **2016,** *2*, 16194.

9. Zhang, J.; Wang, Q.; Zhang, X.; Jiang, J.; Gao, Z.; Jin, Z.; Liu, S., High-performance transparent ultraviolet photodetectors based on inorganic perovskite $CsPbCl_3$ nanocrystals. *RSC Adv.* **2017,** *7*, 36722-36727.
10. Miao, J.; Zhang, F., Recent progress on highly sensitive perovskite photodetectors. *J. Mater. Chem. C* **2019,** *7*, 1741-1791.
11. Nedelcu, G.; Protesescu, L.; Yakunin, S.; Bodnarchuk, M. I.; Grotevent, M. J.; Kovalenko, M. V., Fast Anion-Exchange in Highly Luminescent Nanocrystals of Cesium Lead Halide Perovskites ($CsPbX_3$, X = Cl, Br, I). *Nano Lett.* **2015,** *15*, 5635-5640.
12. Akkerman, Q. A.; D'Innocenzo, V.; Accornero, S.; Scarpellini, A.; Petrozza, A.; Prato, M.; Manna, L., Tuning the Optical Properties of Cesium Lead Halide Perovskite Nanocrystals by Anion Exchange Reactions. *J. Am. Chem. Soc.* **2015,** *137*, 10276-10281.
13. Parobek, D.; Roman, B. J.; Dong, Y.; Jin, H.; Lee, E.; Sheldon, M.; Son, D. H., Exciton-to-Dopant Energy Transfer in Mn-Doped Cesium Lead Halide Perovskite Nanocrystals. *Nano Lett.* **2016,** *16*, 7376-7380.
14. Guria, A. K.; Dutta, S. K.; Adhikari, S. D.; Pradhan, N., Doping Mn^{2+} in Lead Halide Perovskite Nanocrystals: Successes and Challenges. *ACS Energy Lett.* **2017,** *2*, 1014-1021.
15. Xu, K.; Lin, C. C.; Xie, X.; Meijerink, A., Efficient and Stable Luminescence from Mn^{2+} in Core and Core-Isocrystalline Shell $CsPbCl_3$ Perovskite Nanocrystals. *Chem. Mater.* **2017,** *29*, 4265-4272.
16. Mir, W. J.; Mahor, Y.; Lohar, A.; Jagadeeswararao, M.; Das, S.; Mahamuni, S.; Nag, A., Postsynthesis Doping of Mn and Yb into $CsPbX_3$ (X = Cl, Br, or I) Perovskite Nanocrystals for Downconversion Emission. *Chem. Mater.* **2018,** *30*, 8170-8178.
17. Pan, G.; Bai, X.; Yang, D.; Chen, X.; Jing, P.; Qu, S.; Zhang, L.; Zhou, D.; Zhu, J.; Xu, W.; Dong, B.; Song, H., Doping Lanthanide into Perovskite Nanocrystals: Highly Improved and Expanded Optical Properties. *Nano Lett.* **2017,** *17*, 8005-8011.
18. Milstein, T. J.; Kroupa, D. M.; Gamelin, D. R., Picosecond Quantum Cutting Generates Photoluminescence Quantum Yields Over 100% in Ytterbium-Doped $CsPbCl_3$ Nanocrystals. *Nano Letters* **2018,** *18*, 3792-3799.
19. Li, F.; Xia, Z.; Pan, C.; Gong, Y.; Gu, L.; Liu, Q.; Zhang, J. Z., High Br^- Content $CsPb(Cl_yBr_{1-y})_3$ Perovskite Nanocrystals with Strong Mn^{2+} Emission through Diverse Cation/Anion Exchange Engineering. *ACS Appl. Mater. Interfaces* **2018,** *10*, 11739-11746.
20. Chen, D.; Fang, G.; Chen, X., Silica-Coated Mn-Doped $CsPb(Cl/Br)_3$ Inorganic Perovskite Quantum Dots: Exciton-to-Mn Energy Transfer and Blue-Excitable Solid-State Lighting. *ACS Appl. Mater. Interfaces* **2017,** *9*, 40477-40487.
21. Meinardi, F.; Akkerman, Q. A.; Bruni, F.; Park, S.; Mauri, M.; Dang, Z.; Manna, L.; Brovelli, S., Doped Halide Perovskite Nanocrystals for Reabsorption-Free Luminescent Solar Concentrators. *ACS Energy Lett.* **2017,** *2*, 2368-2377.
22. Wang, Q.; Zhang, X.; Jin, Z.; Zhang, J.; Gao, Z.; Li, Y.; Liu, S. F., Energy-Down-Shift $CsPbCl_3$:Mn Quantum Dots for Boosting the Efficiency and Stability of Perovskite Solar Cells. *ACS Energy Lett.* **2017,** *2*, 1479-1486.
23. Parobek, D.; Dong, Y.; Qiao, T.; Son, D. H., Direct Hot-Injection Synthesis of Mn-Doped $CsPbBr_3$ Nanocrystals. *Chem. Mater.* **2018**.

24. Gao, D.; Qiao, B.; Xu, Z.; Song, D.; Song, P.; Liang, Z.; Shen, Z.; Cao, J.; Zhang, J.; Zhao, S., Postsynthetic, Reversible Cation Exchange between Pb^{2+} and Mn^{2+} in Cesium Lead Chloride Perovskite Nanocrystals. *J. Phys. Chem. C* **2017,** *121*, 20387-20395.
25. Xu, W.; Li, F.; Lin, F.; Chen, Y.; Cai, Z.; Wang, Y.; Chen, X., Synthesis of $CsPbCl_3$-Mn Nanocrystals via Cation Exchange. *Adv. Opt. Mater.* **2017,** *5*, 1700520.
26. Xu, K.; Meijerink, A., Tuning Exciton–Mn^{2+} Energy Transfer in Mixed Halide Perovskite Nanocrystals. *Chem. Mater.* **2018,** *30*, 5346-5352.
27. Mir, W. J.; Jagadeeswararao, M.; Das, S.; Nag, A., Colloidal Mn-Doped Cesium Lead Halide Perovskite Nanoplatelets. *ACS Energy Lett.* **2017,** *2*, 537–543.
28. Fei, L.; Yuan, X.; Hua, J.; Ikezawa, M.; Zeng, R.; Li, H.; Masumoto, Y.; Zhao, J., Enhanced luminescence and energy transfer in Mn^{2+} doped $CsPbCl_{3-x}Br_x$ perovskite nanocrystals. *Nanoscale* **2018,** *10*, 19435-19442.
29. Li, G.; Ho, J. Y.-L.; Wong, M.; Kwok, H. S., Reversible Anion Exchange Reaction in Solid Halide Perovskites and Its Implication in Photovoltaics. *J. Phys. Chem. C* **2015,** *119*, 26883-26888.
30. van der Stam, W.; Geuchies, J. J.; Altantzis, T.; van den Bos, K. H. W.; Meeldijk, J. D.; Van Aert, S.; Bals, S.; Vanmaekelbergh, D.; de Mello Donega, C., Highly Emissive Divalent Ion Doped Colloidal $CsPb_{1-x}M_xBr_3$ Perovskite Nanocrystals through Cation Exchange. *J. Am. Chem. Soc.* **2017,** *139*, 4087– 4097.
31. Li, M.; Zhang, X.; Matras-Postolek, K.; Chend, H.-S.; Yang, P., An anion-driven Sn^{2+} exchange reaction in $CsPbBr_3$ nanocrystals towards tunable and high photoluminescence. *J. Mater. Chem. C* **2018,** *6*, 5506-5513.
32. Li, Z.-J.; Hofman, E.; Davis, A. H.; Khammang, A.; Wright, J. T.; Dzikovski, B.; Meulenberg, R. W.; Zheng, W., Complete Dopant Substitution by Spinodal Decomposition in Mn-Doped Two-Dimensional $CsPbCl_3$ Nanoplatelets. *Chem. Mater.* **2018,** *30*, 6400-6409.
33. Kubicki, D. J.; Prochowicz, D.; Pinon, A.; Stevanato, G.; Hofstetter, A.; Zakeeruddin, S. M.; Grätzel, M.; Emsley, L., Doping and phase segregation in Mn^{2+}- and Co^{2+}-doped lead halide perovskites from ^{133}Cs and ^{1}H NMR relaxation enhancement. *J. Mater. Chem. A* **2019,** *7*, 2326-2333.
34. Puglisi, A.; Mondini, S.; Cenedese, S.; Ferretti, A. M.; Santo, N.; Ponti, A., Monodisperse Octahedral α-MnS and MnO Nanoparticles by the Decomposition of Manganese Oleate in the Presence of Sulfur. *Chem. Mater.* **2010,** *22*, 2804-2813.
35. Wong, A.; Sham, S.; Wang, S.; Wu, G., A solid-state ^{133}Cs nuclear magnetic resonance and X-ray crystallographic study of cesium complexes with macrocyclic ligands. *Can. J. Chem.* **2000,** *78*, 975-985.
36. Hart, G. L. W.; Forcade, R. W., Algorithm for generating derivative structures. *Phys. Rev. B* **2008,** *77*, 224115.
37. Sanchez, J. M.; Ducastelle, F.; Gratias, D., Generalized cluster description of multicomponent systems. *Physica A* **1984,** *128*, 334-350.
38. van de Walle, A., Multicomponent multisublattice alloys, nonconfigurational entropy and other additions to the Alloy Theoretic Automated Toolkit. *Calphad* **2009,** *33*, 266-278.
39. Nelson, L. J.; Hart, G. L. W.; Zhou, F.; Ozoliņš, V., Compressive sensing as a paradigm for building physics models. *Phys. Rev. B* **2013,** *87*, 035125.
40. CASMcode: v0.2.1; **2017**; DOI: 10.5281/zenodo.546148.

41. Puchala, B.; Van der Ven, A., Thermodynamics of the Zr-O system from first-principles calculations. *Phys. Rev. B* **2013,** *88*, 094108.
42. Van der Ven, A.; Thomas, J. C.; Xu, Q.; Bhattacharya, J., Linking the electronic structure of solids to their thermodynamic and kinetic properties. *Math. Comput. Simulat.* **2010,** *80*, 1393-1410.
43. van de Walle, A.; Ceder, G., Automating first-principles phase diagram calculations. *J. Phase Equilib.* **2002,** *23*, 348.
44. van de Walle, A.; Asta, M., Self-driven lattice-model Monte Carlo simulations of alloy thermodynamic properties and phase diagrams. *Modell. Simul. Mater. Sci. Eng.* **2002,** *10*, 521.
45. Pedregosa, F.; Varoquaux, G.; Gramfort, A.; Michel, V.; Thirion, B.; Grisel, O.; Blondel, M.; Prettenhofer, P.; Weiss, R.; Dubourg, V.; Vanderplas, J.; Passos, A.; Cournapeau, D.; Brucher, M.; Perrot, M.; Duchesnay, É., Scikit-learn: Machine Learning in Python. *J. Mach. Learn. Res.* **2011,** *12*, 2825-2830.
46. Kresse, G.; Hafner, J., Norm-conserving and ultrasoft pseudopotentials for first-row and transition elements. *J. Phys.: Condens. Matter* **1994,** *6*, 8245.
47. Kresse, G.; Joubert, D., From ultrasoft pseudopotentials to the projector augmented-wave method. *Phys. Rev. B* **1999,** *59*, 1758-1775.
48. Kresse, G.; Furthmüller, J., Efficient iterative schemes for ab initio total-energy calculations using a plane-wave basis set. *Phys. Rev. B* **1996,** *54*, 11169-11186.
49. Kresse, G.; Furthmüller, J., Efficiency of ab-initio total energy calculations for metals and semiconductors using a plane-wave basis set. *Comp. Mater. Sci.* **1996,** *6*, 15-50.
50. Blöchl, P. E., Projector augmented-wave method. *Phys. Rev. B* **1994,** *50*, 17953-17979.
51. Perdew, J. P.; Burke, K.; Ernzerhof, M., Generalized Gradient Approximation Made Simple. *Phys. Rev. Lett.* **1996,** *77*, 3865-3868.
52. Monkhorst, H. J.; Pack, J. D., Special points for Brillouin-zone integrations. *Phys. Rev. B* **1976,** *13*, 5188-5192.
53. Zou, S.; Liu, Y.; Li, J.; Liu, C.; Feng, R.; Jiang, F.; Li, Y.; Song, J.; Zeng, H.; Hong, M.; Chen, X., Stabilizing Cesium Lead Halide Perovskite Lattice through Mn (II)-Substitution for Air-Stable Light-Emitting Diodes. *J. Am. Chem. Soc.* **2017,** *139*, 11443–11450.
54. Yuan, X.; Ji, S.; De Siena, M. C.; Fei, L.; Zhao, Z.; Wang, Y.; Li, H.; Zhao, J.; Gamelin, D. R., Photoluminescence Temperature Dependence, Dynamics, and Quantum Efficiencies in Mn^{2+}-Doped $CsPbCl_3$ Perovskite Nanocrystals with Varied Dopant Concentration. *Chem. Mater.* **2017,** *29*, 8003-8011.
55. Creutz, S. E.; Crites, E. N.; De Siena, M. C.; Gamelin, D. R., Colloidal Nanocrystals of Lead-Free Double-Perovskite (Elpasolite) Semiconductors: Synthesis and Anion Exchange To Access New Materials. *Nano Lett.* **2018,** *18*, 1118-1123.
56. Creutz, S. E.; Crites, E. N.; De Siena, M. C.; Gamelin, D. R., Anion Exchange in Cesium Lead Halide Perovskite Nanocrystals and Thin Films Using Trimethylsilyl Halide Reagents. *Chem. Mater.* **2018,** *30*, 4887-4891.
57. Li, F.; Xia, Z.; Gong, Y.; Gu, L.; Liu, Q., Optical properties of Mn^{2+} doped cesium lead halide perovskite nanocrystals via a cation–anion co-substitution exchange reaction. *J. Mater. Chem. C* **2017,** *5*, 9281-9287.
58. Nenon, D. P.; Pressler, K.; Kang, J.; Koscher, B. A.; Olshansky, J. H.; Osowiecki, W. T.; Koc, M. A.; Wang, L.-W.; Alivisatos, A. P., Design Principles for Trap-Free $CsPbX_3$ Nanocrystals:

Enumerating and Eliminating Surface Halide Vacancies with Softer Lewis Bases. *J. Am. Chem. Soc.* **2018,** *140*, 17760-17772.
59. Beaulac, R.; Archer, P. I.; van Rijssel, J.; Meijerink, A.; Gamelin, D. R., Exciton Storage by Mn^{2+} in Colloidal Mn^{2+}-Doped CdSe Quantum Dots. *Nano Lett.* **2008,** *8*, 2949-2953.
60. Vlaskin, V. A.; Janßen, N.; van Rijssel, J.; Beaulac, R.; Gamelin, D. R., Tunable Dual Emission in Doped Semiconductor Nanocrystals. *Nano Lett.* **2010,** *10*, 3670–3674.
61. Matumura, O., Electron Spin Resonance of Mn-activated Phosphors. *J. Phys. Soc. Jpn.* **1959,** *14*, 108.
62. Šimánek, E.; Müller, K. A., Covalency and hyperfine structure constant A of iron group impurities in crystals. *J. Phys. Chem. Solids* **1970,** *31*, 1027-1040.
63. Gupta, R. P.; Seehra, M. S.; Vehse, W. E., Shift of Néel Temperature and EPR Linewidth of $KMnF_3$ with Mg Doping. *Phys. Rev. B* **1972,** *5*, 92-95.
64. Krebs, J. J., EPR Determination of the Nearest-Neighbor Exchange Constant for Mn^{2+} Pairs in $KZnF_3$. *J. Appl. Phys.* **1969,** *40*, 1137-1139.
65. Bond Energies. In *Encyclopedia of Inorganic Chemistry*, King, R. B.; Crabtree, R. H.; Lukehart, C. M.; Atwood, D. A.; Scott, R. A., Eds. 2006; p DOI: 10.1002/0470862106.id098.
66. De Lucas, M. C. M.; Rodríguez, F.; Prieto, C.; Verdaguer, M.; Moreno, M.; Güdel, H. U., Optical properties and local structure of $MnCl_6^{4-}$ in $ABCl_3:Mn^{2+}$. *Radiat. Eff. Defects Solids* **1995,** *135*, 95-100.
67. McPherson, G. L.; Waguespack, Y. Y.; Vanoy, T. C.; Rodriguez, W. J., Exciton migration in a ''pseudo''-one-dimensional crystal: Luminescence dynamics of doped $CsMnBr_3$. *J. Chem. Phys.* **1990,** *92*, 1768-1774.
68. Ferguson, J.; Guggenheim, H. J.; Tanabe, Y., Exchange Effects in the Electronic Absorption Spectrum of Mn(II) in Perovskite Fluorides. *J. Appl. Phys.* **1965,** *36*, 1046-1047.
69. Bradshaw, L. R.; May, J. W.; Dempsey, J. L.; Li, X.; Gamelin, D. R., Ferromagnetic excited-state Mn^{2+} dimers in $Zn_{1-x}Mn_xSe$ quantum dots observed by time-resolved magnetophotoluminescence. *Phys. Rev. B* **2014,** *89*, 115312.
70. De Fontaine, D., The number of independent pair-correlation functions in multicomponent systems. *J. Appl. Crystallogr.* **1971,** *4*, 15-19.
71. Yin, W.-J.; Yan, Y.; Wei, S.-H., Anomalous Alloy Properties in Mixed Halide Perovskites. *J. Phys. Chem. Lett.* **2014,** *5*, 3625-3631.
72. Tang, W.; Sanville, E.; Henkelman, G., A grid-based Bader analysis algorithm without lattice bias. *J. Phys.: Condens. Matter* **2009,** *21*, 084204.
73. Beberwyck, B. J.; Surendranath, Y.; Alivisatos, A. P., Cation Exchange: A Versatile Tool for Nanomaterials Synthesis. *J. Phys. Chem. C* **2013,** *117*, 19759-19770.
74. De Trizio, L.; Manna, L., Forging Colloidal Nanostructures via Cation Exchange Reactions. *Chem. Rev.* **2016,** *116*, 10852-10887.

Chapter 3: Conduction Band Splittings and Impurity Doping in Colloidal Europium(II) Monochalcogenide Nanocrystals

3.1 Overview

EuS and related ferromagnetic semiconductors are promising materials for spintronic applications because of their ability to generate highly spin-polarized electrical currents. These materials display large magnetically-induced conduction band splittings into spin-polarized bands, which enables their use in spin-filters. We use magnetic circular dichroism (MCD) spectroscopy to demonstrate giant temperature- and field-dependent conduction-band splittings in colloidal EuS and EuSe nanocrystals and discuss this below in Section 3.2. Even though EuS and related materials have such high potential for use in spintronic devices like spin-filters, the low Curie temperature (T_C) for EuS limits practical implementation of such devices. However, the T_C of bulk EuS, can be raised by *n*-doping with trivalent impurity ions such as Gd^{3+}. Electron doping introduces free conduction-band electrons that strengthen the magnetic ordering, raising T_C. In EuS nanostructures, analogous doping has also been explored, but such nanostructures have a tendency for Eu^{3+} impurities due to the synthetic methods, so it is unclear what impact trivalent impurities may have on magnetic ordering. Here in Section 3.3, we report spectroscopic, magnetic, and redox-chemical studies aimed at assessing the role of trivalent impurities in the ferromagnetism of colloidal EuS nanocrystals. Combining post-synthetic redox chemistry with optical and electron paramagnetic resonance (EPR) spectroscopic measurements, we show that reduction of native Eu^{3+} impurities to Eu^{2+} increases the overall magnetization below T_C and simultaneously decreases T_C by ~7%, with no evidence of free conduction-band electrons at any stage. The data suggest that some of the newly formed Eu^{2+} ions participate in the ferromagnetic ordering despite having a different coordination environment than the Eu^{2+} ions of the as-synthesized nanocrystals (*e.g.*, surface *vs* core Eu^{2+}), and we hypothesize that surface-localized charge compensation and the very negative EuS conduction-band-edge potential prevent *n*-doping in these nanocrystals. These results provide a well-controlled assessment of the contribution of trivalent impurities to the magnetism of EuS nanocrystals and additionally demonstrate post-synthetic chemical modulation of the ferromagnetism.

3.2 Giant Band Splittings in EuS and EuSe Magnetic Semiconductor Nanocrystals

Spintronic devices can exploit both the spins and the charges of electrons to control the flow of information. As such, spintronics have generated interest for data storage (e.g. tunnel magnetoresistance or magnetoresistive random access memory) and may play an important role in information processing and quantum computing technologies.[1] The development of such devices relies on understanding the creation and manipulation of spin-polarized currents, characterized by the percent spin polarization at the Fermi energy.[2] 'Spin-filtering', allowing only one type of spin to cross

a magnetic barrier, is an attractive approach to attaining high spin polarization from an unpolarized current. Because spin orientation is conserved in tunnelling, it is possible to use a magnetic tunnel barrier to generate spin-polarized electrons as well as to detect spin.[3] The extent of current spin polarization can also be determined using spin-polarized photoemission, but spin-polarized tunneling has the sub-millielectron volt resolution required for device development.[4]

The first demonstration of spin-filter tunneling in the absence of an applied field used EuS as the ferromagnetic spin-filter,[5] and EuSe provided the first example of fully polarized tunnel current.[6] Europium selenide is metamagnetic,[7] antiferromagnetic at low fields and ferromagnetic at high fields, so its spin-filtering efficiency is strongly field-dependent. The origin of spin-filtering by europium chalcogenides can be understood from the density of states diagram shown schematically in Fig. 3.1. Magnetic exchange interactions couple the half-occupied $4f$ electrons to the conduction band, comprised primarily of Eu^{2+} $5d$ orbitals. At T_C, magnetic ordering of the $4f$ electrons splits the conduction band into spin-up (lowered by ΔE_{ex}) and spin-down (raised by ΔE_{ex}) levels. Conduction-band splitting leads to a majority of one spin orientation at the Fermi level and highly polarized spin currents.[8] The extent of spin polarization depends on the magnitude of the splitting ($2\Delta E_{ex}$).[9] Spin-resolved X-ray absorption spectroscopy has been used to confirm the splitting between spin-up and spin-down levels at the bottom of the conduction band in EuO.[10]

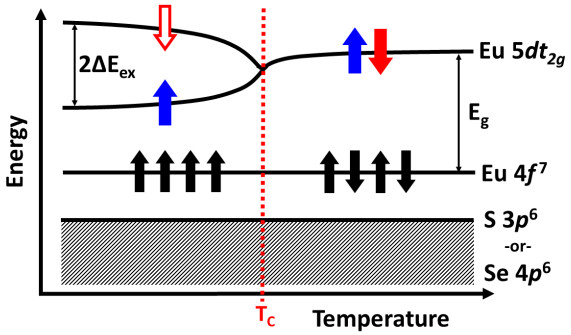

Figure 3.1. The effect of magnetic ordering on the conduction band. The black arrows indicate the spin of localized $4f$ electrons and the colored arrows indicate the spins of promoted charge carriers.

In this work, we report the effect of temperature and magnetic field on the magnetic circular dichroism (MCD) of solution-grown EuS and EuSe nanocrystals. Room-temperature MCD spectra of nanocrystals of EuS have been reported,[11] but we find striking changes in the spectra as a function of temperature and field that indicate a very large conduction-band splitting below T_C. We also report the first MCD study of EuSe of any morphology, again varying temperature and field. Room-temperature Faraday rotation (FR) spectra of EuSe nanomaterials have been reported;[12] but whereas FR is sensitive to long-range order, MCD is sensitive to short-range interactions that are important in this magnetically complex material. Changing temperature and applied field not only aid in sharpening the MCD peaks, but they also provide the opportunity to study changes in the density of states near

the ordering temperature to elucidate the effects of magnetic coupling on the optical properties.

EuS and EuSe nanocrystals were synthesized as previously reported[13] and characterized by X-ray powder diffraction and transmission electron microscopy (see Appendix B). The nanocrystal diameters were approximately 7 ± 1 nm for EuS and 60 ± 20 nm for EuSe, both with cubic morphology. MCD measurements near the ordering temperature reveal a large conduction-band splitting in the EuS nanocrystals. The MCD data for the EuSe nanocrystals indicate two low-temperature magnetic phases (ferri- and ferromagnetic), and this material also exhibits a large conduction-band splitting.

Figure 3.2A plots MCD spectra of the EuS nanocrystals collected at various temperatures between 1.5 and 120 K. The EuS nanocrystal MCD spectra are similar to those of EuS thin films in general shape, peak width, and peak positions.[14-15] We define three peaks for the spectra in Fig. 3.2A: A (1.91 eV for the nano, and 1.92 eV for thin films), B (2.32 eV -vs- 2.31 eV), and a shoulder C (2.48 eV -vs- 2.62 eV). Although the temperature and fields are somewhat different, our highest temperature is lower (120K-vs-RT) and our field is also lower (2T-vs-5T),[14] the expected shifts due to lower temperature and reduced field are in opposite directions and appear to cancel so our values are quite close.

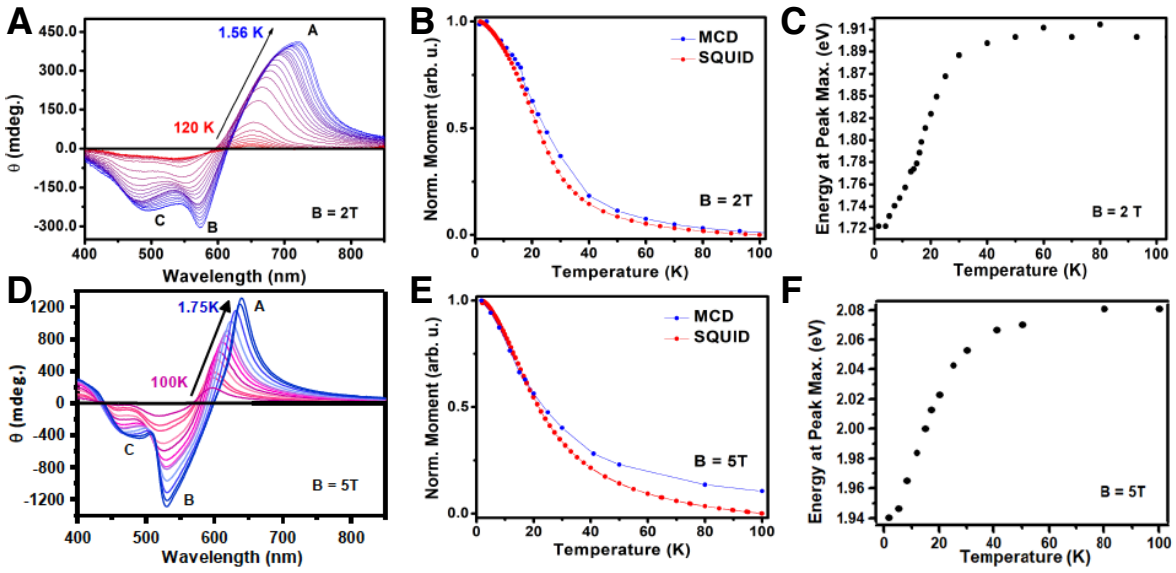

Figure 3.2. Variable-temperature MCD spectra of **(A)** EuS nanocrystals measured at 2 T and **(D)** EuSe nanocrystals measured at 5 T. Normalized temperature-dependent MCD peak-to-peak amplitudes (blue) and magnetic susceptibilities (red) of **(B)** EuS nanocrystals measured at 2T and **(E)** EuSe nanocrystals measured at 5T. The energies of MCD peaks A and B plotted vs temperature for **(C)** the EuS and **(F)** the EuSe nanocrystals at 2 and 5 T, respectively.

The lowest-energy electronic excited state of EuS has a $4f^6 5d(t_{2g})$ configuration, resulting from a $4f$–$5d$ promotion. At high temperatures, the spin degeneracy of this excited state can be split by an applied magnetic field to generate distinct transition energies for absorption of left and right circularly polarized light according to the selection rule ΔM_J ±1. Transitions to higher J values are dominantly left-circularly polarized, while transitions to lower and intermediate J states are dominantly right-circularly polarized.[16-17] Peaks A and B in Figure 3.2 are transitions to the two components of this spin-split $4f^6 5d(t_{2g})$ state. There is some debate in the literature as to the assignment of peak C,[14] whether it is a $4f$–$6s$ excitation or a weak spin-forbidden transition to an S = 5/2 $4f^6 5d(t_{2g})$ state.[18]

Several changes are observed in the MCD spectra of the EuS nanocrystals as the temperature is decreased from 120 K down to 1.50 K (Fig. 3.2A). Because the circular dichroism is proportional to the magnetization,[19] the peak amplitudes increase gradually as the temperature decreases, and then increase more sharply upon reaching the ferromagnetic ordering temperature (T_C ~16.6K). Therefore, the temperature dependence of the MCD intensity (Fig. 3.2B, blue) is quite similar to a plot of χ-vs-T for the same EuS nanocrystals (Fig. 3.2B, red).

The evidence for conduction-band splitting in EuS thin films is a red-shift in the absorption edge,[20] but such splittings can also be determined from spin-polarized electron emission measurements[19] as well as by measuring resistance across tunnel junctions as a function of temperature.[9] Here, a conduction-band splitting in the EuS nanocrystals is evident from the temperature dependence of the energy of peak A, plotted in Fig. 3.2C. Lowering the temperature from 120 K, the energy of peak A remains relatively constant until ~20K, where it drops sharply to reach a maximum redshift of ΔE_{ex} = 0.18 eV at 1.50 K. This inflection temperature (20 K) is again consistent with the magnetic ordering temperature. In bulk, the redshift is greatest for EuO (ΔE_{ex} = 0.23 eV) and is smaller for EuS (ΔE_{ex} = 0.18 eV).[21] The redshift observed in the nanocrystals compares quite well to the shift observed in bulk, and corresponds to a very large conduction band splitting of $2\Delta E_{ex}$ = 0.36 eV.

The 5 K MCD intensity of the EuS nanocrystals saturates at low magnetic fields and shows a hysteresis in field-sweep measurements (Fig. 3.3A, and Fig. C3, Appendix B). The coercive field from these data is 310 Oe (0.031 T). Increasing the field also increases the red shift of peak A, but the magnetization saturates at low applied fields (<0.5 T) which means the conduction band splitting won't change significantly above this field. Interestingly, EuS thin films used as tunnel barriers exhibit 90% spin polarization at zero field, and this spin polarization, like the conduction band splitting is largely independent of applied field.[5]

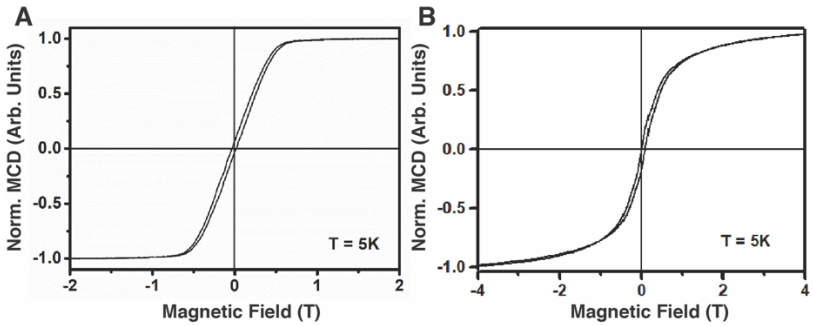

Figure 3.3. MCD intensity plotted vs magnetic field for the EuS nanocrystals monitored at 700 nm **(A)** and the EuSe nanocrystals monitored at 525 nm **(B)**. Both measurements were at temperatures below T_C.

We also used variable-temperature and variable-field MCD to probe the EuSe nanocrystals. Figure 3.2D plots the MCD spectra of the EuSe nanocrystals as a function of temperature. These data appear qualitatively similar to those of the EuS nanocrystals, and the optical transitions have the same assignments. The EuSe nanocrystal MCD spectra are similar to MCD spectra reported for EuSe thin films (variable T, H = 5T);[15,22] however, peak positions were not reported in previous studies. The EuSe nanocrystals exhibit peaks: A (2.08 eV), B (2.38 eV), and at low temperatures C (2.71 eV), as well as a fourth peak D (~3.12 eV) not seen in EuS. As expected from the literature values of E_g for both materials (EuSe>EuS), peak A is higher in energy in the EuSe nanocrystals (2.08 eV) than in the EuS nanocrystals (1.91 eV). In addition, band A is narrower for EuSe than EuS. The width of the 4*f* band has been determined to be ~0.62 eV and unaffected by the anion;[23] however, the crystal-field splitting of the 5*d* orbitals is greater in EuS (Δ_{Oct} estimated at 2.2 eV) than in EuSe (Δ_{Oct} estimated at 1.7 eV),[23] consistent with the assignment of this peak.

The temperature dependence of the EuSe nanocrystal MCD must be interpreted differently from that of the EuS nanocrystals, because EuSe does not have a defined Curie temperature. EuSe has a more complex magnetic phase diagram than EuS because of its nearly equivalent magnitudes of ferromagnetic ($J_1/k(K) = +0.1$) and antiferromagnetic ($J_2/k(K) = -0.09$) exchange-coupling strengths.[24] As a result, EuSe is metamagnetic. Measurements at low temperatures and fields (H < 250 mT, T < 4 K) have found evidence of type II antiferromagnetic ordering (↑↓↑↓), ferrimagnetic ordering (↑↑↓), and type I antiferromagnetic ordering (↑↑↓↓) in bulk EuSe.[25] The field dependence of these transitions provides insight into the strength of the magnetic coupling.

Figure 3.2E plots the EuSe nanocrystal MCD intensity as a function of temperature, in comparison with magnetic susceptibility data collected on the same sample. The temperature dependence for EuSe is broadened relative to the EuS nanocrystal data (Fig. 3.2B). Both the MCD and the magnetic susceptibility reflect the ferromagnetic coupling at 5 T, but the magnetization appears at higher temperatures. The spontaneous magnetization at high temperatures that causes this increase in intensity is not long-range order—there is a noticeable deviation between the MCD intensity, which is still appreciable above 80K, and the magnetic susceptibility, which is diminished by this temperature. The interpretation of MCD spectra of thin films of EuSe, which are quite similar,

is that domains form locally at temperatures ~30K, as described by a near-neighbour spin correlation function.[26]

Large conduction-band splitting is also observed in the EuSe nanocrystals by MCD. Relative to the EuS nanocrystals, the splitting energy is smaller yet it persists at higher temperatures. The conduction-band splitting energy depends on the coupling of the 4*f* and 5*d* electrons and can be estimated as proportional to J_1S (S = 7/2), and J_1 is smaller for EuSe.[27] Consistent with this expectation, we have measured a redshift of ΔE_{ex} = 0.14 eV (at 5T) in the EuSe nanocrystals, which is smaller than the redshift observed in the EuS nanocrystals (0.18 eV). This measured redshift compares well with the literature value for bulk EuSe, ΔE_{ex} = 0.15 eV (H = 1.5 T).[20] Our data lead to a conduction band splitting value of $2\Delta E_{ex}$ = 0.28 eV. In thin films of EuSe, the gradual red-shift with decreasing temperature exhibits a kink at the anti-ferromagnetic ordering temperature of 4 K (T_N);[19] a comparable kink is difficult to discern in the MCD data here because of the higher field used.

The MCD field dependence also provides insight into the complex magnetic ordering in the EuSe nanocrystals. In Figure 3.3, the field dependence of the EuSe 5 K MCD intensity at peak B (525 nm), is similar to the hysteresis curve measured for EuS nanocrystals. Based on this data the coercive field for the EuSe nanocrystals is 850 Oe (0.085 T). However, the field dependence of the EuSe nanocrystal spectra collected at lower temperature (1.75 K, Fig. 3.4A) are more revealing. These data show one spectrum at H < 0.5 T (exemplified by H = 0.25 T, 0.35 T) but show a different spectrum at H > 0.5 T (exemplified by H = 0.75 and 6 T). Both spectra coexist at 0.5 T. The high-field peaks are distinctly red-shifted, as seen in a plot of the peak A energy vs field (Fig. 3.4B). The abrupt step-like change in peak energy seen here corresponds to a red shift of Δ = 0.10 eV between 0.35-0.5 T. A similar effect has been observed in the optical absorption of EuSe epilayers and ascribed to a magnetic phase transition, where at a critical field the magnetism changes from ferrimagnetic (↑↑↓) to ferromagnetic (↑↑↑).[7] The μ_{eff} in the ferrimagnetic phase is ~2/3 of that in the ferromagnetic phase, and therefore the redshift is ~2/3 of the high-field MCD redshift (0.14 eV). The critical field for the EuSe nanocrystals here is slightly larger (>0.35 T) than that reported for thin films (0.3 T), but it is closer in agreement to that determined from EuSe films used as tunnel junctions, where a change in electron-spin polarization due to magnetic ordering was observed at applied fields greater than ~0.5 T.[6] This comparison suggests that the critical field increases as the EuSe dimensions decrease. Such a size effect could conceivably relate to the presence of uncompensated spins at the surfaces of the nanocrystals, or to small changes in unit cell volume with greater surface-to-volume ratios, but the origins of this effect require further investigation.

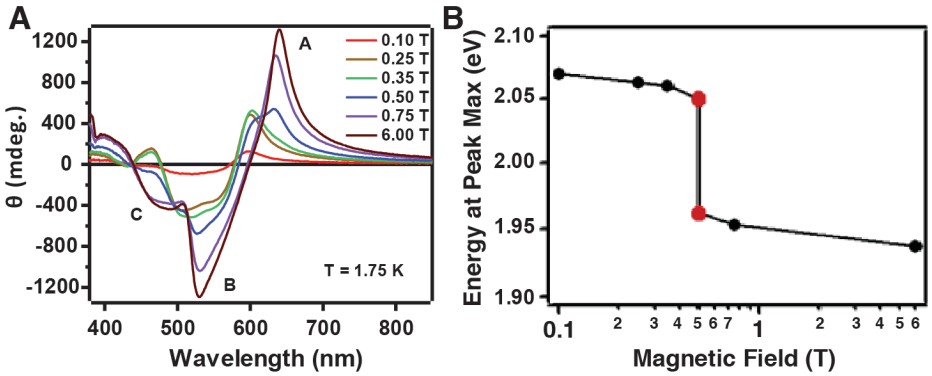

Figure 3.4. (A) Field-dependent MCD spectra of EuSe nanocrystals collected at 1.75 K. The ferrimagnetic phase is observed in the red, brown, and green spectra. The greater magnetic moment of the ferromagnetic phase (purple and black spectra) leads to an abrupt redshift of peak A at the critical temperature where the nanocrystals convert from ferrimagnetic to ferromagnetic. At 0.5 T, blue spectrum, both phases are observable. **(B)** The energy of peak A as a function of magnetic field strength, from the spectral data in the top panel. The red dots show the energies of the two peaks observable in the 0.5 T spectrum.

In conclusion, the temperature dependence of the MCD of both EuS and EuSe nanocrystals reveal large conduction-band splittings in these materials, which is a key attribute for spin-filtering. The conduction-band splitting is greater in the EuS nanocrystals ($2\Delta E_{ex}$ = 0.36 eV-vs- $2\Delta E_{ex}$ = 0.28 eV) and less sensitive to applied field than it is in the EuSe nanocrystals. In addition, the field-dependence of the EuSe nanocrystal MCD spectra show evidence of a critical field at which the nanocrystals convert from ferrimagnetic to ferromagnetic ordering. We are interested in investigating why the critical field is greater in nanocrystals than in the bulk and, in future work, will use small angle neutron scattering to determine whether this trend is due to surface effects.

3.3 The Role of Trivalent Impurity Ions in the Ferromagnetism of Colloidal EuS Nanocrystals

The europium(II) monochalcogenides are a classic group of magnetic semiconductors, displaying rich magnetic ordering ranging from ferromagnetism for EuO and EuS to metamagnetism for EuSe and antiferromagnetism for EuTe.[19] . EuS in particular displays a high degree of electron spin polarization in transport measurements, making this material attractive for spintronic technologies such as spin filters and spin valves.[5,8,28] The low Curie temperature of EuS (T_C = 16.6 K)[19] limits its practical use, but aliovalent doping, typically with Gd^{3+}, has been shown to increase T_C in both bulk[19] and nanocrystalline EuS.[19,29-30] Aliovalent doping generates delocalized conduction-band (CB) electrons that enhances the indirect inter-lanthanide exchange coupling, thereby stabilizing ferromagnetic ordering.[19,29-31] The correlation between carriers and T_C was demonstrated in $Eu_{1-x}Gd_xO$ films grown by MBE, where Gd^{3+} is also S = 7/2.[32] Although carrier modulated T_C enhancement has been observed for other non-redox active trivalent lanthanides, such as La^{3+} or Lu^{3+}, these non-magnetic ions appear contribute to magnetic disorder.[33] Spectroscopic signatures of free carriers also support this mechanism, including the appearance of a mid-infrared (mid-IR) intra-CB transition

observed by absorption spectroscopy[19,34-38] and a temperature-dependent red-shift of the inter-band absorption edge.[35-36] The magnetism becomes more complicated when the dopant is redox active, such as $Sm^{3+/2+}$. In bulk Sm-doped EuO, Sm is trivalent, introducing free electrons and increasing T_C.[39] In bulk Sm-doped EuS, however, Sm is divalent and only *decreases* the overall magnetization through spin dilution.[40] By changing the lattice anion, therefore, the Sm oxidation state is changed and the material's magnetic properties are affected differently. This comparison suggests the intriguing possibility that redox transformations of europium itself (for which both Eu^{2+} and Eu^{3+} are often readily accessible) may possibly tune the magnetic and optical properties of nominally *undoped* europium chalcogenides.

The solution synthesis of EuS nanostructures has been explored as a promising approach to generating solution processable low-dimensional magnetic semiconductors that can be interfaced with other materials with magnetic properties that potentially can be tuned by controlling the nanocrystallite size, shape, and surface chemistry.[41-47] The high surface-to-volume ratios of such nanostructures present complications in terms of stability, crystallinity, and the general difficulty of controlling the speciation of surface ions and ligands, however. In particular, as-synthesized EuS nanocrystals (NCs) typically show partial oxidation of Eu^{2+} to Eu^{3+},[44,46] generally assumed to occur predominantly in amorphous surface layers.[42,48-49] To the extent that such Eu^{3+} ions can be considered as aliovalent impurities, they may behave similarly to the Gd^{3+} or Sm^{3+} dopants mentioned above. Although the presence of such Eu^{3+} is widely acknowledged, its effect on the magnetism of EuS nanostructures has not yet been elucidated.

The research reported here aims to answer two main questions—first, do Eu^{3+} impurities in EuS NCs introduce free charge carriers, as observed with other trivalent dopants in bulk EuS? Second, can the oxidation state of these Eu^{3+} ions be controlled post-synthetically, thereby modulating the magnetic properties of the NCs? To address these questions, we used chemical reductants to tune the Eu^{3+}/Eu^{2+} ratios in colloidal EuS NCs, and we characterized the resulting NCs using optical and electron paramagnetic resonance (EPR) spectroscopies.

We show that the Eu^{3+} impurities in as-synthesized NCs are not charge-compensated by excess CB electrons, and we hypothesize that their excess positive charge is instead compensated by localized surface counter-charges. Additionally, we demonstrate for the first time that it is possible to reduce these native Eu^{3+} ions to Eu^{2+} in free-standing colloidal EuS NCs. This reduction has a modest but clearly detectable impact on the NC magnetism, reducing T_C from 16.1 to 15.0 K (nearly 7%) and increasing the magnetization below T_C. Spectroscopic and magnetic evidence suggests that the newly formed Eu^{2+} ions also partially order ferromagnetically but have a slightly different coordination environment than the Eu^{2+} ions present in the as-synthesized NCs, possibly due to surface proximity.

The synthesis of colloidal EuS NCs was adapted from previous reports[43] and relies upon the high-temperature decomposition of a europium(III) dithiocarbamate precursor (see Methods). The *in situ* reduction of the Eu^{3+} precursor is believed to be facilitated by the ligand, and the oleylamine used as a solvent. Incomplete reduction is likely the source of some of the Eu^{3+} found in the final NCs (*vide infra*). To minimize any further oxidation or hydrolysis, and to ensure that the NCs remained constant

over the course of our experiments, the NCs were prepared, purified, and handled under rigorously air-free conditions.

Figure 3.5 summarizes the general characterization of representative as-synthesized EuS NCs. The absorption spectrum plotted in Fig. 3.5A shows a broad band centered at 500 nm. This band corresponds to the f–$d(t_{2g})$ transition of Eu^{2+} and is considered the band gap of the material.[19] Figure 3.5B shows powder X-ray diffraction data collected for the same EuS NCs. These data index well to the expected pattern for EuS (PDF# 01-071-4399) and reveal no additional crystalline phases. Figure 3.5C,D shows a TEM image of the sample and the associated histogram confirming the NC size distribution. These data show that the NCs are approximately spherical in shape with an average diameter of 5.4 ± 1.1 nm. Overall, these NCs are thus similar to those described previously.[43]

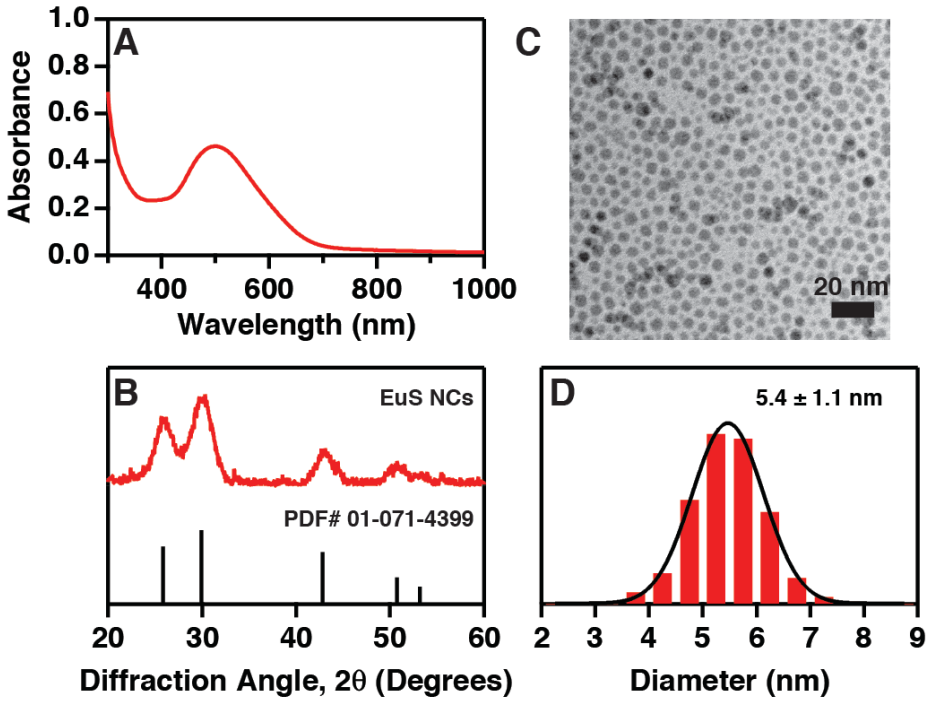

Figure 3.5. Characterization of colloidal EuS nanocrystals. **(A)** Absorption spectra collected at room temperature. The band centered at 500 nm corresponds to the f–$d(t_{2g})$ transition of Eu^{2+}. **(B)** Powder X-ray diffraction data collected for EuS NCs drop-cast on a silicon substrate (red) and corresponding literature pattern for cubic EuS (black, PDF# 01-071-4399). The NC data match the expected peak pattern. **(C)** TEM image of EuS NCs, with scale bar representing 20 nm. **(D)** Size distribution of NCs shown in **(C)** determined by measuring >300 particles, and Gaussian fit, yielding a mean diameter of 5.4 ± 1.1 nm.

Figure 3.6 plots X-ray photoelectron spectroscopy (XPS) data collected for the as-prepared EuS NCs deposited onto a silicon substrate. The survey scan in Fig. 3.6A shows a large C 1*s* signal that was used for energy referencing. A large O 1*s* signal is also observed but because of the substrate it cannot be determined whether this signal arises in part from the NC capping ligands or the NCs

themselves. Figure 3.6B plots high-resolution XPS data in the S 2*p* region. The majority of the signal (94%) is from S^{2-} associated with the NCs. There is a small (6%) signal at 166.6 eV that is assigned to residual SO_3^{2-}, most likely from oxidation of the diethyldithiocarbamate ligands used during synthesis. Figure 3.6C plots a high-resolution scan of the Eu $3d_{5/2}$ region. Two bands are observed in this region, a lower-energy band that is fit to two Gaussian functions centered at 1122.9 and 1125.0 eV and assigned to Eu^{2+}, and a higher energy band centered at 1133.7 eV that is best fit by one Voigt function, corresponding to Eu^{3+}. Both assignments are consistent with literature.[50] The Eu^{2+} signal only accounts for 24% of the total Eu $3d_{5/2}$ signal. Figure 3.6D plots the spectrum in the Eu 4*d* region, showing three major peaks and a clear shoulder. This region is more complicated than the $3d_{5/2}$ region, and this intensity is fitted using four Voigt functions taking into account asymmetry. The two lower energy peaks from the 4*d* region (127.2 and 132.7 eV) are assigned to Eu^{2+} and account for 44% of the signal, in contrast to that found for the Eu $3d_{5/2}$. The two high-energy peaks (135.5 and 141.0 eV) are assigned to Eu^{3+} and account for 56% of the total Eu 4*d* signal. The former peaks are highly asymmetric as a result of splittings caused by the neighboring 4*f* electrons.[50-51] The extensive NC oxidation observed here is similar to what has been reported for EuS NCs as determined by X-ray magnetic circular dichroism[44] and Eu-151 Mössbauer spectroscopy.[46]

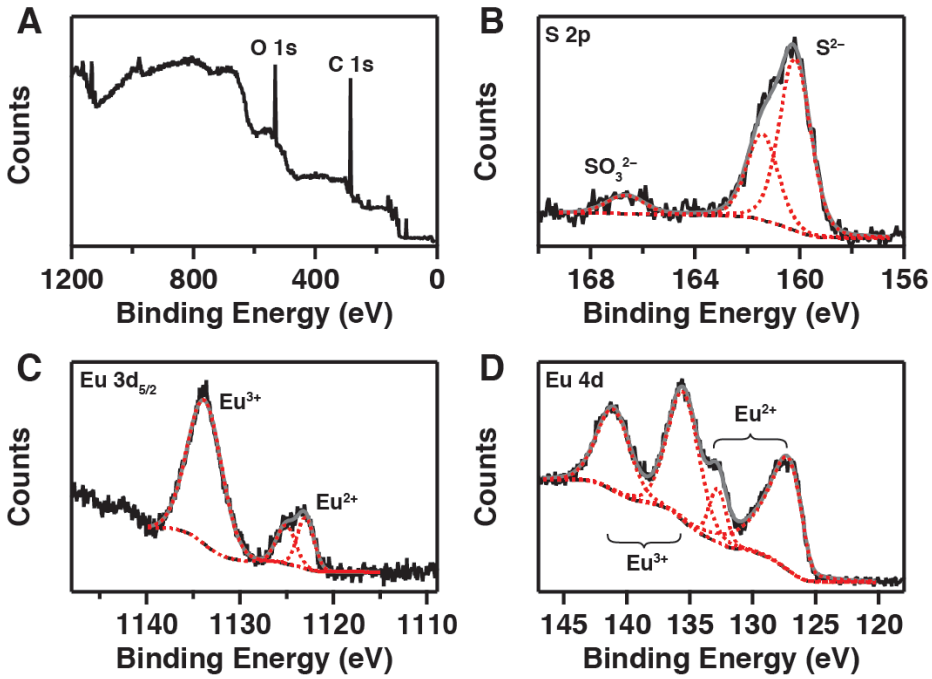

Figure 3.6. X-ray photoelectron spectroscopy (XPS) of EuS nanocrystals deposited on a silicon substrate. **(A)** Survey scan of EuS NCs. The C 1*s* peak was used for energy referencing. **(B)** High-resolution spectra of the S 2*p* region. **(C,D)** High-resolution spectra of the Eu $3d_{5/2}$ and 4*d* regions, respectively. The peaks are deconvolved by simultaneously fitting an inelastic background (black dash). The convolved fit is plotted in gray.

The discrepancy in relative Eu^{2+} content between the $3d_{5/2}$ and $4d$ spectral regions results from the difference in inelastic mean free paths (IMFPs) of electrons in these two energy regions. The $3d_{5/2}$ electrons, with their lower kinetic energy, have an IMFP that is approximately half that of the $4d$ electrons. This difference causes measurements in the $3d_{5/2}$ region to be more sensitive to the NC surfaces than measurements in the $4d$ region, especially after attenuation through the surrounding organics. In general, XPS is a surface-sensitive technique, and even the lower-energy $4d$ spectra selectively probe the NC surfaces. Nonetheless, taken together, these measurements indicate that these NCs have highly oxidized surfaces (>50% Eu^{3+}), with the degree of oxidation decreasing closer to the NC core. These results alone cannot fully differentiate between a gradient mixture of Eu^{3+} and Eu^{2+} within the EuS lattice structure or a "core/shell" structure consisting of a EuS core surrounded by, for example, an amorphous oxidized shell (*e.g.,* Eu_2O_2S). Despite the high Eu^{3+} levels indicated by XPS, there are no optical indications of Eu^{3+} at room temperature, but weak Eu^{3+} *f–f* emission is detected in the low-temperature photoluminescence spectrum of the NCs (see Appendix B).

To evaluate the influence of these Eu^{3+} ions on the NC magnetism, we sought to use an external reducing agent that could modify their valency. Solutions of EuS NCs in THF were treated with various reducing agents while monitoring the absorption spectra. Moderately strong reductants[52] such as decamethylcobaltacene (-1.94 V *vs* Fc^+/Fc) and Na(Hg) (-2.36 V *vs* Fc^+/Fc in THF) had no effect on the NC spectra (see Appendix B); however, stronger reductants such as sodium anthracenide (Na[ANT], -2.47 V *vs* Fc^+/Fc) did cause significant spectral changes. Figure 3.7A plots absorption spectra of EuS NCs collected during the course of anaerobic reduction with Na[ANT]. Each spectrum in the series corresponds to an addition of 0.1 equivalents of Na[ANT] per Eu. The sharp absorption bands between 300 – 400 nm that appear after the first addition of Na[ANT] come from the redox product, anthracene.

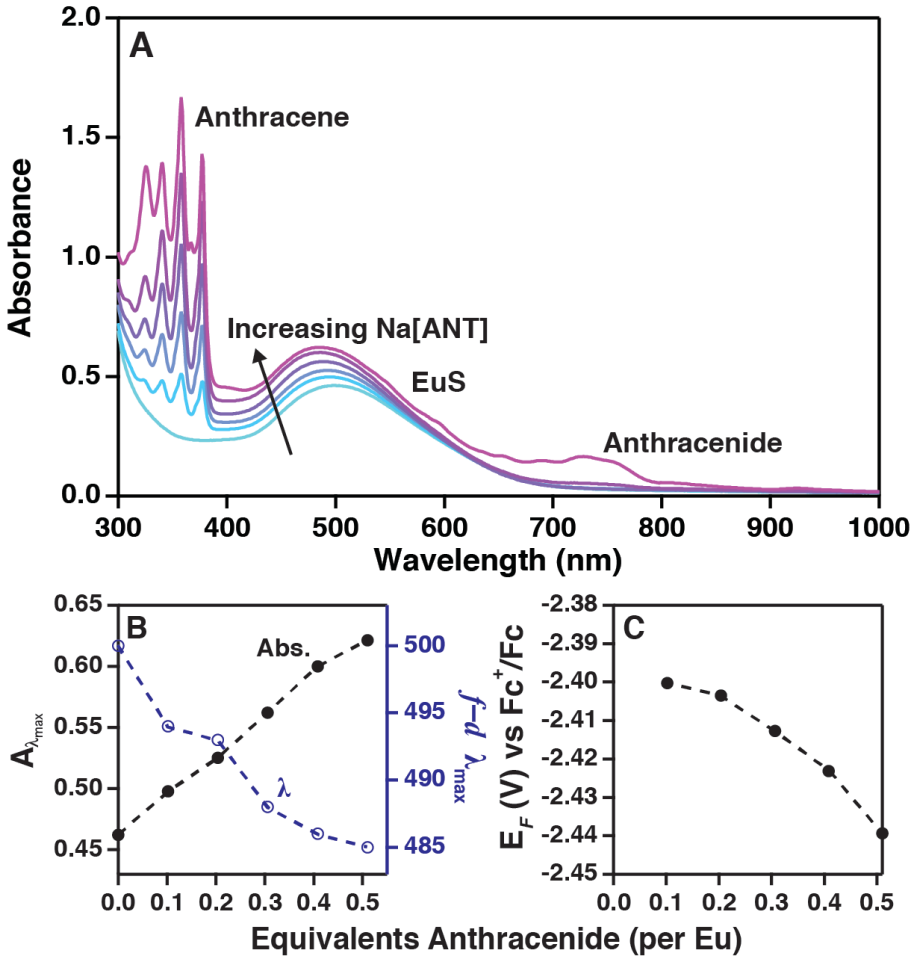

Figure 3.7. Chemical reduction of EuS nanocrystals using sodium anthracenide (Na[ANT]). **(A)** Absorption spectra of EuS NCs with different amounts of the reductant Na[ANT] added. The peaks corresponding to anthracene, EuS f–$d(t_{2g})$, and anthracenide are labeled. **(B)** Absorbance and wavelength of the EuS f–$d(t_{2g})$ band, plotted *vs* equivalents of anthracenide. **(C)** Fermi level of the reaction mixture from **(A)**, determined using eq 3.1. The Fermi level becomes more negative as Na[ANT] is added.

These spectral changes are summarized in Fig. 3.7B. The EuS f–$d(t_{2g})$ band increases in intensity with added Na[ANT], suggesting an increase in the amount of Eu^{2+} in the NCs consistent with reduction of Eu^{3+} to Eu^{2+}. The f–$d(t_{2g})$ band also blue-shifts slightly (77 meV total) with added Na[ANT]. This shift contrasts with the red-shifts observed when CB electrons are introduced into these magnetic semiconductors.[35-36] The NCs also show no new intra-band absorption in the mid-IR after reduction (see Appendix B), confirming the absence of delocalized CB electrons. Instead, the f–$d(t_{2g})$ blue-shift is interpreted as reflecting a different coordination environment around some or all of the newly formed Eu^{2+} ions relative to lattice Eu^{2+} in EuS. For example, these newly reduced Eu^{2+} ions could be exposed to surface-capping ligands at the NC surfaces or could reside in an oxysulfide shell, resulting in a slightly smaller $d(t_{2g})$ ligand-field splitting. Scheme 1 illustrates this proposed surface reduction.

Scheme 3.1. Proposed reduction of Eu^{3+} to Eu^{2+} in EuS NCs by sodium anthracenide, as well as NC re-oxidation by air.

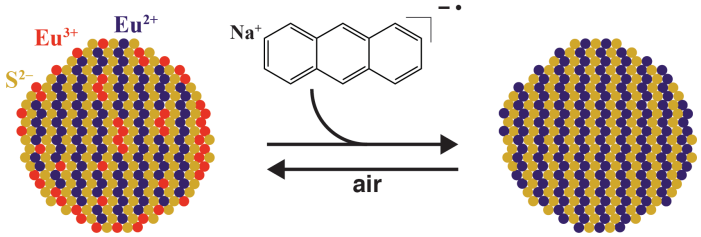

The feature at ~740 nm that appears in the absorption spectrum after the final addition of Na[ANT] comes from the $[ANT]^{\bullet-}$ radical. Observation of this feature suggests that the reaction's equivalence point has been reached. The amount of reductant required to reach the equivalence point is thus ~0.5 equivalents per Eu ion, a value consistent with the observation by XPS (Fig. 3.6) that ~50% of the Eu is Eu^{3+}. As an equilibrium outer-sphere redox reaction, the Fermi level (E_F) of the solution in which the NCs are reduced can be determined from the Nernst equation (eq 1).[53] Here, the concentration of anthracene is measured spectroscopically using the known extinction coefficients of the bands between 300 – 400 nm (see Appendix B), and the standard reduction potential of anthracene is taken as -2.47 V vs Fc^+/Fc in THF.[52] Figure 3.7C plots E_F measured in this way *vs* the equivalents of added anthracenide. As Na[ANT] is added, the Fermi level becomes increasingly negative, ultimately reaching ca. -2.44 V *vs* Fc^+/Fc at the equivalence point. Even at this potential, there is no discernible occupation of the EuS CB, meaning the NC band-edge potential is even more negative than this potential. The band-edge potentials of colloidal EuS NCs have not been measured previously, but the band-edge potentials of colloidal NCs are known to be very sensitive to surface dipoles, shifting by as much as 500 mV in the case of CdSe NCs, for example.[54-56] The most negative potential measured here is ~300 mV more positive than the literature conduction-band-edge potential of bulk EuS, -2.7 ± 0.3 V *vs* Fc^+/Fc,[57] consistent with the absence of CB electrons here.

$$E_F(V) = E_{cell}(V) = E° - 0.02568 \ln \frac{[Anthracenide]_{total\ added} - [Anthracene]}{[Anthracene]} \qquad (3.1)$$

Similar results are obtained for other very strong reductants,[52] including alkali naphthalemide (-3.10 V *vs* Fc^+/Fc) and sodium metal (-3.04 V *vs* Fc^+/Fc). Combined with the observations using Na[ANT] and the less powerful reductants, these reactions suggest that potentials more negative than ca. -2.36 V *vs* Fc^+/Fc are required to reduce Eu^{3+} to Eu^{2+} in these NCs, and hence that the reduced NCs are themselves very strong reductants. Consequently, EuS NCs reduced by this method are not stable in air. Upon exposing a solution of reduced EuS NCs to air, the increased *f–d*(t_{2g}) absorbance is lost and the *f–d*(t_{2g}) band red-shifts back to its starting energy (see Appendix B). Other than the presence of anthracene, the resulting spectrum is essentially indistinguishable from that collected

before reduction. This similarity suggests that the NC reduction is fully reversible—*i.e.*, no degradation or other irreversible transformations occur. This conclusion is supported by TEM measurements, which also show no discernible NC degradation after reduction with Na[ANT] and re-oxidation by air (Appendix B).

The effect of Eu reduction on the EuS NC magnetism was then probed using variable-temperature CW X-band EPR spectroscopy. As non-Kramers ions with a non-magnetic ($J = 0$) ground state, Eu^{3+} ions are generally EPR silent;[58] therefore, any EPR signal is attributable to Eu^{2+}. Figure 3.8A plots representative EPR spectra of EuS NCs reduced with Na[ANT], measured at different temperatures. EPR spectra of the corresponding as-prepared NCs and absorption spectra indicating complete reduction are provided in Appendix B. The EPR intensity is greatest at the lowest temperature (5 K) and it decreases as the temperature is raised. At the highest temperature (80 K) the spectrum is very weak. The EPR spectra in Fig. 3.8A are plotted as $d\chi''/dH$. Integration of these spectra thus yields the EPR susceptibility, χ'', with further integration yielding a value proportional to magnetization, αM. Figure 3.8B plots αM *vs* temperature for the as-prepared and reduced NCs. Both samples show a low-temperature plateau followed by a rapid drop at higher temperature characteristic of a ferromagnetic-to-paramagnetic transition. Figure 3.8C plots the dependence of the EPR linewidth, ΔB_{pp}, on temperature for the as-prepared and reduced NCs. Upon warming from 5 K, the linewidth narrows until a similar critical temperature, beyond which it broadens again. This behavior is also characteristic of ferromagnetic-to-paramagnetic materials.[59-64] The resonance of the as-prepared NCs broadens significantly more than that of the reduced NCs in the ferromagnetic resonance region. We attribute this difference to the presence of Eu^{3+} in the former. Eu^{3+} has significant orbital angular momentum that leads to very fast spin-lattice relaxation, which broadens the ferromagnetic resonance linewidth.[65] Similarly, the Landé g-factor increases as the temperature is raised beyond the critical region (see Appendix B), as observed for bulk EuS.[66] By all measurements, the critical temperature of the reduced NCs is lower than that of the as-prepared NCs.

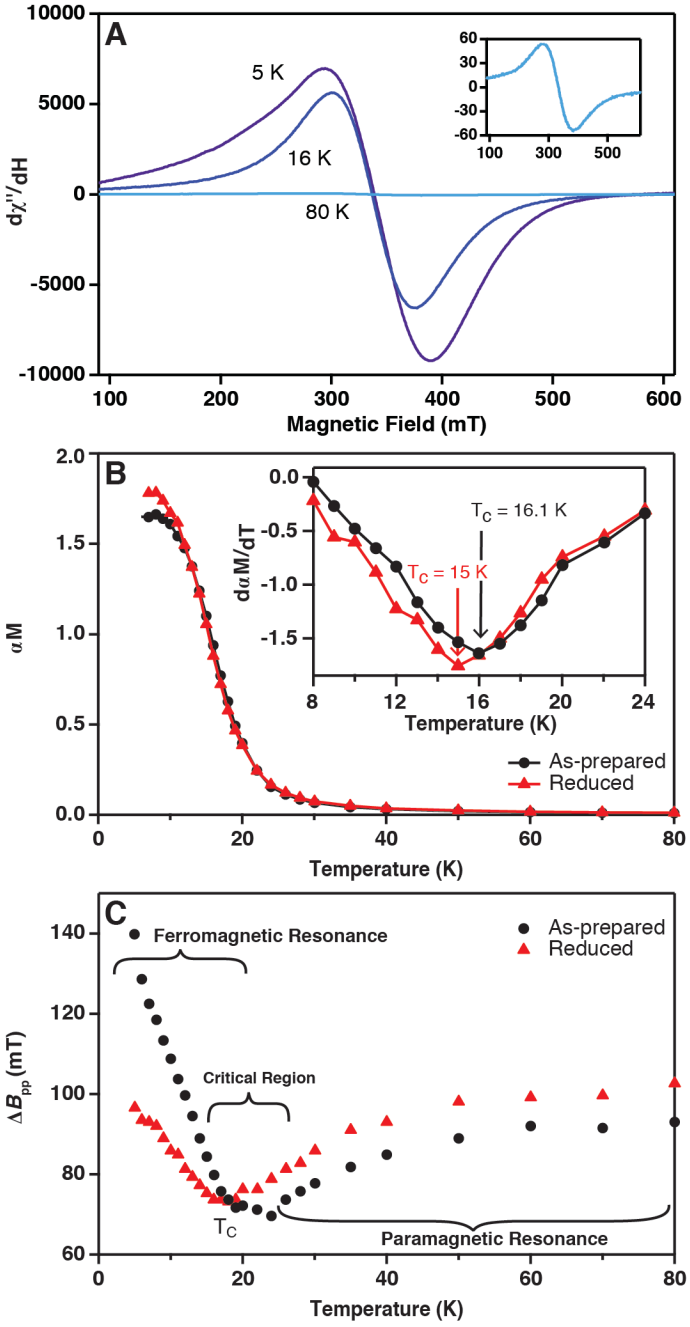

Figure 3.8. EPR data from as-prepared and reduced EuS NCs. **(A)** Representative EPR spectra of reduced EuS NCs collected at 5, 16, and 80 K. Linewidth narrowing in the vicinity of the critical region (~16 K) is apparent. The inset plots a zoom-in of the 80 K spectrum. **(B)** Proportional magnetization (from double-integration of the EPR spectrum) plotted *vs* temperature for the as-prepared (black dots) and fully-reduced (red triangles) EuS NCs. Na[ANT] was used as the reductant. Curie temperatures of 16.1 and 15.0 K for the as-prepared and reduced EuS NCs, respectively, are determined from the minima in the first derivative of the magnetization data (inset). **(C)** The peak-to-peak linewidth (ΔB_{pp}) plotted *vs* temperature. Ferromagnetic resonance and paramagnetic resonance regions indicated.

The Curie temperatures of these NCs are determined from the minima in the first derivative of the αM *vs* T data (Fig. 3.8B, inset). From these data, T_C for the reduced EuS NCs is estimated to be 15.0 K, whereas that of the as-prepared EuS NCs is 16.1 K, corresponding to a decrease of ~7% upon NC reduction. In addition to lowering in T_C, NC reduction also causes a ~7% increase in magnetization (αM) below T_C. This result is consistent with NC reduction generating additional Eu^{2+} species that also partially align ferromagnetically with the core EuS spins. The shift in T_C is likely attributable to the different coordination environment of the newly reduced Eu^{2+} ions, as discussed above, implying a weaker inter-Eu exchange coupling for these Eu^{2+} ions than in the core EuS.

In summary, EuS NCs prepared by literature methods were demonstrated to contain high levels of Eu^{3+} despite rigorously anaerobic NC synthesis and handling conditions. These Eu^{3+} ions could be reduced to Eu^{2+} by reacting the NCs with strong chemical reducing agents. This reduction manifests itself spectroscopically as a blue-shift of the Eu^{2+} f–$d(t_{2g})$ transition and an increase in its absorbance, suggesting that the redox-active Eu ions are located predominantly at the NC surfaces and with a slightly different coordination environment. In bulk, doping EuS with trivalent lanthanides (*e.g.*, Gd^{3+}) can increase T_C by generating excess CB-like electrons (*n* doping). In contrast, the data here suggest that the Eu^{3+} impurities in as-synthesized EuS NCs do not introduce any excess optically-detected CB-like electrons and therefore do not have the same effect. Rather, their elimination by reduction from Eu^{3+} to Eu^{2+} reduces T_C by ~7%. The trivalent Eu^{3+} dopants here do *decrease* the overall NC magnetic moment, as expected for the lower moment compared with Eu^{2+}, and reducing these ions from Eu^{3+} to Eu^{2+} increases the NC magnetic moment below T_C. The experimental shift in T_C upon NC reduction may be due to differences in Eu^{2+} coordination that cause the newly reduced Eu^{2+} to have weaker inter-Eu magnetic exchange coupling, an interpretation supported by the shift in Eu^{2+} f–$d(t_{2g})$ transition energies between original and newly reduced Eu^{2+} ions.

Overall, these results demonstrate successful chemical reduction of colloidal EuS NCs, revealing that the NCs are stable even to very strong reductants, that this reduction is fully reversible, and therefore that the redox states of the constituent cations and hence the magnetism of the EuS NCs can be manipulated post-synthetically. Notably, the present data show no evidence of CB-like electrons in these EuS NCs, either from the abundant Eu^{3+} impurities found in the as-prepared NCs or after exposure of these NCs to strong chemical reductants. In contrast with aliovalent doping of bulk EuS crystals, the excess positive charges of aliovalent impurities in colloidal NCs are readily compensated at the NC surfaces, diminishing the effectiveness of these ions as electronic dopants. The very negative CB-edge potentials implied by these redox titrations ($\geq$ ~-2.44 V *vs* Fc^+/Fc) exacerbate the challenge of stabilizing CB-like electrons in EuS NCs by making such electrons extremely reducing.

3.4 Methods

3.3.1 General considerations. Unless otherwise stated, all measurements and synthetic manipulations were performed using standard Schlenk techniques under a dinitrogen atmosphere, or

in a glovebox under an atmosphere of purified dinitrogen. Anhydrous tetrahydrofuran (THF) was purified through an alumina column pressurized with Ar.

3.3.2 Chemicals. Unless otherwise stated, all chemicals were used as purchased without further purification. Anthracene (99%), decamethylcobaltocene ($CoCp^*_2$), mercury (≥99.99%), naphthalene (99%), 1-octadecene (ODE, 90%), oleylamine (OLA, 70%), selenium powder (-100 mesh, ≥99.5%), diethylamine (>99.5%), diphenylphosphine (98%), 1,10-phenanthroline (99 %), europium(III) trifluoromethanesulfonate (98%), hexadecylamine (HDA, 90%), absolute ethanol (>99.7%), diethyl ether (99.7%), and trioctylphosphine (TOP, >97%) were purchased from Sigma-Aldrich. 2-methyltetrahydrofuran (2-MeTHF, anhydrous, ≥99.0%, Sigma-Aldrich) was further dried over sodium benzophenone and distilled before use. Diethylammonium diethyldithiocarbamate ($(NH_2Et_2)(S_2CNEt_2)$, >97%) was purchased from TCI America or Sigma-Aldrich. Europium(III) chloride hexahydrate ($EuCl_3{\cdot}6H_2O$, 99.9%) was purchased from Strem Chemicals or Sigma-Aldrich. Sodium and potassium metal were purchased from AlfaAesar. Acetone (Fisher, ACS) was dried by reflux over anhydrous $CaSO_4$ and distilled before use. Hexanes (Fisher, ACS) were dried over sodium benzophenone and distilled before use. 2-propanol and acetonitrile were purchased from Fisher.

3.3.3 Synthesis of sodium anthracenide. In a nitrogen-filled glovebox, excess sodium metal was spread in a scintillation vial to make a mirror. Anthracene (0.1 mmol) was then added, followed by 5 mL of THF. The mixture was stirred overnight to form a 0.02 M sodium anthracenide (Na[ANT]) solution. Sodium naphthalenide (0.02 M, Na[NAP]) and potassium anthracenide (0.02 M, K[ANT]) were made analogously.

3.3.4 Preparation of Na(Hg). 0.5% Na(Hg) was prepared by dissolving Na metal (0.0388 g) in Hg metal (5 mL) in a nitrogen-filled glovebox. The sodium metal was added slowly because the reaction is highly exothermic.

3.3.5 $Eu(S_2CNEt_2)_3Phen$ (1). The europium tris-diethyldithiocarbamate phenanthroline single-source precursor was synthesized as previously reported.[67] Briefly, europium(III) chloride hexahydrate was dissolved in isopropyl alcohol and added to a vigorously stirred solution of diethylammonium diethyldithiocarbamate and 1,10-phenanthroline in acetonitrile at room temperature. The orange-red precipitate was collected via vacuum filtration and washed with ice-cold acetonitrile. FT-IR (ν, cm-1): 1490(s), 962(m).

3.3.6 $[Et_2NH][Se_2PPh_2]$ (DSP salt) (2). In a nitrogen-filled glovebox, selenium (7.9 g, 0.10 mol) was mixed with anhydrous ethanol (40 mL). Diphenylphosphine (8.7 mL, 0.05 mol) was added to the slurry. Excess diethylamine (5.3 mL, 0.051 mol) was injected into the reaction and lowered into a water bath at 60°C and stirred for 60 minutes. The solution turned from black to a rust-red color over the course of the reaction. The reaction was cooled to room temperature and then transferred to a freezer at -30° C. A white precipitate formed and was vacuum filtered and washed with ethanol and diethyl ether to isolate the product. FT-IR (ν, cm-1): 1544(w), 1433(s), 1088(m), 751(m), 691(m), 534(s), 514(s), 472(m), 450(m).

3.3.7 $Eu(Se_2PPh_2)_3(MeCN)_2$ (3). In a nitrogen-filled glovebox, **2** (1.3 g, 3.0 mmol) was dissolved in acetonitrile (25 mL). Europium(III) trifluoromethanesulfonate (0.60 g, 1.0 mmol) was

added directly into the ligand solution. The solution started to form a precipitate upon addition of the triflate salt and was stirred for 30 minutes. The product was isolated via gravity filtration and washed with acetonitrile. FT-IR (ν, cm-1): 3047(w), 2296(w), 2266(w), 1480(w), 1435(m), 1323(w), 1307(w), 1178(w), 1160(w), 1092(m), 1063(w), 1025(w), 998(w), 744(m), 690(s), 620(w), 548(m), 514(s), 476(s), 447(w), 421(w).

3.3.8 $(NH_2Et_2)[Eu(S_2CNEt_2)_4]$ (4). $(NH_2Et_2)[Eu(S_2CNEt_2)_4]$ was prepared by adapting literature procedures.[43] Briefly, $(NH_2Et_2)(S_2CNEt_2)$ (2.38 g) was added to an Erlenmeyer flask containing 70 mL of anhydrous ethanol under ambient conditions. In a separate scintillation vial, a stoichiometric amount of $EuCl_3{\cdot}6H_2O$ (0.98 g) was added to 15 mL anhydrous ethanol. The two solutions were stirred to yield homogenous solutions. The europium solution was slowly added to the Erlenmeyer flask to form the red-orange crystals of $(NH_2Et_2)[Eu(S_2CNEt_2)_4]$. The mixture was stirred for twenty minutes to allow complete precipitation of **4**, which was collected by filtration and washed with cold anhydrous ethanol several times. **4** was stored in a desiccator and used within two weeks of synthesis.

3.3.9 EuS/EuSe nanocrystal synthesis. In a 3-necked round bottom flask fitted with a thermocouple for temperature control and reflux condenser, HDA (2.50 g, 10.4 mmol) and ODE (5.0 mL, 25 mmol) were degassed under vacuum at 75°C for 1 hr. In a nitrogen-filled glovebox, **1** (or **3**) (0.334 mmol) were dissolved in 3.0 mL of OLA. The HDA/ODE solution was placed under N_2 and heated to 330°C, and the OLA solution of **1** (or **3**) were injected via syringe. The color change was immediate upon injection, and the reaction was stirred for 1 hour. The reaction was then cooled from 330°C to room temperature and hexanes introduced to disperse the nanocrystals and decanted into a centrifuge tube to remove solid HDA. Nanoparticles were precipitated with EtOH and collected by centrifugation at 4500 rpm for 10 minutes. The pellet was re-dispersed in hexanes and the precipitation and centrifugation procedure was repeated a total of 4 times to wash the nanocrystals. The nanoparticles were re-suspended in hexanes or kept as powders.

3.3.10 Anaerobic synthesis of colloidal EuS nanocrystals. In a typical synthesis, OLA (2.43 mL) was added to a 50 mL three-necked, round-bottom flask fitted with a reflux condenser and a thermocouple for temperature control, and degassed under vacuum for 30 min at 120 °C. TOP (2.27 mL) was injected into the flask and the mixture was degassed for an additional 15 min. The solvent mixture was then heated to a temperature of 280 °C under nitrogen. In a separate scintillation vial, **4** (0.11 g) was added to OLA (1.2 mL). This mixture was stirred to produce a clear red-orange solution. The solution of **4** was injected into the reaction flask at 280 °C and maintained at this temperature for 1 h under constant stirring. The mixture was cooled to room temperature and transferred to a nitrogen-filled glovebox for further purification. The NCs were washed four times by precipitation with acetone followed by centrifugation and suspension in hexanes. The worked-up NCs were stored in the glovebox suspended in ~5 mL of hexanes, which gave a purple-colored colloidal solution.

3.3.11 Reduction titrations. EuS NCs of a known concentration were suspended in a solution of THF and loaded into an air-free cuvette. For reductions using Na[ANT], K[ANT], Na[NAP], and $CoCp_2^*$ a known amount of reductant solution was titrated in to reduce the NCs. The

progress of the titration was monitored by UV-Vis-NIR spectroscopy by collecting a spectrum following each addition of the reductant. The reduction was considered complete when features corresponding to the reductant were observed in the absorption spectrum. For reduction using Na(Hg) an amount of Na(Hg) corresponding to 600 equivalents of Na per Eu was added to a solution of EuS NCs in THF in an air-free cuvette with a Teflon stir bar. The solution was allowed to mix for several days with the progress of the reduction reaction monitored by UV-Vis-NIR spectroscopy. For reduction using Na metal, a freshly cut piece of Na metal was added to a solution of EuS NCs in THF in an air-free cuvette. The progress of the reduction reaction was monitored by UV-Vis-NIR spectroscopy over a 2-week period.

3.3.12 EPR measurements. Continuous-wave electron paramagnetic resonance (EPR) measurements were performed on a Bruker EMX spectrometer operated at X-band frequencies. The sample and probe were mounted inside an Oxford Instruments ESR900 continuous flow cryostat. The temperature was controlled and monitored with an Oxford Instruments ITC5035 temperature controller and a Cernox Resistor CX-1050-AA-1.4L temperature sensor (LakeShore). Anhydrous 2-MeTHF was used as the solvent because it forms a high-quality glass upon rapid freezing. For EPR measurements of reduced EuS NCs, the reductant (0.02 M Na[ANT] dissolved in 2-MeTHF) was titrated into a solution of NCs in 2-MeTHF. The progress of the reduction was monitored by absorption spectroscopy. Once the sample was fully reduced, 350 μL of the sample was transferred to an EPR tube for the measurements. For the EPR measurements of the native EuS NCs, 350 μL of NC solution in 2-MeTHF at the same concentration as in the reduced sample was loaded into an EPR tube. For all EPR measurements, the samples were kept under an N_2 atmosphere.

3.3.13 XPS measurements. All XPS spectra were taken on a Surface Science Instruments S-Probe photoelectron spectrometer. This instrument has a monochromatized Al Kα X-ray source that was operated at 20 mA and 10 kV, and a low-energy electron flood gun for charge neutralization. The samples were drop cast from solution onto silicon substrates and prepared under nitrogen atmosphere. The X-ray analysis area for these acquisitions was approximately 800 m across. Pressure in the analytical chamber during spectral acquisition was less than 5 x 10^{-9} torr. Pass energy for survey and detailed spectra was 150 eV. Data point spacing was 1.0 eV/step for survey spectra and 0.4 eV/step for detailed spectra. Pass energy for high-resolution spectra was 50 eV. Data point spacing was 0.065 eV/step for high-resolution spectra. The take-off angle was 0º. Service Physics Hawk version 7 data analysis software was used to calculate the elemental compositions from peak areas and to fit the peaks of the high-resolution spectra. An inelastic scattering (Shirley) background was used in the analysis.

3.3.14 General characterization. Unless otherwise noted, UV-Vis-NIR absorption spectra were collected using a Varian Cary 500, Varian Cary 5000 or an Agilent Cary 5000 spectrophotometer on THF solutions of NCs or films of NCs drop-cast on quartz substrates. NIR-IR measurements were performed on a Nicolet 8700 FTIR instrument or on a Perkin Elmer FTIR. Samples were prepared for powder X-ray diffraction (XRD) by depositing NCs from solution onto a silicon substrate, and data were collected using a Bruker D8 Discover diffractometer or with a Rigaku Ultima IV diffractometer equipped with a high- speed DTEX silicon-strip detector using Cu Kα radiation at a

scan speed of 1°/min at 40 kV/44 mA. TEM samples were prepared by drop casting suspensions of NCs onto 400 mesh carbon-coated copper grids from TED Pella, Inc. and dried under an inert atmosphere. TEM images were obtained using a FEI TECNAI G2 F20 microscope operated at 200 kV or a JEOL JEM-2100F FEG TEM operated at 200 kV. Size distributions were determined by analysis of >300 individual NCs. Elemental compositions were determined from nitric-acid-digested NC samples using inductively coupled plasma–atomic emission spectroscopy (ICP-AES) with a PerkinElmer 8300 spectrometer. Photoluminescence measurements were performed on drop-coated films of NCs sandwiched between quartz disks and mounted in a closed-cycle helium cryostat. A 405 nm diode laser was used for excitation and the emission was detected by a liquid-nitrogen-cooled CCD mounted on a monochromator. EuS/EuSe samples for magnetic circular dichroism (MCD) were drop-casted as colloids in hexanes onto quartz disks or dry powders were mixed with PDMS then sandwiched between two quartz disks. Low-temperature MCD spectra were conducted with the samples placed in a superconducting magneto-optical cryostat (Cryo-Industries SMC- 1659 OVT) oriented in the Faraday configuration. At helium temperature, the sample was screened for depolarization by matching the CD spectra of a chiral molecule placed along the optical path before and after the sample. Depolarization of the thin films was less than 9%. MCD spectra were collected using an Aviv 40DS spectro-polarimeter.

3.5 References

1. Wolf, S. A.; Awschalom, D. D.; Buhrman, R. A.; Daughton, J. M.; von Molnár, S.; Roukes, M. L.; Chtchelkanova, A. Y.; Treger, D. M. Spintronics: A Spin-Based Electronics Vision for the Future. *Science* **2001,** *294*, 1488.
2. Moodera, J. S.; Miao, G.-X.; Santos, T. S. Frontiers in Spin-Polarized Tunneling. *Phys. Today* **2010,** *63*, 46-51.
3. Miao, G.-X.; Moodera, J. S. Spin manipulation with magnetic semiconductor barriers. *Phys. Chem. Chem. Phys.* **2015,** *17*, 751-761.
4. Soulen, R. J.; Byers, J. M.; Osofsky, M. S.; Nadgorny, B.; Ambrose, T.; Cheng, S. F.; Broussard, P. R.; Tanaka, C. T.; Nowak, J.; Moodera, J. S.; Barry, A.; Coey, J. M. D. Measuring the Spin Polarization of a Metal with a Superconducting Point Contact. *Science* **1998,** *282*, 85.
5. Moodera, J. S.; Hao, X.; Gibson, G. A.; Meservey, R. Electron-Spin Polarization in Tunnel Junctions in Zero Applied Field with Ferromagnetic EuS Barriers. *Phys. Rev. Lett.* **1988,** *61*, 637-640.
6. Moodera, J. S.; Meservey, R.; Hao, X. Variation of the electron-spin polarization in EuSe tunnel junctions from zero to near 100% in a magnetic field. *Phys. Rev. Lett.* **1993,** *70*, 853-856.
7. Kirchschlager, R.; Heiss, W.; Lechner, R. T.; Bauer, G.; Springholz, G. Hysteresis loops of the energy band gap and effective g factor up to 18,000 for metamagnetic EuSe epilayers. *Appl. Phys. Lett.* **2004,** *85*, 67-69.
8. Moodera, J. S.; Santos, T. S.; Nagahama, T. The phenomena of spin-filter tunnelling. *J. Phys.: Condens. Matter* **2007,** *19*, 165202.
9. Santos, T. S.; Moodera, J. S.; Raman, K. V.; Negusse, E.; Holroyd, J.; Dvorak, J.; Liberati, M.; Idzerda, Y. U.; Arenholz, E. Determining Exchange Splitting in a Magnetic Semiconductor by Spin-Filter Tunneling. *Phys. Rev. Lett.* **2008,** *101*, 147201.

10. Steeneken, P. G.; Tjeng, L. H.; Elfimov, I.; Sawatzky, G. A.; Ghiringhelli, G.; Brookes, N. B.; Huang, D. J. Exchange Splitting and Charge Carrier Spin Polarization in EuO. *Phys. Rev. Lett.* **2002,** *88*, 047201.
11. Tsukahara, Y.; Kataoka, T.; Hasegawa, Y.; Kaizaki, S.; Wada, Y. The first observation of the magnetic circular dichroism in EuS nanocrystals. *J. Alloys Compd.* **2006,** *408-412*, 203-206.
12. Hasegawa, Y.; Adachi, T.-a.; Tanaka, A.; Afzaal, M.; O'Brien, P.; Doi, T.; Hinatsu, Y.; Fujita, K.; Tanaka, K.; Kawai, T. Remarkable Magneto-Optical Properties of Europium Selenide Nanoparticles with Wide Energy Gaps. *J. Am. Chem. Soc.* **2008,** *130*, 5710-5715.
13. Dalafu, H. A.; Rosa, N.; James, D.; Asuigui, D. R. C.; McNamara, M.; Kawashima, A.; Omagari, S.; Nakanishi, T.; Hasegawa, Y.; Stoll, S. L. Solid-State and Nanoparticle Synthesis of EuS_xSe_{1-x} Solid Solutions. *Chem. Mater.* **2018,** *30*, 2954-2964.
14. Ferre, J.; Briat, B.; Paparoditis, C.; Pokrzywnicki, S.; Suryanarayanan, R. Magneto-optical properties of EuS thin films: Magnetic circular and linear dichroism. *Solid State Commun.* **1972,** *11*, 1173-1177.
15. Ferre, J.; Billardon, M.; Badoz, J.; Suryanarayanan, R.; Paparoditis, C. Dichroïsme circulaire magnétique de films minces de EuTe et EuSe jusqu'à 5 °K. *J. Phys. Colloq.* **1971,** *32*, C1-930-C1-931.
16. Feinleib, J.; Scouler, W. J.; Dimmock, J. O.; Hanus, J.; Reed, T. B.; Pidgeon, C. R. Spin-Polarized Splittings in the Temperature-Dependent Reflectance of EuO. *Phys. Rev. Lett.* **1969,** *22*, 1385-1388.
17. Dimmock, J. O. Optical Properties of the Europium Chalcogenides. *IBM J. Res. Dev.* **1970,** *14*, 301-308.
18. Schoenes, J. Magnetooptik und elektronische struktur der magnetisch ordnenden europiumchalkogenide. *Z. Physik B* **1975,** *20*, 345-368.
19. Mauger, A.; Godart, C. The magnetic, optical, and transport properties of representatives of a class of magnetic semiconductors: The europium chalcogenides. *Phys. Rep.* **1986,** *141*, 51-176.
20. Wachter, P. The optical electrical and magnetic properties of the europium chalcogenides and the rare earth pnictides. *Crit. Rev. in Solid State Sci.* **1972,** *3*, 189-241.
21. Busch, G.; Wachter, P. Einfluß der magnetischen ordnung auf die optische absorption von ferro- oder antiferromagnetischen halbleitern. *Phys. Konden. Mater.* **1966,** *5*, 232-242.
22. Badoz, J.; Billardon, M.; Boccara, A. C.; Briat, B. Measurement and interpretation of magnetic circular dichroism and magnetic linear dichroism spectra. *Symp. Faraday Soc.* **1969,** *3*, 27-39.
23. Güntherodt, G.; Wachter, P.; Imboden, D. M. Energy level scheme and the effect of magnetic order on the optical transitions in europium chalcogenides. *Phys. Konden. Mater.* **1971,** *12*, 292-310.
24. Zinn, W. Microscopic studies of magnetic properties and interactions recent results on europium-monochalcogenides. *J. Magn. Magn. Mater.* **1976,** *3*, 23-36.
25. Díaz, B.; Granado, E.; Abramof, E.; Torres, L.; Lechner, R. T.; Springholz, G.; Bauer, G. Magnetic ordering and transitions of EuSe studied by x-ray diffraction. *Phys. Rev. B* **2010,** *81*, 184428.
26. Callen, H. B.; Callen, E. Cluster Approximation for Ferromagnets with First- and Second-Neighbor Exchange, with Application to the Europium Chalcogenides. *Phys. Rev.* **1964,** *136*, A1675-A1683.

27. Wachter, P. Europium chalcogenides: EuO, EuS, EuSe and EuTe. In *Handbook on the Physics and Chemistry of Rare Earths*; Elsevier: North-Holland, 1979; Vol. 2, pp 507-574.
28. De Simoni, G.; Strambini, E.; Moodera, J. S.; Bergeret, F. S.; Giazotto, F. Toward the Absolute Spin-Valve Effect in Superconducting Tunnel Junctions. *Nano Lett.* **2018,** *18*, 6369-6374.
29. Kar, S.; Boncher, W. L.; Olszewski, D.; Dollahon, N.; Ash, R.; Stoll, S. L. Gadolinium Doped Europium Sulfide. *J. Am. Chem. Soc.* **2010,** *132*, 13960-13962.
30. Selinsky, R. S.; Han, J. H.; Morales Pérez, E. A.; Guzei, I. A.; Jin, S. Synthesis and Magnetic Properties of Gd Doped EuS Nanocrystals with Enhanced Curie Temperatures. *J. Am. Chem. Soc.* **2010,** *132*, 15997-16005.
31. McGuire, T. R.; Holtzberg, F. Magnetic Ordering of $Eu_{(1-x)}Gd_xS$. *AIP Conf. Proc.* **1972,** *5*, 855-859.
32. Mairoser, T.; Schmehl, A.; Melville, A.; Heeg, T.; Canella, L.; Böni, P.; Zander, W.; Schubert, J.; Shai, D. E.; Monkman, E. J.; Shen, K. M.; Schlom, D. G.; Mannhart, J. Is There an Intrinsic Limit to the Charge-Carrier-Induced Increase of the Curie Temperature of EuO? *Phys. Rev. Lett.* **2010,** *105*, 257206.
33. Mairoser, T.; Loder, F.; Melville, A.; Schlom, D. G.; Schmehl, A. Influence of chemical doping on the magnetic properties of EuO. *Phys. Rev. B* **2013,** *87*, 014416.
34. von Molnár, S.; Kasuya, T. Evidence of Band Conduction and Critical Scattering in Dilute Eu-Chalcogenide Alloys. *Phys. Rev. Lett.* **1968,** *21*, 1757-1761.
35. Schoenes, J.; Wachter, P. Exchange optics in Gd-doped EuO. *Physical Review B* **1974,** *9*, 3097-3105.
36. Bebenin, N. G. On magnetic red shift of absorption edge in EuO. *Solid State Commun.* **1985,** *55*, 823-825.
37. Gambino, R. J.; Fumagalli, P.; Ruf, R. R.; McGuire, T. R.; Bojarczuk, N. Magneto-optic spectra of EuS-Gd and EuS-Tb films. *IEEE Transactions on Magnetics* **1992,** *28*, 2973-2975.
38. Schimpf, A. M.; Knowles, K. E.; Carroll, G. M.; Gamelin, D. R. Electronic Doping and Redox-Potential Tuning in Colloidal Semiconductor Nanocrystals. *Acc. Chem. Res.* **2015,** *48*, 1929-1937.
39. Reisner, A.; Kasinathan, D.; Wirth, S.; Tjeng, L. H.; Altendorf, S. G. Valence state of Sm in single-crystalline EuO thin films. *EPL* **2017,** *117*, 47001.
40. Hedman, L.; Rao, K. V.; Yeshurun, Y. Magnetic properties of Eu substituted SmS. *J. Appl. Phys.* **1981,** *52*, 2155-2157.
41. Mirkovic, T.; Hines, M. A.; Nair, P. S.; Scholes, G. D. Single-Source Precursor Route for the Synthesis of EuS Nanocrystals. *Chem. Mater.* **2005,** *17*, 3451-3456.
42. Zhao, F.; Sun, H.-L.; Su, G.; Gao, S. Synthesis and Size-Dependent Magnetic Properties of Monodisperse EuS Nanocrystals. *Small* **2006,** *2*, 244-248.
43. Regulacio, M. D.; Kar, S.; Zuniga, E.; Wang, G.; Dollahon, N. R.; Yee, G. T.; Stoll, S. L. Size-Dependent Magnetism of EuS Nanoparticles. *Chem. Mater.* **2008,** *20*, 3368-3376.
44. Selinsky, R. S.; Keavney, D. J.; Bierman, M. J.; Jin, S. Element-specific magnetometry of EuS nanocrystals. *Appl. Phys. Lett.* **2009,** *95*, 202501.
45. Hasegawa, Y.; Kumagai, M.; Kawashima, A.; Nakanishi, T.; Fujita, K.; Tanaka, K.; Fushimi, K. First Synthesis of EuS Nanoparticle Thin Film with a Wide Energy Gap and Giant Magneto-Optical Efficiency on a Glass Electrode. *J. Phys. Chem. C* **2012,** *116*, 19590-19596.

46. Johnson, C. E.; Costa, L.; Johnson, J. A.; Brown, D. E.; Somarajan, S.; He, W.; Dickerson, J. H. Mössbauer spectra and superparamagnetism of europium sulfide nanoparticles. *J. Phys. D: Appl. Phys.* **2014,** *47*, 075001.
47. Boncher, W.; Dalafu, H.; Rosa, N.; Stoll, S. Europium chalcogenide magnetic semiconductor nanostructures. *Coord. Chem. Rev.* **2015,** *289–290*, 279-288.
48. Zhao, F.; Sun, H.-L.; Gao, S.; Su, G. Magnetic properties of EuS nanoparticles synthesized by thermal decomposition of molecular precursors. *J. Mater. Chem.* **2005,** *15*, 4209-4214.
49. Hasegawa, Y.; Maeda, M.; Nakanishi, T.; Doi, Y.; Hinatsu, Y.; Fujita, K.; Tanaka, K.; Koizumi, H.; Fushimi, K. Effective Optical Faraday Rotations of Semiconductor EuS Nanocrystals with Paramagnetic Transition-Metal Ions. *J. Am. Chem. Soc.* **2013,** *135*, 2659-2666.
50. Vercaemst, R.; Poelman, D.; Fiermans, L.; Van Meirhaeghe, R. L.; Laflère, W. H.; Cardon, F. A detailed XPS study of the rare earth compounds EuS and EuF_3. *J. Electron. Spectrosc. Relat. Phenom.* **1995,** *74*, 45-56.
51. Kowalczyk, S. P.; Edelstein, N.; McFeely, F. R.; Ley, L.; Shirley, D. A. X-ray photoemission spectra of the 4d levels in rare-earth metals. *Chem. Phys. Lett.* **1974,** *29*, 491-495.
52. Connelly, N. G.; Geiger, W. E. Chemical Redox Agents for Organometallic Chemistry. *Chem. Rev.* **1996,** *96*, 877-910.
53. Carroll, G. M.; Schimpf, A. M.; Tsui, E. Y.; Gamelin, D. R. Redox Potentials of Colloidal n-Type ZnO Nanocrystals: Effects of Confinement, Electron Density, and Fermi-Level Pinning by Aldehyde Hydrogenation. *J. Am. Chem. Soc.* **2015,** *137*, 11163-11169.
54. Brown, P. R.; Kim, D.; Lunt, R. R.; Zhao, N.; Bawendi, M. G.; Grossman, J. C.; Bulović, V. Energy Level Modification in Lead Sulfide Quantum Dot Thin Films through Ligand Exchange. *ACS Nano* **2014,** *8*, 5863-5872.
55. Carroll, G. M.; Tsui, E. Y.; Brozek, C. K.; Gamelin, D. R. Spectroelectrochemical Measurement of Surface Electrostatic Contributions to Colloidal CdSe Nanocrystal Redox Potentials. *Chem. Mater.* **2016,** *28*, 7912-7918.
56. Kroupa, D. M.; Vörös, M.; Brawand, N. P.; McNichols, B. W.; Miller, E. M.; Gu, J.; Nozik, A. J.; Sellinger, A.; Galli, G.; Beard, M. C. Tuning colloidal quantum dot band edge positions through solution-phase surface chemistry modification. *Nat. Commun.* **2017,** *8*, 15257.
57. Eastman, D. E.; Holtzberg, F.; Methfessel, S. Photoemission Studies of the Electronic Structure of EuO, EuS, EuSe, And GdS. *Phys. Rev. Lett.* **1969,** *23*, 226-229.
58. Jewett, J. W.; Wigen, P. E. EPR of Tb^{3+}, Pr^{3+}, Gd^{3+}, and Eu^{3+} ions in single crystal La_2O_2S. *J. Chem. Phys.* **1974,** *61*, 2991-2995.
59. Huber, D. L.; Seehra, M. S. Contribution of the spin-phonon interaction to the paramagnetic resonance linewidth of $CrBr_3$. *J. Phys. Chem. Solids* **1975,** *36*, 723-725.
60. Kondal, S. C.; Seehra, M. S. Shape dependence of the EPR linewidth, resonance field and spin-spin relaxation rate of EuS near Tc. *J. Phys. C: Solid State Phys.* **1982,** *15*, 2471.
61. Oseroff, S. B.; Torikachvili, M.; Singley, J.; Ali, S.; Cheong, S. W.; Schultz, S. Evidence for collective spin dynamics above the ordering temperature in $La_{1-x}Ca_xMnO_{3+\delta}$. *Phys. Rev. B* **1996,** *53*, 6521-6525.
62. Causa, M. T.; Tovar, M.; Caneiro, A.; Prado, F.; Ibañez, G.; Ramos, C. A.; Butera, A.; Alascio, B.; Obradors, X.; Piñol, S.; Rivadulla, F.; Vázquez-Vázquez, C.; López-Quintela, M. A.; Rivas, J.; Tokura, Y.; Oseroff, S. B. High-temperature spin dynamics in CMR manganites: ESR and magnetization. *Phys. Rev. B* **1998,** *58*, 3233-3239.

63. Huber, D. L.; Alejandro, G.; Caneiro, A.; Causa, M. T.; Prado, F.; Tovar, M.; Oseroff, S. B. EPR linewidths in $La_{1-x}Ca_xMnO_3$: $0 \leq x \leq 1$. *Phys. Rev. B* **1999,** *60*, 12155-12161.
64. Niebieskikwiat, D.; Sánchez, R. D.; Caneiro, A.; Morales, L.; Vásquez-Mansilla, M.; Rivadulla, F.; Hueso, L. E. High-temperature properties of the Sr_2FeMoO_6 double perovskite: Electrical resistivity, magnetic susceptibility, and ESR. *Phys. Rev. B* **2000,** *62*, 3340-3345.
65. Turov, E. A. Line width of ferromagnetic resonance absorption. In *Ferromagnetic Resonance*; Vonsovskii, S. V., Ed.; Pergamon: London, 1966; pp 184-230.
66. von Molnar, S.; Lawson, A. W. Ferromagnetic and Paramagnetic Resonance in EuS. *Phys. Rev.* **1965,** *139*, A1598-A1602.
67. Regulacio, M. D.; Tomson, N.; Stoll, S. L. Dithiocarbamate Precursors for Rare-Earth Sulfides. *Chem. Mater.* **2005,** *17*, 3114-3121.

Chapter 4: Two-Dimensional van der Waals Nanoplatelets with Robust Ferromagnetism

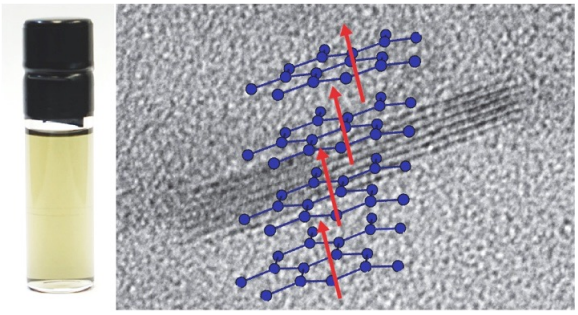

Reproduced with permission from:
De Siena, M. C.; Creutz, S. E.; Regan, A.; Malinowski, P.; Jiang, Q.; Kluherz, K. T.; Zhu, G.; Lin, Z.; De Yoreo, J. J.; Xu, X.; Chu, J.-H.; Gamelin, D. R. Nano Lett. 2020, *20*, 2100-2106.

4.1 Overview

We have synthesized unique colloidal nanoplatelets of the two-dimensional (2D) van der Waals ferromagnet CrI_3 and have characterized these nanoplatelets structurally, magnetically, and by magnetic circular dichroism spectroscopy. The CrI_3 nanoplatelets have lateral dimensions of ~25 nm and thicknesses of only ~4 nm, corresponding to just a few CrI_3 monolayers. Magnetic and magneto-optical measurements demonstrate robust 2D ferromagnetic ordering with Curie temperatures similar to bulk CrI_3, despite their small size. These data also show magnetization steps akin to those observed in micron-sized few-layer 2D sheets associated with concerted spin-reversal of individual CrI_3 layers within few-layer van der Waals stacks. Similar data have also been obtained for $CrBr_3$ and anion-alloyed $Cr(I_{1-x}Br_x)_3$ nanoplatelets. These results represent the first example of lateral nanostructures of 2D van der Waals ferromagnets of any composition. The demonstration of robust ferromagnetism at nanometer lateral dimensions opens new doors for miniaturization in spintronics devices based on van der Waals ferromagnets.

4.2 Main Text

Long-range magnetic order has recently been demonstrated in micron-sized two-dimensional (2D) magnetic semiconductors,[1-2] opening opportunities for atomically thin spintronics.[3-5] For high-density devices, however, a fundamental limitation is the instability of ferromagnetism as lateral sizes approach the nanoscale.[6-7] It is thus of both fundamental and technological importance to explore the magnetic properties of 2D layered magnetic nanostructures, *e.g.*, with length scales similar to modern transistors (~10 - 20 nm). Here, we report successful synthesis of unique colloidal nanoplatelets of 2D magnets CrX_3 (X = I, Br) and their alloys. The miniaturization and associated solution compatibility demonstrated here suggest new opportunities for studying 2D spin effects at the nanoscale and exploiting nanostructuring in high-density spintronics.

An interesting aspect of the ferromagnetism in CrI_3 is that the ground-state ($^4A_2$) single-ion anisotropy (D) of its pseudo-octahedral Cr^{3+} constituents is negligible,[8] yet the Curie temperature is still relatively high (T_C ~ 45 K in monolayers). The magnetic anisotropy underlying T_C comes entirely from the 2D morphology of the individual layers, and specifically from the presence of in-plane (anisotropic) ferromagnetic superexchange interactions that pin the spin orientation of any given Cr^{3+}

and generate a gap in the spin-wave density of states.[8-10] Computational work suggests that the large I^- spin-orbit coupling can introduce substantial single-ion anisotropy beyond the negligible contribution from Cr^{3+}, and that the relative signs of this and the Kitaev anisotropy ultimately determine the magnetic ground state.[9] Ferromagnetic resonance measurements and associated analysis have probed both the strong Kitaev interactions and the anisotropic exchange interactions proposed to be responsible for the 2D ferromagnetic order.[10] As the lateral dimensions of the CrI_3 plane are decreased, this morphological stabilization should diminish due to broken symmetry at the edges, eventually causing the ferromagnetism to be surmountable by thermal fluctuations and the CrI_3 to become superparamagnetic (*i.e.*, decreasing the blocking temperature). For example, ferromagnetic *hcp* cobalt metal has a very high T_C of >1000 K in bulk but becomes superparamagnetic at room temperature in nanocrystals.[11] Additionally, T_C itself could be reduced by lateral truncation. Theory predicts that the electronic structures of CrI_3 nanoribbons should be strongly dependent on their edge structures, displaying quantum size effects in the energy gap and new edge states around the Fermi level.[12] To date, however, there have been no experimental examples of laterally confined 2D magnets of any type. It remains an open question whether 2D ferromagnetism can survive lateral truncation of the 2D structural periodicity.

Here we report the bottom-up synthesis and physical characterization of colloidal few-layer CrX_3 (X = I, Br) nanoplatelets with average lateral dimensions of only ~25 nm, focusing on CrI_3. Common solution routes to colloidal metal-halide nanocrystals[13] frequently involve high-temperature reaction of halide sources (*e.g.*, alkylammonium halides, benzoyl halides, trimethylsilyl halides) with simple metal salts (*e.g.*, metal acetates, carbonates) solubilized by surfactants (*e.g.*, long-chain carboxylates, amines). In our hands, attempts to synthesize CrX_3 *via* similar approaches using simple Cr(III) precursors and common surfactants did not work (see Appendix C). Octahedral Cr(III) is canonically substitutionally inert,[14] making these simple Cr(III) precursors difficult to solubilize and relatively unreactive. We therefore sought more reactive precursors that would be highly soluble in nonpolar, noncoordinating solvents such as alkanes or toluene, and that would also react in a way that produces only innocuous and readily separable byproducts. We found that $Cr(OR)_3$ (R = 1,1-di-*t*-butylethoxide) meets all of these requirements. Similarly, trimethylsilyl iodide (TMSI) was identified as a reactive and alkane-soluble iodide precursor.[15] When an anhydrous toluene solution of $Cr(OR)_3$ with excess TMSI is immersed with vigorous stirring into an oil bath preheated to 135 °C, abrupt formation of a black precipitate is observed after ~5 min. The rapid onset of nucleation under these conditions is well-suited to the formation of high-quality nanocrystals.[16] Because no solubilizing ligands are present, the resulting nanocrystals precipitate from solution rather than forming a colloidal dispersion. They can be separated from the clear supernatant by centrifugation and washing with hexanes. The nanocrystals can then be resuspended in dichloromethane through vigorous ultrasonication to generate a clear, dark-green solution (Fig. 4.1A).

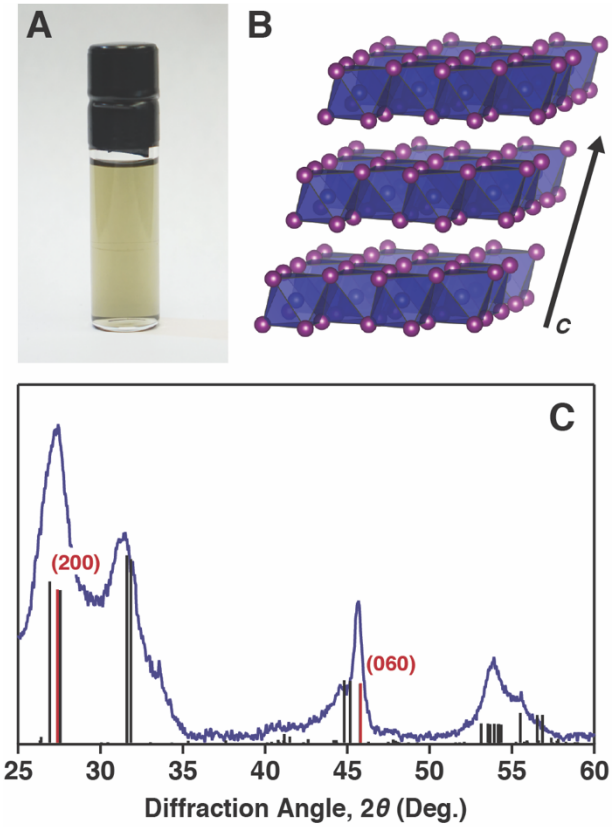

Figure 4.1. (A) Photograph of a solution of CrI_3 nanocrystals in DCM. **(B)** Illustration of the room-temperature crystal structure of bulk CrI_3, showing a section of three monolayers with the nearly ABC stacking arrangement of the monoclinic *C*2/*m* structure.[17] The arrow indicates the direction of the crystallographic *c*-axis. **(C)** Powder X-ray diffraction data for CrI_3 nanocrystals (blue) measured with Cu K_α radiation, compared to a reference pattern for CrI_3 (*C*2/*m*, ICSD Coll. Code 251654).[17] Prominent reflections from planes parallel to the *c*-axis are highlighted in red and labeled with the Miller indices of the corresponding planes.

Interlayer magnetic coupling in CrI_3 is tightly connected to the layer stacking arrangement.[18-19] Figure 4.1B illustrates the lattice structure of bulk CrI_3, which adopts a monoclinic *C*2/*m* structure at room temperature and transitions to a rhombohedral *R*-3 phase below 220 K.[17] Figure 4.1C shows powder X-ray diffraction (PXRD) data collected for the isolated nanocrystals. Although high sensitivity to air complicated the PXRD measurements (see Methods), these data confirm the identity, structure, and morphology of the isolated material as CrI_3, best matching the *C*2/*m* monoclinic phase. In this phase, stacked CrI_3 monolayers are displaced along the *a*-axis with the nearly ABC arrangement[17] associated with antiferromagnetic interlayer coupling.[20-21] Notably, substantial Scherrer broadening is observed in Fig. 4.1C for reflections from planes parallel to the *ab*-plane. Only reflections from planes lying mostly or entirely parallel to the *c*-axis are reasonably narrow. This result suggests substantial crystalline shape anisotropy. As described below, these nanocrystals are in fact CrI_3 nanoplatelets with lateral dimensions ~5 times greater than their few-layer

thicknesses. The (060) reflection at 2θ = 46° is particularly narrow, and its width can be used to estimate a mean lateral nanoplatelet size of ~20 nm for the sample of Fig. 4.1. Notably, these PXRD peak widths and the colloidal stability of these nanocrystals preclude the existence of large bulk-like crystals within this ensemble.

Transmission electron microscopy (TEM) was used to further characterize the CrI_3 nanocrystals and the results are summarized in Fig. 4.2. Figure 4.2A shows an overview TEM image of an ensemble of CrI_3 nanocrystals. The absence of surface ligands causes the nanocrystals to aggregate when cast onto the TEM grids, making it difficult to identify many well-isolated nanocrystals. Figure 4.2B shows a selected-area electron diffraction (SAED) image of the same aggregated nanocrystals. Its integrated profile is shown in Fig. 4.2C compared to the calculated reference lines for CrI_3 ($C2/m$). These data confirm the identity of these nanocrystals as monoclinic CrI_3.

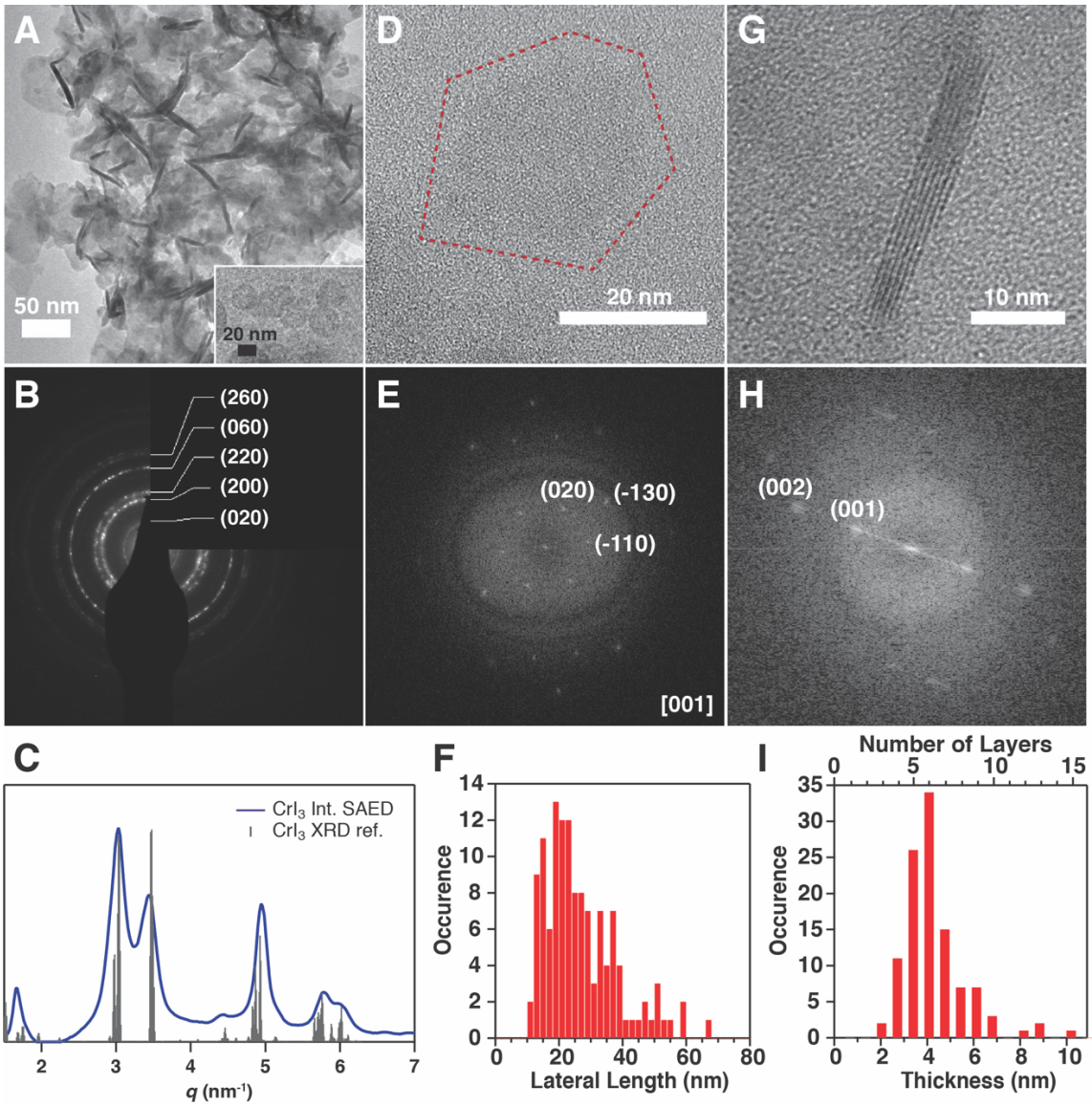

Figure 4.2. **(A)** TEM image of an aggregate of CrI_3 nanoplatelets. Inset: Zoomed in view of a string of isolated nanoplatelets. **(B)** Selected area electron diffraction (SAED) image of aggregated CrI_3 nanoplatelets. The rings are indexed to their corresponding diffraction planes. **(C)** Integrated profile of the SAED diffraction rings, compared to the calculated reference lines for CrI_3 (*C*2/*m*). **(D)** High-resolution TEM image of a single isolated nanoplatelet. **(E)** Fourier transform of the image from panel D, showing peaks consistent with the nanoplatelet being a single crystalline domain with the monoclinic *C*2/*m* structure along the [001] zone axis. **(F)** Distribution of CrI_3 nanoplatelet lateral sizes from a survey of over 100 nanoplatelets, yielding an average width of 26 ± 11 nm. **(G)** Edge-on HRTEM image of a single stack of nanoplatelets. **(H)** Fourier transform of the image from panel G, showing peaks consistent with van der Waals stacked CrI_3 nanoplatelets with the *C*2/*m* structure. **(I)** Distribution of CrI_3 nanoplatelet thicknesses from a survey of over 100 nanoplatelets. The average nanoplatelet thickness is 3.7 ± 0.7 nm, corresponding to 6 ± 1 CrI_3 monolayers. All data were collected at room temperature.

The inset to Fig. 4.2A shows a low-resolution image of several individual nanocrystals side-by-side. These nanocrystals appear disk-like and have low contrast, consistent with thin nanoplatelets. Figure 4.2D shows a high-resolution image of a single nanoplatelet. Although faint, faceting consistent with hexagonal CrI_3 is observable. Careful inspection further reveals lattice fringes in this image. Figure 4.2E plots the Fourier transform of this image, revealing distinct peaks characteristic of single-crystal CrI_3 (*C*2/*m*). The sizes of over 100 individual nanoplatelets were measured, yielding an average width of 26 ± 11 nm (Fig. 4.2F). The smallest nanoplatelets identified were only 10 nm across, and the largest nanoplatelet reached 66 nm across.

Several nanocrystals can be seen lying on their sides, resulting in thin dark stripes in Fig. 4.2A. Figure 4.2G shows a high-resolution TEM image of one isolated edge-on structure, in which six parallel thinner lines are observed. Figure 4.2H plots the Fourier transform of this image, revealing a series of spots that can be indexed to (00*n*) peaks. These data show an interlayer spacing of 0.69 ± 0.07 nm, consistent with the value of 0.66 nm expected from the CrI_3 (*C*2/*m*) crystal structure. Over 100 edge-on nanoplatelets were surveyed, from which an average thickness of 3.7 ± 0.7 nm is obtained (Fig. 4.2I), corresponding to only 6 ± 1 CrI_3 monolayers. Similar results were obtained for $CrBr_3$ nanoplatelets prepared analogously (see Appendix C). Beyond CrI_3 and $CrBr_3$, this synthetic approach also allows formation of anion-alloyed $Cr(I_{1-x}Br_x)_3$ nanoplatelets, providing a mechanism for continuous tuning of the nanoplatelet optical and magnetic properties (see Appendix C).

The electronic structures and magnetism of $CrBr_3$ and $CrCl_3$ single crystals have previously been investigated by transmission and reflection magnetic circular dichroism (MCD) spectroscopies,[22-23] including down to a single monolayer.[2,24-25] Figure 4.3 summarizes the 5 K absorption (extinction) and transmission MCD spectra of representative $CrBr_3$ and CrI_3 nanoplatelet ensembles. MCD spectra are plotted as the differential absorbance of left and right circularly polarized light (ΔA) normalized to the absorbance at the first peak maximum ($A_{max}(^4T_2)$) after accounting for scattering.

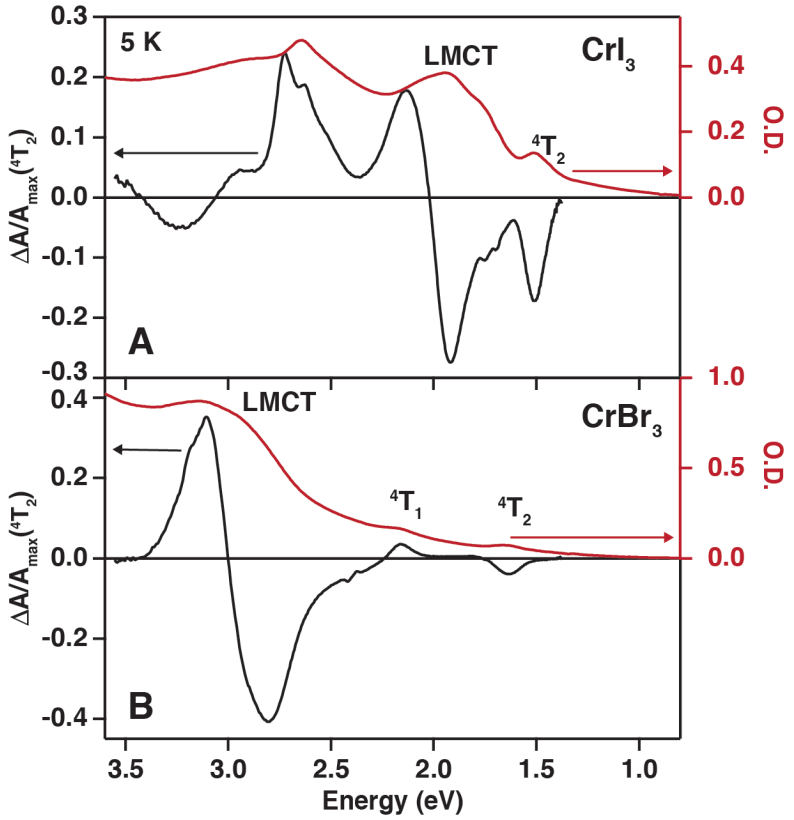

Figure 4.3. Transmission magnetic circular dichroism (MCD) spectra of **(A)** CrI_3 and **(B)** $CrBr_3$ nanoplatelets measured at 5 K and at a magnetic field of 5 T, compared with the 5 K zero-field electronic absorption (extinction) spectra. Absorption axes are labeled by optical density (O.D.). MCD spectra are plotted as $\Delta A/A_{max}(^4T_2)$, *i.e.*, the differential absorbance of left and right circularly polarized light (ΔA) normalized to the absorbance at the first peak maximum ($A_{max}(^4T_2)$) after accounting for the scattering baseline. The assignments of select optical transitions are indicated.

The CrI_3 nanoplatelet spectra (Fig 4.3A) are better understood by first examining the spectra of $CrBr_3$ nanoplatelets (Fig. 4.3B). As in bulk $CrBr_3$,[22-23] the $CrBr_3$ nanoplatelet spectra show two weak absorption features at low energies (1.6, 2.2 eV) attributable to the $^4A_2 \rightarrow {}^4T_2$ and $^4T_1$ ligand-field transitions of pseudo-octahedral $[CrBr_6]^{3-}$. Each band is associated with an MCD feature in which one polarization dominates. To higher energy, a pair of more intense π-type ligand-to-metal charge-transfer (LMCT) transitions appears, centered at ~3 eV and with opposite MCD polarizations.[26-27]

The absorption spectrum of the CrI_3 nanoplatelets (Fig. 4.3A) is very similar to the differential reflection spectrum of bulk CrI_3, but it differs slightly from that reported for monolayer CrI_3,[28] possibly due to interface effects in the latter. In Fig. 4.3A, the $^4T_2$ band remains the lowest-energy transition, but the LMCT transitions have shifted down to ~2.1 eV. A redshift of ~1.1 eV is predicted from the electronegativity difference between Br^- and I^-,[29] in good agreement with the data. To higher energies in the CrI_3 spectra, several additional absorption and MCD features are observed, but overlap between

LMCT and ligand-field transitions complicates band assignments. Both CrI_3 and $CrBr_3$ thus have their absorption gaps determined by the same highly localized $^4A_2 \rightarrow {}^4T_2$ Cr^{3+} ligand-field transition. Notably, the MCD rotational strength of the $^4T_2$ excitation is substantially (~5x) greater in the CrI_3 nanoplatelets than in the $CrBr_3$ nanoplatelets, likely reflecting enhanced configuration interaction with the strongly optically active LMCT states in CrI_3 due to their lower energies.

Variable-temperature and variable-field MCD measurements were performed to assess the magnetism of these CrI_3 and $CrBr_3$ nanoplatelets. Figure 4.4A plots CrI_3 MCD spectra collected at several temperatures between 5 and 200 K (see Appendix C for $CrBr_3$ data). The inset to Fig. 4.4A plots the MCD amplitudes extracted from these data, from which T_C = 54 K is determined. This value is smaller than in bulk (T_C = 61 K),[17] but the trend is consistent with the decrease to T_C = 45 K reported for monolayer CrI_3 sheets.[2] Figure 4.4B plots variable-field MCD spectra of the CrI_3 nanoplatelets collected at 5 K. All of the spectral features show the same field dependence, confirming their common origin. The inset to Fig. 4.4B plots the CrI_3 nanoplatelet MCD intensity as a function of applied field, revealing a sizable hysteresis that confirms retention of ferromagnetism in these nanoplatelets. Multiple distinct inflections are observed at intermediate fields during the field sweep (see Appendix C).

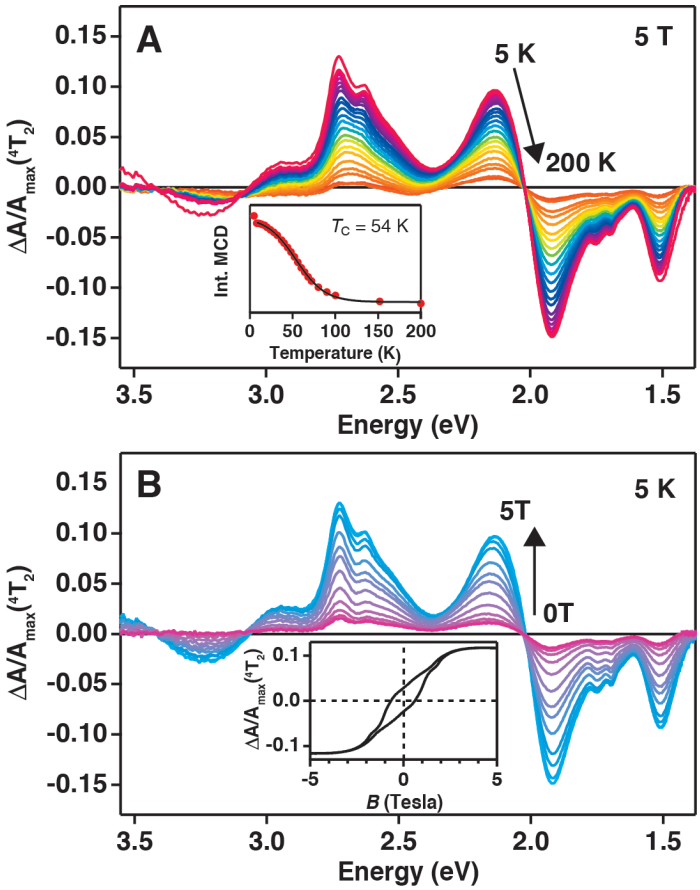

Figure 4.4. (A) Variable-temperature (5 to 200 K) MCD spectra of CrI_3 nanoplatelets measured at 5 T. Inset: Plot of integrated absolute 5 T MCD intensity as a function of temperature. The minimum in the derivative of these data yields a Curie temperature of ~54 K. The solid curve in the inset is a guide to the eye. **(B)** Variable-field (0 - 5T) MCD spectra of CrI_3 nanoplatelets measured at 5 K. Inset: Magnetization *vs* magnetic field plot for CrI_3 nanoplatelets at 5 K, as probed using the MCD signal at 455 nm. The sample was first magnetized at 5 T then swept to -5 T and back to 5 T during data collection.

Figures 4.5A,B compare the MCD hysteresis curve from Fig. 4.4C with magnetic hysteresis data for the same nanoplatelets collected by vibrating sample magnetometry (VSM) on a slightly expanded *x*-axis scale. Although less pronounced, several inflections are also observed in the VSM data. Interestingly, the fields at which these inflections occur coincide almost *exactly* with the fields at which magnetization steps are observed in mechanically exfoliated multilayer CrI_3 sheets. To illustrate, the shaded grey bars in Fig. 4.5 mark the fields at which abrupt magnetization steps occur in four-layer CrI_3 sheets with micron lateral dimensions when magnetized along their easy axis.[24] The steps in the nanoplatelet data appear less abrupt due to orientation averaging because of more gradual magnetization when the external field (*B*) is not along the nanoplatelet easy axis. These steps have been assigned to magnetization reversal of individual CrI_3 monolayers within multilayer stacks.[24] We thus attribute the inflections observed in Fig. 4.5A,B to magnetization reversal of individual monolayers within multilayer CrI_3 nanoplatelets, as depicted schematically in Fig. 4.5D.

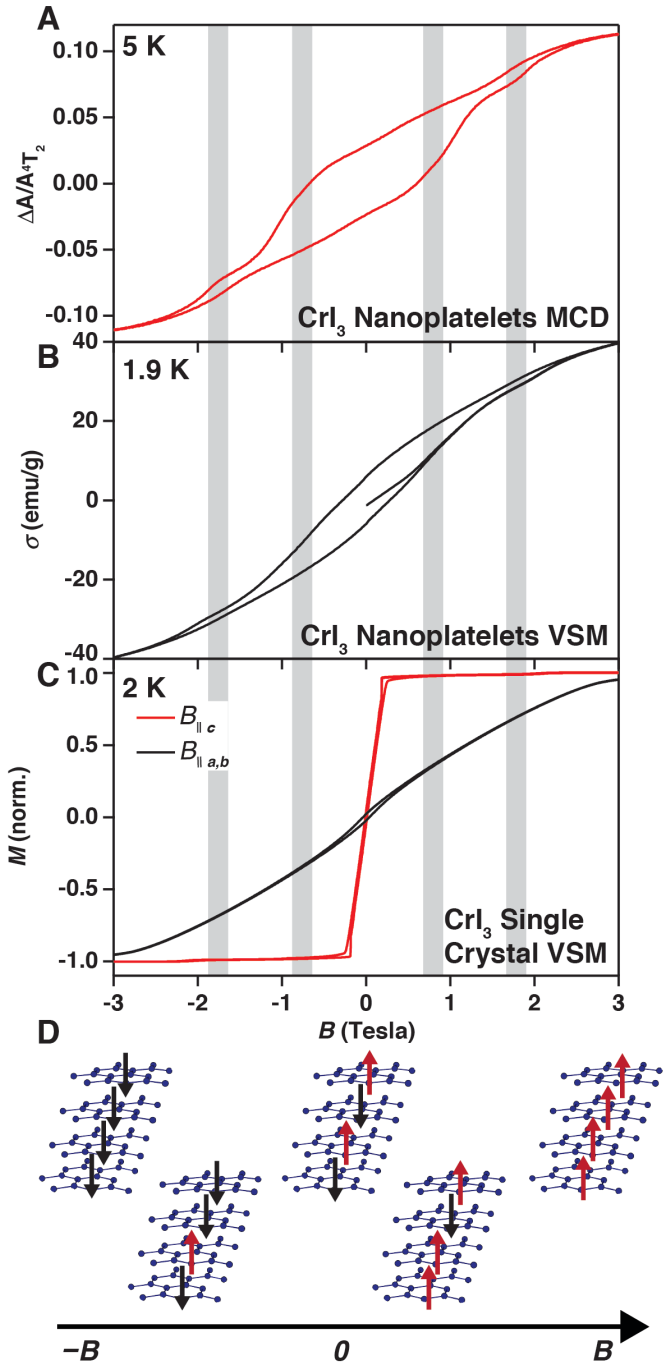

Figure 4.5. Magnetization *vs* field plots measured by **(A)** MCD spectroscopy and **(B)** vibrating sample magnetometry (VSM) on the same sample of randomly oriented CrI_3 nanoplatelets. **(C)** VSM data from a CrI_3 single crystal aligned both parallel and perpendicular to the applied field are also plotted on the same field axis. The vertical gray bars represent the fields at which the spins of individual layers of a four-layer CrI_3 sheet have been reported to flip.[24] **(D)** Schematic of magnetic structures of a representative four-layer CrI_3 nanoplatelet. Purple spheres represent Cr^{3+} ions and I^- ions are omitted. The fields at which transitions between these magnetic arrangements occur are determined by the weak antiferromagnetic interlayer coupling.

The monolayer spin-flip events observed here are signatures of few-layer CrI_3. In these nanoplatelets, however, the fraction of edge Cr^{3+} ions is vastly greater than in exfoliated CrI_3 sheets: Idealizing the nanoplatelets as hexagons, the average CrI_3 nanoplatelet here contains ~2360 Cr^{3+} ions, of which ~10% occupy edge sites. Because of broken translational symmetry, these edge spins are not pinned with the same energies as the core spins, leading to spin canting or lower-temperature spin fluctuations. Lateral miniaturization should thus reduce the barrier to magnetization reversal, but the data here do not show such a reduction. From the magnetocrystalline anisotropy of bulk CrI_3,[30] we estimate that the barrier to monolayer magnetization reversal will not drop below the bulk value of $k_B T_C$ until lateral dimensions reach < ~6.5 nm (~230 Cr^{3+} ions, ~34% edge sites, see Appendix C), consistent with the bulk-like T_C observed in Fig. 4.4A.

The nanoplatelets reported here represent a fundamentally new morphology for this emergent class of materials. The vast majority of few-layer van der Waals ferromagnets like CrI_3 have previously been prepared using mechanical exfoliation of bulk crystals, with only few examples of bottom-up syntheses *via* vapor deposition[31] or cation exchange[32] that still yield micron-sized structures. Remarkably, despite their extremely small (~25 nm) lateral dimensions, these CrI_3 nanoplatelets still show the same robust intra-layer ferromagnetism, interlayer antiferromagnetic coupling, and discrete layer-by-layer spin-flip magnetization as observed in mechanically exfoliated CrI_3 sheets with much larger dimensions. Moreover, T_C appears undiminished by their very small volumes. This successful miniaturization, in conjunction with the unique solution processability of this form of CrI_3, opens interesting avenues for constructing fundamentally new types of programmable 2D magnetic quantum materials, for example, through their integration as localized "spin bubbles" within otherwise non-magnetic 2D heterostructures, through self-assembly into spin-bubble superlattices, through nucleation of lateral heterostructures, or even through combination with other solution-phase materials to construct free-standing nanoscale 2D van der Waals heterostructures with magnetic functionality. More generally, the demonstration that robust ferromagnetism persists in nanoscale CrI_3 indicates the possibility of high-density spintronic devices based on nanopatterned 2D ferromagnetic semiconductors.

4.3 Methods

4.3.1 General considerations. Unless otherwise stated, all measurements and synthetic manipulations were performed using standard Schlenk techniques under a dinitrogen atmosphere, or in a glovebox under an atmosphere of purified dinitrogen. Anhydrous tetrahydrofuran (THF), dichloromethane (DCM), ethyl ether, pentane, and toluene were purified through an alumina column pressurized with argon. Hexanes was further dried over sodium benzophenone and distilled before use. Xylenes was dried by refluxing over calcium hydride and distilled before use. All solvents were stored over 4Å sieves.

4.3.2 Chemicals. Unless otherwise stated, all chemicals were used as received without further purification. Zinc metal, chromium metal (99.995%), anhydrous $CrCl_3$, and I_2 (99.99%) were purchased from Alfa Aesar. Hexamethylacetone, methyllithium (1.6 M in ether), trimethylsilyl

bromide (97%), and trimethylsilyl iodide (97%) were purchased from Sigma Aldrich. $Cr(OCMe^tBu_2)_3$ was synthesized as previously reported.[33]

4.3.3 Synthesis of CrX_3 nanoplatelets. The chromium precursor, $Cr(OCMe^tBu_2)_3$ (20 mg, 0.04 mmol) is dissolved in 2 mL of toluene (X = I) or xylenes (X = Br) in a 25 mL Schlenk tube equipped with a stir bar, giving a light blue solution. A total of 0.70 mmol of trimethylsilyl halide (bromide, iodide, or a mixture of both) is added to the reaction mixture. No observable change occurs. The Schlenk tube is sealed and immersed into a pre-heated oil bath at 135˚C (180˚C for $CrBr_3$) with rapid stirring. After approximately 5 min, the solutions abruptly turned black and opaque, indicating the formation of the CrI_3 nanoplatelets as a precipitate. Heating was continued for an additional 10 min, and then the reaction was removed from the heating bath and allowed to cool to room temperature. The precipitate was separated from the colorless supernatant by centrifugation and washed three times with hexanes (5 mL). The precipitate was finally collected as a suspension in hexanes.

4.3.4 Synthesis of CrI_3 single crystals. Single crystals of CrI_3 were grown by chemical vapor transport using iodine as a self-transport agent following a procedure adapted from the literature with modification.[17] Cr(0) pieces and solid crystalline I_2 were loaded into a quartz tube and sealed under an evacuated argon atmosphere. The quartz tube was 10 cm long, inner diameter 14 mm, and outer diameter 16 mm, and the amount of loaded iodine was determined by ensuring that the pressure inside of the tube reached a value near atmospheric pressure upon reaching the highest growth temperature. The transport of material was achieved using the natural temperature gradient of an open-ended horizontal furnace. The source end of the tube is placed in the hot end of a 650/550˚C temperature gradient and allowed to dwell for 7 days, and then allowed to slowly cool to room temperature. Crystals grew at the cold end of the tube as large, shiny black plates.

4.3.5 Powder X-ray diffraction (XRD) measurements. Samples were prepared for powder XRD by drop-casting suspensions of nanoplatelets from hexanes onto silicon wafers, and protecting them from air by sealing under Kapton film. Data were collected using a Bruker D8 Discover diffractometer.

4.3.6 Magnetic circular dichroism (MCD) and absorption (extinction) measurements. Samples for transmission MCD measurements were prepared by mixing dried nanoplatelets in polydimethylsiloxane (PDMS, viscosity 1,000 cSt). This mixture was then sandwiched between two quartz discs to make a mull suspension. Low-temperature magnetic circular dichroism (MCD) spectra were conducted with the samples placed in a superconducting magneto-optical cryostat (Cryo-Industries SMC-1659 OVT) oriented in the Faraday configuration. Samples were loaded into the cryostat under helium gas to minimize air exposure and sample decomposition. At liquid helium temperatures, the sample was screened for depolarization by matching the CD spectra of a chiral molecule placed along the optical path before and after the sample. Depolarization by the samples was less than 5% in each case. Transmission MCD spectra were collected using an Aviv 40DS spectropolarimeter. UV-Vis absorption (extinction) measurements were performed on similar mulls

using an Agilent Cary 5000 spectrophotometer, and sample cooling was achieved using a flow cryostat with a variable-temperature sample compartment.

4.3.7 Vibrating sample magnetometry (VSM) measurements. A Quantum Design PPMS DynaCool was used for VSM measurements. Powders were loaded into plastic VSM powder sample holders and the single crystal was affixed to the end of a quartz paddle with varnish (VGE 7031). The paddle was then snapped into the VSM brass sample holder with another quartz paddle placed symmetrically above the sample to minimize the background coming from the quartz.

4.3.8 Transmission electron microscopy (TEM) measurements. TEM samples were prepared by drop casting suspensions of nanocrystals onto 400 mesh carbon-coated copper grids purchased from TED Pella, Inc. and dried under an inert atmosphere. Nanocrystal suspensions were prepared by ultrasonication of the materials in dichloromethane at a sonicator frequency of 20 kHz under an inert atmosphere. In a glovebox, TEM grids were loaded into a vacuum transfer holder to prevent sample exposure to air. TEM images were obtained on an FEI Titan microscope operated at 300 kV or on an FEI Tecnai F20 microscope operated at 200 kV. FFT images were generated using ImageJ, and brightness was adjusted to aid visualization.[34]

4.3.9 Energy-dispersive X-ray spectroscopy (EDS) measurements. For EDS analysis of nanoplatelet compositions, samples were drop cast onto silicon substrates and coated with a ~200 nm thick layer of carbon; spectra were acquired in an FEI Sirion Scanning Electron Microscope operating at 30 kV using an Oxford EDS spectrometer. Standardless quantification was used.

4.4 References

1. Gong, C.; Li, L.; Li, Z.; Ji, H.; Stern, A.; Xia, Y.; Cao, T.; Bao, W.; Wang, C.; Wang, Y.; Qiu, Z. Q.; Cava, R. J.; Louie, S. G.; Xia, J.; Zhang, X., Discovery of intrinsic ferromagnetism in two-dimensional van der Waals crystals. *Nature* **2017,** *546*, 265–269.
2. Huang, B.; Clark, G.; Navarro-Moratalla, E.; Klein, D. R.; Cheng, R.; Seyler, K. L.; Zhong, D.; Schmidgall, E.; McGuire, M. A.; Cobden, D. H.; Yao, W.; Xiao, D.; Jarillo-Herrero, P.; Xu, X., Layer-dependent ferromagnetism in a van der Waals crystal down to the monolayer limit. *Nature* **2017,** *546*, 270.
3. Burch, K. S.; Mandrus, D.; Park, J.-G., Magnetism in two-dimensional van der Waals materials. *Nature* **2018,** *563*, 47-52.
4. Gong, C.; Zhang, X., Two-dimensional magnetic crystals and emergent heterostructure devices. *Science* **2019,** *363*, eaav4450.
5. Gibertini, M.; Koperski, M.; Morpurgo, A. F.; Novoselov, K. S., Magnetic 2D materials and heterostructures. *Nat. Nanotech.* **2019,** *14*, 408-419.
6. Weller, D.; Moser, A., Thermal effect limits in ultrahigh-density magnetic recording. *IEEE Trans. Magn.* **1999,** *35*, 4423–4439.
7. Thompson, D. A.; Best, J. S., The future of data storage technology. *IBM J. Res. Dev.* **2000,** *44*, 311–322.
8. Lado, J. L.; Fernández-Rossier, J., On the origin of magnetic anisotropy in two dimensional CrI_3. *2D Materials* **2017,** *4*, 035002.
9. Xu, C.; Feng, J.; Xiang, H.; Bellaiche, L., Interplay between Kitaev interaction and single ion anisotropy in ferromagnetic CrI_3 and $CrGeTe_3$ monolayers. *npj Comp. Mater.* **2018,** *4*, 57.

10. Lee, I.; Utermohlen, F. G.; Weber, D.; Hwang, K.; Zhang, C.; van Tol, J.; Goldberger, J. E.; Trivedi, N.; Hammel, P. C., Fundamental Spin Interactions Underlying the Magnetic Anisotropy in the Kitaev Ferromagnet CrI_3. *Phys. Rev. Lett.* **2020,** *124*, 017201.
11. Puntes, V. F.; Zanchet, D.; Erdonmez, C. K.; Alivisatos, A. P., Synthesis of hcp-Co nanodisks. *J. Am. Chem. Soc.* **2002,** *124*, 12874-12880.
12. Jiang, W.; Li, S.; Liu, H.; Lu, G.; Zheng, F.; Zhang, P., First-principles calculations of magnetic edge states in zigzag CrI_3 nanoribbons. *Phys. Lett. A* **2019,** *383*, 754-758.
13. Shamsi, J.; Urban, A. S.; Imran, M.; Trizio, L. D.; Manna, L., Metal halide perovskite nanocrystals: synthesis, post-synthesis modifications, and their optical properties. *Chem. Rev.* **2019,** *119*, 3296-3348.
14. Taube, H., Rates and mechanisms of substitution in inorganic complexes in solution. *Chem. Rev.* **1952,** *50*, 69-126.
15. Creutz, S. E.; Crites, E. N.; De Siena, M. C.; Gamelin, D. R., Anion exchange in cesium lead halide perovskite nanocrystals and thin films using trimethylsilyl halide reagents. *Chem. Mater.* **2018,** *30*, 4887-4891.
16. Thanh, N. T. K.; Maclean, N.; Mahiddine, S., Mechanisms of nucleation and growth of nanoparticles in solution. *Chem. Rev.* **2014,** *114*, 7610-7630.
17. McGuire, M. A.; Dixit, H.; Cooper, V. R.; Sales, B. C., Coupling of crystal structure and magnetism in the layered, ferromagnetic insulator CrI_3. *Chem. Mater.* **2015,** *27*, 612-620.
18. Soriano, D.; Cardoso, C.; Fernandez-Rossier, J., Interplay between interlayer exchange and stacking in CrI_3 bilayers. *Solid State Commun.* **2019,** *299*, 113662.
19. Sivadas, N.; Okamoto, S.; Xu, X.; Fennie, C. J.; Xiao, D., Stacking-dependent magnetism in bilayer CrI_3. *Nano Lett.* **2018,** *18*, 7658-7664.
20. Jiang, P.; Wang, C.; Chen, D.; Zhong, Z.; Yuan, Z.; Lu, Z.-Y.; Ji, W., Stacking tunable interlayer magnetism in bilayer CrI_3. *Phys. Rev. B* **2019,** *99*, 144401.
21. Ubrig, N.; Wang, Z.; Teyssier, J.; Taniguchi, T.; Watanabe, K.; Giannini, E.; Morpurgo, A. F.; Gibertini, M., Low-temperature monoclinic layer stacking in atomically thin CrI_3 crystals. *2D Mater.* **2019,** *7*, 015007.
22. Bermudez, V. M.; McClure, D. S., Spectroscopic studies of the two-dimensional magnetic insulators chromium trichloride and chromium tribromide—II. *J. Phys. Chem. Solids* **1979,** *40*, 149-173.
23. Bermudez, V. M.; McClure, D. S., Spectroscopic studies of the two-dimensional magnetic insulators chromium trichloride and chromium tribromide—I. *J. Phys. Chem. Solids* **1979,** *40*, 129-147.
24. Song, T.; Cai, X.; Tu, M. W.-Y.; Zhang, X.; Huang, B.; Wilson, N. P.; Seyler, K. L.; Zhu, L.; Taniguchi, T.; Watanabe, K.; McGuire, M. A.; Cobden, D. H.; Xiao, D.; Yao, W.; Xu, X., Giant tunneling magnetoresistance in spin-filter van der Waals heterostructures. *Science* **2018,** *360*, 1214-1218.
25. Jiang, S.; Li, L.; Wang, Z.; Mak, K. F.; Shan, J., Controlling magnetism in 2D CrI_3 by electrostatic doping. *Nat. Nanotech.* **2018,** *13*, 549-553.
26. Dillon, J. F.; Kamimura, H.; Remeika, J. P., Magneto-optical properties of ferromagnetic chromium trihalides. *J. Phys. Chem. Solids* **1966,** *27*, 1531-1549.
27. Shinagawa, K.; Sato, H.; Ross, H. J.; McAven, L. F.; Butler, P. H., Charge-transfer transitions in chromium trihalides. *J. Phys.: Cond. Matter* **1996,** *8*, 8457-8463.

28. Seyler, K. L.; Zhong, D.; Klein, D. R.; Gao, S.; Zhang, X.; Huang, B.; Navarro-Moratalla, E.; Yang, L.; Cobden, D. H.; McGuire, M. A.; Yao, W.; Xiao, D.; Jarillo-Herrero, P.; Xu, X., Ligand-field helical luminescence in a 2D ferromagnetic insulator. *Nat. Physics* **2018,** *14*, 277-281.
29. Jørgensen, C. K., Electron transfer spectra. *Prog. Inorg. Chem.* **1970,** *12*, 101–158.
30. Richter, N.; Weber, D.; Martin, F.; Singh, N.; Schwingenschlögl, U.; Lotsch, B. V.; Kläui, M., Temperature-dependent magnetic anisotropy in the layered magnetic semiconductors CrI_3 and $CrBr_3$. *Phys. Rev. Mater.* **2018,** *2*, 024004.
31. Grönke, M.; Buschbeck, B.; Schmidt, P.; Valldor, M.; Oswald, S.; Hao, Q.; Lubk, A.; Wolf, D.; Steiner, U.; Büchner, B.; Hampel, S., Chromium Trihalides CrX_3 (X = Cl, Br, I): Direct Deposition of Micro- and Nanosheets on Substrates by Chemical Vapor Transport. *Adv. Mater. Interfaces* **2019,** *6*, 1901410.
32. Yang, H.; Wang, F.; Zhang, H.; Guo, L.; Hu, L.; Wang, L.; Xue, D.-J.; Xu, X., Solution Synthesis of Layered van der Waals (vdW) Ferromagnetic $CrGeTe_3$ Nanosheets from a Non-vdW Cr_2Te_3Template. *J. Am. Chem. Soc.* **2020**, *142*, 4438-4444.
33. Groysman, S.; Villagrán, D.; Nocera, D. G., Pseudotetrahedral d0, d1, and d2 metal–oxo cores within a tris(alkoxide) platform. *Inorg. Chem.* **2010,** *49*, 10759-10761.
34. Schneider, C. A.; Rasband, W. S.; Eliceiri, K. W., NIH Image to ImageJ: 25 years of image analysis. *Nat. Methods* **2012,** *9*, 671-675.

Appendix A: *Supplementary Information for Chapter 2*
Spinodal Decomposition During Anion Exchange in
Colloidal Mn^{2+}-Doped $CsPbX_3$ (X = Cl, Br) Perovskite Nanocrystals

Reproduced with permission from:
De Siena, M. C.; Sommer, D. E.; Creutz, S. E.; Dunham, S. T.; Gamelin, D. R. Chem. Mater. 2019, *31*, 7711-7722.

A.1 Additional elemental analysis.

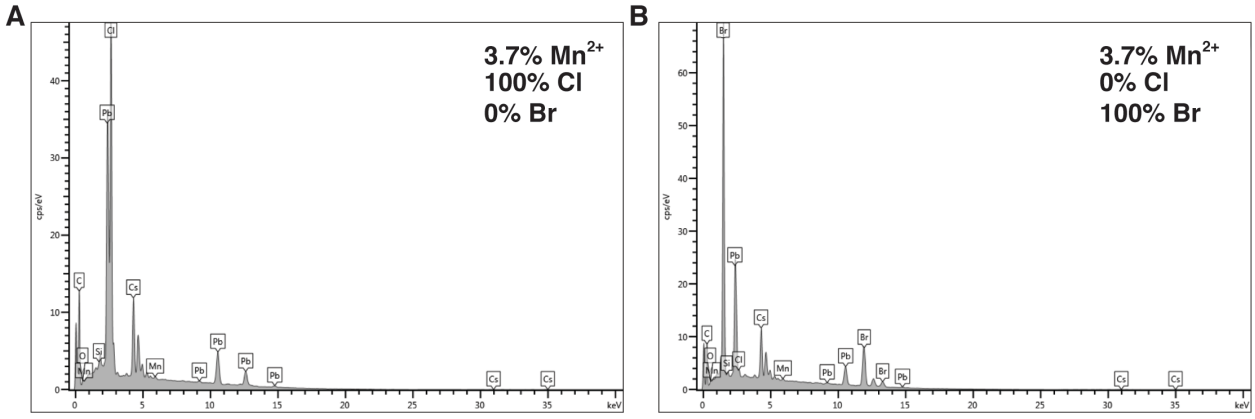

Figure A1. EDX spectra of **(A)** Mn^{2+}:$CsPbCl_3$ NCs, and of **(B)** Mn^{2+}:$CsPbBr_3$ NCs made from these Mn^{2+}:$CsPbCl_3$ NCs *via* anion exchange. The data indicate complete halide exchange and retention of all Mn^{2+} (3.7 % relative to total B-site cations).

A.2 Additional anion and cation exchange results.

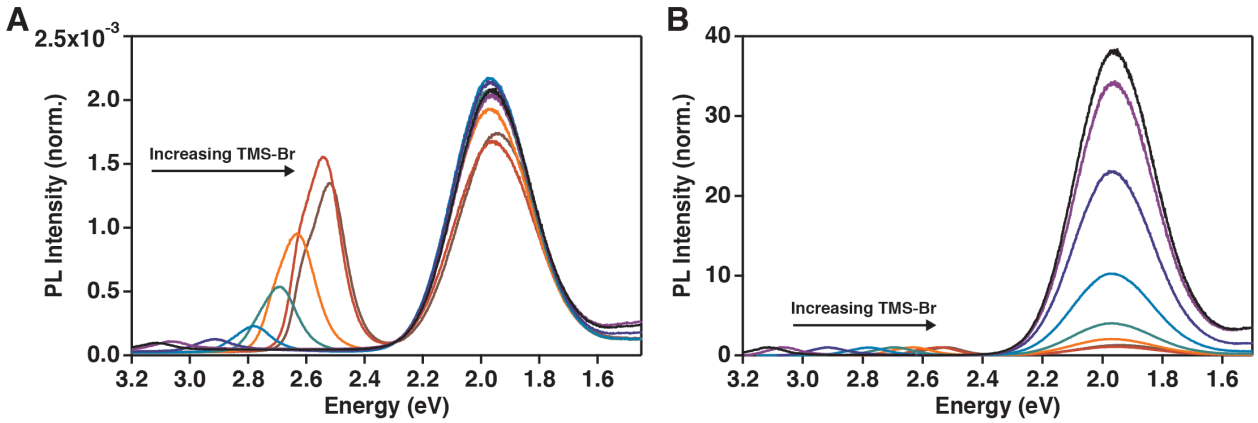

Figure A2. Room-temperature PL spectra of 1.1% Mn^{2+}:$CsPbCl_3$ NCs collected during the course of the anion-exchange reaction from Figure 2.2B, **(A)** normalized to the total integrated PL intensity, and **(B)** normalized to the exciton peak intensity. The NCs were excited at 375 nm.

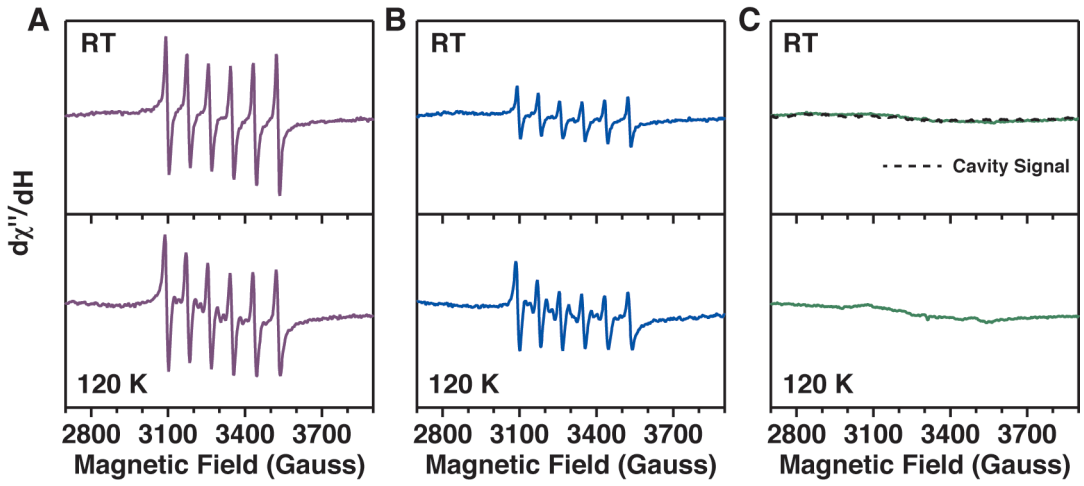

Figure A3. X-band EPR spectra of 1.1% Mn^{2+}:$CsPb(Cl_{1-x}Br_x)_3$ NCs at selected points during the course of a Cl → Br anion-exchange reaction involving Mn^{2+}:$CsPbCl_3$ NCs and TMS-Br. Spectra were measured at both room temperature and 120 K. The spectra in **(A)** correspond to the starting 1.1% Mn^{2+}:$CsPbCl_3$ NCs. The spectra in **(B)** correspond to the same Mn^{2+}:$CsPb(Cl_{1-x}Br_x)_3$ NCs halfway through the Cl → Br anion exchange, with an excitonic peak at 2.71 eV corresponding to x = 0.7. The spectra in **(C)** are from the same NCs after complete anion exchange to Mn^{2+}:$CsPbBr_3$, with an excitonic peak at 2.51 eV. The room-temperature EPR cavity signal is also plotted in (C) as a dashed line. The y-axis is the same for all plots.

The low-temperature EPR spectra in (A) and (B) show additional hyperfine lines that most likely arise from a zero-field splitting. Additionally, there are no new EPR features upon cooling in any of these three samples. This latter result suggests that there are most likely no other Mn^{2+} species that are relaxing to quickly to be observed at room temperature, and hence that the loss of EPR intensity during anion exchange is not associated with the formation of new Mn^{2+} species that are independent of the NCs.

Mn^{2+} incorporation from solution during Cl^- → Br^- anion exchange

Figure A4 summarizes the PL and EPR spectra of undoped $CsPbCl_3$ measured before and after conversion to $CsPbBr_3$, performing the reaction in the presence of solvated $Mn(oleate)_2$ at a concentration that reflects the total amount of Mn^{2+} in the NC sample of Figure 2.3. $Mn(oleate)_2$ was chosen because oleic acid and oleylamine were used in the NC synthesis and, with no other soluble anions present, these would be the most likely ligands available to any Mn^{2+} ejected from the NCs during anion exchange. When $Mn(oleate)_2$ is added to a solution of $CsPbCl_3$ NCs, the Mn^{2+} incorporates into the NC, as evidenced by appearance of the characteristic Mn^{2+} *d-d* luminescence and EPR signal discussed above. When $Mn(oleate)_2$ is instead added to $CsPbBr_3$ NCs, we observe no changes in either the PL or EPR spectra. Figure A5 shows the EPR spectrum of $Mn(oleate)_2$; this

spectrum only becomes measurable at concentrations that are several orders of magnitude greater than the ones used in this experiment. This spectrum is heavily broadened and suggests that in solution $Mn(oleate)_2$ forms aggregates that have short T_1 relaxation times, making the species difficult to detect at the concentrations used in the experiment. This comparison suggests that if Mn^{2+} were indeed ejected from the NCs upon anion exchange then there would not be sufficient Mn^{2+} in solution to observe by EPR under these conditions. No sensitized Mn^{2+} PL would be observed in this case, either, however. $Mn(oleate)_2$ does not display detectable Mn^{2+} *d-d* luminescence when excited with 405 nm light under these conditions, in contrast with the fully anion-exchanged NCs. These results support the conclusion drawn above that Mn^{2+} ejection from the NCs during anion exchange cannot explain the observations in Figure 2.3.

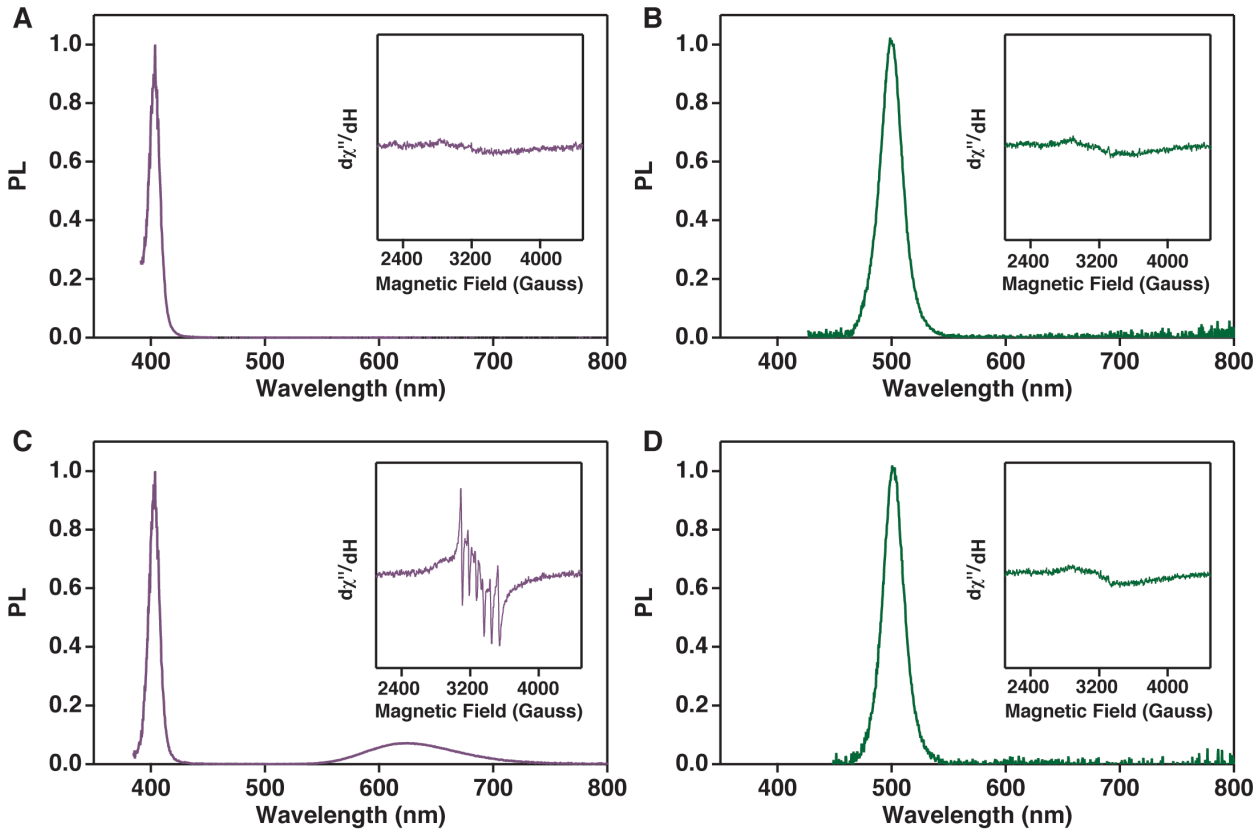

Figure A4. **(A)** Room-temperature PL spectra and X-band EPR spectra (inset) for undoped $CsPbCl_3$ NCs. There is only excitonic PL and no EPR signal is observed. **(B)** Room-temperature PL spectra and X-band EPR spectra (inset) for undoped $CsPbBr_3$ NCs made from the sample in (A) by anion exchange with TMS-Br. Only excitonic PL is observed and no EPR signal. **(C)** Room temperature PL spectra and X-band EPR spectra (inset) for undoped $CsPbCl_3$ NCs with the addition of $Mn(oleate)_2$. Both excitonic and Mn^{2+} *d-d* PL are observed. Also, a Mn^{2+} EPR signal is observed with a hyperfine splitting constant of $80.9x10^{-4}$ cm^{-1} consistent with *in situ* formation of Mn^{2+}:$CsPbCl_3$ NCs. **(D)** Room-temperature PL spectra and X-band EPR spectra (inset) of undoped $CsPbBr_3$ NCs with added $Mn(oleate)_2$ made from the sample in (A) by anion exchange using TMS-Br. Only excitonic PL is observed. No Mn^{2+} PL or EPR signal is observed. In all samples, the NC concentration is kept constant and is the same as the concentration of NCs used in the Mn^{2+}:$CsPbCl_3$ EPR titration experiments described in Chapter 2. The amount of $Mn(oleate)_2$ added in (C) and (D) corresponds to the amount of Mn^{2+} in the Mn^{2+}:$CsPbCl_3$ NCs used for the EPR experiments described in Chapter 2. The *y*-axes of the EPR spectra are the same for all spectra, corrected for the Q value, allowing quantitative comparison.

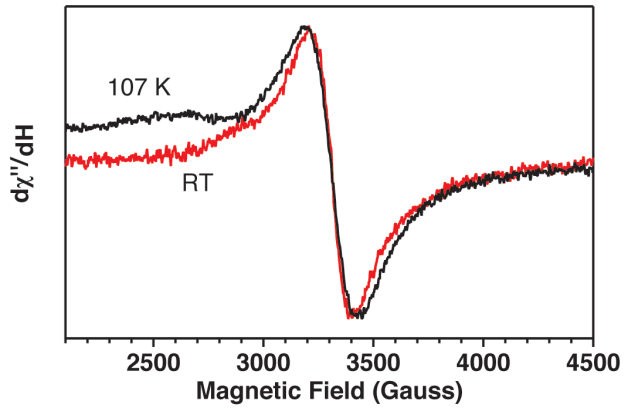

Figure A5. X-band EPR spectra of 100 μM $Mn(oleate)_2$ dissolved in 3-methylpentane, measured at both room-temperature and 107 K. Only one broad transition is observed, suggesting that $Mn(oleate)_2$ is most likely aggregated in this solvent.

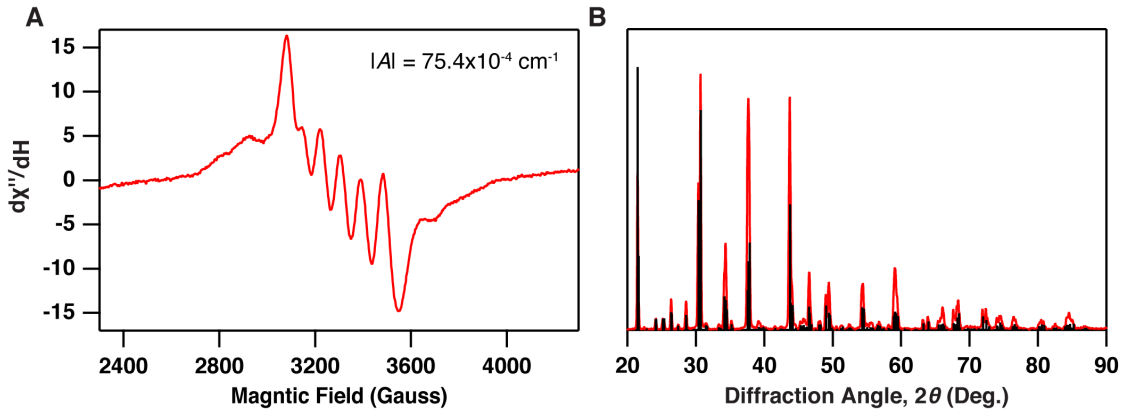

Figure A6. (A) Room-temperature X-band EPR spectra of 0.1% Mn^{2+}:$CsPbBr_3$ bulk powder. The spectrum shows a resonance at g = 2.0, split into six sharp Mn^{2+} hyperfine lines with a hyperfine coupling constant of 75.4×10^{-4} cm^{-1}. **(B)** Powder X-ray diffraction data collected for 0.1% Mn^{2+}:$CsPbBr_3$ bulk on a silicon substrate (red) and corresponding literature pattern for orthorhombic $CsPbBr_3$ phase (black). The data match the expected peak pattern.

A.3 Additional variable-temperature photoluminescence results and analysis

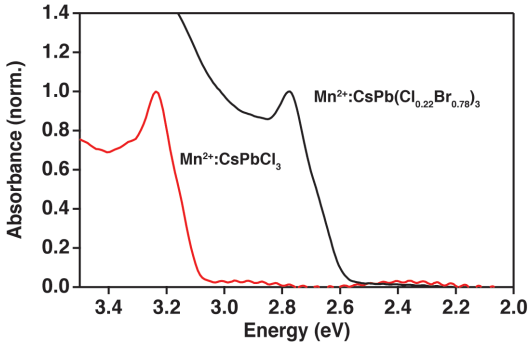

Figure A7. Room-temperature absorption spectra of Mn^{2+}:$CsPbCl_3$ and Mn^{2+}:$CsPb(Cl_{1-x}Br_x)_3$ NCs. These NCs were used to measure the PL decay curves and spectra presented in Figure 2.3. The composition parameter in the alloyed sample is estimated from these peak energies to be x = 0.78.

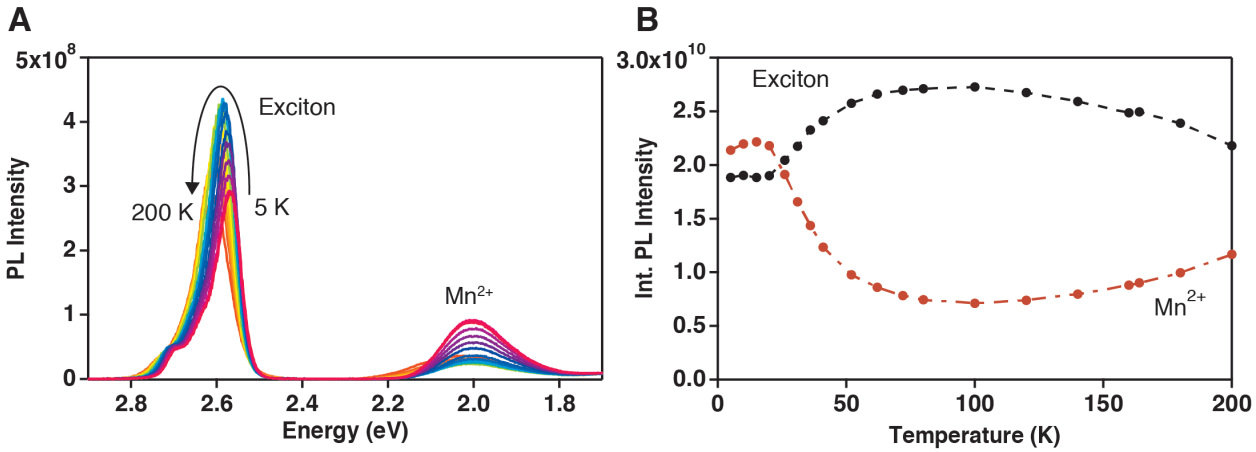

Figure A8. (A) Variable-temperature PL spectra of 1.1% Mn^{2+}:$CsPb(Cl_{1-x}Br_x)_3$ (x = 0.78) NCs. **(B)** Summary of the integrated intensities of the excitonic and Mn^{2+} PL features over this temperature range. The NCs were excited at 405 nm.

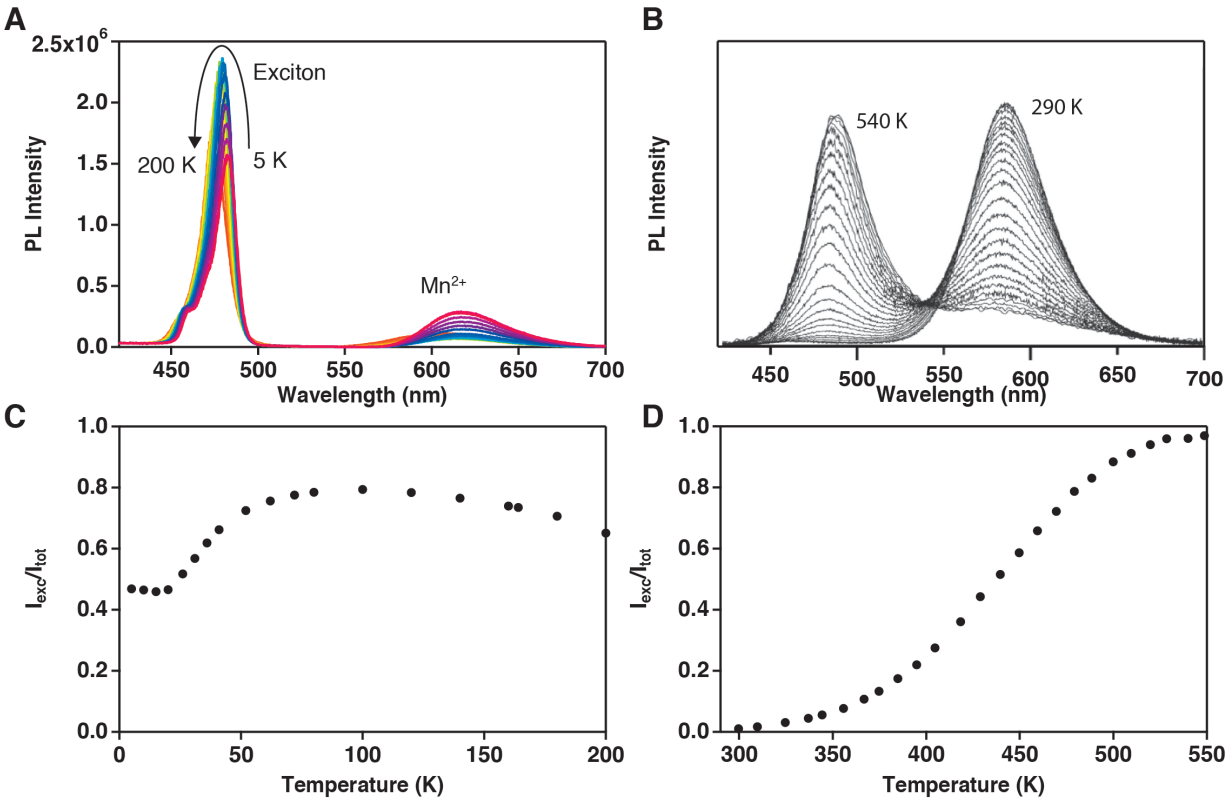

Figure A9. Variable-temperature PL spectra of **(A)** 1.1% Mn^{2+}:$CsPb(Cl_{1-x}Br_x)_3$ (x = 0.78) and **(B)** $Zn_{1-x}Mn_xSe$/ZnS/CdS/ZnS NCs. Temperature dependence of the integrated excitonic PL intensity normalized to the total integrated PL intensity for **(C)** 1.1% Mn^{2+}:$CsPb(Cl_{1-x}Br_x)_3$ (x = 0.78) and **(D)** $Zn_{1-x}Mn_xSe$/ZnS/CdS/ZnS NCs. Panels B and D adapted with permission from Ref. 1. Copyright 2011 American Chemical Society.

A.4 Additional simulation results

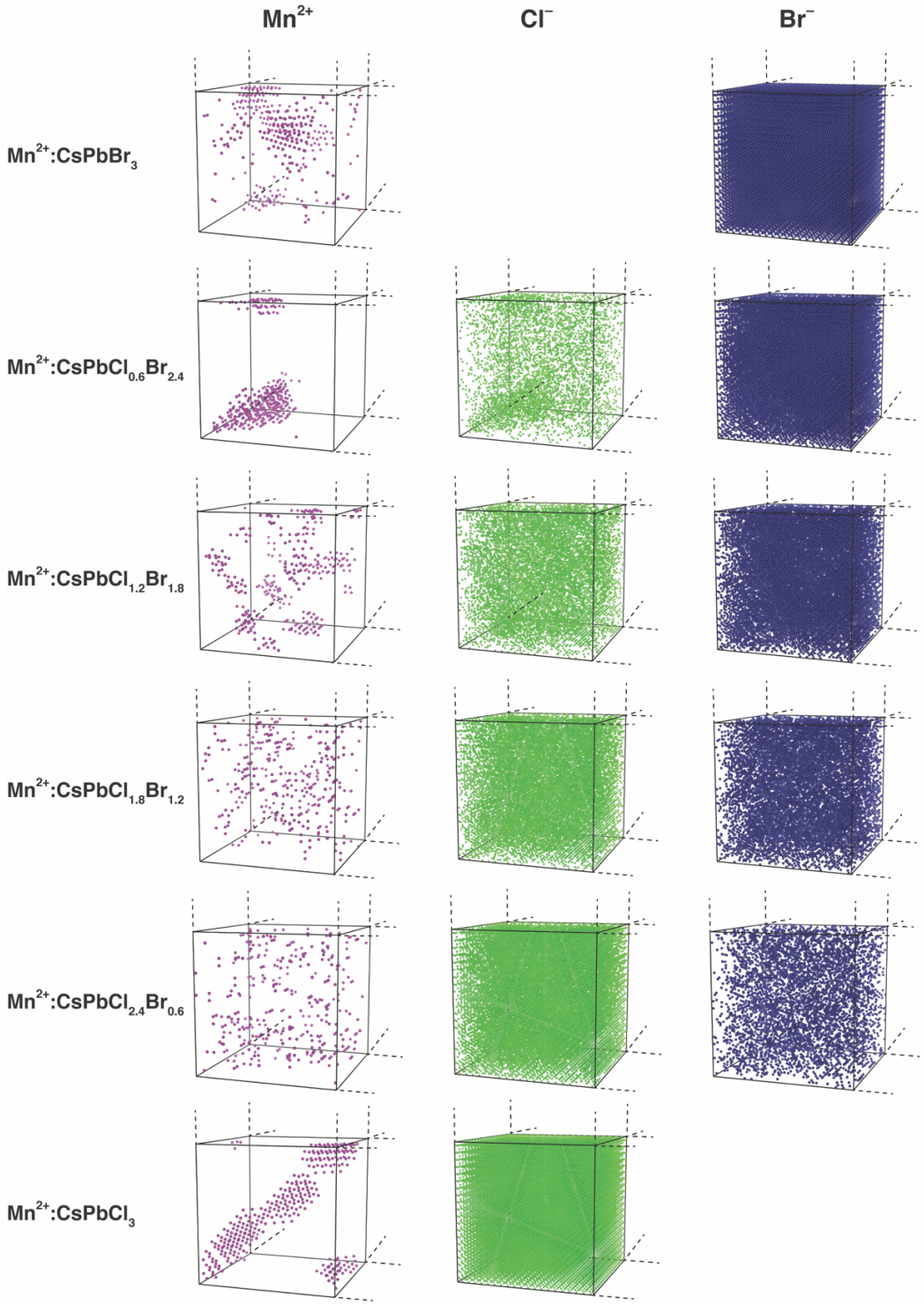

Figure A10. Room-temperature equilibrium atomic distributions within a 4% Mn^{2+}:$CsPbX_3$ supercell predicted by canonical Monte Carlo simulation. The distributions for Mn^{2+}, Cl^-, and Br^- ions are shown at specific halide concentrations corresponding to different extents of anion exchange.

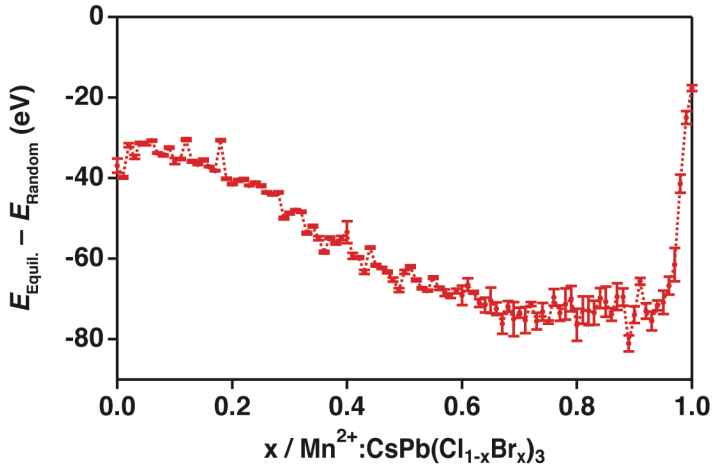

Figure A11. Energy minimization trajectory plotting the energy difference between random and equilibrium configurations predicted by canonical Monte Carlo simulation for varying halide composition with 4% Mn^{2+}. Each data point characterizes the degree to which the equilibrium configurations are stabilized by short-range ordering.

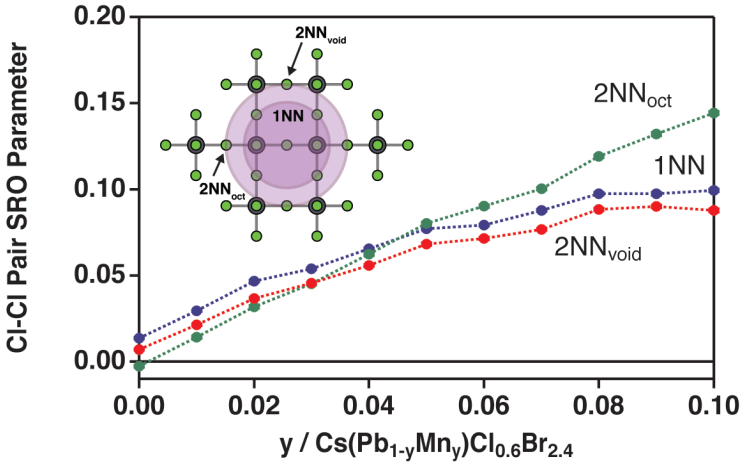

Figure A12. Short-range order (SRO) parameters, $\eta_i^{(Cl|Cl)}$, for Cl^- pairs under varying Mn^{2+} doping as predicted by canonical Monte Carlo simulation with 20% Cl^-. The lower bound for $\eta_i^{(A|A)}$ is not shown for the sake of scale. Chloride clustering is found to increase for increasing Mn^{2+} incorporation. Pairing on 2NN (oct) sites in the same halide octahedron coordinating Pb/Mn sites becomes dominant past 5% Mn^{2+}, compared to 2NN (void) sites on distinct octahedra. The inset shows the 1NN and two different 2NN sites around a central anion with chloride ions in green and lead/manganese ions in gray.

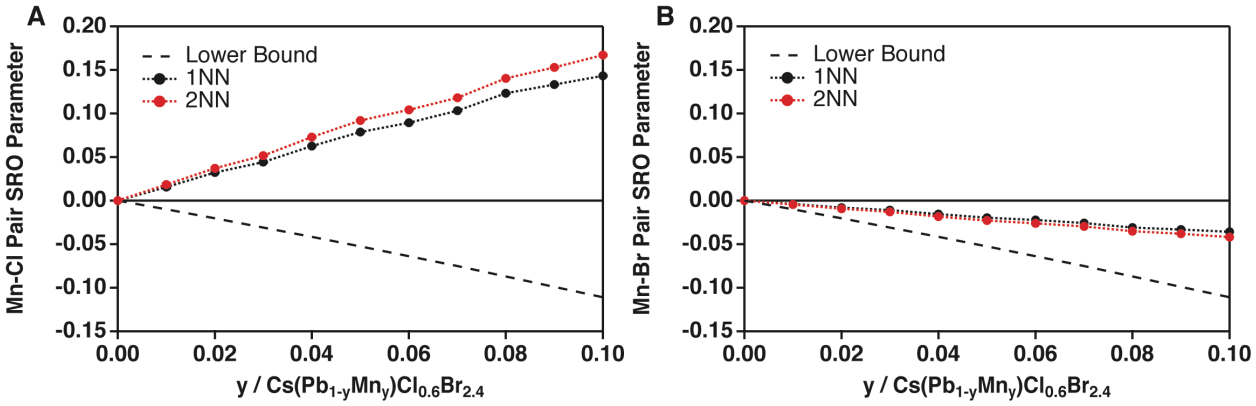

Figure A13. Short-range order (SRO) parameters $\eta_i^{(\mathrm{X}|Mn)}$ for Cl^--Mn^{2+} pairs **(A)** and Br^--Mn^{2+} pairs **(B)** under varying Mn^{2+} doping as predicted by canonical Monte Carlo simulation with 20% Cl^-. These results show that Cl^--Mn^{2+} pairs are correlated and that Br^--Mn^{2+} pairs are anticorrelated suggesting that Mn^{2+} has a propensity to cluster into regions of high chloride content.

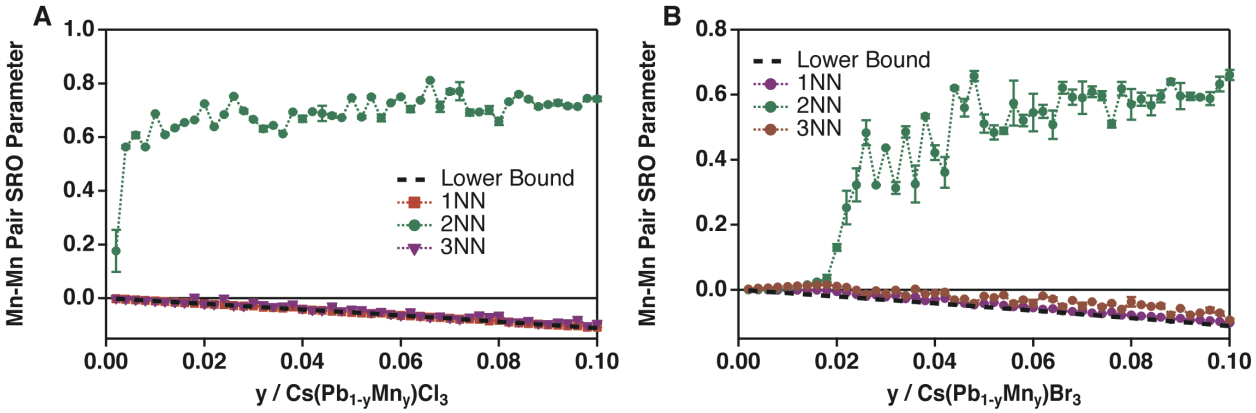

Figure A14. Short-range order (SRO) parameters, $\eta_i^{(\mathrm{Mn}|\mathrm{Mn})}$, for Mn^{2+} pairs under varying Mn^{2+} doping in pure $CsPbCl_3$ **(A)** and pure $CsPbBr_3$ **(B)** as predicted by canonical Monte Carlo simulation. Mn^{2+} clusters with 2NN SRO are found to nucleate, *via* spinodal decomposition, at very dilute Mn^{2+} concentrations in $CsPbCl_3$ and at approximately 1.75% Mn^{2+} concentrations in $CsPbBr_3$.

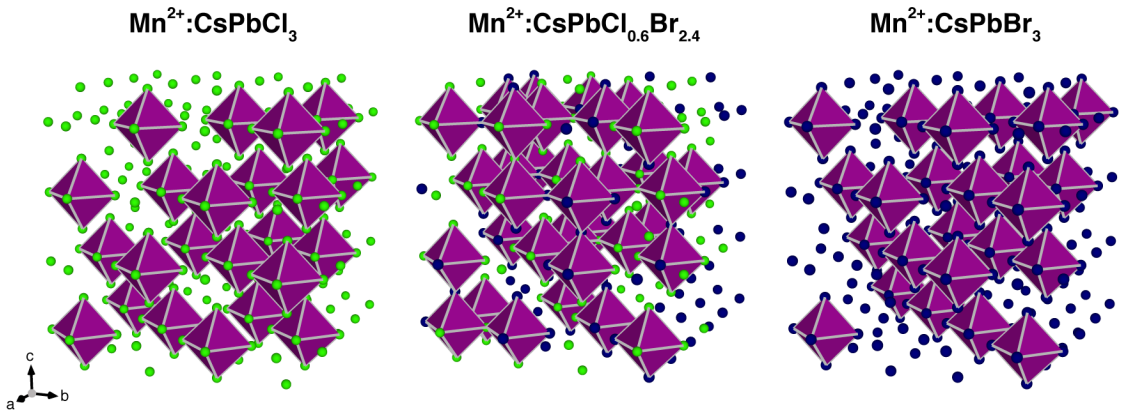

Figure A15. Room temperature equilibrium distribution of atoms within regions of high Mn^{2+} concentrations within a 4% Mn^{2+}:$CsPbX_3$ supercell predicted by canonical Monte Carlo simulation. For simplicity only Mn^{2+} octahedra (fuchsia) and halide atoms (chloride, green; bromide, blue) are shown. In both the pure chloride and bromide supercells, the Mn^{2+} 2NN ordering is seen as independent Mn^{2+} octahedra. In the mixed halide alloy sample there is no strong ordering at the 2NN and Mn^{2+} octahedra will share corners.

A.5 ^{133}Cs solid-state NMR results and analysis

A recent report described the use of ^{133}Cs NMR to study the possibility of Mn^{2+} cluster formation in Mn^{2+}:$CsPbX_3$ (X = Cl, Br) bulk powders (Ref. 33 of Chapter 2). We applied the same methodology to our Mn^{2+}:$CsPbCl_3$ and anion-exchanged Mn^{2+}:$CsPbBr_3$ NCs in an attempt to gain additional insight into Mn^{2+} clustering. T_1 relaxation times of the ^{133}Cs nuclei were measured using saturation-recovery methods as described in the experimental section in Chapter 2. Proximity to a paramagnetic Mn^{2+} ion should be reflected in a shortened T_1 time for ^{133}Cs nuclei due to the paramagnetic relaxation enhancement (PRE) effect; this effect decays with distance as $1/r^6$, making it an intimate reporter of the local environment around a nucleus.

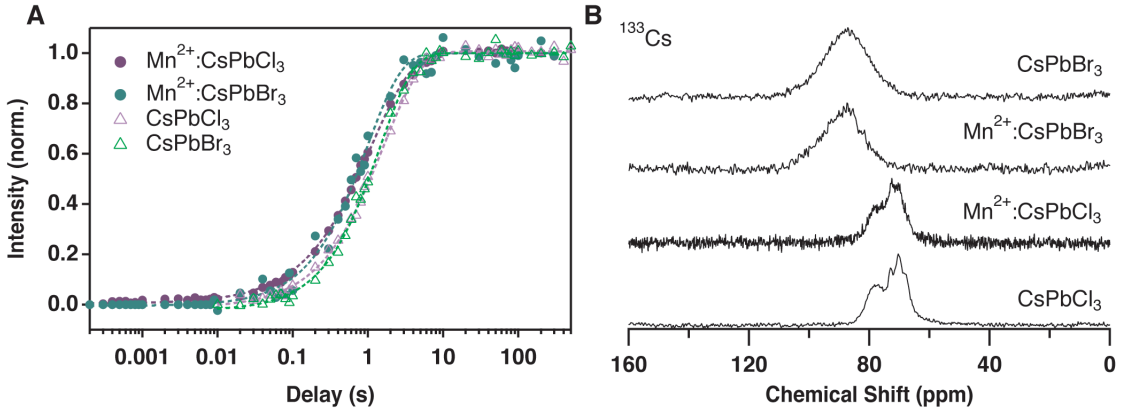

Figure A16. (A) ^{133}Cs T_1 build-up curves for 1% Mn^{2+}-doped and undoped perovskite NCs measured by saturation-recovery methods. **(B)** Corresponding ^{133}Cs NMR spectra collected at 16.5 T, 3 kHz MAS, and 298 K.

Because Mn^{2+} doping should lead to a distribution of Cs-Mn distances and thus a distribution of relaxation times, the saturation-recovery curves in Figure S14A were fit using a stretched-exponential function:

$$I(\tau) = y_0 + Ae^{-\left(\frac{\tau}{T_1}\right)^{\beta}} \quad \text{(A1)}$$

Here, the stretching factor β provides a metric for the distribution of relaxation times. For a system where all the ^{133}Cs nuclei have the same T_1 (*e.g.*, bulk $CsPbBr_3$, see Table S1), $\beta = 1$. A value of $\beta = 0.5$ has been shown theoretically to correspond to a random distribution of paramagnetic dopants in the absence of spin diffusion.[2] Therefore, successful fitting to a stretched exponential with β values close to 0.5 can be taken as evidence of a random or near-random dopant distribution. On the other hand, the presence of large paramagnetic $CsMnX_3$ clusters should manifest itself as a distinct double exponential or some more complex behavior.

Table A1. Average ^{133}Cs T_1 relaxation times of 1% Mn^{2+}:$CsPbCl_3$ NCs and 1% Mn^{2+}:$CsPbBr_3$ NCs, the latter synthesized by anion exchange, compared to undoped NCs and bulk materials from the literature.

Material	^{133}Cs T_1 (s)	Stretching Parameter, β	Reference
$CsPbCl_3$ NCs	1.62 ± 0.04	0.862 ± 0.024	this work
$CsPbCl_3$ bulk	45.9 ± 0.1	0.941 ± 0.002	Ref. 33 of Chapter 2
Mn^{2+}:$CsPbCl_3$ NCs	1.12 ± 0.02	0.805 ± 0.012	this work
$CsPbBr_3$ NCs	1.44 ± 0.04	0.972 ± 0.037	this work
$CsPbBr_3$ bulk	109 ± 1	0.999 ± 0.007	Ref. 33 of Chapter 2
Mn^{2+}:$CsPbBr_3$ NCs	0.98 ± 0.05	0.935 ± 0.062	this work

Our measurements of the ^{133}Cs NMR immediately revealed T_1 times for undoped $CsPbCl_3$ and $CsPbBr_3$ nanocrystals that are much shorter (by almost two orders of magnitude) than those measured in bulk. This result is perhaps not surprising because accelerated spin-lattice relaxation in smaller grain sizes is a known phenomenon.[3-5] To the best of our knowledge, there are no reported systematic studies of T_1 NMR relaxation times in colloidal perovskite nanocrystals. These short relaxation times for the undoped nanocrystals means that PRE effects from the Mn^{2+} dopants are less readily observed, and detailed interpretation of our saturation-recovery curves (Figure A16A) was consequently not possible. As expected, we do see shorter average T_1 times in our doped nanocrystals compared to the undoped nanocrystals, but the difference is relatively small due to the already short T_1 times of the latter. If our hypothesis of Mn^{2+} clustering in anion-exchanged Mn^{2+}:$CsPbBr_3$ were correct, we might expect to observe biexponential curves rather than stretched exponentials. We do

see a β factor closer to 1 in our fit of the Mn^{2+}:$CsPbBr_3$ nanocrystal data (see Table A1) relative to the Mn^{2+}:$CsPbCl_3$ nanocrystal fit, consistent with this hypothesis, but we also observe a similar difference between the undoped $CsPbCl_3$ and $CsPbBr_3$ nanocrystals. The origin of this behavior is not yet clear. Overall, these NMR measurements do not provide any clear evidence in favor of or against the hypothesized Mn^{2+}-rich minority phase.

A.6 References

1. McLaurin, E. J.; Vlaskin, V. A.; Gamelin, D. R., Water-Soluble Dual-Emitting Nanocrystals for Ratiometric Optical Thermometry. J. Am. Chem. Soc. 2011, 133, 14978-14980.
2. Tse, D.; Hartmann, S. R., Nuclear Spin-Lattice Relaxation Via Paramagnetic Centers Without Spin Diffusion. Phys. Rev. Lett. 1968, 21, 511-514.
3. Scholz, G.; Dörfel, I.; Heidemann, D.; Feist, M.; Stösser, R., Nanocrystalline CaF2 particles obtained by high-energy ball milling. J. Solid State Chem. 2006, 179, 1119-1128.
4. Abdellatief, M.; Abele, M.; Leoni, M.; Scardi, P., Solid State Nuclear Magnetic Resonance and X-ray Diffraction Line Profile Analysis of heavily deformed fluorite. Thin Solid Films 2013, 530, 44-48.
5. Dempah, K. E.; Lubach, J. W.; Munson, E. J., Characterization of the Particle Size and Polydispersity of Dicumarol Using Solid-State NMR Spectroscopy. Mol. Pharm. 2017, 14, 856-865.

Appendix B: *Supplementary Information for Chapter 3*
Conduction Band Splittings and Impurity Doping in Colloidal Europium(II) Monochalcogenide Nanocrystals

B.1 Additional characterization for Chapter 3, Section 3.2

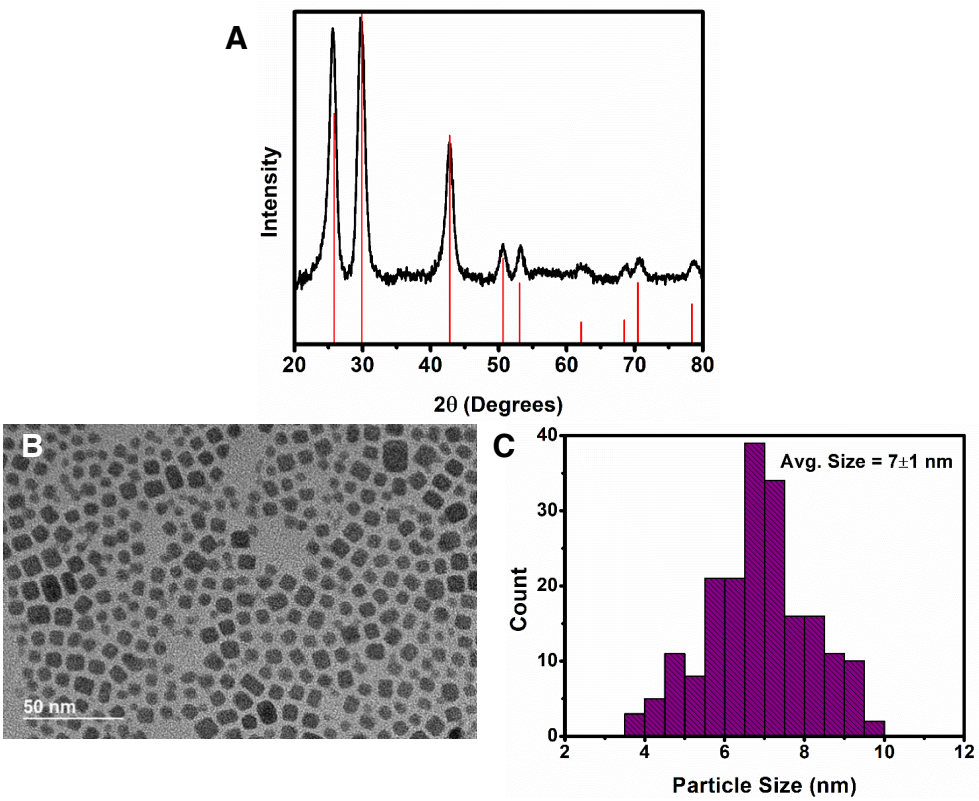

Figure B1. X-ray Powder Diffraction Pattern **(A)** and Transmission Electron Microscopy of EuS nanocrystals **(B)** with histogram (171 counts) **(C)**.

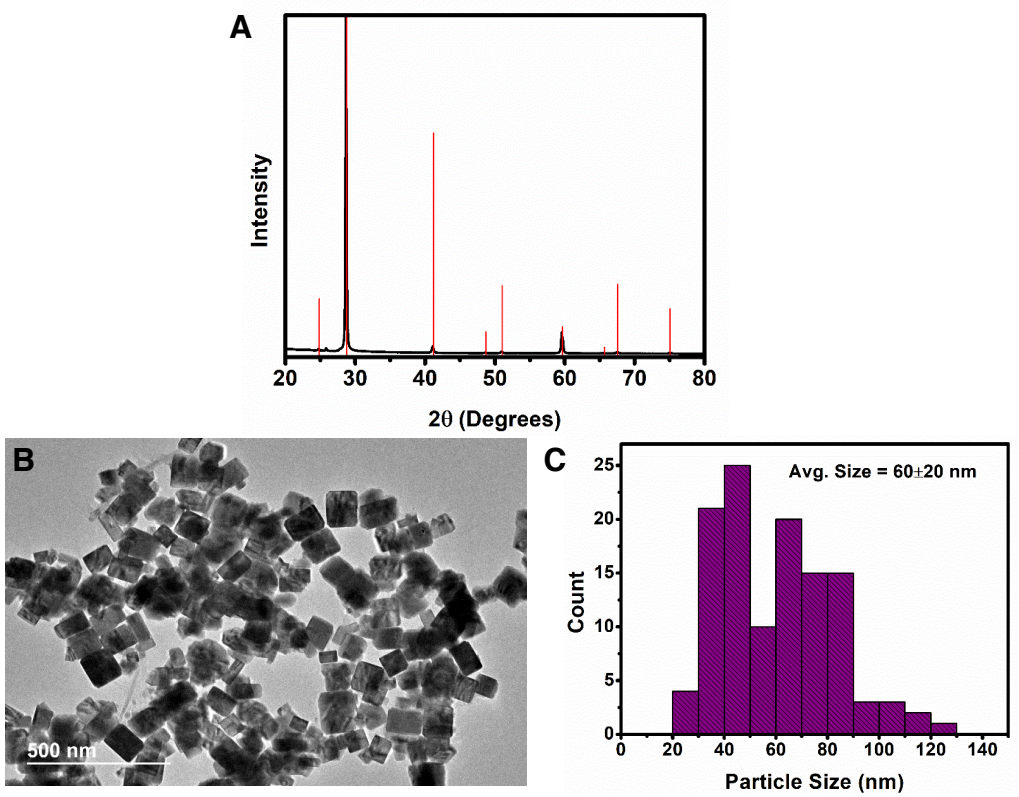

Figure B2. X-ray Powder Diffraction Pattern **(A)** and Transmission Electron Microscopy **(B)** of EuSe nanocrystals with histogram (176 counts) **(C)**.

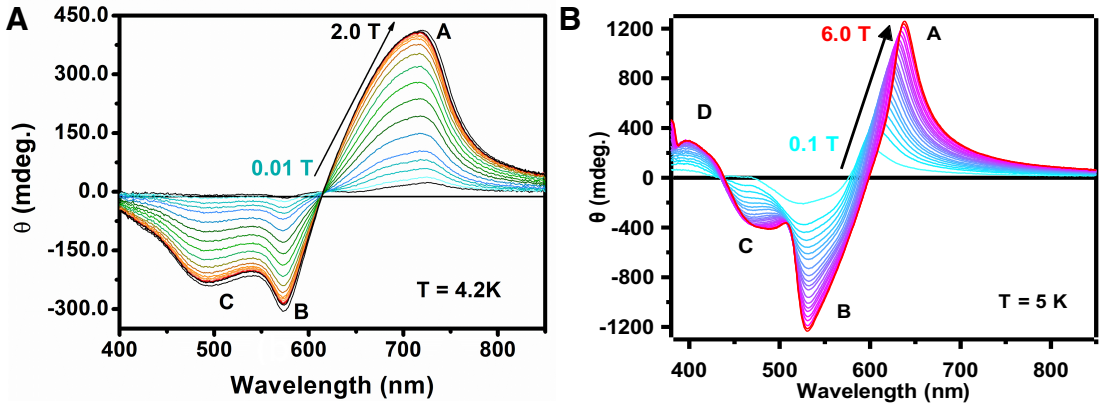

Figure B3. Normalized Field-Dependent MCD spectra of **(A)** EuS nanocrystals at 4.2K and **(B)** EuSe nanocrystals at 5K.

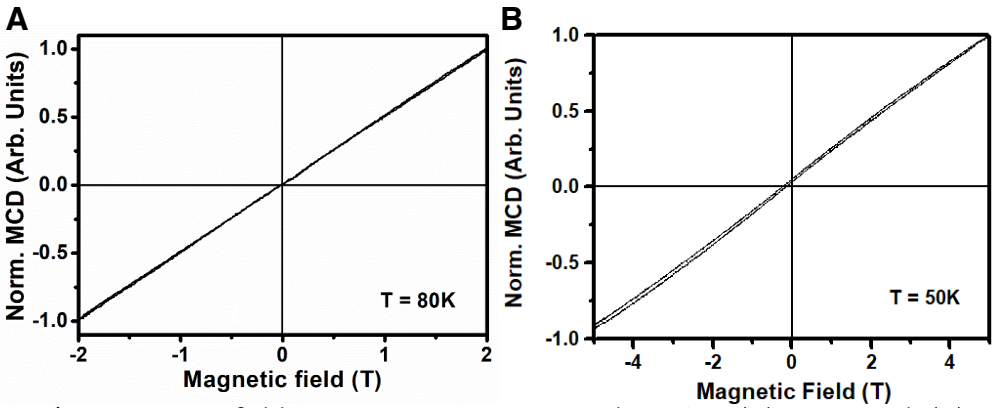

Figure B4. Magnetic field versus MCD intensity above Tc **(A)**: EuS and **(B)**: EuSe nanocrystals).

B.2 Additional characterization for Chapter 3, Section 3.3

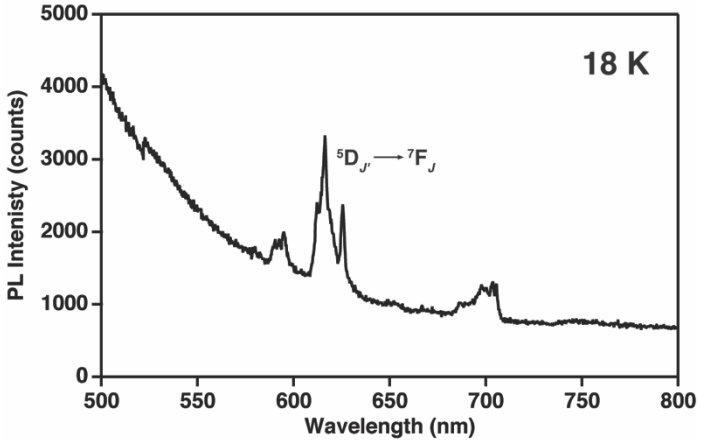

Figure B5. Representative photoluminescence spectrum of EuS nanocrystals. The main transition centered at ~620 nm are assigned to the *f–f* transitions of Eu^{3+}. This suggests the sample contains Eu^{3+} defects. Notably, there is no broadband luminescence that is typical of either EuS[1] or Eu^{2+}:CaS.[2] The broad tail of a higher energy feature is seen and this feature is tentatively assigned to either ligand emission or some other trap in the nanocrystals. The sample temperature is 18 K.

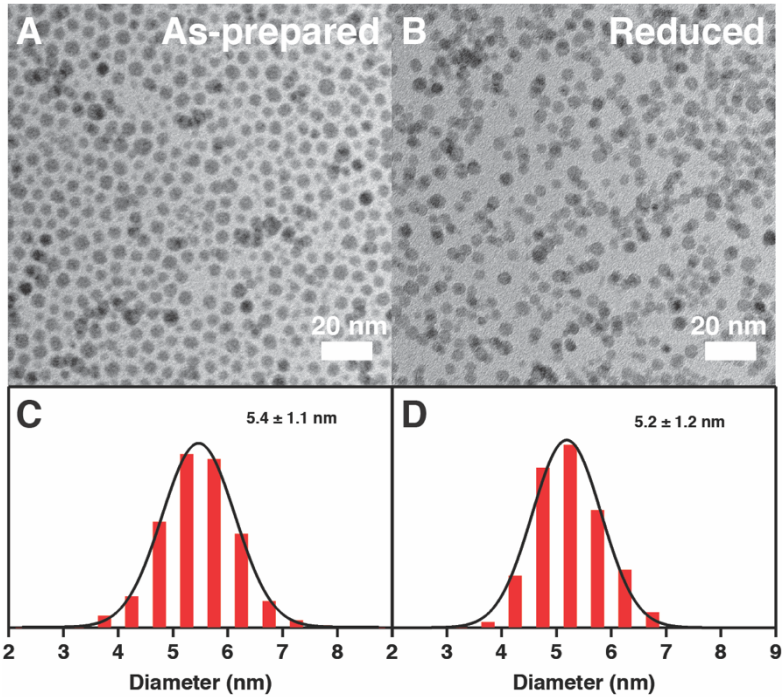

Figure B6. TEM images and corresponding size distributions of EuS nanocrystals before and after reduction with sodium anthracenide. There is no obvious change to the morphology of the EuS NCs after the reduction experiments as seen in the images for the as-prepared **(A)** and reduced **(B)** NCs. Likewise, there is no significant change to the size distribution between the as-prepared **(C)** and reduced **(D)** NCs. This suggests that the reductant is not etching or destroying the NCs in some other way.

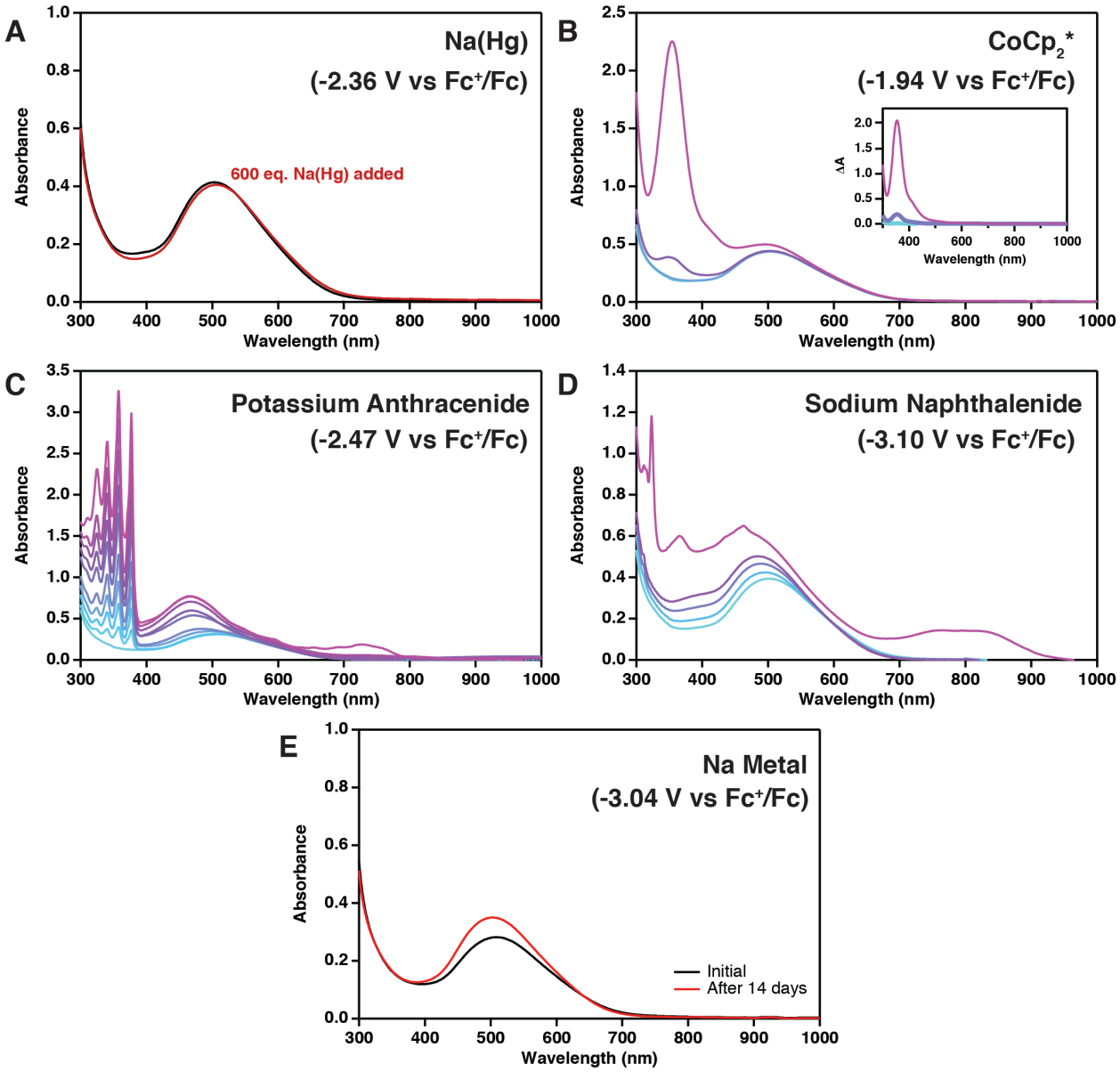

Figure B7. Reduction behavior of EuS nanocrystals with varied common reductants. The EuS nanocrystals do not show any reduction behavior when the strength of the reductant is insufficient as seen with both 0.5% Na(Hg) **(A)** and with $CoCp_2^*$ **(B)**. The inset shows the change in absorption with added $CoCp_2^*$ and is consistent with the absorption of pure $CoCp_2^*$ suggesting that the absorption change in the sample is not the result of reduced EuS NCs. In **(C)** reduction behavior is observed with potassium anthracenide. This reductant does not show any significant differences in behavior to sodium anthracenide as discussed in Chapter 3, Section 3.3. Even stronger reductants such as sodium naphthalenide **(D)** and sodium metal in THF **(E)** result in the typical reduction behavior of EuS NCs. It is noted that the reduction of EuS with sodium metal is considerably slower that the homogeneous reductants most likely attributed to its heterogeneous nature. Strengths of reductants are taken from the literature and given in each panel.[3]

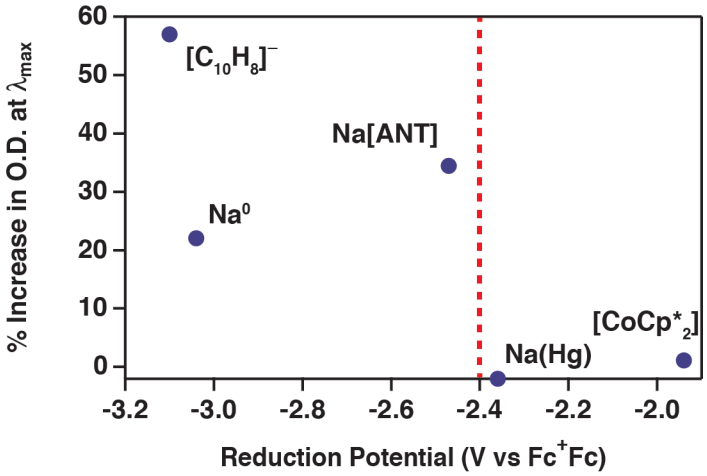

Figure B8. Summary of reduction behavior of EuS nanocrystals with varied common reductants plotting the percent increase in the optical density at λ_{max} of the *f–d*(t_{2g}) transition vs the standard reduction potentials[3] of the reductants used here. The red vertical line is a guide to the eye for the cutoff region for reduction of EuS NCs.

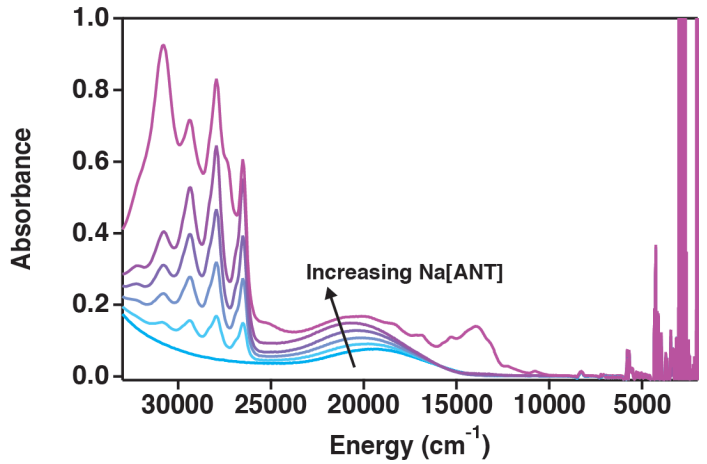

Figure B9. UV-Vis-MIR absorption spectra of EuS nanocrystals during chemical reduction using sodium anthracenide. There is no new NIR intraband or plasmonic band observed during this reduction process.

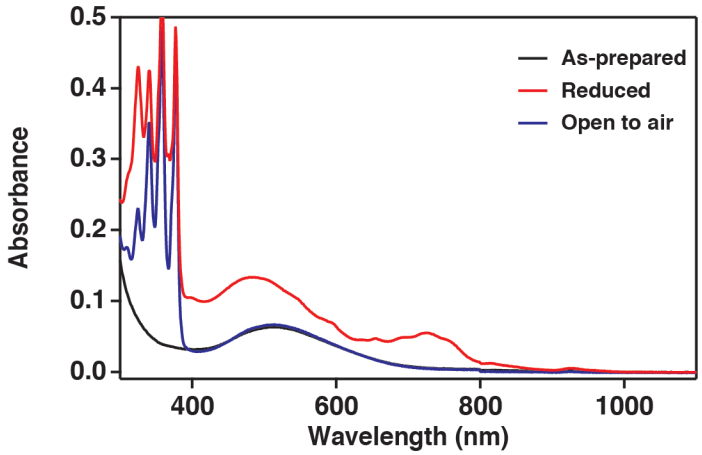

Figure B10. Absorption spectra for as-prepared EuS NCs (black), maximally reduced (red), and upon exposure to air (blue). After air exposure, the as-prepared absorption spectrum is recovered with the added absorption between 300 – 400 nm attributed to anthracene. This illustrates the reversibility of this reduction process.

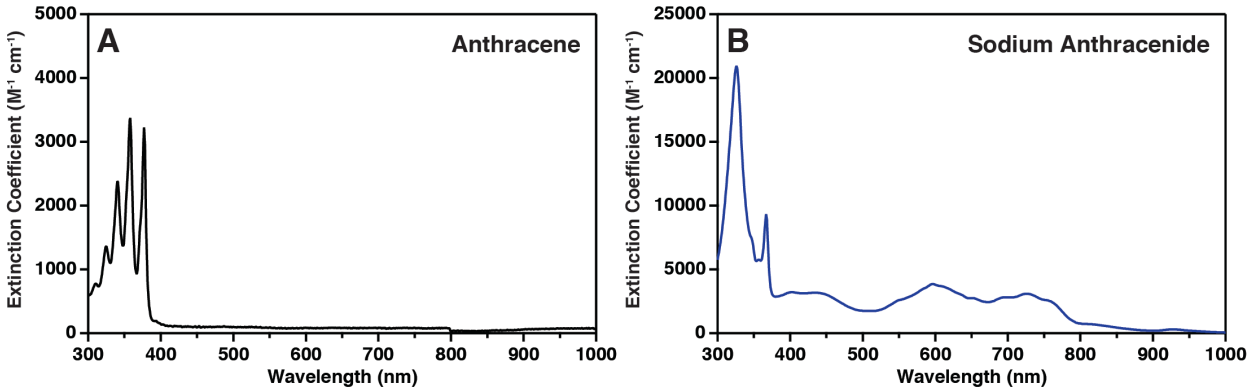

Figure B11. Optical extinction spectra for anthracene **(A)** and sodium anthracenide **(B)**. The extinction coefficients were taken from these spectra for determining the concentrations of reductant needed for approximating the Fermi energy of the system.

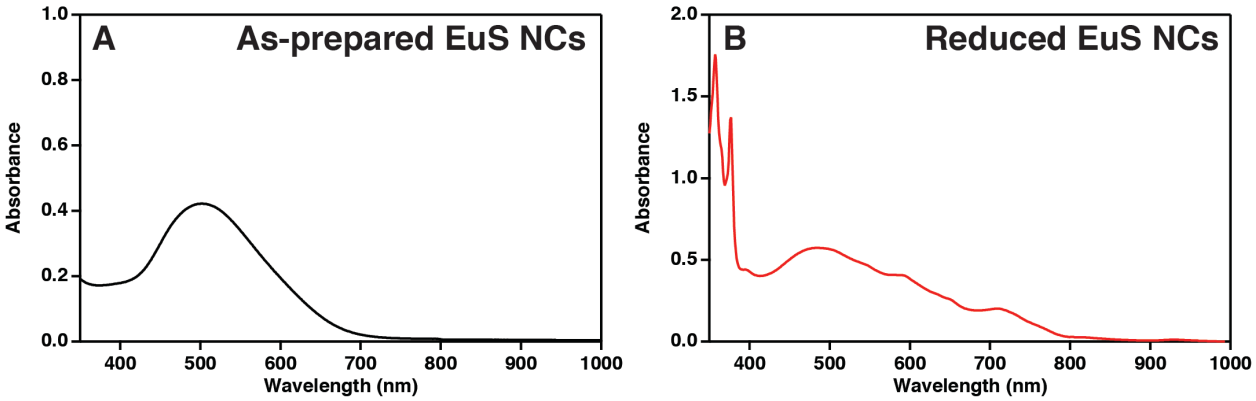

Figure B12. Absorption of the as-prepared **(A)** and reduced **(B)** EuS sample used for the EPR measurements. The reduced sample clearly shows the characteristic increase in the intensity and slight blue-shift of the *f–d* transition (centered at ~490 nm) as well as the sodium anthracenide transition (seen at 750 nm). Both samples used for EPR measurements have the same concentration of EuS NCs.

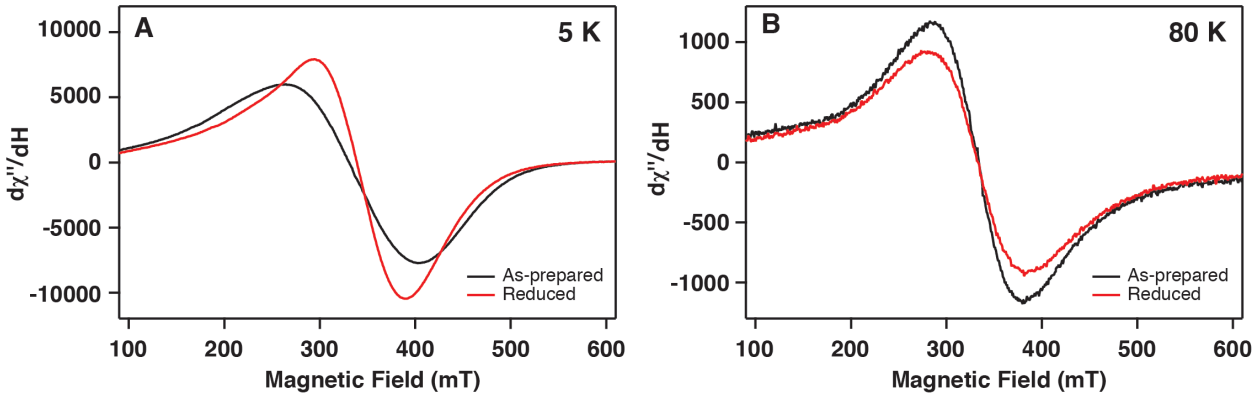

Figure B13. Representative EPR spectra of as-prepared and reduced EuS NCs collected at 5 **(A)** and 80 K **(B)**.

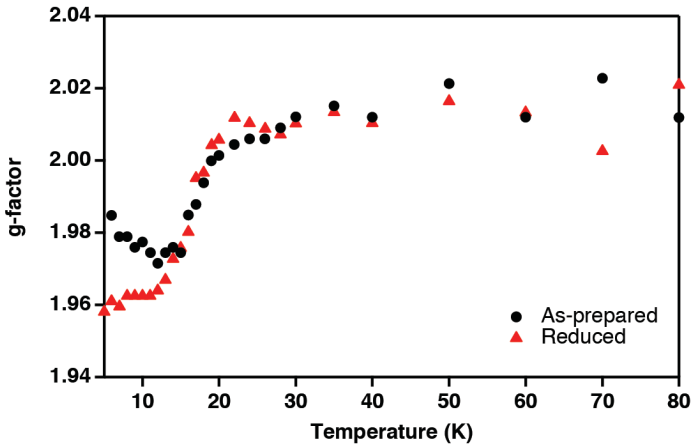

Figure B14. Temperature-dependence of the EPR *g* factor for as-prepared and reduced EuS NCs. The *g* factors of both the as-prepared and reduced NCs sharply decrease in the critical region.

B.3 References

1. Chen, W.; Zhang, X.; Huang, Y. Luminescence enhancement of EuS nanoclusters in zeolite. *Appl. Phys. Lett.* **2000,** *76*, 2328-2330.
2. Zhao, Y.; Rabouw, F. T.; van Puffelen, T.; van Walree, C. A.; Gamelin, D. R.; de Mello Donegá, C.; Meijerink, A. Lanthanide-Doped CaS and SrS Luminescent Nanocrystals: A Single-Source Precursor Approach for Doping. *J. Am. Chem. Soc.* **2014,** *136*, 16533-16543.
3. Connelly, N. G.; Geiger, W. E. Chemical Redox Agents for Organometallic Chemistry. *Chem. Rev.* **1996,** *96*, 877-910.

Appendix C: *Supplementary Information for Chapter 4* Two-Dimensional van der Waals Nanoplatelets with Robust Ferromagnetism

Reproduced with permission from:
De Siena, M. C.; Creutz, S. E.; Regan, A.; Malinowski, P.; Jiang, Q.; Kluherz, K. T.; Zhu, G.; Lin, Z.; De Yoreo, J. J.; Xu, X.; Chu, J.-H.; Gamelin, D. R. Nano Lett. 2020, *20*, 2100-2106.

C.1 Additional description of the synthesis of CrI_3 nanoplatelets. Attempts to synthesize CrX_3 using, e.g., Cr(III) acetylacetonate, Cr(III) nitrate, or "Cr(III) acetate"[1] in carboxylate and amine surfactants either gave no readily isolable product, formed unidentified amorphous precipitates, or formed chromium oxide.[2] In most cases, we observed no reaction or even dissolution of these simple precursors until very high temperatures (>330 °C) were reached and sustained for extended periods.

By contrast, CrX_3 nanocrystals could be successfully prepared using $Cr(OR)_3$ (R = 1,1-di-*t*-butylethoxide) as the Cr(III) precursor. $Cr(OR)_3$ is a three-coordinate, highly air-sensitive complex of the bulky alkoxide "ditox" (2,2-di-*t*-butylethoxy) ligand, and it is highly soluble in alkane and arene solvents including pentane, toluene, and octadecene.[3] The anion source was trimethylsilyl halide (TMSX, X = I, Br). $Cr(OR)_3$ and TMSI do not undergo any observable reaction at room temperature or upon mild (<100 °C) heating, likely due to the considerable steric bulk of the reagents. Heating an anhydrous toluene solution of $Cr(OR)_3$ with excess TMSX to 135 °C initiates nucleation of CrX_3 nanoplatelets. Reaction of the alkane-soluble iodide precursor TMSX with the alkoxide ligands of $Cr(OR)_3$ putatively releases the halide concomitant with formation of a silyl ether byproduct (Me_3SiOR). This silyl ether byproduct likely undergoes further decomposition in situ. The overall synthesis is summarized in Scheme C1.

Scheme C1. Synthesis of CrX3 (X = I, Br) nanoplatelets

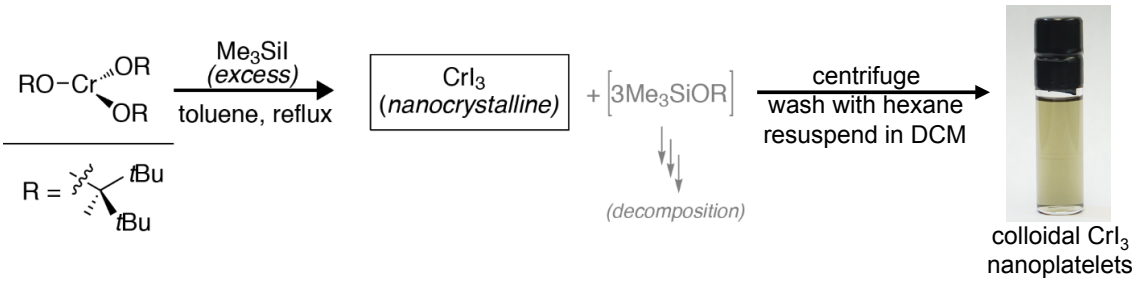

Figure C1 shows data from TEM measurements on $CrBr_3$ nanoplatelets. These data are similar to those presented for CrI_3 nanoplatelets in the main text.

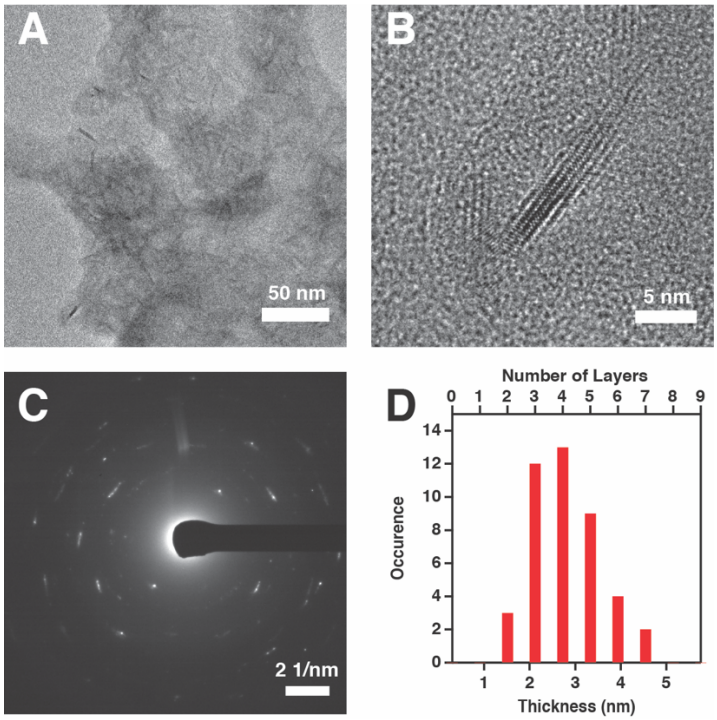

Figure C1: Characterization of $CrBr_3$ nanoplatelets. **(A)** TEM image of an aggregate of $CrBr_3$ nanoplatelets. **(B)** HR-TEM image of a $CrBr_3$ nanoplatelet lying on its short side. Lattice fringes are clearly seen. The nanocrystal in this image shows 5 individual $CrBr_3$ monolayers within the van der Waals nanoplatelet structure. **(C)** Selected area electron diffraction (SAED) image of aggregated $CrBr_3$ nanoplatelets. **(D)** Distribution of $CrBr_3$ nanoplatelet thicknesses, determined by measuring the sizes of >40 individual nanocrystals.

C.2 Inflections in magnetization data of CrI_3 nanoplatelets. The data in the main text show multiple distinct inflections at intermediate fields during the MCD field sweep measurement of CrI_3 nanoplatelets. These inflections are more easily seen in the derivative of the field sweep data, as shown in Figure C2.

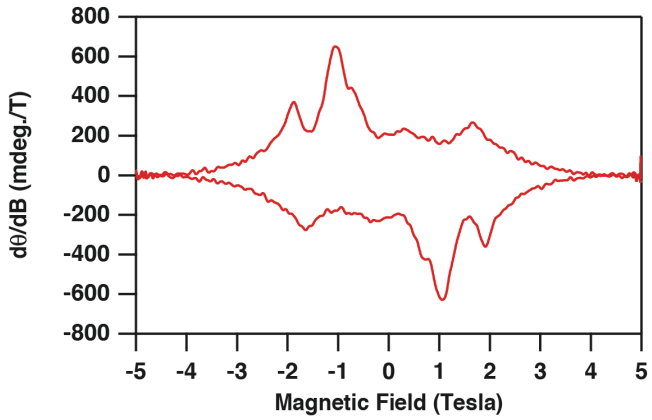

Figure C2: Inflections in the MCD magnetization *vs* magnetic field data for CrI_3 nanoplatelets. First derivative of the MCD magnetization field sweep data presented in the inset to Fig. 4.4b of Chapter 4. The derivative highlights the inflections in the hysteresis loop. These inflections are assigned to spin flip events of individual CrI_3 layers.

C.3 Anion alloying and its effects on spectroscopy and T_C. $Cr(I_{1-x}Br_x)_3$ nanoplatelets were prepared by mixing TMSI and TMSBr anion precursors during the synthesis. Varying the ratio of TMSI to TMSBr changes the ratio of Br^- to I^- incorporated into the nanoplatelets, and this ratio can be finely tuned across the entire range of $0 \leq x \leq 1$, but the nanoplatelet stoichiometry differs from the nominal (precursor) stoichiometry of the reaction. To illustrate, Figure C3A plots the analytical I^- contents measured in a series of $Cr(I_{1-x}Br_x)_3$ nanoplatelets as a function of the amount of TMSI added during synthesis. Halide compositions were determined by analysis of EDX data and by Vegard's law analysis of the (060) XRD reflection (inset of Figure C3A); both approaches yield the same results. The elevated I^- incorporation into the nanoplatelets is attributed to the greater reactivity of TMSI compared to TMSBr. These data demonstrate facile chemical control over the anion compositions in these colloidal CrX_3 nanoplatelets.

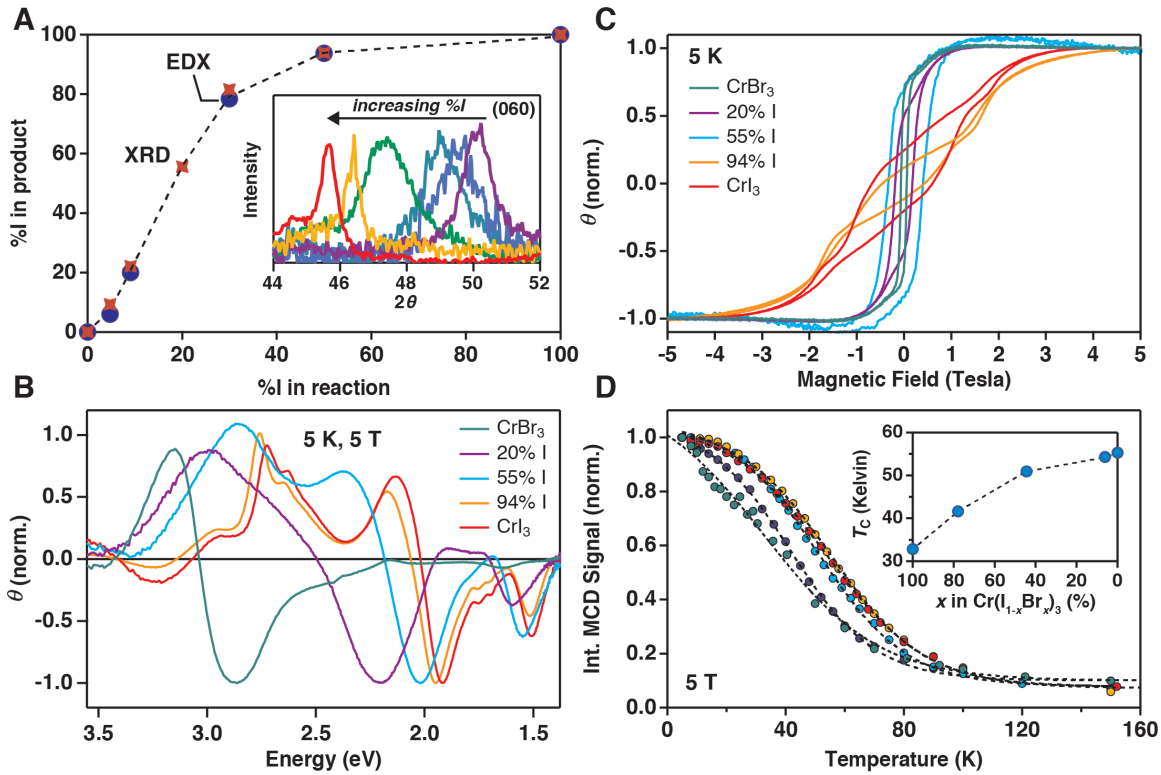

Figure C3: Structural and magnetic characterization of alloyed $Cr(I_{1-x}Br_x)_3$ nanoplatelets. **(A)** Measured mole percentage of iodide in the product for a given nominal iodide percentage in the reactants (TMSI and TMSBr). Compositions were determined by both XRD (Vegard's law, red crosses) and SEM/EDX (purple circles) measurements, which agree well. Inset: powder XRD data for the different alloy compositions, ranging from CrI_3 (red) to $CrBr_3$ (purple). The (060) reflection, typically the best resolved in the PXRD data, is shown. The dashed curve is a guide to the eye. **(B)** MCD spectra measured at 5 K and 5 T for different alloy compositions (given compositions are as determined by PXRD). **(C)** Field vs. magnetization sweeps for four different compositions of randomly oriented $Cr(I_{1-x}Br_x)_3$ nanoplatelets. **(D)** Integrated absolute MCD signal as a function of temperature for four different compositions of $Cr(I_{1-x}Br_x)_3$. Inset: Curie temperatures determined from the data in panel C and plotted as a function of iodide content for $Cr(I_{1-x}Br_x)_3$ nanoplatelets. The dashed curves are guides to the eye.

Anion alloying has dramatic effects on the nanoplatelet optical spectra and, in particular, on the stability of the ferromagnetic phase. Figure C3B plots 5 K, 5 T MCD spectra of a series of $Cr(I_{1-x}Br_x)_3$ nanoplatelets with x ranging from 0 to 1. The energies of both the ligand-field and LMCT transitions redshift with decreasing x, as expected from the endpoint data in Figure 4.3 of Chapter 4. Figure C3C plots magnetic hysteresis data measured by MCD for the same samples. Increasing x reduces the coercivity, narrowing the hysteresis. Whereas spin-flip inflections are clearly visible in the hysteresis data for the CrI_3 ($x = 0.00$) and lightly bromide-doped ($x = 0.06$) nanoplatelets, such features become less evident at higher x, where B_{sat} is diminished. Nevertheless, even in the $CrBr_3$ nanoplatelets a small foot in the magnetization curve is seen at ~0.3 T that appears to stem from the same

phenomenon. Figure C3D plots the integrated MCD intensity (absolute) as a function of temperature for the various $Cr(I_{1-x}Br_x)_3$ nanoplatelets. The spectra used for this analysis are presented in Figure C4. T_C values determined from these data are summarized in the inset of Figure C3D, which shows that T_C decreases as x increases, reaching T_C = 33 K at x = 1 ($CrBr_3$). This value of T_C is slightly smaller than the value (37 K) reported for bulk $CrBr_3$,[4] suggesting confinement effects in $CrBr_3$ similar to those found in the CrI_3 nanoplatelets.

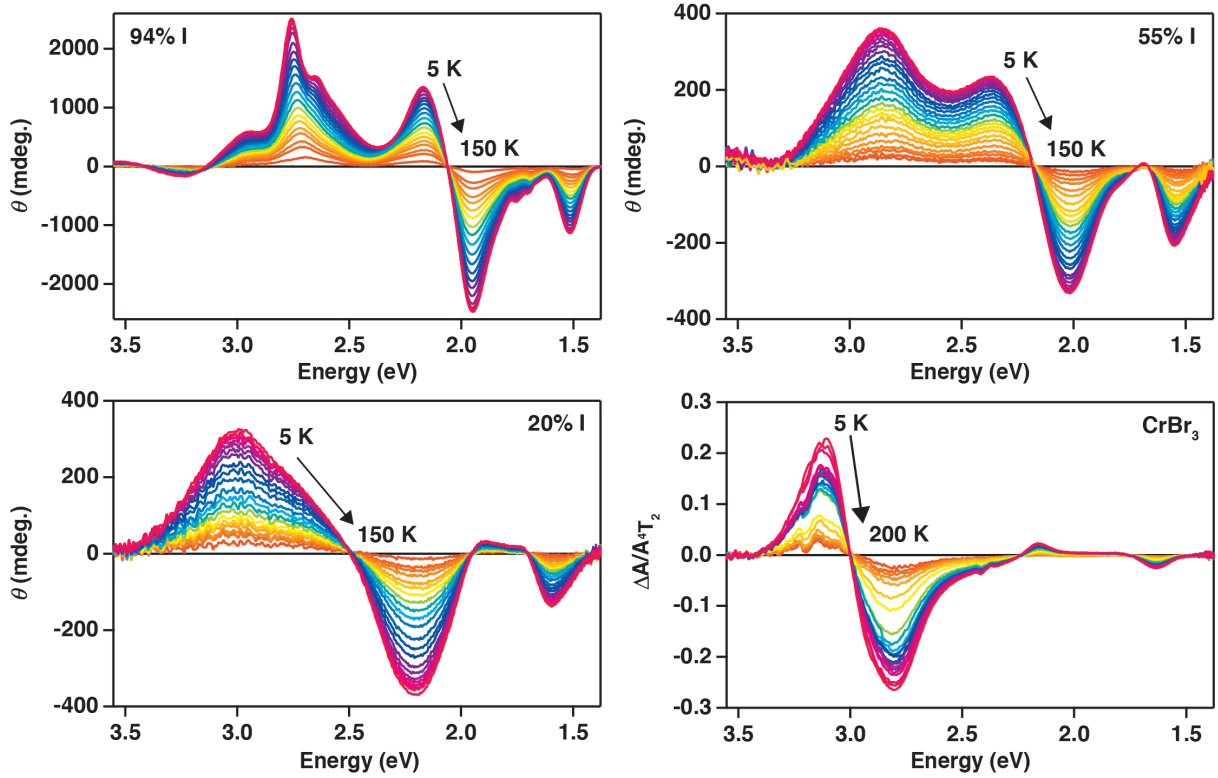

Figure C4: Variable-temperature magnetic circular dichroism spectra of $Cr(I_{1-x}Br_x)_3$ nanoplatelets. Temperature dependence (5 to 150 K) of the MCD spectra of $Cr(I_{1-x}Br_x)_3$ nanoplatelets, measured at 5 T. These spectra were used to determine the data points in Figure C3D.

C.4 Estimation of the energy barrier to magnetization reversal in CrI_3 nanoplatelets. The Néel-Arrhenius equation (eq C1) describes the time constant for aligned spins to reverse their orientation:

$$\tau_N = \tau_0 e^{KV/k_B T} \tag{C1}$$

where τ_0 is the attempt time, K is the magnetocrystalline anisotropy constant, and V is the particle volume. The product KV represents the energy barrier to spin reversal of the single-domain particle. Idealizing the CrI_3 nanoplatelets as hexagons, we can express this energy barrier as:

$$E_{spin\ reversal} = K \cdot \frac{3\sqrt{3}}{8} d^2 h \tag{C2}$$

where d is the platelet diagonal and h is its height. K has been measured for bulk CrI_3 where it is found to be temperature dependent.[5] Taking the values of K = 50 kJ/m^3 (0.31 meV/nm^3) measured at ~T_C and 300 kJ/m^3 (1.86 meV/nm^3) measured at low temperature, and using the interlayer spacing of 0.65 nm for the hexagon height, Figure C5 plots KV (meV) as a function of nanoplatelet size (d). For comparison, $k_B T_C$ is also plotted. This analysis shows that with these assumptions, $KV > k_B T_C$ for CrI_3 dimensions larger than d ~ 6.5 nm.

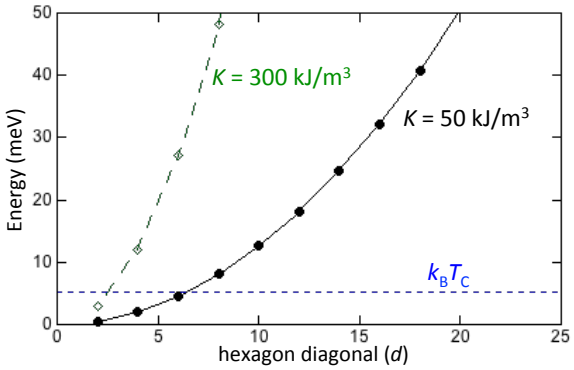

Figure C5: Size dependence of the barrier to magnetization reversal in CrI_3 nanoplatelets. Plots of estimated barriers to magnetization reversal (KV) for CrI_3 as a function of nanoplatelet size. Energy barriers were estimated from eq C2 for two different experimental (ref. 5) values of the volumetric anisotropy constant, K. K = 50 kJ/m^3 (0.31 meV/nm^3) was measured at ~T_C, and K = 300 kJ/m^3 (1.86 meV/nm^3) was measured in the low-temperature limit. For comparison, the value of $k_B T$ at T_C is also included in the plot.

C.5 References

1. Eshel, M.; Bino, A., Polynuclear chromium(III) carboxylates: Part 2. Chromium(III) acetate -- what's in it? *Inorg. Chim. Acta* **2001,** *320*, 127-132.
2. Jana, N. R.; Chen, Y.; Peng, X., Size- and shape-controlled magnetic (Cr, Mn, Fe, Co, Ni) oxide nanocrystals via a simple and general approach. *Chem. Mater.* **2004,** *16*, 3931-3935.
3. Groysman, S.; Villagrán, D.; Nocera, D. G., Pseudotetrahedral d0, d1, and d2 metal–oxo cores within a tris(alkoxide) platform. *Inorg. Chem.* **2010,** *49*, 10759-10761.
4. Tsubokawa, I., On the magnetic properties of a $CrBr_3$ single crystal. *J. Phys. Soc. Jpn.* **1960,** *15*, 1664-1668.
5. Richter, N.; Weber, D.; Martin, F.; Singh, N.; Schwingenschlögl, U.; Lotsch, B. V.; Kläui, M., Temperature-dependent magnetic anisotropy in the layered magnetic semiconductors CrI_3 and $CrBr_3$. *Phys. Rev. Mater.* **2018,** *2*, 024004.

Bibliography

1. Abdellatief, M.; Abele, M.; Leoni, M.; Scardi, P. Solid State Nuclear Magnetic Resonance and X-ray Diffraction Line Profile Analysis of heavily deformed fluorite. *Thin Solid Films* **2013,** *530*, 44-48.

2. Abramchuk, M.; Jaszewski, S.; Metz, K. R.; Osterhoudt, G. B.; Wang, Y.; Burch, K. S.; Tafti, F. Controlling Magnetic and Optical Properties of the van der Waals Crystal $CrCl_{3-x}Br_x$ via Mixed Halide Chemistry. *Adv. Mater.* **2018,** *30*, 1801325.

3. Agrawal, A.; Johns, R. W.; Milliron, D. J. Control of Localized Surface Plasmon Resonances in Metal Oxide Nanocrystals. *Annu. Rev. Mater. Res.* **2017,** *47*, 1-31.

4. Akkerman, Q. A.; D'Innocenzo, V.; Accornero, S.; Scarpellini, A.; Petrozza, A.; Prato, M.; Manna, L. Tuning the Optical Properties of Cesium Lead Halide Perovskite Nanocrystals by Anion Exchange Reactions. *J. Am. Chem. Soc.* **2015,** *137*, 10276-10281.

5. Akkerman, Q. A.; Gandini, M.; Di Stasio, F.; Rastogi, P.; Palazon, F.; Bertoni, G.; Ball, J. M.; Prato, M.; Petrozza, A.; Manna, L. Strongly emissive perovskite nanocrystal inks for high-voltage solar cells. *Nat. Energy* **2016,** *2*, 16194.

6. Akkerman, Q. A.; Rainò, G.; Kovalenko, M. V.; Manna, L. Genesis, challenges and opportunities for colloidal lead halide perovskite nanocrystals. *Nat. Mater.* **2018,** *17*, 394-405.

7. Badoz, J.; Billardon, M.; Boccara, A. C.; Briat, B. Measurement and interpretation of magnetic circular dichroism and magnetic linear dichroism spectra. *Symp. Faraday Soc.* **1969,** *3*, 27-39.

8. Barrows, C. J.; Vlaskin, V. A.; Gamelin, D. R. Absorption and Magnetic Circular Dichroism Analyses of Giant Zeeman Splittings in Diffusion-Doped Colloidal $Cd_{1-x}Mn_xSe$ Quantum Dots. *J. Phys. Chem. Lett.* **2015,** *6*, 3076-3081.

9. Beaulac, R.; Archer, P. I.; Gamelin, D. R. Luminescence in colloidal Mn^{2+}-doped semiconductor nanocrystals. *J. Solid State Chem.* **2008,** *181*, 1582-1589.

10. Beaulac, R.; Archer, P. I.; van Rijssel, J.; Meijerink, A.; Gamelin, D. R. Exciton Storage by Mn^{2+} in Colloidal Mn^{2+}-Doped CdSe Quantum Dots. *Nano Lett.* **2008,** *8*, 2949-2953.

11. Beaulac, R.; Feng, Y.; May, J. W.; Badaeva, E.; Gamelin, D. R.; Li, X. Orbital pathways for Mn^{2+}-carrier sp-d exchange in diluted magnetic semiconductor quantum dots. *Phys. Rev. B* **2011,** *84*, 195324.

12. Beaulac, R.; Schneider, L.; Archer, P. I.; Bacher, G.; Gamelin, D. R. Light-Induced Spontaneous Magnetization in Doped Colloidal Quantum Dots. *Science* **2009,** *325*, 973.

13. Bebenin, N. G. On magnetic red shift of absorption edge in EuO. *Solid State Commun.* **1985,** *55*, 823-825.

14. Beberwyck, B. J.; Surendranath, Y.; Alivisatos, A. P. Cation Exchange: A Versatile Tool for Nanomaterials Synthesis. *J. Phys. Chem. C* **2013,** *117*, 19759-19770.

15. Bermudez, V. M.; McClure, D. S. Spectroscopic studies of the two-dimensional magnetic insulators chromium trichloride and chromium tribromide—II. *J. Phys. Chem. Solids* **1979,** *40*, 149-173.

16. Bermudez, V. M.; McClure, D. S. Spectroscopic studies of the two-dimensional magnetic insulators chromium trichloride and chromium tribromide—I. *J. Phys. Chem. Solids* **1979,** *40*, 129-147.

17. Blöchl, P. E. Projector augmented-wave method. *Phys. Rev. B* **1994,** *50*, 17953-17979.

18. Boles, M. A.; Ling, D.; Hyeon, T.; Talapin, D. V. The surface science of nanocrystals. *Nat. Mater.* **2016,** *15*, 141-153.

19. Boncher, W.; Dalafu, H.; Rosa, N.; Stoll, S. Europium chalcogenide magnetic semiconductor nanostructures. *Coord. Chem. Rev.* **2015,** *289–290*, 279-288.

20. Bond Energies. In *Encyclopedia of Inorganic Chemistry*; King, R. B., Crabtree, R. H., Lukehart, C. M., Atwood, D. A., Scott, R. A., Eds.; 2006; p DOI: 10.1002/0470862106.id098.

21. Bradshaw, L. R.; May, J. W.; Dempsey, J. L.; Li, X.; Gamelin, D. R. Ferromagnetic excited-state Mn^{2+} dimers in $Zn_{1-x}Mn_xSe$ quantum dots observed by time-resolved magnetophotoluminescence. *Phys. Rev. B* **2014,** *89*, 115312.

22. Brown, P. R.; Kim, D.; Lunt, R. R.; Zhao, N.; Bawendi, M. G.; Grossman, J. C.; Bulović, V. Energy Level Modification in Lead Sulfide Quantum Dot Thin Films through Ligand Exchange. *ACS Nano* **2014,** *8*, 5863-5872.

23. Burch, K. S.; Mandrus, D.; Park, J.-G. Magnetism in two-dimensional van der Waals materials. *Nature* **2018,** *563*, 47-52.

24. Busch, G.; Wachter, P. Einfluß der magnetischen ordnung auf die optische absorption von ferro- oder antiferromagnetischen halbleitern. *Phys. Konden. Mater.* **1966,** *5*, 232-242.

25. Callen, H. B.; Callen, E. Cluster Approximation for Ferromagnets with First- and Second-Neighbor Exchange, with Application to the Europium Chalcogenides. *Phys. Rev.* **1964,** *136*, A1675-A1683.

26. Cape, J. A.; White, R. L.; Feigelson, R. S. EPR Study of the Structure of $CsPbCl_3$. *J. Appl. Phys.* **1969,** *40*, 5001-5005.

27. Carroll, G. M.; Schimpf, A. M.; Tsui, E. Y.; Gamelin, D. R. Redox Potentials of Colloidal n-Type ZnO Nanocrystals: Effects of Confinement, Electron Density, and Fermi-Level Pinning by Aldehyde Hydrogenation. *J. Am. Chem. Soc.* **2015,** *137*, 11163-11169.

28. Carroll, G. M.; Tsui, E. Y.; Brozek, C. K.; Gamelin, D. R. Spectroelectrochemical Measurement of Surface Electrostatic Contributions to Colloidal CdSe Nanocrystal Redox Potentials. *Chem. Mater.* **2016,** *28*, 7912-7918.

29. Causa, M. T.; Tovar, M.; Caneiro, A.; Prado, F.; Ibañez, G.; Ramos, C. A.; Butera, A.; Alascio, B.; Obradors, X.; Piñol, S.; Rivadulla, F.; Vázquez-Vázquez, C.; López-Quintela, M. A.; Rivas, J.; Tokura, Y.; Oseroff, S. B. High-temperature spin dynamics in CMR manganites: ESR and magnetization. *Phys. Rev. B* **1998,** *58*, 3233-3239.

30. Chen, D.; Fang, G.; Chen, X. Silica-Coated Mn-Doped $CsPb(Cl/Br)_3$ Inorganic Perovskite Quantum Dots: Exciton-to-Mn Energy Transfer and Blue-Excitable Solid-State Lighting. *ACS Appl. Mater. Interfaces* **2017,** *9*, 40477-40487.

31. Chen, W.; Zhang, X.; Huang, Y. Luminescence enhancement of EuS nanoclusters in zeolite. *Appl. Phys. Lett.* **2000,** *76*, 2328-2330.

32. Cohen, M. I.; Young, K. F.; Chang, T. T.; Brower, W. S. Phase Transitions in $CsPbCl_3$. *J. Appl. Phys.* **1971,** *42*, 5267-5272.

33. Comin, A.; Manna, L. New materials for tunable plasmonic colloidal nanocrystals. *Chem. Soc. Rev.* **2014,** *43*, 3957-3975.

34. Connelly, N. G.; Geiger, W. E. Chemical Redox Agents for Organometallic Chemistry. *Chem. Rev.* **1996,** *96*, 877-910.

35. Creutz, S. E.; Crites, E. N.; De Siena, M. C.; Gamelin, D. R. Colloidal Nanocrystals of Lead-Free Double-Perovskite (Elpasolite) Semiconductors: Synthesis and Anion Exchange To Access New Materials. *Nano Lett.* **2018,** *18*, 1118-1123.

36. Creutz, S. E.; Crites, E. N.; De Siena, M. C.; Gamelin, D. R. Anion Exchange in Cesium Lead Halide Perovskite Nanocrystals and Thin Films Using Trimethylsilyl Halide Reagents. *Chem. Mater.* **2018,** *30*, 4887-4891.

37. Dalafu, H. A.; Rosa, N.; James, D.; Asuigui, D. R. C.; McNamara, M.; Kawashima, A.; Omagari, S.; Nakanishi, T.; Hasegawa, Y.; Stoll, S. L. Solid-State and Nanoparticle Synthesis of EuS_xSe_{1-x} Solid Solutions. *Chem. Mater.* **2018,** *30*, 2954-2964.

38. De Fontaine, D. The number of independent pair-correlation functions in multicomponent systems. *J. Appl. Crystallogr.* **1971,** *4*, 15-19.

39. De Lucas, M. C. M.; Rodríguez, F.; Prieto, C.; Verdaguer, M.; Moreno, M.; Güdel, H. U. Optical properties and local structure of $MnCl_6^{4-}$ in $ABCl_3:Mn^{2+}$. *Radiat. Eff. Defects Solids* **1995,** *135*, 95-100.

40. De Simoni, G.; Strambini, E.; Moodera, J. S.; Bergeret, F. S.; Giazotto, F. Toward the Absolute Spin-Valve Effect in Superconducting Tunnel Junctions. *Nano Lett.* **2018,** *18*, 6369-6374.

41. De Trizio, L.; Manna, L. Forging Colloidal Nanostructures via Cation Exchange Reactions. *Chem. Rev.* **2016,** *116*, 10852-10887.

42. Dempah, K. E.; Lubach, J. W.; Munson, E. J. Characterization of the Particle Size and Polydispersity of Dicumarol Using Solid-State NMR Spectroscopy. *Mol. Pharm.* **2017,** *14*, 856-865.

43. CASMcode: v0.2.1; **2017**; DOI: 10.5281/zenodo.546148.

44. Díaz, B.; Granado, E.; Abramof, E.; Torres, L.; Lechner, R. T.; Springholz, G.; Bauer, G. Magnetic ordering and transitions of EuSe studied by x-ray diffraction. *Phys. Rev. B* **2010,** *81*, 184428.

45. Dietl, T. A ten-year perspective on dilute magnetic semiconductors and oxides. *Nat. Mater.* **2010,** *9*, 965-974.

46. Dillon, J. F.; Kamimura, H.; Remeika, J. P. Magneto-optical properties of ferromagnetic chromium trihalides. *J. Phys. Chem. Solids* **1966,** *27*, 1531-1549.

47. Dimmock, J. O. Optical Properties of the Europium Chalcogenides. *IBM J. Res. Dev.* **1970,** *14*, 301-308.

48. Eastman, D. E.; Holtzberg, F.; Methfessel, S. Photoemission Studies of the Electronic Structure of EuO, EuS, EuSe, And GdS. *Phys. Rev. Lett.* **1969,** *23*, 226-229.

49. Eaton, G. R.; Eaton, S. S.; Barr, D. P.; Weber, R. T., Quantitative EPR. Springer: Vienna, 2010.

50. Eshel, M.; Bino, A. Polynuclear chromium(III) carboxylates: Part 2. Chromium(III) acetate -- what's in it? *Inorg. Chim. Acta* **2001,** *320*, 127-132.

51. Fei, L.; Yuan, X.; Hua, J.; Ikezawa, M.; Zeng, R.; Li, H.; Masumoto, Y.; Zhao, J. Enhanced luminescence and energy transfer in Mn^{2+} doped $CsPbCl_{3-x}Br_x$ perovskite nanocrystals. *Nanoscale* **2018,** *10*, 19435-19442.

52. Feinleib, J.; Scouler, W. J.; Dimmock, J. O.; Hanus, J.; Reed, T. B.; Pidgeon, C. R. Spin-Polarized Splittings in the Temperature-Dependent Reflectance of EuO. *Phys. Rev. Lett.* **1969,** *22*, 1385-1388.

53. Ferguson, J.; Guggenheim, H. J.; Tanabe, Y. Exchange Effects in the Electronic Absorption Spectrum of Mn(II) in Perovskite Fluorides. *J. Appl. Phys.* **1965,** *36*, 1046-1047.

54. Ferre, J.; Billardon, M.; Badoz, J.; Suryanarayanan, R.; Paparoditis, C. Dichroïsme circulaire magnétique de films minces de EuTe et EuSe jusqu'à 5 °K. *J. Phys. Colloq.* **1971,** *32*, C1-930-C1-931.

55. Ferre, J.; Briat, B.; Paparoditis, C.; Pokrzywnicki, S.; Suryanarayanan, R. Magneto-optical properties of EuS thin films: Magnetic circular and linear dichroism. *Solid State Commun.* **1972,** *11*, 1173-1177.

56. Furdyna, J. K. Diluted magnetic semiconductors. *J. Appl. Phys.* **1988,** *64*, R29-R64.

57. Gambino, R. J.; Fumagalli, P.; Ruf, R. R.; McGuire, T. R.; Bojarczuk, N. Magneto-optic spectra of EuS-Gd and EuS-Tb films. *IEEE Trans. Magn.* **1992,** *28*, 2973-2975.

58. Gao, D.; Qiao, B.; Xu, Z.; Song, D.; Song, P.; Liang, Z.; Shen, Z.; Cao, J.; Zhang, J.; Zhao, S. Postsynthetic, Reversible Cation Exchange between Pb^{2+} and Mn^{2+} in Cesium Lead Chloride Perovskite Nanocrystals. *J. Phys. Chem. C* **2017,** *121*, 20387-20395.

59. Gibertini, M.; Koperski, M.; Morpurgo, A. F.; Novoselov, K. S. Magnetic 2D materials and heterostructures. *Nat. Nanotech.* **2019,** *14*, 408-419.

60. Gong, C.; Li, L.; Li, Z.; Ji, H.; Stern, A.; Xia, Y.; Cao, T.; Bao, W.; Wang, C.; Wang, Y.; Qiu, Z. Q.; Cava, R. J.; Louie, S. G.; Xia, J.; Zhang, X. Discovery of intrinsic ferromagnetism in two-dimensional van der Waals crystals. *Nature* **2017,** *546*, 265–269.

61. Gong, C.; Zhang, X. Two-dimensional magnetic crystals and emergent heterostructure devices. *Science* **2019,** *363*, eaav4450.

62. Grönke, M.; Buschbeck, B.; Schmidt, P.; Valldor, M.; Oswald, S.; Hao, Q.; Lubk, A.; Wolf, D.; Steiner, U.; Büchner, B.; Hampel, S. Chromium Trihalides CrX_3 (X = Cl, Br, I): Direct Deposition of Micro- and Nanosheets on Substrates by Chemical Vapor Transport. *Adv. Mater. Interfaces* **2019,** *6*, 1901410.

63. Groysman, S.; Villagrán, D.; Nocera, D. G. Pseudotetrahedral d0, d1, and d2 metal–oxo cores within a tris(alkoxide) platform. *Inorg. Chem.* **2010,** *49*, 10759-10761.

64. Güntherodt, G.; Wachter, P.; Imboden, D. M. Energy level scheme and the effect of magnetic order on the optical transitions in europium chalcogenides. *Phys. Konden. Mater.* **1971,** *12*, 292-310.

65. Gupta, R. P.; Seehra, M. S.; Vehse, W. E. Shift of Néel Temperature and EPR Linewidth of $KMnF_3$ with Mg Doping. *Phys. Rev. B* **1972,** *5*, 92-95.

66. Guria, A. K.; Dutta, S. K.; Adhikari, S. D.; Pradhan, N. Doping Mn^{2+} in Lead Halide Perovskite Nanocrystals: Successes and Challenges. *ACS Energy Lett.* **2017,** *2*, 1014-1021.

67. Hart, G. L. W.; Forcade, R. W. Algorithm for generating derivative structures. *Phys. Rev. B* **2008,** *77*, 224115.

68. Hasegawa, Y.; Adachi, T.-a.; Tanaka, A.; Afzaal, M.; O'Brien, P.; Doi, T.; Hinatsu, Y.; Fujita, K.; Tanaka, K.; Kawai, T. Remarkable Magneto-Optical Properties of Europium Selenide Nanoparticles with Wide Energy Gaps. *J. Am. Chem. Soc.* **2008,** *130*, 5710-5715.

69. Hasegawa, Y.; Kumagai, M.; Kawashima, A.; Nakanishi, T.; Fujita, K.; Tanaka, K.; Fushimi, K. First Synthesis of EuS Nanoparticle Thin Film with a Wide Energy Gap and Giant Magneto-Optical Efficiency on a Glass Electrode. *J. Phys. Chem. C* **2012,** *116*, 19590-19596.

70. Hasegawa, Y.; Maeda, M.; Nakanishi, T.; Doi, Y.; Hinatsu, Y.; Fujita, K.; Tanaka, K.; Koizumi, H.; Fushimi, K. Effective Optical Faraday Rotations of Semiconductor EuS Nanocrystals with Paramagnetic Transition-Metal Ions. *J. Am. Chem. Soc.* **2013,** *135*, 2659-2666.

71. Hedman, L.; Rao, K. V.; Yeshurun, Y. Magnetic properties of Eu substituted SmS. *J. Appl. Phys.* **1981,** *52*, 2155-2157.

72. Hillhouse, H. W.; Beard, M. C. Solar cells from colloidal nanocrystals: Fundamentals, materials, devices, and economics. *Curr. Opin. Colloid Interface Sci.* **2009,** *14*, 245-259.

73. Houtepen, A. J.; Hens, Z.; Owen, J. S.; Infante, I. On the Origin of Surface Traps in Colloidal II–VI Semiconductor Nanocrystals. *Chem. Mater.* **2017,** *29*, 752-761.

74. Huang, B.; Clark, G.; Navarro-Moratalla, E.; Klein, D. R.; Cheng, R.; Seyler, K. L.; Zhong, D.; Schmidgall, E.; McGuire, M. A.; Cobden, D. H.; Yao, W.; Xiao, D.; Jarillo-Herrero, P.; Xu, X. Layer-dependent ferromagnetism in a van der Waals crystal down to the monolayer limit. *Nature* **2017,** *546*, 270.

75. Huber, D. L.; Alejandro, G.; Caneiro, A.; Causa, M. T.; Prado, F.; Tovar, M.; Oseroff, S. B. EPR linewidths in $La_{1-x}Ca_xMnO_3$: $0 \leq x \leq 1$. *Phys. Rev. B* **1999,** *60*, 12155-12161.

76. Huber, D. L.; Seehra, M. S. Contribution of the spin-phonon interaction to the paramagnetic resonance linewidth of $CrBr_3$. *J. Phys. Chem. Solids* **1975,** *36*, 723-725.

77. Jana, N. R.; Chen, Y.; Peng, X. Size- and shape-controlled magnetic (Cr, Mn, Fe, Co, Ni) oxide nanocrystals via a simple and general approach. *Chem. Mater.* **2004,** *16*, 3931-3935.

78. Jewett, J. W.; Wigen, P. E. EPR of Tb^{3+}, Pr^{3+}, Gd^{3+}, and Eu^{3+} ions in single crystal La_2O_2S. *J. Chem. Phys.* **1974,** *61*, 2991-2995.

79. Jiang, P.; Wang, C.; Chen, D.; Zhong, Z.; Yuan, Z.; Lu, Z.-Y.; Ji, W. Stacking tunable interlayer magnetism in bilayer CrI_3. *Phys. Rev. B* **2019,** *99*, 144401.

80. Jiang, S.; Li, L.; Wang, Z.; Mak, K. F.; Shan, J. Controlling magnetism in 2D CrI_3 by electrostatic doping. *Nat. Nanotech.* **2018,** *13*, 549-553.

81. Jiang, W.; Li, S.; Liu, H.; Lu, G.; Zheng, F.; Zhang, P. First-principles calculations of magnetic edge states in zigzag CrI_3 nanoribbons. *Phys. Lett. A* **2019,** *383*, 754-758.

82. Johnson, C. E.; Costa, L.; Johnson, J. A.; Brown, D. E.; Somarajan, S.; He, W.; Dickerson, J. H. Mössbauer spectra and superparamagnetism of europium sulfide nanoparticles. *J. Phys. D: Appl. Phys.* **2014,** *47*, 075001.

83. Jones, M.; Lo, S. S.; Scholes, G. D. Quantitative modeling of the role of surface traps in CdSe/CdS/ZnS nanocrystal photoluminescence decay dynamics. *Proc. Natl. Acad. Sci.* **2009,** *106*, 3011.

84. Jordan, A.; Scholz, R.; Wust, P.; Fähling, H.; Roland, F. Magnetic fluid hyperthermia (MFH): Cancer treatment with AC magnetic field induced excitation of biocompatible superparamagnetic nanoparticles. *J. Magn. Magn. Mater.* **1999,** *201*, 413-419.

85. Jørgensen, C. K. Electron transfer spectra. *Prog. Inorg. Chem.* **1970,** *12*, 101–158.

86. Kang, J.; Wang, L.-W. High Defect Tolerance in Lead Halide Perovskite $CsPbBr_3$. *J. Phys. Chem. Lett.* **2017,** *8*, 489-493.

87. Kar, S.; Boncher, W. L.; Olszewski, D.; Dollahon, N.; Ash, R.; Stoll, S. L. Gadolinium Doped Europium Sulfide. *J. Am. Chem. Soc.* **2010,** *132*, 13960-13962.

88. Kirchschlager, R.; Heiss, W.; Lechner, R. T.; Bauer, G.; Springholz, G. Hysteresis loops of the energy band gap and effective g factor up to 18,000 for metamagnetic EuSe epilayers. *Appl. Phys. Lett.* **2004,** *85*, 67-69.

89. Kittilstved, K. R.; Gamelin, D. R. Activation of High-T_C Ferromagnetism in Mn^{2+}-Doped ZnO using Amines. *J. Am. Chem. Soc.* **2005,** *127*, 5292-5293.

90. Knowles, K. E.; Hartstein, K. H.; Kilburn, T. B.; Marchioro, A.; Nelson, H. D.; Whitham, P. J.; Gamelin, D. R. Luminescent Colloidal Semiconductor Nanocrystals Containing Copper: Synthesis, Photophysics, and Applications. *Chem. Rev.* **2016,** *116*, 10820-10851.

91. Kondal, S. C.; Seehra, M. S. Shape dependence of the EPR linewidth, resonance field and spin-spin relaxation rate of EuS near Tc. *J. Phys. C: Solid State Phys.* **1982,** *15*, 2471.

92. Kowalczyk, S. P.; Edelstein, N.; McFeely, F. R.; Ley, L.; Shirley, D. A. X-ray photoemission spectra of the 4d levels in rare-earth metals. *Chem. Phys. Lett.* **1974,** *29*, 491-495.

93. Krause, M. M.; Kambhampati, P. Linking surface chemistry to optical properties of semiconductor nanocrystals. *Phys. Chem. Chem. Phys.* **2015,** *17*, 18882-18894.

94. Krebs, J. J. EPR Determination of the Nearest-Neighbor Exchange Constant for Mn^{2+} Pairs in $KZnF_3$. *J. Appl. Phys.* **1969,** *40*, 1137-1139.

95. Kresse, G.; Furthmüller, J. Efficient iterative schemes for ab initio total-energy calculations using a plane-wave basis set. *Phys. Rev. B* **1996,** *54*, 11169-11186.

96. Kresse, G.; Furthmüller, J. Efficiency of ab-initio total energy calculations for metals and semiconductors using a plane-wave basis set. *Comp. Mater. Sci.* **1996,** *6*, 15-50.

97. Kresse, G.; Hafner, J. Norm-conserving and ultrasoft pseudopotentials for first-row and transition elements. *J. Phys.: Condens. Matter* **1994,** *6*, 8245.

98. Kresse, G.; Joubert, D. From ultrasoft pseudopotentials to the projector augmented-wave method. *Phys. Rev. B* **1999,** *59*, 1758-1775.

99. Kroupa, D. M.; Vörös, M.; Brawand, N. P.; McNichols, B. W.; Miller, E. M.; Gu, J.; Nozik, A. J.; Sellinger, A.; Galli, G.; Beard, M. C. Tuning colloidal quantum dot band edge positions through solution-phase surface chemistry modification. *Nat. Commun.* **2017,** *8*, 15257.

100. Kubicki, D. J.; Prochowicz, D.; Pinon, A.; Stevanato, G.; Hofstetter, A.; Zakeeruddin, S. M.; Grätzel, M.; Emsley, L. Doping and phase segregation in Mn^{2+}- and Co^{2+}-doped lead halide perovskites from ^{133}Cs and ^{1}H NMR relaxation enhancement. *J. Mater. Chem. A* **2019,** *7*, 2326-2333.

101. Lado, J. L.; Fernández-Rossier, J. On the origin of magnetic anisotropy in two dimensional CrI_3. *2D Materials* **2017,** *4*, 035002.

102. Lee, I.; Utermohlen, F. G.; Weber, D.; Hwang, K.; Zhang, C.; van Tol, J.; Goldberger, J. E.; Trivedi, N.; Hammel, P. C. Fundamental Spin Interactions Underlying the Magnetic Anisotropy in the Kitaev Ferromagnet CrI_3. *Phys. Rev. Lett.* **2020,** *124*, 017201.

103. Li, F.; Xia, Z.; Gong, Y.; Gu, L.; Liu, Q. Optical properties of Mn^{2+} doped cesium lead halide perovskite nanocrystals via a cation–anion co-substitution exchange reaction. *J. Mater. Chem. C* **2017,** *5*, 9281-9287.

104. Li, F.; Xia, Z.; Pan, C.; Gong, Y.; Gu, L.; Liu, Q.; Zhang, J. Z. High Br^- Content $CsPb(Cl_yBr_{1-y})_3$ Perovskite Nanocrystals with Strong Mn^{2+} Emission through Diverse Cation/Anion Exchange Engineering. *ACS Appl. Mater. Interfaces* **2018,** *10*, 11739-11746.

105. Li, G.; Ho, J. Y.-L.; Wong, M.; Kwok, H. S. Reversible Anion Exchange Reaction in Solid Halide Perovskites and Its Implication in Photovoltaics. *J. Phys. Chem. C* **2015,** *119*, 26883-26888.

106. Li, M.; Zhang, X.; Matras-Postolek, K.; Chend, H.-S.; Yang, P. An anion-driven Sn^{2+} exchange reaction in $CsPbBr_3$ nanocrystals towards tunable and high photoluminescence. *J. Mater. Chem. C* **2018,** *6*, 5506-5513.

107. Li, X.; Wu, Y.; Zhang, S.; Cai, B.; Gu, Y.; Song, J.; Zeng, H. $CsPbX_3$ Quantum Dots for Lighting and Displays: Room-Temperature Synthesis, Photoluminescence Superiorities, Underlying Origins and White Light-Emitting Diodes. *Adv. Funct. Mater.* **2016,** *26*, 2435-2445.

108. Li, Z.-J.; Hofman, E.; Davis, A. H.; Khammang, A.; Wright, J. T.; Dzikovski, B.; Meulenberg, R. W.; Zheng, W. Complete Dopant Substitution by Spinodal Decomposition in Mn-Doped Two-Dimensional $CsPbCl_3$ Nanoplatelets. *Chem. Mater.* **2018,** *30*, 6400-6409.

109. Liu, W.; Lin, Q.; Li, H.; Wu, K.; Robel, I.; Pietryga, J. M.; Klimov, V. I. Mn^{2+}-Doped Lead Halide Perovskite Nanocrystals with Dual-Color Emission Controlled by Halide Content. *J. Am. Chem. Soc.* **2016,** *138*, 14954-14961.

110. Mairoser, T.; Loder, F.; Melville, A.; Schlom, D. G.; Schmehl, A. Influence of chemical doping on the magnetic properties of EuO. *Phys. Rev. B* **2013,** *87*, 014416.

111. Mairoser, T.; Schmehl, A.; Melville, A.; Heeg, T.; Canella, L.; Böni, P.; Zander, W.; Schubert, J.; Shai, D. E.; Monkman, E. J.; Shen, K. M.; Schlom, D. G.; Mannhart, J. Is There an Intrinsic Limit to the Charge-Carrier-Induced Increase of the Curie Temperature of EuO? *Phys. Rev. Lett.* **2010,** *105*, 257206.

112. Matumura, O. Electron Spin Resonance of Mn-activated Phosphors. *J. Phys. Soc. Jpn.* **1959,** *14*, 108.

113. Mauger, A.; Godart, C. The magnetic, optical, and transport properties of representatives of a class of magnetic semiconductors: The europium chalcogenides. *Phys. Rep.* **1986,** *141*, 51-176.

114. McAlister, S. P.; Furdyna, J. K.; Giriat, W. Magnetic susceptibility and spin-glass transition in $Zn_{1-x}Mn_xTe$. *Phys. Rev. B* **1984,** *29*, 1310-1314.

115. McGuire, M. A.; Dixit, H.; Cooper, V. R.; Sales, B. C. Coupling of crystal structure and magnetism in the layered, ferromagnetic insulator CrI_3. *Chem. Mater.* **2015,** *27*, 612-620.

116. McGuire, T. R.; Holtzberg, F. Magnetic Ordering of $Eu_{(1-x)}Gd_xS$. *AIP Conf. Proc.* **1972,** *5*, 855-859.

117. McLaurin, E. J.; Vlaskin, V. A.; Gamelin, D. R. Water-Soluble Dual-Emitting Nanocrystals for Ratiometric Optical Thermometry. *J. Am. Chem. Soc.* **2011,** *133*, 14978-14980.

118. McPherson, G. L.; Waguespack, Y. Y.; Vanoy, T. C.; Rodriguez, W. J. Exciton migration in a ''pseudo''-one-dimensional crystal: Luminescence dynamics of doped $CsMnBr_3$. *J. Chem. Phys.* **1990,** *92*, 1768-1774.

119. Meinardi, F.; Akkerman, Q. A.; Bruni, F.; Park, S.; Mauri, M.; Dang, Z.; Manna, L.; Brovelli, S. Doped Halide Perovskite Nanocrystals for Reabsorption-Free Luminescent Solar Concentrators. *ACS Energy Lett.* **2017,** *2*, 2368-2377.

120. Miao, G.-X.; Moodera, J. S. Spin manipulation with magnetic semiconductor barriers. *Phys. Chem. Chem. Phys.* **2015,** *17*, 751-761.

121. Miao, J.; Zhang, F. Recent progress on highly sensitive perovskite photodetectors. *J. Mater. Chem. C* **2019**.

122. Milstein, T. J.; Kroupa, D. M.; Gamelin, D. R. Picosecond Quantum Cutting Generates Photoluminescence Quantum Yields Over 100% in Ytterbium-Doped $CsPbCl_3$ Nanocrystals. *Nano Lett.* **2018,** *18*, 3792-3799.

123. Mir, W. J.; Jagadeeswararao, M.; Das, S.; Nag, A. Colloidal Mn-Doped Cesium Lead Halide Perovskite Nanoplatelets. *ACS Energy Lett.* **2017,** *2*, 537–543.

124. Mir, W. J.; Mahor, Y.; Lohar, A.; Jagadeeswararao, M.; Das, S.; Mahamuni, S.; Nag, A. Postsynthesis Doping of Mn and Yb into $CsPbX_3$ (X = Cl, Br, or I) Perovskite Nanocrystals for Downconversion Emission. *Chem. Mater.* **2018,** *30*, 8170-8178.

125. Mirkovic, T.; Hines, M. A.; Nair, P. S.; Scholes, G. D. Single-Source Precursor Route for the Synthesis of EuS Nanocrystals. *Chem. Mater.* **2005,** *17*, 3451-3456.

126. Monkhorst, H. J.; Pack, J. D. Special points for Brillouin-zone integrations. *Phys. Rev. B* **1976,** *13*, 5188-5192.

127. Moodera, J. S.; Hao, X.; Gibson, G. A.; Meservey, R. Electron-Spin Polarization in Tunnel Junctions in Zero Applied Field with Ferromagnetic EuS Barriers. *Phys. Rev. Lett.* **1988,** *61*, 637-640.

128. Moodera, J. S.; Meservey, R.; Hao, X. Variation of the electron-spin polarization in EuSe tunnel junctions from zero to near 100% in a magnetic field. *Phys. Rev. Lett.* **1993,** *70*, 853-856.

129. Moodera, J. S.; Miao, G.-X.; Santos, T. S. Frontiers in Spin-Polarized Tunneling. *Phys. Today* **2010,** *63*, 46-51.

130. Moodera, J. S.; Santos, T. S.; Nagahama, T. The phenomena of spin-filter tunnelling. *J. Phys.: Condens. Matter* **2007,** *19*, 165202.

131. Nag, A.; Chakraborty, S.; Sarma, D. D. To Dope Mn^{2+} in a Semiconducting Nanocrystal. *J. Am. Chem. Soc.* **2008,** *130*, 10605-10611.

132. Nedelcu, G.; Protesescu, L.; Yakunin, S.; Bodnarchuk, M. I.; Grotevent, M. J.; Kovalenko, M. V. Fast Anion-Exchange in Highly Luminescent Nanocrystals of Cesium Lead Halide Perovskites ($CsPbX_3$, X = Cl, Br, I). *Nano Lett.* **2015,** *15*, 5635-5640.

133. Nelson, H. D.; Bradshaw, L. R.; Barrows, C. J.; Vlaskin, V. A.; Gamelin, D. R. Picosecond Dynamics of Excitonic Magnetic Polarons in Colloidal Diffusion-Doped $Cd_{1-x}Mn_xSe$ Quantum Dots. *ACS Nano* **2015,** *9*, 11177-11191.

134. Nelson, H. D.; Li, X.; Gamelin, D. R. Computational Studies of the Electronic Structures of Copper-Doped CdSe Nanocrystals: Oxidation States, Jahn–Teller Distortions, Vibronic Bandshapes, and Singlet–Triplet Splittings. *J. Phys. Chem. C* **2016,** *120*, 5714-5723.

135. Nelson, L. J.; Hart, G. L. W.; Zhou, F.; Ozoliņš, V. Compressive sensing as a paradigm for building physics models. *Phys. Rev. B* **2013,** *87*, 035125.

136. Nenon, D. P.; Pressler, K.; Kang, J.; Koscher, B. A.; Olshansky, J. H.; Osowiecki, W. T.; Koc, M. A.; Wang, L.-W.; Alivisatos, A. P. Design Principles for Trap-Free $CsPbX_3$ Nanocrystals: Enumerating and Eliminating Surface Halide Vacancies with Softer Lewis Bases. *J. Am. Chem. Soc.* **2018,** *140*, 17760-17772.

137. Neuwelt, E. A.; Hamilton, B. E.; Varallyay, C. G.; Rooney, W. R.; Edelman, R. D.; Jacobs, P. M.; Watnick, S. G. Ultrasmall superparamagnetic iron oxides (USPIOs): a future alternative magnetic resonance (MR) contrast agent for patients at risk for nephrogenic systemic fibrosis (NSF)? *Kidney Int.* **2009,** *75*, 465-474.

138. Niebieskikwiat, D.; Sánchez, R. D.; Caneiro, A.; Morales, L.; Vásquez-Mansilla, M.; Rivadulla, F.; Hueso, L. E. High-temperature properties of the Sr_2FeMoO_6 double perovskite: Electrical resistivity, magnetic susceptibility, and ESR. *Phys. Rev. B* **2000,** *62*, 3340-3345.

139. Norris, D. J.; Efros, A. L.; Erwin, S. C. Doped Nanocrystals. *Science* **2008,** *319*, 1776.

140. Ochsenbein, S. T.; Feng, Y.; Whitaker, K. M.; Badaeva, E.; Liu, W. K.; Li, X.; Gamelin, D. R. Charge-controlled magnetism in colloidal doped semiconductor nanocrystals. *Nat. Nanotechnol.* **2009,** *4*, 681-687.

141. Oseroff, S. B.; Torikachvili, M.; Singley, J.; Ali, S.; Cheong, S. W.; Schultz, S. Evidence for collective spin dynamics above the ordering temperature in $La_{1-x}Ca_xMnO_{3+\delta}$. *Phys. Rev. B* **1996,** *53*, 6521-6525.

142. Pan, G.; Bai, X.; Yang, D.; Chen, X.; Jing, P.; Qu, S.; Zhang, L.; Zhou, D.; Zhu, J.; Xu, W.; Dong, B.; Song, H. Doping Lanthanide into Perovskite Nanocrystals: Highly Improved and Expanded Optical Properties. *Nano Lett.* **2017,** *17*, 8005-8011.

143. Parak, W. J.; Gerion, D.; Pellegrino, T.; Zanchet, D.; Micheel, C.; Williams, S. C.; Boudreau, R.; Gros, M. A. L.; Larabell, C. A.; Alivisatos, A. P. Biological applications of colloidal nanocrystals. *Nanotechnology* **2003,** *14*, R15-R27.

144. Parobek, D.; Dong, Y.; Qiao, T.; Son, D. H. Direct Hot-Injection Synthesis of Mn-Doped $CsPbBr_3$ Nanocrystals. *Chem. Mater.* **2018**.

145. Parobek, D.; Roman, B. J.; Dong, Y.; Jin, H.; Lee, E.; Sheldon, M.; Son, D. H. Exciton-to-Dopant Energy Transfer in Mn-Doped Cesium Lead Halide Perovskite Nanocrystals. *Nano Lett.* **2016,** *16*, 7376-7380.

146. Pedregosa, F.; Varoquaux, G.; Gramfort, A.; Michel, V.; Thirion, B.; Grisel, O.; Blondel, M.; Prettenhofer, P.; Weiss, R.; Dubourg, V.; Vanderplas, J.; Passos, A.; Cournapeau, D.; Brucher, M.; Perrot, M.; Duchesnay, É. Scikit-learn: Machine Learning in Python. *J. Mach. Learn. Res.* **2011,** *12*, 2825-2830.

147. Perdew, J. P.; Burke, K.; Ernzerhof, M. Generalized Gradient Approximation Made Simple. *Phys. Rev. Lett.* **1996,** *77*, 3865-3868.

148. *Phosphor Handbook*, 2nd ed.; Yen, W., Shionoya, S., Yamamoto, H., Eds.; CRC Press: Boca Raton, 2007.

149. Piepho, S. B.; Schatz, P. N. *Group theory in spectroscopy: with applications to magnetic circular dichroism*; Wiley: New York, 1983.

150. Pradhan, N.; Das Adhikari, S.; Nag, A.; Sarma, D. D. Luminescence, Plasmonic, and Magnetic Properties of Doped Semiconductor Nanocrystals. *Angew. Chem. Int. Ed.* **2017,** *56*, 7038-7054.

151. Protesescu, L.; Yakunin, S.; Bodnarchuk, M. I.; Krieg, F.; Caputo, R.; Hendon, C. H.; Yang, R. X.; Walsh, A.; Kovalenko, M. V. Nanocrystals of Cesium Lead Halide Perovskites ($CsPbX_3$, X = Cl, Br, and I): Novel Optoelectronic Materials Showing Bright Emission with Wide Color Gamut. *Nano Lett.* **2015,** *15*, 3692-6.

152. Pu, C.; Ma, J.; Qin, H.; Yan, M.; Fu, T.; Niu, Y.; Yang, X.; Huang, Y.; Zhao, F.; Peng, X. Doped Semiconductor-Nanocrystal Emitters with Optimal Photoluminescence Decay Dynamics in Microsecond to Millisecond Range: Synthesis and Applications. *ACS Cent. Sci.* **2016,** *2*, 32-9.

153. Puchala, B.; Van der Ven, A. Thermodynamics of the Zr-O system from first-principles calculations. *Phys. Rev. B* **2013,** *88*, 094108.

154. Puglisi, A.; Mondini, S.; Cenedese, S.; Ferretti, A. M.; Santo, N.; Ponti, A. Monodisperse Octahedral α-MnS and MnO Nanoparticles by the Decomposition of Manganese Oleate in the Presence of Sulfur. *Chem. Mater.* **2010,** *22*, 2804-2813.

155. Puntes, V. F.; Zanchet, D.; Erdonmez, C. K.; Alivisatos, A. P. Synthesis of hcp-Co nanodisks. *J. Am. Chem. Soc.* **2002,** *124*, 12874-12880.

156. Regulacio, M. D.; Kar, S.; Zuniga, E.; Wang, G.; Dollahon, N. R.; Yee, G. T.; Stoll, S. L. Size-Dependent Magnetism of EuS Nanoparticles. *Chem. Mater.* **2008,** *20*, 3368-3376.

157. Regulacio, M. D.; Tomson, N.; Stoll, S. L. Dithiocarbamate Precursors for Rare-Earth Sulfides. *Chem. Mater.* **2005,** *17*, 3114-3121.

158. Reisner, A.; Kasinathan, D.; Wirth, S.; Tjeng, L. H.; Altendorf, S. G. Valence state of Sm in single-crystalline EuO thin films. *EPL* **2017,** *117*, 47001.

159. Richter, N.; Weber, D.; Martin, F.; Singh, N.; Schwingenschlögl, U.; Lotsch, B. V.; Kläui, M. Temperature-dependent magnetic anisotropy in the layered magnetic semiconductors CrI_3 and $CrBr_3$. *Phys. Rev. Mater.* **2018,** *2*, 024004.

160. Sanchez, J. M.; Ducastelle, F.; Gratias, D. Generalized cluster description of multicomponent systems. *Physica A* **1984,** *128*, 334-350.

161. Santos, T. S.; Moodera, J. S.; Raman, K. V.; Negusse, E.; Holroyd, J.; Dvorak, J.; Liberati, M.; Idzerda, Y. U.; Arenholz, E. Determining Exchange Splitting in a Magnetic Semiconductor by Spin-Filter Tunneling. *Phys. Rev. Lett.* **2008,** *101*, 147201.

162. Schimpf, A. M.; Knowles, K. E.; Carroll, G. M.; Gamelin, D. R. Electronic Doping and Redox-Potential Tuning in Colloidal Semiconductor Nanocrystals. *Acc. Chem. Res.* **2015,** *48*, 1929-1937.

163. Schneider, C. A.; Rasband, W. S.; Eliceiri, K. W. NIH Image to ImageJ: 25 years of image analysis. *Nat. Methods* **2012,** *9*, 671-675.

164. Schoenes, J. Magnetooptik und elektronische struktur der magnetisch ordnenden europiumchalkogenide. *Z. Physik B* **1975,** *20*, 345-368.

165. Schoenes, J.; Wachter, P. Exchange optics in Gd-doped EuO. *Phys. Rev. B* **1974,** *9*, 3097-3105.

166. Scholz, G.; Dörfel, I.; Heidemann, D.; Feist, M.; Stösser, R. Nanocrystalline CaF_2 particles obtained by high-energy ball milling. *J. Solid State Chem.* **2006,** *179*, 1119-1128.

167. Selinsky, R. S.; Han, J. H.; Morales Pérez, E. A.; Guzei, I. A.; Jin, S. Synthesis and Magnetic Properties of Gd Doped EuS Nanocrystals with Enhanced Curie Temperatures. *J. Am. Chem. Soc.* **2010,** *132*, 15997-16005.

168. Selinsky, R. S.; Keavney, D. J.; Bierman, M. J.; Jin, S. Element-specific magnetometry of EuS nanocrystals. *Appl. Phys. Lett.* **2009,** *95*, 202501.

169. Seyler, K. L.; Zhong, D.; Klein, D. R.; Gao, S.; Zhang, X.; Huang, B.; Navarro-Moratalla, E.; Yang, L.; Cobden, D. H.; McGuire, M. A.; Yao, W.; Xiao, D.; Jarillo-Herrero, P.; Xu, X. Ligand-field helical luminescence in a 2D ferromagnetic insulator. *Nat. Physics* **2018,** *14*, 277-281.

170. Shamsi, J.; Urban, A. S.; Imran, M.; Trizio, L. D.; Manna, L. Metal halide perovskite nanocrystals: synthesis, post-synthesis modifications, and their optical properties. *Chem. Rev.* **2019,** *119*, 3296-3348.

171. Shinagawa, K.; Sato, H.; Ross, H. J.; McAven, L. F.; Butler, P. H. Charge-transfer transitions in chromium trihalides. *J. Phys.: Cond. Matter* **1996,** *8*, 8457-8463.

172. Šimánek, E.; Müller, K. A. Covalency and hyperfine structure constant A of iron group impurities in crystals. *J. Phys. Chem. Solids* **1970,** *31*, 1027-1040.

173. Sivadas, N.; Okamoto, S.; Xu, X.; Fennie, C. J.; Xiao, D. Stacking-dependent magnetism in bilayer CrI_3. *Nano Lett.* **2018,** *18*, 7658-7664.

174. Smith, A. M.; Nie, S. Semiconductor Nanocrystals: Structure, Properties, and Band Gap Engineering. *Acc. Chem. Res.* **2010,** *43*, 190-200.

175. Song, T.; Cai, X.; Tu, M. W.-Y.; Zhang, X.; Huang, B.; Wilson, N. P.; Seyler, K. L.; Zhu, L.; Taniguchi, T.; Watanabe, K.; McGuire, M. A.; Cobden, D. H.; Xiao, D.; Yao, W.; Xu, X. Giant tunneling magnetoresistance in spin-filter van der Waals heterostructures. *Science* **2018,** *360*, 1214-1218.

176. Soriano, D.; Cardoso, C.; Fernandez-Rossier, J. Interplay between interlayer exchange and stacking in CrI_3 bilayers. *Solid State Commun.* **2019,** *299*, 113662.

177. Soulen, R. J.; Byers, J. M.; Osofsky, M. S.; Nadgorny, B.; Ambrose, T.; Cheng, S. F.; Broussard, P. R.; Tanaka, C. T.; Nowak, J.; Moodera, J. S.; Barry, A.; Coey, J. M. D. Measuring the Spin Polarization of a Metal with a Superconducting Point Contact. *Science* **1998,** *282*, 85.

178. Steeneken, P. G.; Tjeng, L. H.; Elfimov, I.; Sawatzky, G. A.; Ghiringhelli, G.; Brookes, N. B.; Huang, D. J. Exchange Splitting and Charge Carrier Spin Polarization in EuO. *Phys. Rev. Lett.* **2002,** *88*, 047201.

179. Stefan, M.; Nistor, S. V.; Ghica, D.; Mateescu, C. D.; Nikl, M.; Kucerkova, R. Substitutional and surface Mn^{2+} centers in cubic ZnS:Mn nanocrystals. A correlated EPR and photoluminescence study. *Phys. Rev. B* **2011,** *83*, 045301.

180. Stoll, S.; Schweiger, A. EasySpin, a comprehensive software package for spectral simulation and analysis in EPR. *J. Magn. Reson.* **2006,** *178*, 42-55.

181. Swarnkar, A.; Marshall, A. R.; Sanehira, E. M.; Chernomordik, B. D.; Moore, D. T.; Christians, J. A.; Chakrabarti, T.; Luther, J. M. Quantum dot–induced phase stabilization of α-$CsPbI_3$ perovskite for high-efficiency photovoltaics. *Science* **2016,** *354*, 92-95.

182. Talapin, D. V.; Lee, J.-S.; Kovalenko, M. V.; Shevchenko, E. V. Prospects of Colloidal Nanocrystals for Electronic and Optoelectronic Applications. *Chem. Rev.* **2010,** *110*, 389-458.

183. Tang, W.; Sanville, E.; Henkelman, G. A grid-based Bader analysis algorithm without lattice bias. *J. Phys.: Condens. Matter* **2009,** *21*, 084204.

184. Taube, H. Rates and mechanisms of substitution in inorganic complexes in solution. *Chem. Rev.* **1952,** *50*, 69-126.

185. Thanh, N. T. K.; Maclean, N.; Mahiddine, S. Mechanisms of nucleation and growth of nanoparticles in solution. *Chem. Rev.* **2014,** *114*, 7610-7630.

186. Thompson, D. A.; Best, J. S. The future of data storage technology. *IBM J. Res. Dev.* **2000,** *44*, 311–322.

187. Tse, D.; Hartmann, S. R. Nuclear Spin-Lattice Relaxation Via Paramagnetic Centers Without Spin Diffusion. *Phys. Rev. Lett.* **1968,** *21*, 511-514.

188. Tsubokawa, I. On the magnetic properties of a $CrBr_3$ single crystal. *J. Phys. Soc. Jpn.* **1960,** *15*, 1664-1668.

189. Tsui, E. Y.; Hartstein, K. H.; Gamelin, D. R. Selenium Redox Reactivity on Colloidal CdSe Quantum Dot Surfaces. *J. Am. Chem. Soc.* **2016,** *138*, 11105-11108.

190. Tsukahara, Y.; Kataoka, T.; Hasegawa, Y.; Kaizaki, S.; Wada, Y. The first observation of the magnetic circular dichroism in EuS nanocrystals. *J. Alloys Compd.* **2006,** *408-412*, 203-206.

191. Turov, E. A. Line width of ferromagnetic resonance absorption. In *Ferromagnetic Resonance*; Vonsovskii, S. V., Ed.; Pergamon: London, 1966; pp 184-230.

192. Ubrig, N.; Wang, Z.; Teyssier, J.; Taniguchi, T.; Watanabe, K.; Giannini, E.; Morpurgo, A. F.; Gibertini, M. Low-temperature monoclinic layer stacking in atomically thin CrI_3 crystals. *2D Mater.* **2019,** *7*, 015007.

193. Vaills, Y.; Buzaré, J. Y. EPR studies of Gd^{3+} centres in the cubic phase of $CsCaCl_3$ and $CsPbCl_3$. *J. Phys. Chem. Solids* **1987,** *48*, 363-370.

194. van de Walle, A. Multicomponent multisublattice alloys, nonconfigurational entropy and other additions to the Alloy Theoretic Automated Toolkit. *Calphad* **2009,** *33*, 266-278.

195. van de Walle, A.; Asta, M. Self-driven lattice-model Monte Carlo simulations of alloy thermodynamic properties and phase diagrams. *Modell. Simul. Mater. Sci. Eng.* **2002,** *10*, 521.

196. van de Walle, A.; Ceder, G. Automating first-principles phase diagram calculations. *J. Phase Equilib.* **2002,** *23*, 348.

197. van der Stam, W.; Geuchies, J. J.; Altantzis, T.; van den Bos, K. H. W.; Meeldijk, J. D.; Van Aert, S.; Bals, S.; Vanmaekelbergh, D.; de Mello Donega, C. Highly Emissive Divalent Ion Doped Colloidal $CsPb_{1-x}M_xBr_3$ Perovskite Nanocrystals through Cation Exchange. *J. Am. Chem. Soc.* **2017,** *139*, 4087–4097.

198. Van der Ven, A.; Thomas, J. C.; Xu, Q.; Bhattacharya, J. Linking the electronic structure of solids to their thermodynamic and kinetic properties. *Math. Comput. Simulat.* **2010,** *80*, 1393-1410.

199. Vercaemst, R.; Poelman, D.; Fiermans, L.; Van Meirhaeghe, R. L.; Laflère, W. H.; Cardon, F. A detailed XPS study of the rare earth compounds EuS and EuF_3. *J. Electron. Spectrosc. Relat. Phenom.* **1995,** *74*, 45-56.

200. Viswanatha, R.; Pietryga, J. M.; Klimov, V. I.; Crooker, S. A. Spin-Polarized Mn^{2+} Emission from Mn-Doped Colloidal Nanocrystals. *Phys. Rev. Lett.* **2011,** *107*, 067402.

201. Vlaskin, V. A.; Janßen, N.; van Rijssel, J.; Beaulac, R.; Gamelin, D. R. Tunable Dual Emission in Doped Semiconductor Nanocrystals. *Nano Lett.* **2010,** *10*, 3670–3674.

202. von Molnár, S.; Kasuya, T. Evidence of Band Conduction and Critical Scattering in Dilute Eu-Chalcogenide Alloys. *Phys. Rev. Lett.* **1968,** *21*, 1757-1761.

203. von Molnar, S.; Lawson, A. W. Ferromagnetic and Paramagnetic Resonance in EuS. *Phys. Rev.* **1965,** *139*, A1598-A1602.

204. Wachter, P. The optical electrical and magnetic properties of the europium chalcogenides and the rare earth pnictides. *Crit. Rev. in Solid State Sci.* **1972,** *3*, 189-241.

205. Wachter, P. Europium chalcogenides: EuO, EuS, EuSe and EuTe. In *Handbook on the Physics and Chemistry of Rare Earths*; Elsevier: North-Holland, 1979; Vol. 2, pp 507-574.

206. Wang, Q.; Zhang, X.; Jin, Z.; Zhang, J.; Gao, Z.; Li, Y.; Liu, S. F. Energy-Down-Shift $CsPbCl_3$:Mn Quantum Dots for Boosting the Efficiency and Stability of Perovskite Solar Cells. *ACS Energy Lett.* **2017,** *2*, 1479-1486.

207. Weinstein, J. S.; Varallyay, C. G.; Dosa, E.; Gahramanov, S.; Hamilton, B.; Rooney, W. D.; Muldoon, L. L.; Neuwelt, E. A. Superparamagnetic Iron Oxide Nanoparticles: Diagnostic Magnetic Resonance Imaging and Potential Therapeutic Applications in Neurooncology and Central Nervous System Inflammatory Pathologies, a Review. *J. Cereb. Blood Flow Metab.* **2009,** *30*, 15-35.

208. Weller, D.; Moser, A. Thermal effect limits in ultrahigh-density magnetic recording. *IEEE Trans. Magn.* **1999,** *35*, 4423–4439.

209. Wolf, S. A.; Awschalom, D. D.; Buhrman, R. A.; Daughton, J. M.; von Molnár, S.; Roukes, M. L.; Chtchelkanova, A. Y.; Treger, D. M. Spintronics: A Spin-Based Electronics Vision for the Future. *Science* **2001,** *294*, 1488.

210. Wong, A.; Sham, S.; Wang, S.; Wu, G. A solid-state ^{133}Cs nuclear magnetic resonance and X-ray crystallographic study of cesium complexes with macrocyclic ligands. *Can. J. Chem.* **2000,** *78*, 975-985.

211. Xu, C.; Feng, J.; Xiang, H.; Bellaiche, L. Interplay between Kitaev interaction and single ion anisotropy in ferromagnetic CrI_3 and $CrGeTe_3$ monolayers. *npj Comp. Mater.* **2018,** *4*, 57.

212. Xu, K.; Lin, C. C.; Xie, X.; Meijerink, A. Efficient and Stable Luminescence from Mn^{2+} in Core and Core-Isocrystalline Shell $CsPbCl_3$ Perovskite Nanocrystals. *Chem. Mater.* **2017,** *29*, 4265-4272.

213. Xu, K.; Meijerink, A. Tuning Exciton–Mn^{2+} Energy Transfer in Mixed Halide Perovskite Nanocrystals. *Chem. Mater.* **2018,** *30*, 5346-5352.

214. Xu, W.; Li, F.; Lin, F.; Chen, Y.; Cai, Z.; Wang, Y.; Chen, X. Synthesis of $CsPbCl_3$-Mn Nanocrystals via Cation Exchange. *Adv. Opt. Mater.* **2017,** *5*, 1700520.

215. Yang, H.; Wang, F.; Zhang, H.; Guo, L.; Hu, L.; Wang, L.; Xue, D.-J.; Xu, X. Solution Synthesis of Layered van der Waals (vdW) Ferromagnetic $CrGeTe_3$ Nanosheets from a Non-vdW Cr_2Te_3Template. *J. Am. Chem. Soc.* **2020**, *142*, 4438-4444.

216. Yang, J.; Choi, M. K.; Kim, D.-H.; Hyeon, T. Designed Assembly and Integration of Colloidal Nanocrystals for Device Applications. *Adv. Mater.* **2016,** *28*, 1176-1207.

217. Yin, W.-J.; Yan, Y.; Wei, S.-H. Anomalous Alloy Properties in Mixed Halide Perovskites. *J. Phys. Chem. Lett.* **2014,** *5*, 3625-3631.

218. Yu, M. K.; Jeong, Y. Y.; Park, J.; Park, S.; Kim, J. W.; Min, J. J.; Kim, K.; Jon, S. Drug-Loaded Superparamagnetic Iron Oxide Nanoparticles for Combined Cancer Imaging and Therapy In Vivo. *Angew. Chem. Int. Ed.* **2008,** *47*, 5362-5365.

219. Yuan, X.; Ji, S.; De Siena, M. C.; Fei, L.; Zhao, Z.; Wang, Y.; Li, H.; Zhao, J.; Gamelin, D. R. Photoluminescence Temperature Dependence, Dynamics, and Quantum Efficiencies in Mn^{2+}-Doped $CsPbCl_3$ Perovskite Nanocrystals with Varied Dopant Concentration. *Chem. Mater.* **2017,** *29*, 8003-8011.

220. Zhang, H.; Jin, M.; Xia, Y. Noble-Metal Nanocrystals with Concave Surfaces: Synthesis and Applications. *Angew. Chem. Int. Ed.* **2012,** *51*, 7656-7673.

221. Zhang, J.; Wang, Q.; Zhang, X.; Jiang, J.; Gao, Z.; Jin, Z.; Liu, S. High-performance transparent ultraviolet photodetectors based on inorganic perovskite $CsPbCl_3$ nanocrystals. *RSC Adv.* **2017,** *7*, 36722-36727.

222. Zhang, X.; Lin, H.; Huang, H.; Reckmeier, C.; Zhang, Y.; Choy, W. C. H.; Rogach, A. L. Enhancing the Brightness of Cesium Lead Halide Perovskite Nanocrystal Based Green Light-Emitting Devices through the Interface Engineering with Perfluorinated Ionomer. *Nano Lett.* **2016,** *16*, 1415.

223. Zhao, F.; Sun, H.-L.; Gao, S.; Su, G. Magnetic properties of EuS nanoparticles synthesized by thermal decomposition of molecular precursors. *J. Mater. Chem.* **2005,** *15*, 4209-4214.

224. Zhao, F.; Sun, H.-L.; Su, G.; Gao, S. Synthesis and Size-Dependent Magnetic Properties of Monodisperse EuS Nanocrystals. *Small* **2006,** *2*, 244-248.

225. Zhao, Y.; Rabouw, F. T.; van Puffelen, T.; van Walree, C. A.; Gamelin, D. R.; de Mello Donegá, C.; Meijerink, A. Lanthanide-Doped CaS and SrS Luminescent Nanocrystals: A Single-Source Precursor Approach for Doping. *J. Am. Chem. Soc.* **2014,** *136*, 16533-16543.

226. Zheng, W.-C. Investigation of the EPR spectra of $CsPbCl_3:Mn^{2+}$ and $CsSrCl_3:Mn^{2+}$ in the cubic-tetragonal phase transition. *Ferroelectrics* **1995,** *166*, 91-94.

227. Zhou, K.; Li, Y. Catalysis Based on Nanocrystals with Well-Defined Facets. *Angew. Chem. Int. Ed.* **2012,** *51*, 602-613.

228. Zinn, W. Microscopic studies of magnetic properties and interactions recent results on europium-monochalcogenides. *J. Magn. Magn. Mater.* **1976,** *3*, 23-36.

229. Zou, S.; Liu, Y.; Li, J.; Liu, C.; Feng, R.; Jiang, F.; Li, Y.; Song, J.; Zeng, H.; Hong, M.; Chen, X. Stabilizing Cesium Lead Halide Perovskite Lattice through Mn(II)-Substitution for Air-Stable Light-Emitting Diodes. *J. Am. Chem. Soc.* **2017,** *139*, 11443–11450.

230. Zverev, G. M.; Prokhorov, A. M. Electron Paramagnetic Resonance and Spin-Lattice Relaxation of Co^{2+} in Corundum. *Sov. Phys. JETP* **1961,** *12*, 41-45.